NDT-based Performance Prediction for Wrinkled Composites under Compressive Load

by

Ningbo Xie

Department of Mechanical Engineering

A dissertation submitted to the University of Bristol in accordance with the requirements for award of the degree of Doctor of Philosophy in the Faculty of Engineering in September 2018.

Word count: Approx. 45,000

Abstract

The work in this thesis aimed to develop a method to transfer the three-dimensional (3D) non-destructive characterised data into finite-element models containing as-manufactured structural details. Two types of fibre-misalignment defects: out-of-plane wrinkles and in-plane waviness, were investigated and a quasi-isotropic layup $[45^o/90^o/-45^o/0^o]_{ns}$ was chosen as the representative industrial layup sequence for validation purposes. A pivotal part of the work was the development of the transfer process to automatically and faithfully convert the output of non-destructive characterisation inversion methods into finite-element models containing these two types of defect.

For out-of-plane wrinkles, using this transfer method and previously validated modelling techniques, a series of models were exercised under compressive load to identify the hierarchy and interdependences of wrinkle parameters, covering the wrinkle severity, shape and extent. The outcome indicated that the maximum out-of-plane wrinkle angle from the load direction was the governing factor to influence the compressive strength and this should be the key parameter to be measured non-destructively when wrinkles are detected in the components.

For in-plane waviness, it was studied both experimentally and numerically. First, the in-plane waviness was introduced into 0° plies by a specially designed rig and four waviness-severity coupons were manufactured to investigate the compressive damage process influenced by this in-plane waviness. Two High-speed cameras were used, focusing on the edge and the front face of the coupon waviness region to capture the failure modes and their sequences. X-ray CT techniques were also applied to identify the internal failure activities when the loading process was interrupted for some samples, before the ultimate damage was reached. Numerical models were then created in Abaqus/Explicit following a similar method to the out-of-plane case but requiring significant further development in order to faithfully model samples that could also be created experimentally. These were validated against the experimental recordings. Both experimental and numerical studies showed the dominant failure modes were delamination and splitting due to in-plane waviness incorporated in the samples.

Acknowledgements

First, I would like to express my sincere gratitude to my supervisors, Prof. Robert Smith and Prof. Stephen Hallett, for their precious and continuous support during my PhD study period. Without their help and encouragement, this work would definitely not come to shape. Thanks for their valuable suggestions and trust when I came across problems during the research, from which I solved the problem and also gained my confidence gradually.

During this nearly four-year time, I have obtained such a lot help from many people, including UNDT composites team, lab support team, lab technicians and many other people. Special thanks should be mentioned for the help of numerical models from Dr. Supratik Mukhopadhyay, he helped me a lot to learn numerical models from zero. Dr. Bing Zhang should also be thanked for his help for my model learning process. Thank Dr. Antonio Melro for his help about the work related to fibre volume fraction in this thesis. I would also like to show my thanks to Mr Mike Jones, he has given me many useful suggestions and help to manufacture high-quality specimens. Miss Christina Fraij is another person who should be mentioned, she helped me to do the CT scans and we often had chat and attended conferences together during these years.

Great thanks to Engineering and Physical Sciences Research Council (EPSRC), UK, for the financial support, and thank Rolls-Royce plc for the permission to use data from reference [1].

Last but not the least, I would express my great thanks to my parents for their endless support all the time, not just these four years. Just because of their love, support and encouragement, I can always pursue my dreams. Thank all my friends and other family members to make me what I am today.

Author’s declaration

I declare that the work in this dissertation was carried out in accordance with the requirements of the University's *Regulations and Code of Practice for Research Degree Programmes* and that it has not been submitted for any other academic award. Except where indicated by specific reference in the text, the work is the candidate's own work. Work done in collaboration with, or with the assistance of, others, is indicated as such. Any views expressed in the dissertation are those of the author.

SIGNED: .....Ningbo Xie..... DATE:.....28/09/2018.....

Table of Contents

List of Figures

List of Tables

List of symbols

Chapter 2

ϕ_0: the angle of fracture plane with the through-the-thickness direction when suffering matrix cracking

σ_{11} & σ_{22}: longitudinal stress and transverse stress

τ_{12}: in-plane shear stress

Y_c: transverse compressive strength

σ_n, τ_T & τ_L: normal stress and two shear stress components acting on the fracture plane

S_T & S_L: transverse and longitudinal shear strength

μ_T & μ_L: frictional coefficients at transverse and longitudinal direction

τ_{eff}^{T} & τ_{eff}^{L}: effective transverse and longitudinal shear stress on the facture plane

Subscript m: represents the calculation will be done on the misalignment frame

Subscript is: stands for the in-situ effect

w: kink-band width

θ: fibre-rotation angle

β: the angle between the kink-band to the plane normal to the loading direction

θ_i: initial fibre misalignment angle

X_c: compressive failure stress

γ_0: shear strain at fibre failure

σ_a, σ_b & τ_{ab}: normal stress, transverse stress and shear stress in 2D fibre misalignment frame before fibre rotation

σ_{a^m}, σ_{b^m} & $\tau_{a^m b^m}$: normal stress, transverse stress and shear stress in 2D fibre misalignment frame after fibre rotation

θ_C: fibre misalignment angle at fibre failure

G: strain-energy-release rate

K: stress-intensity factors or stiffness

G_{I}, G_{II} or G_{III}: energy release rate for crack mode I, II or III

G_c: critical energy release rate

σ: traction in cohesive zone modelling technique

δ: separation (displacement) in cohesive zone modelling technique

δ_f: separation at the full failure in cohesive zone modelling technique

α: coefficient used in power law to adjust the criterion to best fit the specific material

η: coefficient used in B-K law to reflect the different mode ratios

G_{I} & G_{II}: energy release rate for pure Mode I and Mode II

G_{IC} & G_{IIC}: critical energy release rate for pure Mode I and Mode II

$(\delta, \lambda, \theta)$: one method to stands for wrinkle amplitude, wavelength and maximum angle

(A, L, θ): another method to stands for wrinkle amplitude, wavelength and maximum angle, or represents waviness amplitude, wavelength and maximum angle.

D: damage variable

F: force

A_d: area caused by cracks

A: nominal area without any crack

$\tilde{\sigma}$: effective stress

σ: nominal stress

σ_{1i} & γ_{1i}: shear stress and shear strain (engineering).

σ_{max}: interface strength

δ_e: displacement at the onset of delamination

δ_m: mixed-mode displacement

δ_{I} & δ_{II}: pure opening and shear mode displacement

σ_{I} & σ_{II}; stress in pure opening and shear mode

$\sigma_{\mathrm{I}}^{max}$ & $\sigma_{\mathrm{II}}^{max}$: strength in pure opening and shear mode

δ_m^e: displacement at the onset of delamination in mixed mode

δ_m^f: displacement at full failure in mixed mode

K_{I} & K_{II}: tensile and shear stiffness

σ_{I}^Y & σ_{II}^Y: yield stresses for opening and shear modes

θ_{I} and θ_{II}: angle of mode I or mode II to the mixed mode

τ_{mat}: resultant shear stress of matrix cracking

σ_{mat}: driving stress of matrix cracking

ε_{mat}^0 & σ_{mat}^0: strain and maxim driving stress at failure initiation point of matrix cracking

ε_{mat}^f: strain at complete failure of matrix cracking

G_{mat}: critical energy release rate of matrix cracking

G_n, G_T & G_L: energy release rates of normal and two shear modes under matrix cracking

L_{mat}: characteristic length under matrix cracking

D_{mat}: damage variable to govern matrix cracking

ψ: the angle of rotation to form a kink plane

γ_{mi}: shear strain at the initial misalignment frame in 3D kink mechanism

G_{kink}: fibre fracture energy

ε_{kink}^f: strain at complete fibre failure

D_{kink}: damage variable to govern fibre failure

Chapter 3

$\overrightarrow{OA}$: vector to stands for local fibre-tow orientation

$\overrightarrow{OB}$: vector to stands for that vertical to fibre tows within the plane

$\overrightarrow{OC}$: vector to stands for that vertical the plane where fibre tows are aligned

θ: out-of-plane fibre orientation

φ: in-plane fibre orientation

(X, Y, Z): global coordinate system

(A, B, C): local coordinate system

d: wrinkle displacement (fibre misaligned undulation)

A: wrinkle amplitude

L: wrinkle wavelength

w_1: Wrinkle Gaussian Half-Width

θ_a: maximum wrinkle angle measured from the coupon edge

θ_b: maximum wrinkle angle in the simulator by taking the arc-tangent of the maximum of the first-order derivative of the used equation

θ_c: maximum wrinkle angle measured from the reconstructed FE-mesh image

Chapter 4

θ: maximum wrinkle angle

x_0: wrinkle-centre location

x_1: x-offset phase parameter

A_0: wrinkle amplitude at the wrinkle's centre

(x_0, y_0, i_0): the centre of the wrinkle

w_2: Transverse Wrinkle Half-Width

n: Wrinkle Half-Height

i: interface index

A_i: wrinkle amplitude in the ith interface

$A_{i_{mid}}$: mid-ply wrinkle amplitude

FVF_{local}: local FVF

FVF_{nom}: nominal FVF

$thickness_{local}$: local ply thickness

$thickness_{nom}$: nominal ply thickness

CV: coefficient of variance

y_{width}: the width of the model or the coupon

$z_{thickness}$: the thickness of the model or the coupon

$Area\_wrinkle$: the area of the wrinkle based on the defined iso-amplitude

$Cross\ Sectional\ Area(\%)$: the percentage of the wrinkle area to the total cross-sectional area, based on the defined iso-amplitude

N: total number of plies

a: suggested parameter to combine w_2 and n

Chapter 5

A: waviness amplitude

L: waviness wavelength

θ_{max}: maximum waviness angle

θ_{5c}: measured maximum waviness angle on uncured ply with low-amplitude waviness

θ_{10c}: measured maximum waviness angle on uncured ply with high-amplitude waviness

θ_1: measured maximum waviness angle on a wavy ply from the coupon of Level-1-Mid

θ_2: measured maximum waviness angle on a wavy ply from the coupon of Level-1-All

θ_3: measured maximum waviness angle on a wavy ply from the coupon of Level-2-Mid

θ_4: measured maximum waviness angle on a wavy ply from the coupon of Level-2-All

Chapter 6

i: element ID

Δy_i: y-coordinate movement of the ith element

x_i: length in x direction of the ith element, obtained from Map-A

φ_i: in-plane fibre orientation of the ith element, obtained from Map-B

u_1^A, u_2^A or u_3^A: x, y or z -direction displacement of node in group A

u_1^B, u_2^B or u_3^B: x, y or z -direction displacement of node in group B

a: waviness-region length

w: waviness-region width

List of Abbreviations

AFP: automated fibre placement

CDM: Continuum damage mechanics

CFRP: carbon-fibre reinforced polymer

CT: computed tomography

CTE: coefficients of thermal expansion

CZM: cohesive zone model or cohesive zone modelling

ET: eddy current testing

FE: finite element

FFT: fast Fourier transformation

FMC: Full Matrix Capture

FVF: fibre volume fraction

ICST: Imperial College standard test

MC: matrix cracking

MFIA: multiple field image analysis

NDT: non-destructive testing

PBCs: periodic boundary conditions

RTM: resin transfer moulding

TFM: Total Focusing Method

UT: ultrasonic testing

VCCT: Virtual Crack Closure Technique

2D: two-dimensional or two dimensions

3D: three-dimensional or three dimensions

List of Nomenclature

C3D8R: 8-node linear-brick solid elements with a reduced integration algorithm

COH3D8: 8-node cohesive elements

GUI: Graphical User Interface

Level-1-Mid: middle two 0° plies with low-amplitude waviness

Level-1-All: all four 0° plies with low-amplitude waviness

Level-2-Mid: middle two 0° plies with high-amplitude waviness

Level-2-All: all four 0° plies with high-amplitude waviness

Map-A: Ply-Interface Depth map

Map-B: In-plane Orientation map

Rectangular-mesh: mesh using normal rectangular-shaped brick elements

Skew-mesh: mesh using skewed brick elements

VUMAT: user-defined subroutine to define the mechanical constitutive behaviour of a material and specifically suitable for Abaqus/Explicit.

Chapter 1
Introduction

1.1 General description

Composite materials, particularly continuous fibre-reinforced polymer composites, have been increasingly applied for the manufacture of structural components across a variety of fields, from sports applications to the aviation industry. In the latter, the design and manufacture of components using these materials has been highly advantageous due to their outstanding structural performance and low weight. The latest generation of civil aircraft, namely the Boeing 787 [2] and A350 XWB [3], have at least 50% composite materials used in their structures. However, unlike traditional materials such as metal that behave in an isotropic manner, composites show directional preferences depending upon the fibre alignment; hence, the design and manufacturing theory and relative potential failure criteria of composites needs to be developed and better understood. Distinct types of imperfections, or deviations from the design and material specifications, can arise during the manufacturing process. Depending on the structural characteristics of composites, these imperfections can be characterised as fibre-path misalignment, missing plies, porosity, inclusion of foreign objects, or variation of local fibre volume fraction (FVF) etc. These phenomena can affect the fibres, surrounding matrix, or the interfaces between them.

Compared with destructive testing methods used to identify and verify the internal micro- and meso-structures of composite materials and components, the non-destructive testing (NDT) approach is widely used to assist in the design, manufacturing, and service stages, as it provides internal information without causing any damage to the components or structures. Among NDT techniques available, ultrasonic and X-ray computed tomography (CT) are the most frequently used methods for the non-destructive inspection of composites. Beyond conventional inspection methods, NDT-acquired data can be used by state-of-the-art NDT inversion methods to further characterise the geometry of the structures [4–7] and even reconstruct the material properties encompassed in them

[8,9]. These characterisation outputs can be in either in two dimensions (2D) or three dimensions (3D).

1.2 Thesis motivations and objectives

The features of the interfaces between layers or plies in laminated composites make the performance characteristics, failure modes, failure initiation and defect propagation of this material dependant on the extent of conformance to the designed configurations and fibre orientations. This needs to be better understood to assist with the design, manufacturing, and in-service stages of composites. Dependant on the development of finite-element modelling (FE) technique and three-dimensional (3D) non-destructive characterisation, there is the possibility to combine them (FE & 3D-characterisation techniques) to create models containing as-manufactured structural details, in order to understand the composites failure process, whilst replacing excessive experimental work. The first objective of this thesis is to develop a transfer-process 'bridge' to convert the inverted NDT information into numerical models for mechanical-performance estimations. The models, relying on the inverted data, would comprise more specific geometrical details, as manufactured in a particular component.

Fibre misalignment, forming as either out-of-plane wrinkles or in-plane waviness, can cause a sudden and catastrophic failure under quasi-static compressive load. Although the negative effects from out-of-plane wrinkles have been identified in previous research, such as that of Mukhopadhyay et al. [1], it is still not clear which key parameters govern the knock-down of compressive failure strength, or which geometric aspect should be emphasised in the evaluation process when a wrinkle has already arisen in a structure. For identifying and understanding the interdependencies of out-of-plane wrinkle parameters, a second objective of the thesis is a systematic and rigorous multi-dimensional parametric study, aiming to provide some guidance to the design, manufacturing, and NDT inspection stages for the composites.

Unlike the numerous studies for out-of-plane wrinkles, literature about the effect of in-plane waviness is relatively limited due to the difficulty of manually introducing controllable waviness into laminates.

The third objective in this thesis is to introduce in-plane waviness into an IM7/8552 laminate in the 0^o plies at the designed severity in a controlled manner and link the experimental performance of these laminates to an FE-modelling approach. The choice of using pre-preg lamina IM7/8852 instead of resin-infused dry fibre was for the purpose of the numerical modelling study as the material properties of IM7/8552 have been extensively identified in previous research, e.g. [1] [10][11][12][13].

1.3 Structure of the thesis

Following the objectives stated above, the layout of this thesis after the literature review starts from the development of the transfer process and then moves to the study of the specific imperfections of fibre misalignment for both out-of-plane wrinkles and in-plane waviness. The detailed structure is as follows:

- Chapter 2 presents a literature review in the relevant fields that are covered in this thesis. The review begins with non-destructive characterisation techniques for carbon-fibre reinforced polymer (CFRP) composites. It then reviews the failure mechanisms of composites under quasi-static compressive load. After that, the review focuses on previous research on the effects of out-of-plane wrinkles and in-plane waviness, covering both experimental and numerical aspects. Subsequently, the continuum damage modelling technique, failure theories, and material properties used specifically in this thesis are presented. Finally, the major gaps in the literature that form the scope of the research in this thesis are stated.
- Chapter 3 develops the transfer process to combine the NDT-based characterisation technique with the finite-element modelling technique in an innovative way, for the realization of numerical-model creation based on the as-manufactured structural geometry and deviations from design. Two characterised material-property maps, storing the information of geometrical details and local in-plane fibre orientations, are generated by NDT inversion or simulation and can be applied to define the geometry of the numerical model through the transfer process. Two options are considered and provided in the transfer process: either a

uniform fibre volume fraction (FVF) in the whole model, or FVF changing inversely with the local ply thickness.

- Based on the existing experimental and numerical studies for the out-of-plane wrinkles accomplished by Mukhopadhyay et al. [1], chapter 4 develops out-of-plane wrinkle models by the transfer process using their modelling techniques and theories. The validation of these models also uses their experimental results [1]. After validation, a series of models is created to allow a systematic study of the key parameters for wrinkles governing the compressive strength among a range of parameters, including those defining wrinkle severity, shape and extent, which could provide guidance for non-destructive measurement. The investigation shows a dominant dependence on the wrinkle's maximum wrinkle angle, with an additional dependence on wavelength when this is small. Wrinkle extent also has some influence.
- Chapter 5 documents the experimental study for the laminates with manually introduced in-plane waviness. The waviness severity was controlled by a specially-designed rig and the wavy area was located at the central region along the coupon-length direction. Samples with four waviness-severity levels were tested under uniaxial compressive load until ultimate failure occurred. High-speed video was set up to capture the damage sequences and locations in the period immediately before the catastrophic failures. X-ray computed tomography (CT) technique was used to identify the internal damage events, when the loading process was interrupted before compressive failure and then subsequent dye penetrant was applied to the samples to enhance the imaging of the precursor damage.
- Following the in-plane waviness experimental study, chapter 6 documents the numerical study for in-plane waviness. The geometry of the model was based on the samples tested in chapter 5 and controlled by the transfer process. Finite-element models, containing the continuum damage modelling technique with cohesive zones at the ply interfaces and within the wavy plies were developed to simulate the failure events captured in chapter 5. The predicted failures were in good agreement with the observations in the experimental process. Further investigations using periodic boundary conditions (PBC) indicated that the

performance of samples containing in-plane waviness might be dominated by failure originating from the inevitable edge effect due to the finite sample width.

- Finally, in chapter 7, this thesis is completed by documenting conclusions based on the research. Possible future working directions and further potential improvements to the presented work are also listed.

Chapter 2

Literature review

2.1 Introduction

A composite material is a combination of two or more constituents [14] that forms a new material. This new material generally possesses better properties than its constituent parts or possesses a new property that the constituents do not include (assuming the combination is well designed). Based on the functions that the constituents within the composites provide, they are divided into the reinforcement-phase and the matrix-phase. Due to their high strength-to-weight ratio, fibre-reinforced composites have been widely used in weight sensitive sectors, such as the aerospace or automotive industries [14]. Among the diverse types of fibre-reinforced composites, carbon fibre is of more interest to the structural designers because of its high strength and stiffness along the fibres, combined with a low density. Pre-preg layup [14] is a process to manufacture high-performance composites, in order to achieve optimal properties at required load-bearing orientations, through carefully designing the layup sequences.

Conventionally, non-destructive testing (NDT) is a widely used tool to detect gross defects, such as delamination, porosity, etc., without causing any damage to the components. Beyond the very little information about the internal structures provided by the conventional NDT methods, new state-of-art methods [4–7,15–18] have been suggested to overcome this issue, dependent on the development of two-dimensional (2D) or three-dimensional (3D) inversion techniques for the data from these methods. In terms of the characterisation of fibre paths and variations from ideal trajectories in CFRP, eddy current [15,16], X-ray computed tomography (CT) [7] and ultrasonic techniques [4–6,17,18] are proposed. The development of this field using eddy currents is currently limited to the 2D response at the surface, so it is not currently capable of full 3D characterisation, while the latter two methods are more developed in 3D and more likely to be used in the industry. Due to these newly developed characterisation methods, it is possible to characterise the internal structural features of CFRP for

further research and analysis. Numerical models to estimate the mechanical performance of CFRP, based on these characterised outputs, are a typical and effective usage.

The theme of this thesis is to develop a transfer process which can combine both aspects: characterised NDT data of composites and numerical modelling techniques, to provide predictions of the mechanical performance, through creating numerical models based on the NDT data. Therefore, the sequence to review the literature starts with addressing the development of characterisation techniques based on NDT data for CFRP in section 2.2, in terms of the requirements for creating finite element (FE) meshes of coupon-sized components. A review of the major failure mechanisms for composites is in section 2.3. Following that, there is an examination of previous work regarding fibre misalignment imperfections (section 2.4), and a review focused on the specific numerical modelling techniques used in this thesis (section 2.5). Finally, the description of the research scope based on the literature is given in section 2.6.

2.2 Characterisation and Inversion Techniques Based on Non-Destructive Testing (NDT) Methods for CFRP

Recent research has been conducted aiming to characterise the as-manufactured structures with greatest accuracy through either a 2D- or 3D-characterisation process based on the eddy current, X-ray CT or ultrasonic techniques [4–7,15–18]. In order to create numerical models of CFRP comprising fibre misalignment based on those characterised data, at least three kinds of data are required: 1) ply-interface locations, 2) out-of-plane fibre angles and 3) in-plane fibre angles, on a minimum resolution of one element per ply in depth and covering the model size of a coupon. The lateral spacing of the data could be larger than that for the depth, which needs to be on a ply-by-ply basis, and the accuracy for the angle measurement should also be at its optimum capability of each method as the latter work (Chapter 4) in this thesis will show the significant influence of out-of-plane wrinkle angle on the compressive strength. Mechanical material properties could either be decided from the characterisation or be assigned in the numerical model directly if they are already known.

2.2.1 Characterisation based on eddy current testing (ET)

Compared with ultrasonic and X-ray CT testing methods, which offer full 3D capability at high resolution, the eddy current technique, is limited to providing a low-resolution understanding of the structure of CFRP in terms of dominant fibre alignments. More recent work is beginning to identify the distribution of fibre orientations as a function of depth location. However, this method is still in the early development stage to cover the 2D surface response and lacks capability to create the full 3D characterisation data for the FE model creation.

As early as 1994, Lange and Mook [19] used a rotating probe with high-frequency (above 7.5 MHz) eddy currents to measure the surface effects of a range of stacking sequences. They could measure fibre orientations when fibres deviated from 0^o by 3^o to 12^o in CFRP, their measurement could give an accuracy at $5.62° \pm 2.62°$ for 3^o case and $10.9° \pm 1.1°$ for 12^o case. However, their method was only capable to detect in-plane angles and did not relate to any out-of-plane fibre angle identifications or the distribution of the different orientations in the depth of the material. Subsequently in 2009, Yin et al. [20] identified the in-plane fibre orientation for unidirectional CFRP and cross-ply CFRP with a woven layer followed by a laminate stacking as [0^o/45^o/90^o/135^o], the cross-ply CFRP had suffered an impact damage before the eddy current scanning. Fibre orientations in both samples could be recognised, but their research just indicated the ability to identify the effect of in-plane fibre orientations at the surface, limited to 2D scope, in addition they did not comment on the accuracy of their measurement. Mook et al. [21] then also improved the capability to characterise in-plane fibre orientations for both unidirectional and [90^o/45^o/0^o/135^o] CFRP, they showed the penetration depth to be sensitive to in-plane fibre orientation up to 3 mm deep. Although their research was focused on 2D, as well, the improved sensitivity with a greater depth gave the potential to characterise more information, such as stacking sequence of a laminate. Heuer et al. [22,23] showed the identification of in-plane wavy regions in CFRP, as well, through detecting different samples with removing fibre bundles from specific layers. More recently, Mizukami et al. [16] applied the eddy current technique to detect both in-plane and out-of-plane waviness in CFRP with a specially designed probe. For the in-plane fibre waviness, a waviness with the amplitude and wavelength at 1.1 mm and 15.9 mm was

introduced into a thin unidirectional sample (0.5mm thickness); and for the out-of-plane fibre wrinkles, they used the sample with wrinkles located from the surface to a point at about 25 mm depth, with the maximum amplitude of 3.5 mm. The results indicated the qualitive ability to identify both the waviness location/shape and the wrinkle location, but not showing or evaluating the quantitative capability to characterise the accuracy for amplitude, wavelength or the angle.

From the above review relating to eddy current, it is obvious that this technique is still limited to two dimensional surface response at the current stage. Hence, more work remains to be accomplished to obtain the full 3D characterisation for CFRP, especially in the respect of improving the sensitivity to characterise out-of-plane fibre path.

2.2.2 Characterisation based on X-ray computed tomography (CT)

Due to its longer history of use, the 3D characterisation technique using X-ray computed tomography has developed to a stage where the characterised data provides enough information required to create a full 3D FE mesh. However, as there is a limitation of pixel count across the CT machine detector, there has to be a trade-off between the resolution (voxel size) and the coupon size to be scanned. Determination of in-plane and out-of-plane fibre orientation does not require resolution of each fibre, just the fibre tows and plies, requiring a voxel size of about 31 μm [17], allowing much larger coupons (approx. 50 mm across) than would be possible when fibres need to be resolved individually.

In Requena et al. [24], the researchers used μCT scans to characterise the orientations of fibre alignments in CFRP with a cubic voxel size of $(0.7 \times 0.7 \times 7\ \mu m)^3$, they first applied a self-developed computer algorithm to recognise the individual carbon fibres, then the fibre alignment, in both the out-of-plane and in-plane directions were measured directly, hence the information needed for the mesh creation could be meet. However, although the individual fibre with the diameter of about 7 μm could be recognised, the total coupon size that could be scanned and reconstructed was very small, only a 2.95 mm^3 volume of CFRP in their case. Sutcliffe et al. [7] also determined both the out-of-plane and in-plane fibre-path angles in CFRP components by applying the multiple field image analysis (MFIA) method to both polished sections and X-ray images. And recently, in 2015,

William and Michael [25] tracked the individual fibre path of AS4/3501-6 and reconstructed the 3D structure automatically, detected by X-ray CT, through a 12-step process. Their research therefore possessed the capability to provide the data required for the FE mesh. In addition, Latil et al. [26] characterised fibre path in 3D field dependent on the in-situ X-ray micro CT images, which could also provide the information needed for FE models. However, all three suffered the same limitation as in Requena et al. [24] research, their reconstructed coupon size was too small compared to industrial components.

In addition to determine the fibre centrelines and orientations from high resolution (small voxel size) CT scans, many researchers have sought methods to develop numerical meshes based on the characterised CT data. The work done by Nikishkov et al. [27] has obtained a good-quality of FE mesh distribution to represent fibre alignments, based on X-ray CT information. They used a derivative of a spline function to approximate fibre-tow slopes in the selected fibre-curve segments, using an edge-detection technique. Four examples of mesh generation on the cross section of different coupons were presented in this paper, and the range of element sizes was between 0.25 mm and 1.65 mm. However, all four meshes were just for 2D models. Later, Czabaj et al. [28] successfully created a numerical mesh representing individual fibres in a very tiny section in Abaqus, based on X-ray CT data. A fibre-segmentation algorithm was first applied to the CT image to obtain the virtual-fibre coordinates and diameters, before these were converted into a 3D spline which was imported into Abaqus to reconstruct the micro-structure, with some subtraction/mesh process before the automatic mesh in Abaqus. However, the size of the mesh presented in Czabaj et al. [28] was too small (only $169 \times 169 \times 169$ μm) to be representative of a real component and lacked failure mechanisms embedded in the model for further performance prediction. Sencu et al. [29] and his co-workers generated a similar FE mesh to Czabaj et al. [28] to reconstruct the individual fibres in three dimensions, dependent on the CT technique. Similarly, the mesh created in Abaqus by Sencu et al. [29] was small, only a 50 μm cube. In a more recent research, Seon et al. [8] did the work similar to this thesis. They characterised the in-plane and out-of-plane fibre misalignment based on the X-ray CT technique and those characterisations were transferred into FE meshes as one element per ply with

modified LaRC04 [30] failure criteria included to simulate the four-point bending failure response. For the out-of-plane wrinkles mesh generation, the ply wrinkle was controlled by a linear decaying function based on 2D sectional slices of CT scan data, and the in-plane waviness was defined by the local in-plane rotation angles, in accordance with the in-plane slices of CT data.

2.2.3 Characterisation based on ultrasonic testing (UT)

Compared to the CT technique, ultrasonic characterisation has been more widely used in the component-quality evaluation stage due to its capability for large-size components. However, since it is impossible to recognise individual fibres in the ultrasonic scan, the fibre alignments are identified through tracking the fibre-tows by their tell-tale variations in inter-ply resin-layer thickness and the location of resin layers between plies, to provide data required for building the FE mesh.

As early in 1995, Wooh and Daniel [31] set up the transducers in transmit-received mode with one transmitting transducer mounted on the 'hill' or 'valley' point of the sample including the out-of-plane wrinkles, and another receiving transducer was mounted on the opposite point of this transmitting transducer. Here, the 'hill' or 'valley' point stands for the internal peak or lowest point of wrinkles encompassed in the components. Several more receiving transducers were mounted in pairs on the top/bottom sample surfaces, at the locations of interest. By comparing the received signals between transducers on the non-wrinkled and wrinkled locations, their method showed the potential to detect fibre wrinkles. Since this was a very early research, they did not give any characterised results quantitively. Later, Zardan et al. [32] detected out-of-plane wrinkles in CFRP, depending on the studies of deviation of incident angle as the interfaces were not parallel where wrinkles were located and the double scanning technique (double through transmission). Pain and Drinkwater [33] combined amplitude and phase using Total Focusing Method (TFM) imaging from Full Matrix Capture (FMC) array-based data acquisition, with average scattering-matrix methods to characterise the out-of-plane fibre misalignment. However, all the three research papers above only characterised the out-of-plane wrinkle region, not showing an attempt to transfer the characterised data into FE mesh. More recently, Sandhu et al. [34] used B-scan images to identify plies. Focusing particularly on the characterisation of out-of-plane wrinkles, the estimation of fibre alignments was based on the multiple field image

analysis method (MFIA) by the developed algorithm. A wrinkled FE mesh was created based on the characterisation data. However, their final 3D FE mesh was obtained through the extrusion of assumed 2D geometry determined from a B-scan slice, rather than reconstructed from a full 3D characterisation, containing the full 3D profile of as-manufactured wrinkle features.

In this area of research, the group of Smith et al. [9,35,36] has made significant progress; their characterisation focused on the tracking of both out-of-plane wrinkles and in-plane waviness, and the 3D FE mesh has been created based on the characterised data. Their characterisation technique also provided the data required to create FE meshes covered in the following chapters of this thesis. In 2009, Smith et al [37][38] obtained a 3D characterisation of CFRP to qualitatively extract the in-plane and out-of-plane fibre waviness, based on the 2D fast Fourier transformation (2D-FFT) method. Then their characterisation [5] went further to measure the out-of-plane angles of fibre-tow paths. Three approaches were compared to achieve this, namely (1) an image-gradient (Canny) method, (2) Rotated periodic filters, and (3) a Radon transform method. The results showed that the angle measured by the Radon transform method was more consistent with the original image. Following that in 2016, their research [4] extended to accurately characterising the fibre undulations in a more complicated situation in CFRP, in a wedge-shaped specimen containing ply-drops. Most recently, they [35] successfully tracked the ply locations to represent out-of-plane wrinkles in a full coupon size based on the ultrasonic scan and the analytical model [36] was used to track the interface layers when composites containing wrinkles, ply-drops or impact damage. Dependent on their characterised data, the interface-layer locations, out-of-plane wrinkle and in-plane waviness angles could be calculated. Beyond the geometrical characterisation, Smith et al. [6][17] have tried to create a 3D numerical model based on ultrasonic data, defining the node locations and fibre vectors for the mesh creation and local material orientation assignment, and the failure mechanisms have been included in the model to simulate the compressive failures in their recent progress [9].

2.3 Descriptions of Compressive Failure Mechanisms in Composites

Pre-preg composite structures are manufactured from the stacking process of thin plies or lamina to form a laminate, as illustrated in Figure 2.1, and the definition of three orthogonal axes based on a single ply (Figure 2.2). Hence, there are three possible failure locations: at the interface between adjacent plies (inter-lamina failure), in the matrix and fibres within the ply (intra-lamina failure). Soden et al. [39][40][41] compared the predictive capabilities of 19 theories of different loading cases proposed by different researchers up to 2003. They concluded that none of the theories reviewed would give complete agreement with their testing results. This review will focus on several widely accepted failure modes at each failure location in CFRP, and is limited to the compressive loading scenario, to cover the failure types that have been observed experimentally and simulated in numerical models in the following chapters of this thesis.

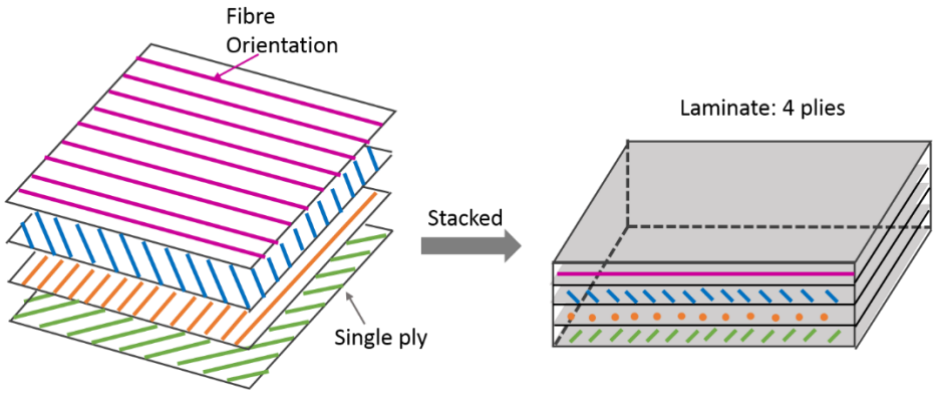

Figure 2.1 Illustration of a laminate, through the stacking process of individual layers.

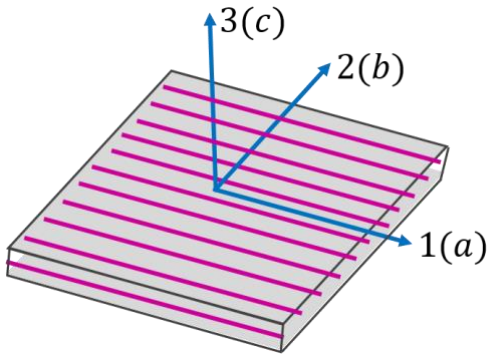

Figure 2.2 Illustration of the alignment of the three axes, on a single continuous fibre ply.

2.3.1 Intra-lamina failure mechanism

Under compressive load, the intra-lamina failure is either matrix-dominated or fibre-dominated. Hashin and Rotem [42] pointed out that these two failure modes could be treated as distinct, based on their experimental observations. It is also possible to have separation of fibres and matrix within a ply (referred to 'splitting') under compression. Hence, this section will present the review as the sequence of matrix cracking, fibre failure, and splitting, with highlights the failure criteria for the first two (matrix cracking and fibre failure).

2.3.1.1 Matrix cracking

When the compressive load is transverse to the fibres, the failure will be dominated by matrix cracking. After Hashin and Rotem [42,43] suggested a 2D failure criterion in 1973 (Eq. (2.1))[42] and 3D failure criterion in 1980 (Eq. (2.2)) [43] that were governed by the stress vector components associated with a plane, many researchers have put forward modifications to form new laws in order to make the predictions more consistent with experimental results. Here, three criteria will be reviewed, suggested by Sun et al. [44], Puck and Schürmann [45,46] and Dávila et al.[30,47,48].

Sun et al. [44][49] modified Hashin's 2D [42] quadratic interaction law (Eq. (2.1)), by simply adding a similar 'friction' influential parameter as used by Puck to form an effective in-plane shear stress (Eq. (2.3)). However, they did not make any attempt to calculate or estimate the angle of the crack plane.

Puck and Schürmann [45,46] pioneered the calculation and experimental capture of the angle of the inclined plane, $\phi_0 = 53^\circ \pm 2^\circ$ (indicated in Figure 2.3), when the composite suffers a compressive load. In Puck's criterion [45,46], they suggested three failure modes, depending on the value of transverse stress. When the stress is tensile, it is named Mode-A and its fracture plane will be vertical. When the stress gradually becomes compressive at the small magnitude region, the failure is governed by τ_L, the shear stress on the fracture plane, and is defined as Mode-B, at which the fracture angle (ϕ_0) remains at 0°. As the compressive load increases further, it finally changes to Mode-C (Eq. (2.4)) at which the fracture angle increases to the final $\sim 53^\circ$, forming an inclined plane. In Mode-C, the

transverse compressive load has a benefit to increases the matrix shear strength and impedes the shear fracture, by an internal 'friction' term proportional to the normal stress (σ_n) on the fracture plane. The final cracking is directly caused by the shear failure of the matrix.

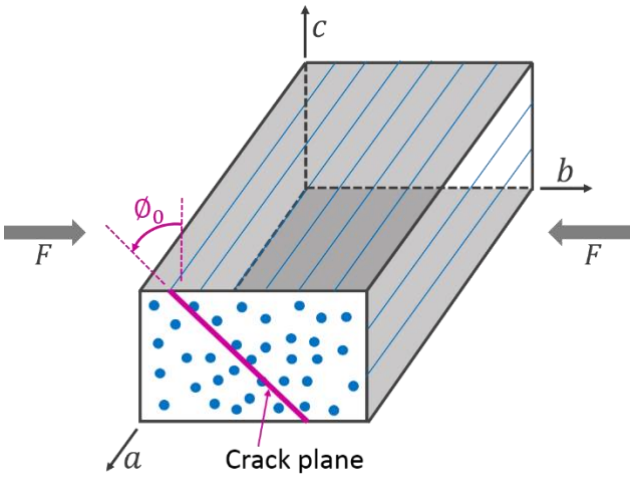

Figure 2.3 Illustration of the inclined crack plane of a unidirectional composites, under the transverse compressive load [45][50].

Based on Puck's criterion, Dávila et al. made certain modifications and developed a series of criteria [30,47,48] to govern failure in the matrix. Their research started from the 2D case (LaRC02) [47]. Unlike Puck's law, in which normal stress, σ_n influenced the shear strength, the 'friction-like' effect of LaRC02 [47] is added to the shear stress (Eq. (2.5)) to form the effective shear stress acting on the incline fracture plane. In addition, the researchers pointed that when the compressive longitudinal load along fibres is smaller than the matrix compressive strength (Y_c) to form a biaxial compression loading case, matrix cracking could also occur without any fibre damage or the formation of a kink band. In this case, the effective shear stress in the numerator (Eq. (2.5)) will change to be calculated at the misalignment frame. Later, in the suggested LaRC03 [48], the criterion remains similar, but the in-situ effect is considered and the strength in the denominator is modified to be the in-situ term (Eq.(2.6)). Finally, the criterion was expanded to three dimensions and formed LaRC04 [30]. In LaRC04, the law (Eq. (2.7)) controlling the initiation of cracking is similar to Puck's law, but the term of in-situ longitudinal shear strength (S_{is}^{L}) on the crack plane is defined.

Table 2.1 Summary of the failure criteria [42–45][30,47,48] to govern the transverse compressive matrix cracking ($\sigma_{22} < 0$).

Criteria Name	Failure Criterion	Equation No.
Hashin's Law (1973) [42]	$\left(\frac{\sigma_{22}}{Y_c}\right)^2 + \left(\frac{\tau_{12}}{S_L}\right)^2 = 1$	(2.1)
Hashin's Law (1980) [43]	$\left(\frac{\sigma_{22}}{2S_T}\right)^2 + \left[\left(\frac{Y_c}{2S_T}\right)^2 - 1\right]\frac{\sigma_{22}}{Y_c} + \left(\frac{\tau_{12}}{S_L}\right)^2 = 1$	(2.2)
Sun's Criterion (1996) [44]	$\left(\frac{\sigma_{22}}{Y_c}\right)^2 + \left(\frac{\tau_{12}}{S_L - \mu\sigma_{22}}\right)^2 = 1$	(2.3)
Puck's Law (1998) [45]	$\left(\frac{\tau_T}{S_T - \mu_T\sigma_n}\right)^2 + \left(\frac{\tau_L}{S_L - \mu_L\sigma_n}\right)^2 = 1$	(2.4)
LaRC02 (2003) [47]	$\left(\frac{\tau_{eff}^T}{S_T}\right)^2 + \left(\frac{\tau_{eff}^L}{S_L}\right)^2 = 1, \quad when\ \sigma_{11} \geq Y_c$ $\left(\frac{\tau_{eff}^{mT}}{S_T}\right)^2 + \left(\frac{\tau_{eff}^{mL}}{S_L}\right)^2 = 1, \quad when\ \sigma_{11} < Y_c$	(2.5)
LaRC03 (2005) [48]	$\left(\frac{\tau_{eff}^T}{S_T}\right)^2 + \left(\frac{\tau_{eff}^L}{S_L^{is}}\right)^2 = 1, \quad when\ \sigma_{11} \geq Y_c$ $\left(\frac{\tau_{eff}^T}{S_T}\right)^2 + \left(\frac{\tau_{eff}^L}{S_L^{is}}\right)^2 = 1, \quad when\ \sigma_{11} \geq Y_c$	(2.6)
LaRC04 (2005) [30]	$\left(\frac{\tau_T}{S_T - \mu_T\sigma_n}\right)^2 + \left(\frac{\tau_L}{S_L^{is} - \mu_L\sigma_n}\right)^2 = 1,$ when $\sigma_{11} \geq Y_c$ $\left(\frac{\tau_T^m}{S_T - \mu_T\sigma_n^m}\right)^2 + \left(\frac{\tau_L^m}{S_L^{is} - \mu_L\sigma_n^m}\right)^2 = 1,$ when $\sigma_{11} < Y_c$	(2.7)

The summary of the criteria governing the transverse compressive matrix cracking, from Eq. (2.1) to Eq. (2.7) as reviewed above, is listed in Table 2.1. The terms related are defined as:

- σ_{11} & σ_{22}: longitudinal stress and transverse stress
- τ_{12}: in-plane shear stress
- Y_c: transverse compressive strength

- σ_n, τ_T & τ_L: normal stress and two shear stress components acting on the fracture plane (Figure 2.15)
- S_T & S_L: transverse and longitudinal shear strength
- μ_T & μ_L: frictional coefficients at transverse or longitudinal direction
- τ_{eff}^{T} & τ_{eff}^{L}: effective transverse or longitudinal shear stress on the facture plane
- Subscript m: represents the calculation will be done on the misalignment frame
- Subscript is: stands for the in-situ effect

2.3.1.2 Fibre failure

When an axial compressive load is applied to high fibre volume fraction composites, the failure is fibre-failure dominated. Fibre micro-buckling and fibre kinking are two of the most widely accepted modes to account for this failure type. Both mechanisms rely on initial imperfections, such as fibre initial misalignment [51], and they can be treated as distinct mechanisms, or regarded as the formation of kinking as a consequence of fibre micro-buckling [51][52]. This subsection focuses on the kinking mechanism, with highlights of some related criteria.

Many studies of experimental work have shown the formation of the kink band [51–54] prior to the occurrence of the fibre failure. This phenomenon occurs in a localised region across the specimen, where fibres rotate at various degrees and the matrix suffers shear deformation. Generally, three important parameters shown in Figure 2.4, namely kink-band width (w), fibre-rotation angle (θ), and the angle between the kink-band to the plane normal to the loading direction (β), are used to define a kink band [51]. Based on experimental observations, Schultheisz and Wass [51] found that the formation of the kinking was initiated by a local event, such as fibre buckling or matrix crack, and this process was accompanied by stress redistribution and related to the local microstructural defects, like fibre misalignment. Subsequently, Vogler and Kyriakides [55–57] used a specifically designed loading fixture to investigate the kinking initiation and propagation process. They discovered that, under pure uniaxial compressive load [55,56], the initiation of a kink band was the dynamic event with some splitting, and the compressive stress remained constant during the kink-propagation process in their specifically designed loading case. The fibre failure was caused by the excessive

bending of fibres to form a final kink-band with a fibre rotation (θ) at about 40°, and the band inclined (β) at around 15°. However, when studies were carried out using a biaxial testing device to supply a combined compression-shear loading [57], a quasi-static kink-band initiation and propagation events could be recorded, with a smaller fibre rotation ($\sim 26^{\circ}$) and band inclination ($\sim 12^{\circ}$) angles. In more recent research, Pimenta et al. [54] identified the process to form a kink-band as three stages, (1) elastic stage, (2) plastic stage, (3) fibre-failure stage when the kink-band was observable. These researchers pointed out that the key feature to identify transformation from the elastic to plastic stage was the beginning of matrix yielding, which was also the important characteristic triggering the formation of a kink-band.

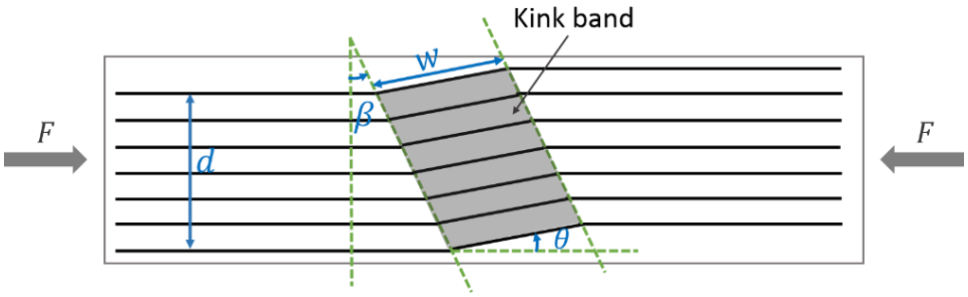

Figure 2.4 Illustration of the geometry of a kink band of unidirectional laminate, under compressive load [51].

In terms of the criteria suggested to simulate or govern this kinking fibre failure, they gradually progressed from 2D into 3D cases. Argon [58] made a pioneering contribution to this field focusing upon and analysing this phenomenon. His 2D analysis argued that the fibre rotation was triggered by shear stress between fibres, caused by an assumed initial fibre misalignment (θ_i). The rotation of fibres would bring about a further increase in the shear stress, and vice versa. This loop finally led to instability and fibre failures. The relationship between compressive failure stress (X_c) and matrix longitudinal shear strength (S_L) could be connected by the initial fibre misalignment (θ_i), given by

$$X_c = \frac{S_L}{\theta_i} \tag{2.8}$$

Based on the plastic kinking stress suggested by Argon [58], Budiansky and Fleck [59] assumed the result of kink band remaining perpendicular to the axial load ($\beta = 0$) and introduced the elastic-perfectly plastic 2D stress as

$$X_c = \frac{S_L}{\theta_i + \gamma_0} \tag{2.9}$$

Where γ_0 stands for the failure shear strain.

They later claimed that [60] the matrix plastic deformation contained a phenomenon of strain hardening, rather than showing perfect plastic behaviour.

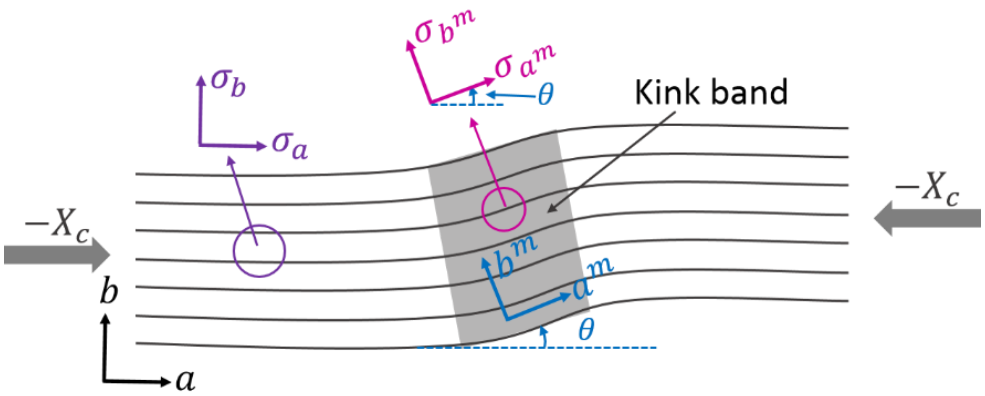

Figure 2.5 2D fibre misalignment frame under pure compressive axial load [48][30].

Similarly with matrix cracking, a series of failure criteria from LaRC02 to LaRC04 [30,47,48], were developed by Dávila and his co-workers, to govern the fibre compressive failure. LaRC02 and LaRC03 [47,48] were limited to the 2D plane stress field, with the major difference that the in-situ effect for the longitudinal shear strength (S_L) was considered in LaRC03 [48]. The researchers also assumed that the initial fibre misalignment would trigger the fibre rotations to form a misaligned frame. The global plane stress (σ_a, σ_b, τ_{ab}) was thus transformed to the new frame (σ_{a^m}, σ_{b^m}, $\tau_{a^m b^m}$), as illustrated in Figure 2.5. The index to judge the fibre failure was, actually, controlled by the matrix criteria in LaRC02/03. When putting the stress on the new frame (σ_{a^m}, σ_{b^m}, $\tau_{a^m b^m}$) into the matrix criteria with the assumption that the compressive strength (X_c) was a known property, Eq. (2.5) became

$$X_c(sin\theta_c cos\theta_c - \mu_L sin^2\theta_c) = S_L \tag{2.10}$$

After solving this equation (Eq. (2.10)), the fibre misalignment angle (θ_C) at failure could be calculated by

$$\theta_C = tan^{-1}\left(\frac{1-\sqrt{1-4(\frac{S_L}{X_c}+\mu_L)(\frac{S_L}{X_c})}}{2(\frac{S_L}{X_c}+\mu_L)}\right) \tag{2.11}$$

They also stated that, if μ_L and shear strain were neglected and θ_C remained small, Eq. (2.10) would be the same as Argon's law (Eq. (2.8)). LaRC04 [30] was the extension of the 2D phenomenon into a more general case in three dimensions, and the final check of the fibre failure also depended on the matrix crack criterion in LaRC04. The details relating to the 3D stress transformations in LaRC04 due to the fibre and kink-band rotations were the same as Pinho's model [50], which is discussed later in this chapter.

Finally, based on the studies listed above, Pinho et al. [50,61] extended the 2D kink-governed criteria into the 3D field. The details for his 3D kinking model are presented in sub-section 2.5.2.

2.3.1.3 Splitting

Here, splitting is specifically defined as the intra-lamina separation of fibres and matrix (Figure 2.6). It is initiated under compression due to the existence of local imperfections introduced during the manufacturing stage [62], such as fibre misalignment or geometric discontinuities. It has been identified that the initiation of splitting is due to the occurrence of shear stress [63][53], and is always combined with other mechanisms. Kumar et al. [63] observed a slight longitudinal splitting on the in-plane shear fracture plane by using a fractographic technique. Prabhakar and Wass [64] regarded this mechanism as being associated with the formation of kinking. The energy was released by splitting when the strain within the band exceeded the strain limit at the fibre/matrix interface. Gutkin et al. [53] assessed that the splitting was the consequence of coalescence of matrix microcracks at the kink-band tip (Figure 2.6), during the kink-band propagation process. They also indicated the dominant stress state at the inter-fibre region was shear stress. Based on the numerical modelling results, Gutkin

et al. [65] argued that the transition between kinking and splitting is difficult to identify but analysis of the stress-strain curve might give some indications. As splitting was a fibre-matrix interface failure mechanism [66], numerical techniques for the inter-lamina damage (delamination) could be applied, which are reviewed next in subsection 2.3.2.

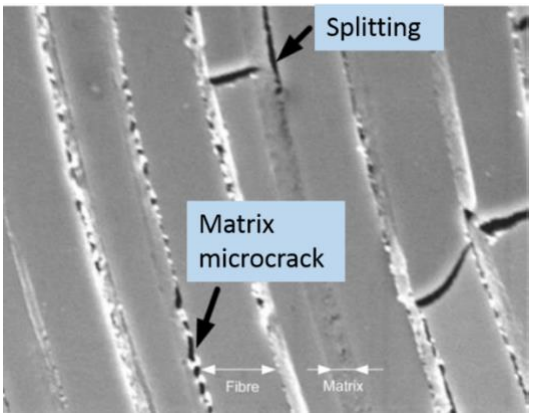

Figure 2.6 Image showing splitting damage [53].

2.3.2 Inter-lamina failure mechanism (delamination)

One of the most common failure mechanism for laminated composites is a separation at interfaces between two lamina, termed 'delamination'. There are many techniques to simulate this phenomenon, fracture mechanics and cohesive zone modelling being two of the most widely accepted.

Irwin et al. [67] defined the material cracks into three modes: opening mode, forward-shear mode, and parallel-shear mode. They suggested the term of strain-energy-release rate (G) to relate to the crack behaviour around the crack tip, which could be expressed by the stress-intensity factors (K), based on the Griffith's theory [68]. With the same assumption supposed by Irwin [67] that the energy released during the crack extension is identical to the amount required to close it to its original length if the size of crack is small, a representative technique, named Virtual Crack Closure Technique (VCCT), was suggested [69], which was later applied to composite structures [70] in a wide range of scenarios. Using this technique, a pre-assumed crack plane is defined and the energy release rate for each crack mode (G_{I}, G_{II} or G_{III}) can be obtained from the nodal forces and displacements calculated by the model [71,72].

The cohesive zone model (CZM) is another technique widely used to simulate the onset and propagation of delamination [73][74], and overcomes the need of a pre-defined delaminated area and can simulate the onset and propagation of delamination simultaneously. The idea of cohesive zone models are based on the research of Dugdale [75] and Barenblatt [76], in which they discovered that the stresses in the plastic zone (cohesive zone) ahead of the crack either remain constant and equal to the yield strength [75], or vary following the deformation [76]. Later, Hillerborg et al. [77] suggested a finite element model with the concept of the cohesive zone, to simulate the initiation and propagation of cracks in a concrete beam. Their model was limited at Mode I and assumed a linear relation between the traction and crack opening width, due to its optimal agreement with the tensile test results. In fact, Camanho et al. [74] point out that this cohesive zone technique could be identical to Griffith's theory [68], when the cohesive zone is small enough to be neglected.

The cohesive zone technique relates the interface traction with its relative displacement, represented by traction vs. separation curves (Figure 2.7). For either the pure Mode I, II and III, or the mixed-Mode, the initiation of the crack is triggered when the stress reaches the peak point (strength) on the traction vs. displacement curves. Once the crack is initiated, the stress decreases gradually to zero, such that the total area under the curve, known as critical energy release rate (G_c), reflects the energy released to generate the unit surface area of the crack. G_c could be calculated by

$$G_C = \int_0^{\delta_f} \sigma d\delta \tag{2.12}$$

Where, σ stands for the traction, δ means the relative separation (displacement), and δ_f is the separation at the full failure.

Many research groups have investigated and proposed different laws to define the traction vs. separation curves [74], such as linear elastic perfectly plastic, linear elastic-progressive softening, or linear elastic-regressive softening. Among them, Needleman [78][79] suggested exponential functions to describe the traction vs. separation relationship (Figure 2.7 (a)). Tvergaard and Hutchinson [80] used a trapezoidal traction-separation relationship (Figure 2.7 (b)) to simulate the fracture process for the elastic-plastic solids, and, later, Cui and Wisnom [81] applied spring elements and the elastic

perfectly elastic law (Figure 2.7 (c)) to govern the initiation and propagation of delamination, the difference between this and the trapezoidal law being the sudden reduction of the stress from the maximum to zero. Finally, Figure 2.7 (d) indicates the bilinear law used by several researchers [82–84], in which a linear relationship is defined for both before and after the delamination initiation.

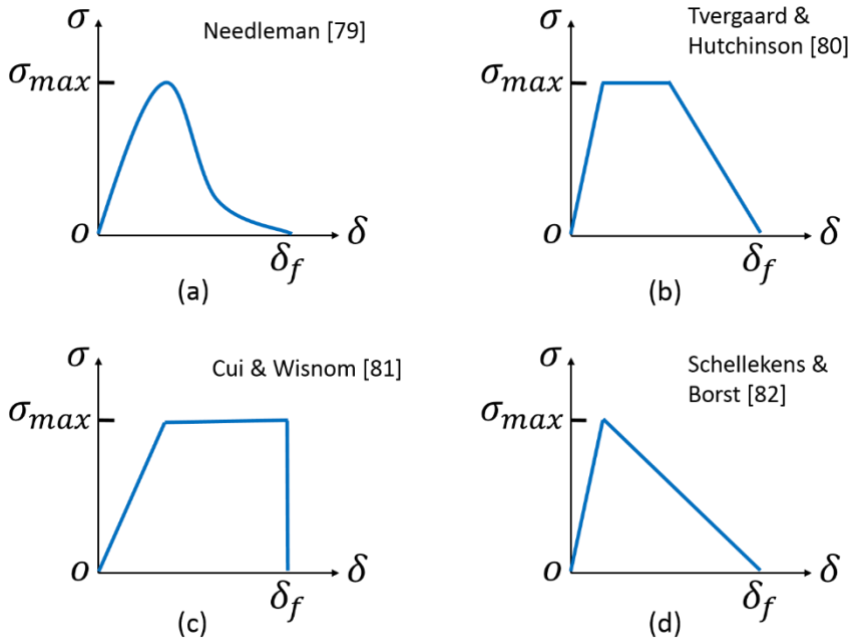

Figure 2.7 Traction vs. Separation curves, proposed by various literatures.

When approaching the mixed-mode region, which is more common in practical applications, the interaction between pure modes needs to be considered [85] for developing the onset and propagation law. For onset, the quadratic criterion, suggested by Brewer and Lagace [86], has been widely accepted to represent this interaction effect [73][11][87]. In terms of the delamination growth under mixed mode, various criteria have been proposed [73], of which the power law [88][89] and B-K law [90] are two of the most widely used. The first mentioned uses the coefficient, α, to adjust the criterion to best fit the specific material, and, in general, the value is in the range of $\alpha \in (1.0 - 2.0)$ [11]. This power law is explained by

$$\left(\frac{G_{\mathrm{I}}}{G_{\mathrm{IC}}}\right)^{\alpha} + \left(\frac{G_{\mathrm{II}}}{G_{\mathrm{IIC}}}\right)^{\alpha} = 1 \qquad (2.13)$$

In the B-K law, the coefficient, η, is applied to reflect the different mode ratios as explained by

$$G_{\mathrm{IC}} + (G_{\mathrm{IIC}} - G_{\mathrm{IC}})\left(\frac{G_{\mathrm{II}}}{G_{\mathrm{T}}}\right)^{\eta} = 1, \qquad G_{\mathrm{T}} = G_{\mathrm{I}} + G_{\mathrm{II}}$$
$$G_{\mathrm{IC}} + (G_{\mathrm{IIC}} - G_{\mathrm{IC}})\left(\frac{G_{\mathrm{shear}}}{G_{\mathrm{T}}}\right)^{\eta} = 1, \qquad G_{\mathrm{T}} = G_{\mathrm{I}} + G_{shear}\ (if\ Mode\ \mathrm{III}\ occurs) \tag{2.14}$$

In Eq. (2.13) and Eq. (2.14):

G_{I} & G_{II}: energy release rate for pure Mode I and Mode II, respectively.

G_{IC} & G_{IIC}: critical energy release rate for pure Mode I and Mode II, respectively.

2.4 Fibre-Misalignment Imperfections in Composites

Fibre-misalignment is one type of 'defect', which is defined as an "irregularity in a material or structure that causes it to depart from its specification as defined during the design process" [91]. This non-conformance of material or structure relative to the design always relates to the manufacturing stage, and it could be reduced or eliminated if rigid control is applied to the manufacturing procedures. Potter [92] carried out a systematic study of the origins of various defects and variabilities which can arise in composites during manufacturing, and a taxonomy for all defects is given at the end of this paper. In terms of the category of fibre misalignment within the geometry-defects block, the defects belonging to this type could be fibre direction errors or wrinkled and wavy fibres (out-of-plane, in-plane, or combined in/out-of-plane). The origin of the latter is generally related to in-process factors. According to the geometrical characteristics of the fibre path, defects/features related to fibre misalignment could be categorised further as out-of-plane wrinkles, in-plane waviness, ply-drop, or other issues such as gap, overlap, or twisted tow (Figure 2.8). The first two types (wrinkles and waviness) refer to the continuous fibre tows deviating from the ideal trajectory through the thickness or limited within the plane, and these defects are the main subjects of investigation in this thesis.

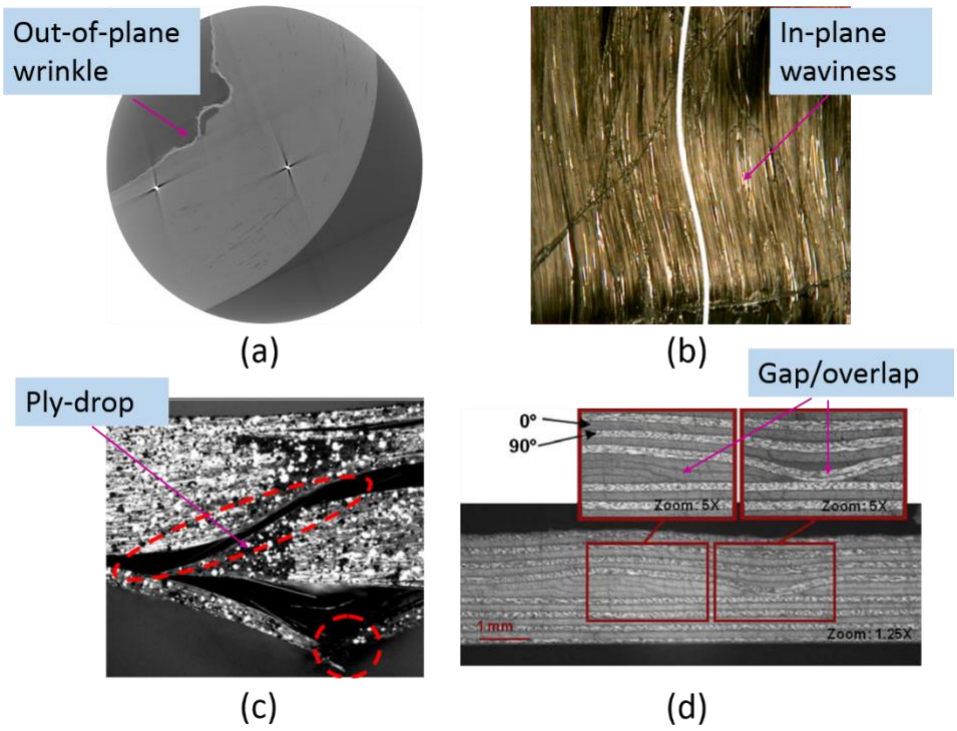

Figure 2.8 Typical fibre-misalignment related defects/features, (a) out-of-plane wrinkle [93], (b) in-plane waviness [91], (c) ply-drop [94], (d) gap/overlap [95].

2.4.1 Reasons for the formation of continuous-fibre misalignment

The reasons for misalignment of continuous fibres, out-of-plane wrinkles, and in-plane waviness, are not rigidly distinct and may depend on the laminate constraint [96]. As studied by Potter [92], the origins of fibre misalignment defects could be related to various manufacturing process factors or errors. He categorised them into four groups. The first type of fibre misalignment was formed in the as-delivered lamina [92][97] and was caused by the wrapping of the prepreg onto a drum for storage. In this process, the fibre path length of the outside surface would be longer than that of the inside, causing the accommodation of this path difference to buckle the inside fibres to form a wrinkle or waviness. Moreover, when the rolled prepreg was unwrapped and flattened, the viscoelastic nature would result in the fibre undulations not being fully relieved and thus retaining some waviness. The second source [91] was from the layup process when the lamina was formed to a radius. Fibres on the inside of the radius would be buckled due to the compression, finally leading to a region of fibre misalignment. The third factor [92] was related to the process of consolidation, such as autoclave or resin transfer moulding (RTM). The misalignment formation was a result of coefficient of friction

between the tool and the reinforcement (autoclave) or because the fibre was compacted to one side away from its normal place due to the resin richness (RTM) [98]. The final origin set out by Potter et al. [92] was closely related to the residual stresses due to the mismatch of coefficients of thermal expansion (CTE). Instances of expansion differences could exist on different scales, namely: (1) micro-scale between fibre and matrix due to their different thermal properties; (2) lamina-scale where coefficients being different between parallel and perpendicular to the fibres; (3) laminate-scale of different stresses through the thickness; and, lastly, (4) component scale where the resin-rich zones cause the additional stresses. Tool-part interactions could also be attributed to the influence of different expansion coefficients [92][99] to generate the fibre misalignment due to the strain or stress gradient. Parlevliet et al. [100] and Kugler et al. [96] also noticed the effects of thermal stress on the formation of fibre waviness. Beyond this, Kugler et al. [96] investigated eight processing factors and surmised that only three have an influence on the generation of fibre waviness: laminate length, tool plate material, and cooling rate. The first two factors provided the driving force to form the waviness by the effect of tool/plate CTE mismatch, while the third factor mentioned caused the temporal gradient before giving indirect effect to the tool/part CTE. Many other researchers have found similar reasons causing the fibre misalignment as Potter [92]; for example, Dodwell et al. [101] pointed out that during the debulking process of lay-up of a convex radius, the axial compression applied to the layers on the surface (outer layers) caused wrinkles if they are not able to slip/shear with each other freely due to the high resistance. Lightfoot et al. [102] developed a method to form a wrinkle/waviness region relying on the shear force between plies and the tool, caused by the CTE and ply slippage which reversely implied the origins for wrinkles formation. More recently, Hallander et al. [103][104] identified that wrinkle extent could be reduced by either the increase of buckling resistance through co-stacking critical layers, or the reduction of the compression in single layers. Finally, regarding the automated tape laying (ATL) method, it is also possible to cause the wrinkles if the turning radius of the placement head is too small [105].

2.4.2 Out-of-plane wrinkles

2.4.2.1 Parameters to characterise the severity of wrinkles

Out-of-plane wrinkling refers to the undulations of continuous fibre tows through the thickness. There are basically three parameters required to describe a wrinkle's shape: maximum undulation (amplitude), repeated distance of the wrinkles (wavelength), and its maximum inclination (maximum angle). The detailed definitions for these three geometrically-related parameters may differ between different authors. Figure 2.9 illustrates two representative definitions, in which the Figure 2.9 (a) $(\delta, \lambda, \theta)$ is more widely used, but the definition of Figure 2.9 (b) was also used by some people, such as Hsiao et al. [106], the main difference between the definitions is related the choice of amplitude to describe the maximum undulation. The $(amplitude, wavelength, maximum\ angle)$ are labelled as $(\delta, \lambda, \theta)$ and (A, L, θ), respectively.

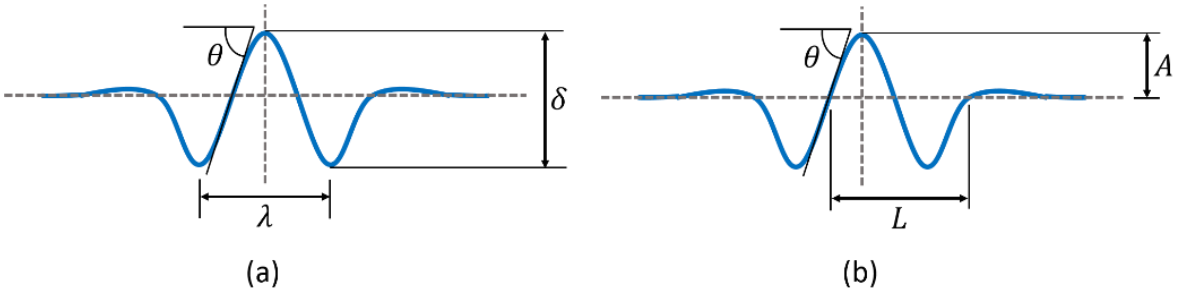

Figure 2.9 Two types of schematic of out-of-plane geometric parameters, (a) parameter-definition following Wang et al. [107], (b) another set of parameter definitions [106].

In terms of the severity-governed parameters for the wrinkles which are most influential to failure performance, there is no consensus. All the parameters defined in Figure 2.9, or combinations thereof, have each been proposed by different researchers to define a wrinkle. Hsiao and Daniel [106] used amplitude and wavelength to characterise wrinkles, assuming a sinusoidal wrinkle shape. They proposed a representative volume truncated at a single period of the wrinkle, with amplitude reducing linearly from the mid-plane to the sample surfaces, and finally used the amplitude/wavelength ratio to represent the wrinkle's severity. Many other researchers, such as Garnich et al. [108], Adams et al. [109], Eskandari et al. [110] and others [111][12][112], also applied amplitude/wavelength ratio to describe wrinkle severity. Adams and Hyer [113] also used this ratio to account for the wrinkle

severity but took the layer thickness as the baseline to describe the wrinkle geometry. In this case, the maximum severity contains an amplitude of up to 1.5-layer thickness and the wavelength of nine-layer thickness. They pointed out that the maximum angle could be related to the amplitude/wavelength ratio with an arc-tangent expression. There are many researchers who chose maximum angle to define wrinkle severity, such as Bloom et al. [114], Lemanski et al. [94], Mukhopadhyay et al.[1], Sutcliffe et al. [7]. Wang et al. [107][115] used amplitude/wavelength ratio to express the wrinkle severity, whilst at the same time highlighting that maximum angle was crucial in affecting the composite strength. Beyond the definitions listed above, several other methods have been suggested to define a wrinkle. Fedulov et al. [116] used the wrinkle height as a fraction of laminate thickness, and Potter et al. [91] applied both the maximum angle and the ratio of wrinkle height relative to the nominal thickness. Caiazzo et al. [117] used a polynomial to describe the wrinkle shape, with amplitude reducing linearly to the sample surfaces, with the peak height and the wrinkle extent in the load direction the 'gross' measures of the defect size. Wisnom and Atkinson [118] used a cosine function in terms of the amplitude and wavelength to fit the wrinkle geometry and chose the maximum angle to represent the wrinkle's severity, while more recently, El-Hajjar et al. [119] developed a Gaussian function to characterise 'bell-curve' wrinkles, the maximum amplitude (waviness height) at one surface was designed to be diminished at the opposite one, thus forming samples with one flat surface and one concave 'bell' surface, and the wrinkle-amplitude reduction through the thickness related to the distance from the maximum-amplitude surface. In the results, they chose 'waviness height' to describe the wrinkle severity or extent. The application of Gaussian functions to describe the wrinkle extent was also adopted in this thesis, but the range of wrinkle metrics investigated is significantly greater. Therefore, due to the lack of a consensus which wrinkle parameters governing the failures as discussed in the review above, it suggests the need for a thorough study to identify and understand the interdependencies of parameters and determine a hierarchy of wrinkle-parameter importance.

2.4.2.2 Failure modes and strength in CFRP composites with wrinkles under compression

Many researchers have proved the significant negative influence of wrinkles on the CFRP composites under compression. Adams and Hyer [113] introduced the manual out-of-plane wrinkles into the cross-ply laminates for a static compression experiment. The test results from various wrinkle-severity specimens were compared with those from the pristine wrinkle-free coupons and the comparison showed that the strength reduction increased with larger value of δ/λ (Figure 2.9 (a)); for example, when δ/λ was 0.042, the knock-down was 34%. They also stated that the failure modes were the through-the-thickness matrix cracking and delamination. Hsiao and Daniel [106] investigated a wrinkle's influence on compressive performance of unidirectional composites through experimental tests and analytical models. They found that both Young's Modulus and compressive strength were significantly affected by the wrinkle's severity. The reduction of the strength was more than 50% if the ratio, A/L (Figure 2.9 (b)), changed from 0 to 0.20, and its dominant failure modes were delamination and layer buckling initiated by the interlaminar shear stress. Wisnom and Atkinson [118] manufactured two unidirectional wrinkled specimens with the maximum misalignment angle at 3.9° and 5.6 °, separately. Compared with the straight-fibre specimens, the compressive strength reduction was 40% and 54% for the two wrinkled specimens, respectively. Their finite-element analysis also gave similar strength levels. Bradley et al. [111] designed two types of wrinkled cross-ply laminates: a single wavy layer and three nested wavy layers, and reported a reduction of the compressive strength compared with the wrinkle-free laminate of 12.1% for the single layer wave and 35.8% for the three nested wavy layers (an approximate reduction of three times on the former). They also indicated the large interlaminar shear and normal strains in the wrinkle region caused by the wrinkles. Khan et al. [98] manufactured specimens by using dry carbon fibres and liquid resin and found that the compressive strength reduction could be as high as 71.5% if all the fibres through the thickness contained approximately 29° out-of-plane misalignment. Wang et al. [107] designed three methods to introduce the wrinkled misalignment into CFRP, before Lemanski et al. [94] did the numerical analysis for these specimens under compression. Four configurations were investigated, named L2, T2, L10 and T10, with the maximum misalignment angle of 8° (L2 and T2) and 30° (L10

and T2). The modelled performance was in a good agreement with the tested results for both failure loads and failure modes. It could also be concluded that an approximate 55% reduction was observed when the maximum angle increased from 8° to 30°, either from the case L2 to L10, or from T2 to T10. Potter et al. [91] also indicated the decreasing tendency of compressive strength following the wrinkle severity, by the four-point flexural bending test. A maximum reduction of 50% has been reported for the highest severity case, when the height of wrinkles was 60% of the nominal thickness. More recently, Mukhopadhyay et al. [1] manufactured three different severity-level wrinkled specimens with maximum angles of 5.6°, 9.9° and 11.4° for compression testing. The experimental failure stress showed a reduction of 18%, 33% and 33% for each case, respectively, compared with the tested wrinkle-free value. Their numerical modelling work gave similar failure modes and strength predictions as the experimental recordings, with the fibre-failure dominated failure for the lower severity wrinkle case (5.6°) and delamination failure dominating at the higher severity wrinkle (11.4°). The threshold wrinkle severity causing this mode change was identified at 8°~9° from their model work. Ferreira et al. [120] also established the reduction of compression stress when the wrinkled angle varied from 0° to 18°, through the FE modelling work on a cross-ply laminate. Therefore, from the discussed review, it indicates the need to take all the failure modes of matrix cracking, fibre failure and delamination into consideration when using the numerical models to investigate the failure process of CFRP induced by out-of-plane wrinkles.

2.4.3 In-plane waviness defects

In contrast to the out-of-plane wrinkles, here, in-plane waviness means the continuous fibre through the trajectory deviates from the ideal path within the plane (perpendicular to the thickness) of the laminate. Similarly to out-of-plane wrinkles, the geometrical description of in-plane waviness needs three parameters: wavelength (L), amplitude (A) and maximum angle (θ). Figure 2.10 illustrates the two methods to define the waviness shape, full sine-wave [121] or half sine-wave [91].

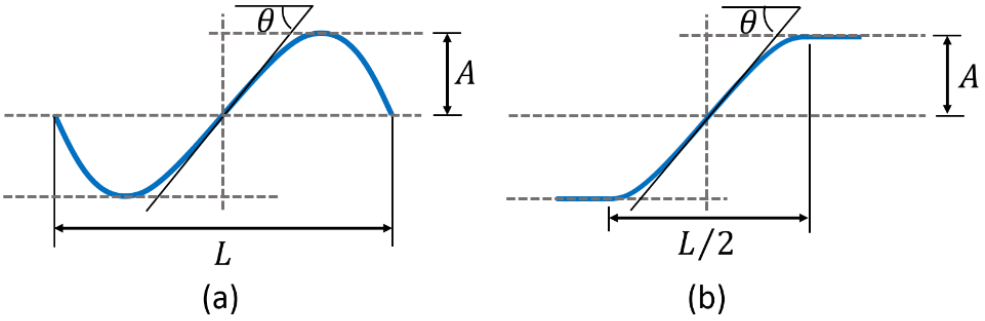

Figure 2.10 Schematic of in-plane geometric parameters, (a) Full sine-wave following Zhao et al.[121], (b) Half sine-wave (kink-shape) following Potter et al. [91].

2.4.3.1 Methods to introduce artificial waviness into composites

Several methods have been applied to introduce artificial in-plane waviness into composites. Potter [91] et al. pointed out that the as-supplied in-plane fibre misalignment could exist due to the prepreg being wound onto a drum for transportation and storage. In order to introduce controllable waviness into the laminates, they [122] designed a rig to shear the prepreg to the desired the waviness extent. The final wavy region was in a half-sine shape (Figure 2.10 (b)). To get a better result, the lamina was heated for easier deformation. Lightfoot et al. [102] manually laid down the unidirectional prepreg into a U-shaped mould, with the 90^{o} ply better fitting the curvature and defined as non-bridged ply, while the 0^{o} ply was defined as the bridged ply since it did not ideally follow the radius of the mould because of its stiffness. Due to the CTE mismatch and ply slippage between plies with different orientations, shear force was generated between non-bridged and bridged plies, which caused the ply movement. Finally, the wavy region was formed during the consolidation process. However, the drawback of this method was the lack of ability to control the severity of waviness. Recently, Zhao et al. [121] proposed an experimental set-up and procedures to manufacture in-plane waviness, which simulated the waviness formation in the automated fibre placement (AFP) process. They also explained the mechanisms behind it: the compressive roller in AFP process introduced bending deformation of prepreg tows. Because of a larger width relative to the tow's thickness, the major bending deformation would be limited to the width direction. Based on the classical bending theory of a beam [14], the inner surface would buckle under compression to form in-plane waviness. Wisnom and Atkinson [123] made artificial in-plane waviness by laying up unidirectional prepreg on a curved

plate; after consolidation, the laminate was forced to be flattened then to be cured, with an extra aluminium plate on the top which was also within the vacuum bag.

2.4.3.2 Failures in composites with waviness under compression

When the laminate includes in-plane waviness, its negative influence on the compressive performance has been proven by different researchers, by either experimental or modelling work. Khan et al. [98] carried out an investigation of the influence of waviness on woven fibre composites. The in-plane waviness presented a shape as shown in Figure 2.10 (b), with the maximum angle of 30°, the length ($^{L}/_{2}$) of 16 mm, and width ($2A$) at 7 mm. When the specimen was compressed using the Imperial College Standard Test (ICST) rig [124], the crack-initiated and failure stresses were captured 35.2% and 24.8% lower than the pristine values, respectively. The failure type was observed as delamination, located at the interface of the outer-most angled plies and the adjacent wrinkled plies. The author also mentioned that the reason for this location might relate to where fibre tows terminated due to the edge of coupons. Lee and Soutis et al. [10] used the fibre micro-buckling model suggested by Budiansky [59] to show the detrimental influence of in-plane fibre misalignment on the compressive strength of unidirectional laminates (IM7/8552 or T800/924C). The model indicated a 40% knock-down even when the misaligned angle was changed by about 2°~3°. Lemanski and Sutcliffe [125] developed two models: (1) 'beam-and-shell' model; and (2) 'rebar-and-solid' model, and proved that the second of these ('rebar-and-solid') was appropriate to predict the composite compressive performance with misaligned fibres without considering fibre bending stiffness, when the fibre volume fraction has limited variance. Then they applied the 'rebar-and-solid' model to investigate the influence of waviness on compressive strength and reached the conclusions that the strength reduced rapidly up to 50% when misalignment angle increased from 0° to 10°; whereas, after 20°, the reduction trend tended to be flat. Other factors, such as the proportion of wavy-region width to the coupon width, the position of wavy region (middle or edge), also appeared to have some effect. Later, following the same approach of 'rebar-and-solid' model', Sutcliffe [126] developed a plane strain FE model with elastic-perfectly plastic response to simulate the effect from random waviness in compressive strength. Random waviness was represented by the misalignment angle standard deviation, and the reduction of

strength was also observed due to the increase of the waviness severity. Fedulov et al. [127] simulated the potential effect of fibre misalignment on compressive strength originating from the automatic tape laying (ATL) process. Their model was based on Zinoviev's damage model [128] and realised by the USDFLD subroutine in Abaqus/Standard. Both cross-ply and quasi-isotropic layup formulations were studied and the modelled results gave a linear reduction for the failure initiation load and 16% knock-down for the final failure load, caused by the fibre waviness. From this review, it indicates that published research focused on in-plane waviness is not as extensive as that for out-of-plane wrinkles, especially for CFRP under in-plane compression. Hence, this suggests the need for more investigations to fully understand the compressive failure of CFRP when in-plane waviness is present.

2.4.4 Fibre volume fraction (FVF) related to fibre misalignment

Potter [92] pointed out that, accompanying the formation of fibre-misalignment (wrinkle or waviness) region, a resin-rich zone could be generated in either the autoclave or resin transfer moulding (RTM) process. Some fibres would be squeezed or loosened, and this would cause the local fibre volume fraction (FVF) to deviate from the nominal value. Lee and Soutis [10][129] gave indirect evidence for this phenomenon when they showed that for a unidirectional laminate (T800/924C), the total thickness (2 mm to 8 mm) would bring a small increase of standard deviation of the fibre angle distribution (0.9^o to 1.9^o), and the larger standard deviation indicated a poorer fibre alignment. They also showed that this thickness would have some effect on FVF, 7% FVF decrease having been recorded for the 8 mm unidirectional laminate, compared to the 2 mm specimen. Hence, this might suggest a relationship between fibre alignments and FVF. Melro et al. [130] did a systematic investigation on how FVF influences the elastic properties of unidirectional composites, based on the material of AS4/3501-6. Various analytical methods have been applied to calculate the six elastic properties (longitudinal/transverse Young's modulus, shear modulus and Poisson's ratio) relative to the change of FVF. The results indicated obvious variations for all six elastic properties when FVF changes, for example, when FVF changed from 40% to 65%, longitudinal Young's Modulus would increase by more than 50%.

Many people have identified that the variation of FVF would affect the compressive strength or modulus of composites. Rosen [131] suggested equations indicating the association between compressive strength of unidirectional composites and fibre volume fraction. Later, Lo and Chim [132] modified Rosen's equation to general instances of where the compressive strength of unidirectional composites would be affected by the change of FVF. They also listed many previous experimental investigations showing the influence of FVF on the compressive strength. Lee and Waas [66] manufactured and tested six unidirectional CFRP specimens with different FVF, from 10% to 60%, under static compression. The tested compressive strength showed a significant increase from 100 MPa to around 460 MPa, when FVF changed from 10% to 60%. They also developed FE models with different initial fibre misalignment angles to investigate the influence of FVF on compressive strength. In each initial misaligned angle case, the strength vs. FVF curve indicated a similar increasing trend as obtained from their experimental test.

For a more specific case of the relationship of FVF to fibre misalignment, Martinez et al. [133] plotted curves of compressive strength against fibre misalignment severity. When FVF changed from 0.3 to 0.5, the comparisons between the data on two FVF-value curves at the same severity showed a significant increase of strength, affected by the 0.2-magnitude increase of FVF. Lemanski and Sutcliffe [125] pointed out the necessity of including the variation of local FVF for large-waviness defects in order to achieve accurate numerical modelling predictions through comparison of two numerical models, with or without containing the change of FVF. Hence, it is necessary to consider the influence of FVF when developing the numerical models where fibre misalignments are present.

2.5 Numerical Modelling Techniques Used in This Thesis for Laminate Failure Analysis Under Compression

2.5.1 Continuum damage mechanics (CDM) models

The continuum damage mechanics (CDM) model, first used by Ladeveze and Dantec [134] to simulate the failure for laminated composites, is a technique to simulate damage propagation. To apply this modelling technique, individual plies are assumed as homogeneous materials and an internal damage variable, D, is defined relating to the specific macroscopic material properties

according to the predefined failure criteria, such as modulus or strains. The evolution of the damage is reflected by the progressively degraded process of the properties, imposed by the damage variable D. For example (Figure 2.11) [135][136], when a homogeneous material block suffers a force (F) causing cracks within the area of A_d, then the effective area would be $(A - A_d)$, and the effective stress ($\tilde{\sigma}$) during the damage growth process could be expressed by

$$\tilde{\sigma} = \frac{F}{A - A_d} = \frac{F}{A(1 - {A_d}/{A})} = \frac{\sigma}{(1 - D)} \tag{2.15}$$

This effective stress ($\tilde{\sigma}$) is related with the nominal stress (σ) by the damage variable, D. In the undamaged block, the damage variable remains at zero, it gradually increases to unity at the point where the damage is such that the block cannot support any stress/strain at all.

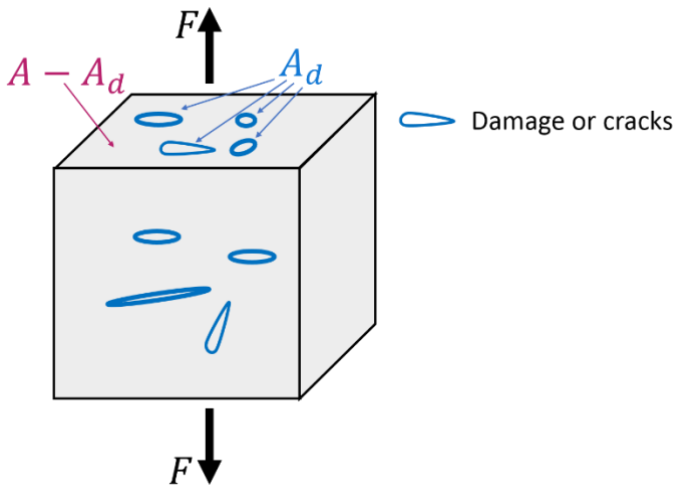

Figure 2.11 Illustration of effective area on a damaged material [135][136].

There are many researchers applying the CDM technique to simulate the intra-lamina failure process, as it can simulate the onset and propagation of failures simultaneously and is tolerable to all failure modes. Most of the literature mentioned in subsection 2.3 applied this technique. Beyond these, Maimí et al. [137] first developed a continuum damage model to predict the onset and evolution of intralaminar failure mechanisms in two dimensions. The damage initiation functions were described by LaRC04 law [30] and the predicted failure loads matched well [138] with the experimental test results, which were carried out on the open-hole quasi-isotropic specimens with tensile load. Later the

researchers expanded the model into three dimensions. Camanho et al. [139] also developed a 3D continuum damage model to simulate matrix cracks. In their model, the criterion for tensile transverse fracture was proposed by Catalanotti et al. [140], and the matrix crack under compressive transverse fracture was governed by the modified Puck's law [45], adding the consideration of the in-situ effect into the shear strength (S_L and S_T) (Eq. (2.4)). The validations of their model were conducted by comparisons with the experimental tests on unidirectional specimens under off-axis compression, or on centre-cracked and on open-hole specimens under tension. A good agreement with all three types of test results indicated the ability of their model to capture the failure mechanisms and predict the failure stresses. Moreover, the good agreement between modelled and test results from both research works [137][139] further implied the capability of CDM technique to simulate the onset and evolution of damage, with appropriate failure criteria and softening laws.

2.5.2 Numerical models used in this thesis

Numerical models are developed in this thesis to account for the performance of quasi-isotropic laminates under compression, containing fibre misalignment imperfections (out-of-plane wrinkles or in-plane waviness) as reviewed in subsection 2.4. Mukhopadhyay et al. [1,135] have stated that, the failures triggered by the compressive load for wrinkled composite components would be caused by fibre failure or delamination, interacting with matrix cracking. Hence, it is appropriate to include all three failure modes to obtain a better accuracy for performance prediction.

Each single ply was modelled by the hexahedral 8-noded elements (C3D8R), with one element per ply. Limited thickness (0.01 mm) of 8-noded cohesive element (COH3D8) were embedded into every interface to allow for the simulation of a non-self-similar crack, i.e. a delamination. All the mechanical constitutive behaviours used in this thesis were defined through VUMAT subroutines (a file allowing the user to define the mechanical constitutive behaviour of a material as they required and specifically suitable for Abaqus/Explicit [141]) for Abaqus/Explicit, implemented by Mukhopadhyay et al. [1,135]. Here in this subsection, brief descriptions are presented.

2.5.2.1 Undamaged material response

For the IM7/8552 material, linear-elastic orthotropic thermo-mechanical properties, as listed in Table 2.2, were assigned to each ply [1,135], to define the linear response. Groups of properties labelled as E, G, ν and α in Table 2.2 represent elastic modulus, shear modulus, Poission ratio and thermal expansion coefficients, respectively. Based on the experimental data of Makeev et al. [12], Mukhopadhyay et al. [1,135] used the least-square fit to obtain two parameters, A and B, to reflect the non-linear relation of the shear stress-strain response (Eq. (2.16)) of IM7/8552, which were assigned to the loading stage of the two shear components (in-plane and through-thickness). In the case of IM7/8552, they found that the best fit was when $A = 145$ MPa and $B = 38$, as described by

$$\sigma_{1i} = sgn(\gamma_{1i})\left(A\left(1 - e^{-B|\gamma_{1i}|}\right)\right) \qquad i = 2,3 \tag{2.16}$$

where, σ_{1i} & γ_{1i}: shear stress and shear strain (engineering). The engineering shear strain is the total shearing angle under a simple shear state, while the tensor strain is just half of the shearing angle when suffering the pure shear stress [14]. sgn denotes the signum function to extract the sign of a real number [142].

Table 2.2 Undamaged linear-elastic properties of IM7/8552 [1][11].

$E11$ (MPa)	$E22$ (MPa)	$E33$ (MPa)	$G12$ (MPa)	$G13$ (MPa)	$G23$ (MPa)	υ_{12}	υ_{13}	υ_{23}	α_{11} (/℃)	α_{22} (/℃)	α_{33} (/℃)
161,000	11,380	11,380	5170	5170	3980	0.32	0.32	0.436	0	3e-5	3e-5

2.5.2.2 Cohesive zone modelling (CZM) technique for static damage analysis

Jiang et al. [11] and Harper et al. [143] have shown that the cohesive-zone modelling technique can predict delamination with a good qualitative and quantitative agreement with test results. Hence, the modelling work presented here was based on their formulations [11] and coded as VUMAT by Mukhopadhyay et al. [1,135], the major advantage of using VUMAT is that more output information can be reflected by the specific user-defined parameters. In this thesis, every interface was represented by cohesive elements, which are available in Abaqus [144], as shown in Figure 2.12. The bilinear

traction-separation law [82] was adopted to govern the delamination process. Figure 2.13 and Figure 2.14 illustrate this law under either pure mode or mixed mode. It is widely known that to control the whole crack process for a pure mode, three parameters are required, namely: (1) stiffness (K); (2) interface strength (σ_{max}); and (3) critical strength energy release rate (G_C). The penalty stiffness, K, relates to the displacement between top/bottom surfaces to the relative tractions, which should remain high to ensure the rigid connection of elements before delamination initiation. The influence of the penalty stiffness to the relative separation could be thought of as a spring effect [84]. Interface strength (σ_{max}) defines the initiation moment of delamination, when the displacement is expressed as δ_e. Finally, the critical energy release rate (G_C), defined as the area under the curve, is used to determine the complete failure displacement, δ_f, when combined with the other two parameters.

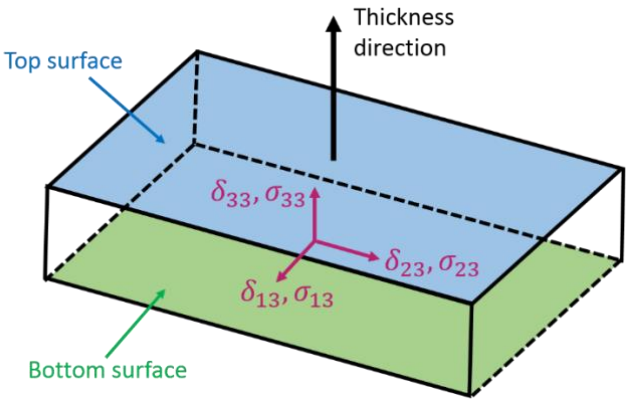

Figure 2.12 Schematic of a cohesive element, indicating the relative displacement between top and bottom surfaces and stress components.

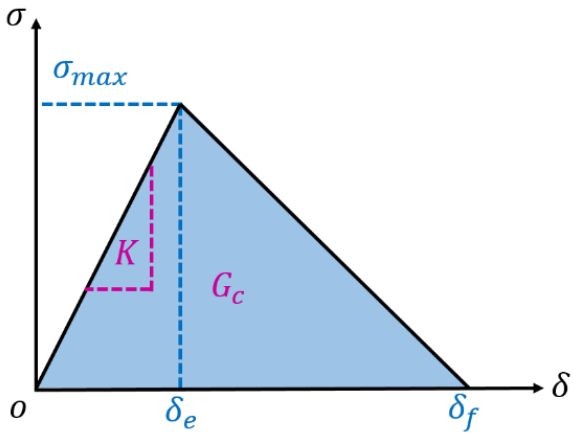

Figure 2.13 Schematic of the bilinear traction-separation law under pure mode.

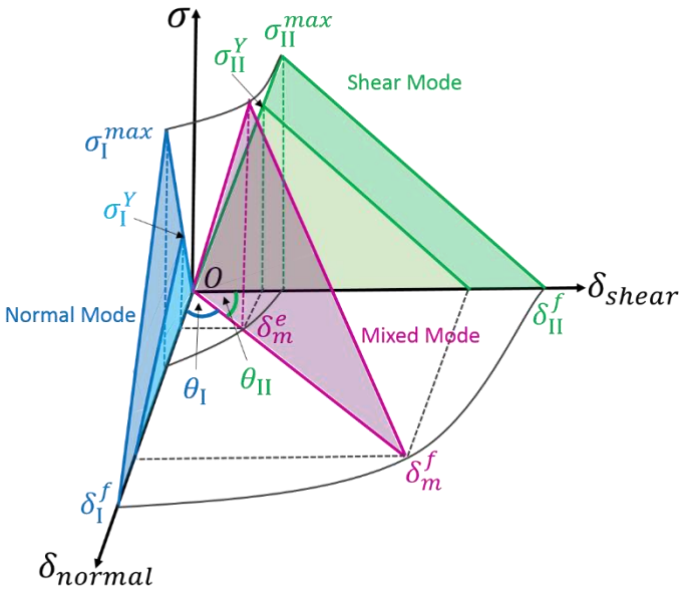

Figure 2.14 Schematic of the bilinear traction-separation law under mixed mode.

For the mixed mode, Jiang et al. [11] have given a detailed explanation to develop cohesive element models for the delamination simulation. As illustrated in Figure 2.14, the mixed mode (Pink plane) displacement (δ_m) could be obtained from the pure opening mode (δ_{I}) and pure shear mode (δ_{II}), which are represented by blue ($O\_\sigma_{\mathrm{I}}^{max}\_\delta_{\mathrm{I}}^f$) and green ($O\_\sigma_{\mathrm{II}}^{max}\_\delta_{\mathrm{II}}^f$) planes, respectively. The equation used to calculate δ_m is as

$$\delta_m = \sqrt{\langle\delta_{\mathrm{I}}\rangle^2 + {\delta_{\mathrm{II}}}^2} \tag{2.17}$$

where, the use of Macaulay bracket <> means the compressive normal traction has no effect on the onset of delamination as

$$\langle\delta_{\mathrm{I}}\rangle = \begin{cases} \delta_{\mathrm{I}}, & if\ \delta_{\mathrm{I}} > 0 \\ 0, & if\ \delta_{\mathrm{I}} \le 0 \end{cases} \tag{2.18}$$

While the resultant shear displacement is calculated by

$$\delta_{\mathrm{II}} = \sqrt{{\delta_{13}}^2 + {\delta_{23}}^2} \tag{2.19}$$

The onset of delamination under mixed mode is then governed by the quadratic damage initiation criterion as

$$\sqrt{\left(\frac{\langle\sigma_{\mathrm{I}}\rangle}{\sigma_{\mathrm{I}}^{max}}\right)^2+\left(\frac{\sigma_{\mathrm{II}}}{\sigma_{\mathrm{II}}^{max}}\right)^2}=1 \tag{2.20}$$

where $\sigma_{\mathrm{I}}^{max}$ and $\sigma_{\mathrm{II}}^{max}$ are the strength in pure opening and shear mode.

Once the delamination has been initiated, power law (Eq. (2.13)) was applied to control the propagation process until forming a complete interface failure. Here, the parameter of α was set to be unity.

If the angle between the pure mode and mixed mode is defined for opening mode as

$$cos\theta_{\mathrm{I}}=\frac{\delta_{\mathrm{I}}}{\delta_m} \tag{2.21}$$

and for shear mode as

$$cos\theta_{\mathrm{II}}=\frac{\delta_{\mathrm{II}}}{\delta_m} \tag{2.22}$$

Then the displacement at the moment of onset (δ_m^e) could be

$$\delta_m^e=\frac{1}{\sqrt{\left(\frac{K_{\mathrm{I}}cos\theta_{\mathrm{I}}}{\sigma_{\mathrm{I}}^{max}}\right)^2+\left(\frac{K_{\mathrm{II}}cos\theta_{\mathrm{II}}}{\sigma_{\mathrm{II}}^{max}}\right)^2}} \tag{2.23}$$

and complete failure (δ_m^f) can be defined as

$$\delta_m^f=\left(\left(\frac{\sigma_{\mathrm{I}}^Y cos\theta_{\mathrm{I}}}{2G_{\mathrm{I}C}}\right)^\alpha+\left(\frac{\sigma_{\mathrm{II}}^Y cos\theta_{\mathrm{II}}}{2G_{\mathrm{II}C}}\right)^\alpha\right)^{-1/\alpha} \tag{2.24}$$

where, the parameters of K_{I} and K_{II}, are the tensile and shear stiffness. $G_{\mathrm{I}C}$ and $G_{\mathrm{II}C}$ stand for the critical energy release rate at two pure modes, and the parameter of α is the same as used in power law. σ_{I}^Y and σ_{II}^Y mean the yield stresses for the respective modes, θ_{I} and θ_{II} represent the angle of mode I or mode II to the mixed mode, as labelled in Figure 2.14.

In addition, a damage variable, D, degrading the interface traction from the maximum at onset point ($D = 0$) to zero at complete failure ($D = 1$), was introduced in Jiang et al. [11] to track the accumulated damage severity by

$$D = \max\left(0, \frac{\delta_m - \delta_m^e}{\delta_m^f - \delta_m^e}\right) \tag{2.25}$$

Finally, the properties related to IM7/8552 to simulate delamination are summarised in Table 2.3 [11][143].

Table 2.3 Properties of IM7/8552 to simulate delamination [11][143].

G_{IC} (N/mm)	G_{IIC} (N/mm)	K_I (N/mm^3)	K_{II} (N/mm^3)	σ_I^{max} (MPa)	σ_{II}^{max} (MPa)	α
0.26	1.002	10^5	10^5	60	90	1

2.5.2.3 Crack-plane modelling technique for transverse matrix cracking

The implementation of continuum damage models to simulate matrix cracking under compressive load was also developed by Mukhopadhyay et al. [1,135], through a VUMAT, following Pinho's research [50,61]. Based on Puck's theory, the matrix cracking under compression was on an inclined plane. At a certain angle of ϕ to the normal plane (Figure 2.15), the failure initiation was checked by the Eq. (2.4) [45]. The stress components on the crack plane, σ_n, τ_L and τ_T, can be obtained from the components on the (a, b, c) frame, and fracture plane angle, ϕ, through the Mohr-Coulomb failure criterion [50].

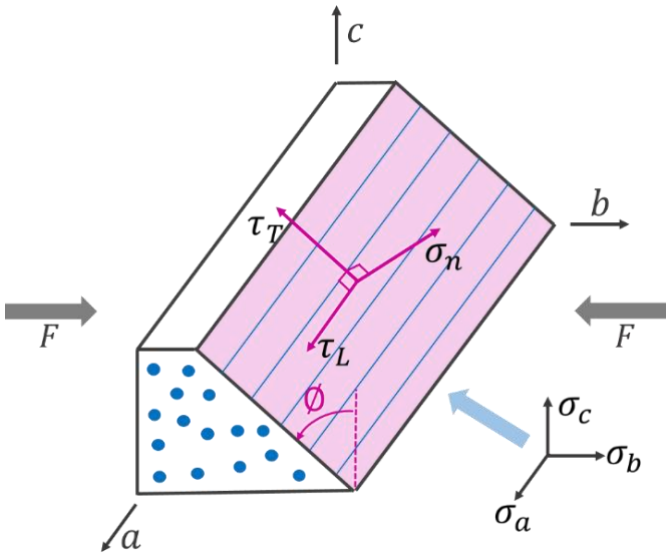

Figure 2.15 Schematic of stress components on the crack plane [50][61].

The materials used to simulate matrix cracking for IM7/8552 are listed in Table 2.4. In the VUMAT code for matrix cracking developed by Mukhopadhyay et al [135][1], the orientation of the crack plane was determined by iterating from 0° to 180°, until the failure initiation condition of Eq. (2.4) was met at a specific angle. Then the resultant shear stress (τ_{mat}) and driving stress (σ_{mat}) could be obtained on this crack plane by

$$\tau_{mat} = \sqrt{{\tau_T}^2 + {\tau_L}^2} \tag{2.26}$$

$$\sigma_{mat} = \sqrt{\langle\sigma_n\rangle^2 + {\tau_{mat}}^2} \tag{2.27}$$

The Macaulay bracket was used to indicate that only the tensile normal stress had effects on the crack formation. The relationships between two shear components, and the resultant shear component with the normal stress, are illustrated in Figure 2.16 by the angle of β and ω. Thus, relative strains could be defined by the same angles (β and ω) and the strains at failure initiation point (ε^0_{mat}) was also determined at the maximum driving stress (σ^0_{mat}). The damage evolution process was controlled by the power law (Eq. (2.13)) [88][89], with a mixed mode critical energy release rate (G_{mat}) to combine all the pure mode energy release rates (G_n, G_T and G_L) together. Strains at complete failure (ε^f_{mat}) [61] was calculated by

$$\varepsilon_{mat}^{f} = \frac{2G_{mat}}{\sigma_{mat}^{0} L_{mat}} \tag{2.28}$$

where, L_{mat} is a characteristic length to ensure that the energy calculation is independent of the mesh size, calculated based on the element edge dimensions following the procedures suggested by Pinho [61]. Finally, a damage variable (D_{mat}), was also introduced in VUMAT, to degrade the stress components on the crack plane and reflect the accumulated failures from zero (no damage) to unity (complete failure), following the bilinear law (Figure 2.13).

Table 2.4 Properties of IM7/8552 to simulate matrix cracking and fibre failure [61][1][12][143][10].

Y_C (MPa)	S_L (MPa)	G_{IC} (N/mm)	G_{IIC} (N/mm)	G_{kink} (N/mm)	α	θ_i (°)
250	113	0.26	1.002	80	1	1.5

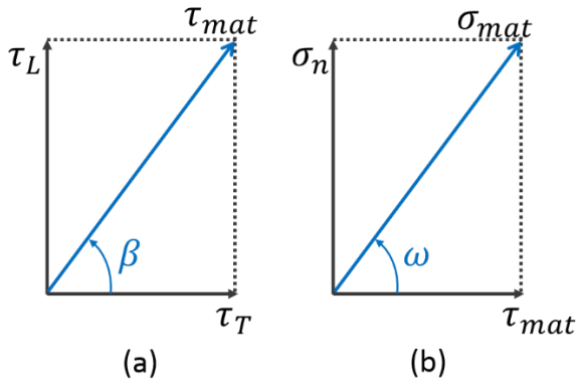

Figure 2.16 Illustration of angles between stress components on the crack plane, (a) angle (β) between two shear components, (b) angle (ω) between resultant shear and normal components [135][1].

2.5.2.4 Kink-formation modelling technique for fibre failure

The fibre failure was also simulated with a continuum damage model, following Pinho's 3D kink criterion [50][61] and implemented as a VUMAT by Mukhopadhyay et al. [135][1]. The material properties of IM7/8552 for this failure mode simulation are recorded in Table 2.4. Based on Pinho et al. [50][61], fibre failure was located in a kink plane (Figure 2.17), which was aligned at an angle of ψ

to the (a, b) plane of the lamina coordinate. This extent of the rotation can be determined by the relation of normal/shear stresses as indicated in

$$tan2\psi = \frac{2\tau_{bc}}{\sigma_b - \sigma_c} \tag{2.29}$$

The stress components on the frame (a, b, c) could thus be transformed to the frame of (a, b^{ψ}, c^{ψ}), by the angle of ψ. Then on the kink plane under axial compression, the assumption of the initial fibre misalignment (θ_i) would cause the shear stress to further rotate fibres by angle θ, and the stress components on the frame of (a, b^{ψ}, c^{ψ}) would finally rotated to the frame of (a^m, b^m, c^{ψ}). In the misaligned frame (a^m, b^m, c^{ψ}), the transverse matrix crack failure criterion (Eq. (2.4)) [45] was used again to check the onset of failure, and the power law [88][89] was used to govern the failure propagation to form a kink band at complete fibre failure.

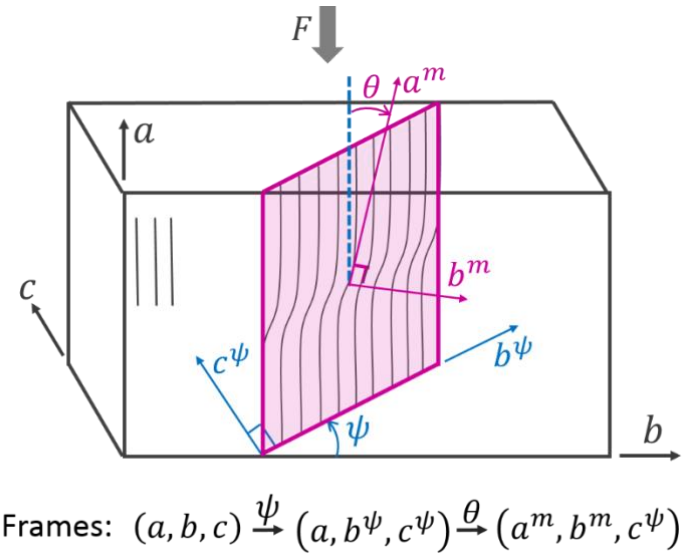

Figure 2.17 Schematic of the 3D kink band following Pinho's criterion [50][61].

The fibre misalignment angle at failure (θ) [61][1] was determined by

$$\theta = sgn(\tau_{ab^{\psi}})(\theta_i + \gamma_{mi}) \tag{2.30}$$

where, γ_{mi} stands for the shear strain at the initial misalignment frame, sgn means the signum function to extract the sign of a real number [142].

In the VUMAT code [135][1], γ_{mi} was calculated from the corresponding shear stress following the non-linear relationship defined in Eq. (2.16). The initial fibre misalignment angle (θ_i) was fixed at 1.5°, determined by calibrating the pristine model against compression strength tests [1]. Mukhopadhyay et al. [135] stated that when this angle is larger than 3° it could cause a negative influence on the modelling accuracy, which showed a good agreement with the research of Yurgartis [145]. During the failure evolution process, a fibre fracture energy (G_{kink}) was introduced in the code [1]. The strain at complete failure (ε_{kink}^{f}) could thus be obtained with a similar equation of Eq. (2.28) in which the items were replaced by the corresponding ones in the kink-band frame. A damage variable (D_{kink}) relating to the kink-band strains was also introduced into the code [1], to degrade the stress components on the kink-band frame following the bilinear law (Figure 2.13), in order to track this kind of failure mode.

2.6 Summary and Research Scope Based on the Literature Review

The research scope presented in this thesis is derived from the major gaps in the literature reviewed above, and it specifically coves three aspects:

(1) As indicated in the literature, many researchers have attempted to characterise material property data based on non-destructive testing, and some of them obtained high-quality data to meet the requirements for FE mesh creation. Interface locations, out-of-plane wrinkle and in-plane waviness angles are the three basic requirements for the development of the FE mesh when fibre misalignment is present. Based on the 3D characterisation data work conducted by Smith et al. [35][36] on the ultrasonic technique, further research was carried out in this thesis to transfer their 3D characterisation data into FE models with as-manufactured structural details.

(2) The negative influence due to fibre misalignment (out-of-plane wrinkles or in-plane waviness) is known to be significant. The full understanding of failure mechanisms behind compression tests for composites is highly important, due to their sudden and catastrophic nature. For out-of-plane wrinkles, many researchers, such as Mukhopadhyay et al. [1], have

identified the dominant failure modes and indicated the close dependence of compressive strength on wrinkle severity. But different geometrical parameters have been chosen to represent or characterise the wrinkle severity among researchers and there is no consensus as to which parameters or their combinations occupy the dominant position. Therefore, a rigorous and systematic study is required to give the answer to this issue. A suggested methodology to transfer the as-manufactured features to the numerical meshes accommodating the appropriate failure modes, based on the 3D characterised data, was developed to realise this objective, since this aim could not be achieved experimentally due to the very large number of highly controlled specimens required and the difficulty of precisely controlling specific parameters of wrinkle, nor has it been possible in the past using numerical models because of the time and manual effort required to create each different model.

(3) In terms of the fibre misalignment limited to the in-plane direction, the related research was not as varied or deep as that for out-of-plane wrinkles, due to the difficulty of manufacturing a controllable wavy region. Consequently, it is appropriate to focus on this region to have a better understanding how in-plane waviness initiates and governs the compressive failures of carbon-fibre laminates, in both experimental and numerical ways.

Chapter 3

Transfer process from characterised NDT data into FE models

The aim of this chapter is to develop a transfer process to combine the characterisation techniques based on NDT methods with FE modelling, to realise the objective of creating FE models of as-manufactured structures. The appropriate transfer process needs to 'understand' the inverted NDT information and convert it into input files for creating FE models using appropriate assumptions. The whole process is illustrated diagrammatically in Figure 3.1 and starts from the characterisation technique where an Inversion Process [4–6,17] inverts the raw NDT response data into three-dimensional (3D) maps of actual material properties.

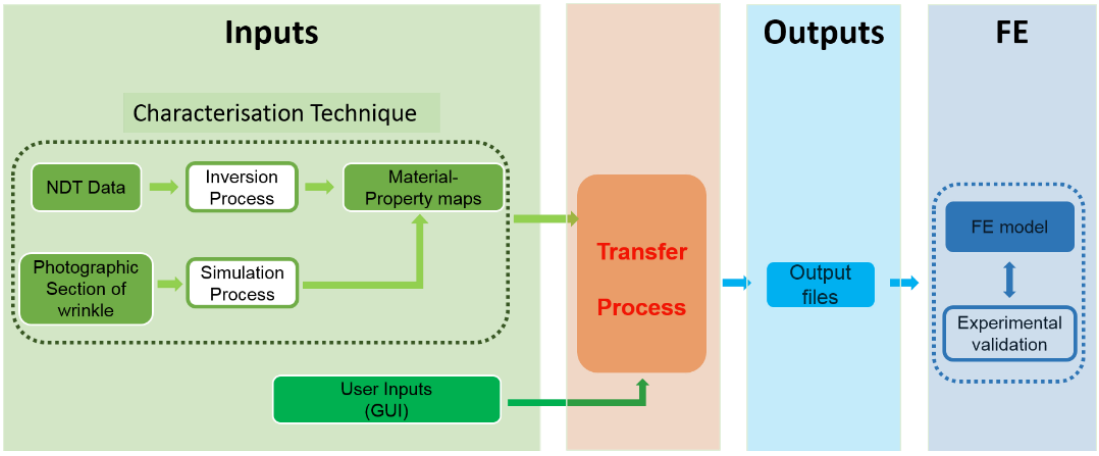

Figure 3.1 The schematic diagram from NDT data into FE model.

3.1 Transfer-process inputs and outputs

Two 3D material-property maps are created by the Characterisation Technique and these maps are inputs to the transfer process (Figure 3.1). One map is named the Ply-Interface Depth map (Map-A) to define the local depth of every grid point along each ply interface and, therefore, includes the distances between two adjacent inter-ply layers and the out-of-plane ply angles. The rectangular grids

chosen to extract data by the inversion process are uniformly spaced within each ply-interface; hence all the distances between adjacent grid points are the same, forming a grid of squares. The other material-property map is called the In-plane Orientation map (Map-B) to store the local in-plane fibre-tow orientation angles. The transfer process developed and reported in this thesis assumes the Characterisation Technique has already been applied, the two 3D property maps have been produced and they are available as inputs to the transfer process.

The transfer process is a Matlab-based script and a Graphical User Interface (GUI) (Appendix A) was created to control the user-input model-related parameters, e.g. element mesh size, choice of uniform or non-uniform FVF within models, etc. This process or GUI converts the inputs, the material-property maps (i.e. Map-A and Map-B) and GUI input parameters, into a series of files for building an FE model, with appropriate assumptions. Those files are the outputs of the transfer process.

Ideally, the two material-property maps should be inverted from NDT data as shown in the upper track of the green 'input' box in Figure 3.1, and the NDT inversion information will give all the required material details, e.g. local variance of ply thickness, in-plane and out-of-plane fibre-tow directions and local fibre volume fraction (FVF). Then the transfer process would convert all the information into nodes, elements and the properties within each element in the FE model. However, not all the material information can currently be inverted from NDT data for the coupons mentioned in this thesis, which possess unrealistic ply-quantity variations around the wrinkled region for the out-of-plane wrinkle coupons. Also, the inversion process for in-plane waviness samples is still being refined. Hence, an alternative procedure was proposed following the lower input track. This simulated procedure also provided a significant benefit for the following parametric study that is reported in Chapter 4, and becomes a clear way to separate the pre-process inversion work completed by other team members and the work covered in this thesis. The simulation produces the same format of the above two material-property maps (Map-A and Map-B) using a Matlab-based simulator. It is based on the graphical measurement of coupon-edge images as performed by Mukhopadhyay et al. [1] for the out-of-plane wrinkle models, or from the maximum waviness angle calculation for the in-plane waviness model. These details will be covered in the following Chapter 4 and Chapter 6 and the

wrinkle case is mainly mentioned in this chapter for clarity. All the FE models created by the transfer process in this thesis used simulated maps.

3.2 Operator-defined modelling options

The operator-defined modelling options were realised via a Graphical User Interface (GUI) (Appendix A), which was developed to give a rapid, user-friendly method for creating FE models from simulated or NDT-based input information. This GUI defines the user inputs for the model creation and controls the triggering of the transfer process to read the input files and write the relevant output files. Several aspects of the models can be controlled by the user:

- Selection of creating an out-of-plane wrinkle model or an in-plane waviness model by the transfer process
- Choice of material-property maps
- Extension of model with end parts/elements:

  Used to artificially add extra parts of a specified length, at the two ends along the load direction to extend the model size, in the case where the inverted NDT data does not cover a sufficient size of the component for realistic modelling of its performance. This modification is acceptable and beneficial if these small geometric modifications are sufficiently far from the imperfect region and would not have significant influence on the predicted stresses [146].
- Reduction in element size:

  As the FE model's accuracy relies on the element size [146], the modelled results will tend to be more accurate as the element size becomes smaller, until it becomes almost unchanged from one element size to the next. NDT-inverted material-property maps are usually spaced at the scan step-size and do not always give a fine enough element size for accurate modelling, hence this option provides an ability to adjust it by a suitable factor, according to the mesh study, prior to model creation.
- Loading conditions:

This choice allows the user to input the specific loading conditions. In the current version of the GUI, only the selection of tensile or compressive, displacement-controlled or velocity-controlled loading conditions have been developed.

- The choice of different FVF assumption:

  If a non-uniform FVF needs to be used it assumes that fibres do not move laterally, so FVF must change with ply thickness to conserve the number of fibres per ply per linear width. This is appropriate to the more realistic case of naturally occurring wrinkles. It is also derivable from the interface-location NDT inversion information.
- FVF is also dependent on in-plane waviness and can vary significantly within a ply. This information will be calculated from in-plane fibre-orientation inversion from NDT data in the future.
- In case of in-plane waviness, this GUI provides a choice, whether to skew the elements in the x and y directions to track the fibres.

3.3 Transfer-process assumptions

Several assumptions are made when calling the transfer process, as follows:

1) A uniform 0.01 mm thickness is assumed for all the resin-layer interfaces between plies because this is not currently determined experimentally by inversion of the NDT data. This is based on a non-toughened resin layer which would have a thickness of 0.005 mm to 0.015 mm [147], so the resin layers are modelled as cohesive elements with a thickness of 0.01 mm. The thickness of the ply elements (Figure 3.2) above and below each resin layer are adjusted to give the correct measured (inverted from NDT) ply spacing and interface location. The extreme situation where resin rich zone appears is not coved in this thesis.

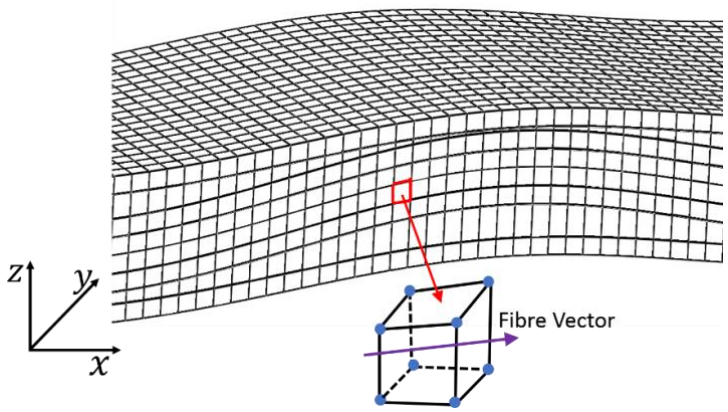

Figure 3.2 The schematic of ply elements fluctuations to represent wrinkles.

2) If a finer mesh is required for the model than is provided by the inversion of the NDT data, it is assumed that the actual wrinkle shape is as smooth as possible between the interface-depth measured points, so that a cubic-spline interpolation is a reasonable approximation to the actual shape.

3) The out-of-plane fibre angle is required in order to orientate the 3D stiffness axes within each element. This is assumed to be derived from the mean slope of the interfaces above and below the ply at the element in question. The exact method for achieving this is described in more detail below in sub-section 3.4.

4) An assumption is made that the fibres are uniformly distributed within the structure and the FVF is kept constant for every element at a nominal value of 57.70% [148] even for the wrinkled regions. The validity of this assumption and its repercussions are studied later in this chapter. In the specimens fabricated for this study, the nominal ply spacing of 0.25 mm is arrived at from the fact that two lamina of IM7/8552 [148] (nominal thickness: 0.125 mm) with the same fibre-orientation are laid-up together in the experiment to form one ply. In order to form the wrinkle, the number of 0.125 mm lamina in a ply is locally varied from 1 to 5 (Figure 3.3) and, during cure, the wrinkle forms in order to restore a uniform FVF. This is appropriately modelled as only ply-element thickness variations, based on the interface location information, assuming no change to the fibre volume fraction (FVF). However, constant FVF would not be appropriate for other causes of wrinkling.

5) For in-plane waviness, the FVF is still assumed not to vary within the wavy ply, even though in the actual specimens it does for the method used to create the samples for this study, a further discussion about how this local FVF was affected by the introduced waviness is presented in Chapter 6.

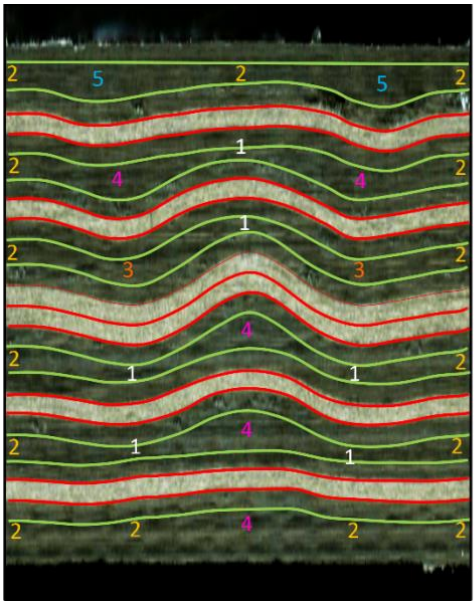

Figure 3.3 Optical image of edge of specimen with expanded vertical axis, overlaid resin-layer lines and labels to show the number of 0.125mm layers locally in each 90-degree ply, whilst this would normally be two.

3.4 Development of the transfer-process

The transfer process starts with refining the mesh to an acceptable element size based on the mesh study for each specific case (wrinkles [1] or waviness in section 6.4.1.4, as explained later) and defining the local material orientation for each element based on the material-property maps (Figure 3.4). All the information related to node location, node connectivity in each element and fibre orientation of each element, are stored in internal arrays. This information is written into separate files as the outputs of the transfer process, which are then imported into Abaqus/Explicit to reconstruct the structure and complete the computation for performance predictions. Table 3.1 lists the output files for the model creation as displayed in the bottom box in Figure 3.4.

Table 3.1 Lists of the output files created by the transfer process for the model creation.

Name	Contents
Model.inp	Top-level model-creation output file. Referencing other output files that are called by Abaqus when the model is created. Create part, instance, assembly. Define section assignment, amplitude, boundary conditions, etc.
Node.inp	Stores the Node coordinate.
Element.inp	Stores 8 node numbers defining each element and the element type (C3D8R & COH3D8).
Orientation.inp	Stores the 3D fibre orientation in each element.
Step.inp	Defines loading steps and output-parameter requests.
Material.inp	Defines all the material properties and behaviours.
NSET.inp	Assigns nodes in a group as a node set.
ELSET.inp	Assigns elements in a group as an element set.
Others	Other related output files if needed.

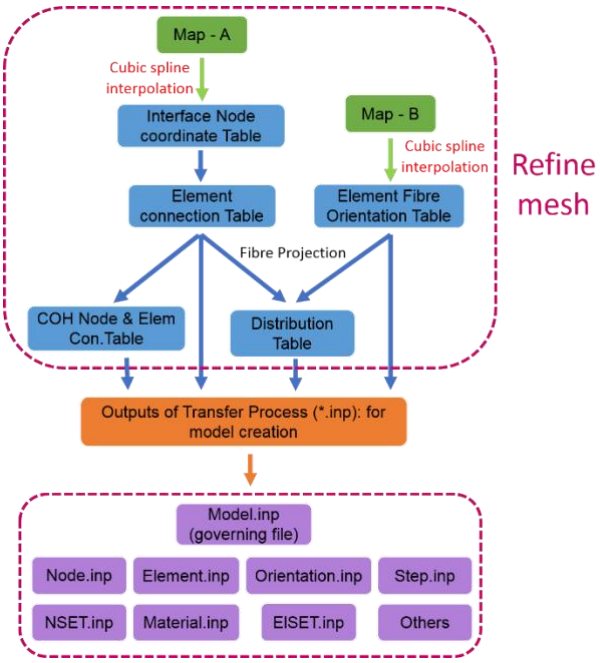

Figure 3.4 The schematic diagram of basic layout of transfer process (Elem Con. Means Element Connectivity).

Map-A displays the overall shape (Figure 3.5 (a)) of the model by defining the z-coordinate of each interface at specific points, which are uniformly distributed in the x_y plane. It thus also contains the ply thickness and out-of-plane ply angle information. If a finer spacing of elements is required between the uniform points of Map-A, a cubic-spline interpolation function [149] is used to interpolate the z-coordinate for the extra nodes, in order to refine the mesh to an acceptable size and also smooth the wrinkled region if necessary. Figure 3.5 (b) shows an example to explain this. After the interpolation, a typital NDT-measured step (0.5 mm) is divided into two elements (0.25 mm per element length). 0.25 mm was chosen based on the mesh study from previous work by Mukhopadhyay et al. [1], where one model was computed for each of a range of element sizes and an acceptable element size was assigned when the results converged. A pair of models created by the suggested transfer process in this chapter also confirmed the 0.25 mm choice, as with two different element sizes (0.25 mm vs. 0.20 mm) being computed, their predictions for the failure stress were 404.387 MPa and 404.266 MPa, respectively. After refining the mesh, 8-node linear-brick solid elements with a reduced integration algorithm (C3D8R) are defined to assign the ply-element type in the output file, as the reduced-integration elements are computationally economical. An additional 'enhanced' section control is added to control the potential effect of hourglassing [150], which is a spurious zero-energy deformation mode. The reason to form this phenomenon is illustrated in Figure 3.6 [151], when a reduced-integration linear element is subjected to a bending moment. After the deformation, two vertical dotted lines still remain at the same angle and same length in this element, which suggests a zero-strain condition at the integration point, and due to the lack of stiffness in this mode, the element could not resist this deformation and it would lead to meaningless results.

Extra nodes are inserted following the same out-of-plane and in-plane trends of the existing ply nodes to develop cohesive elements (COH3D8). They are used to simulate delamination when inserted at the interface between two plies, or to allow the initiation and propagation of intra-ply matrix crack (splitting) if inserted within the ply.

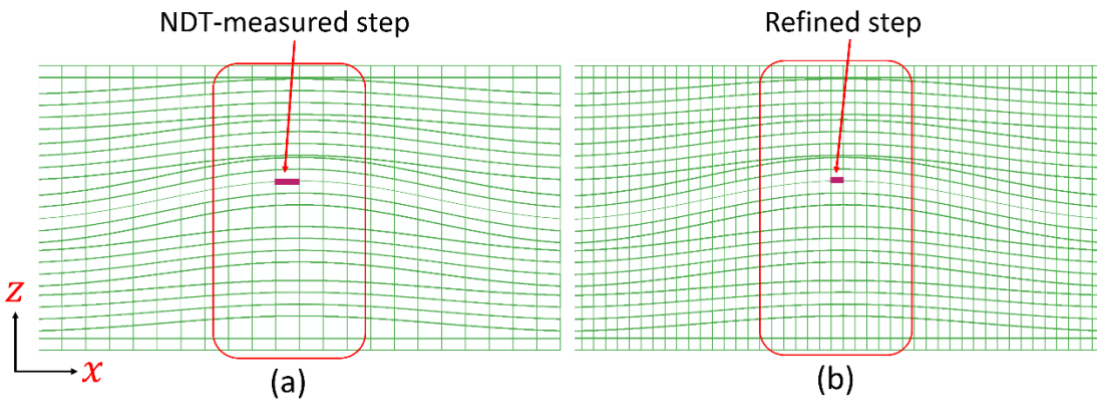

Figure 3.5 FE mesh reconstructed in ABAQUS, (a) without interpolation, (b) with interpolation by the cubic spline function to divide an NDT-measured step into two elements.

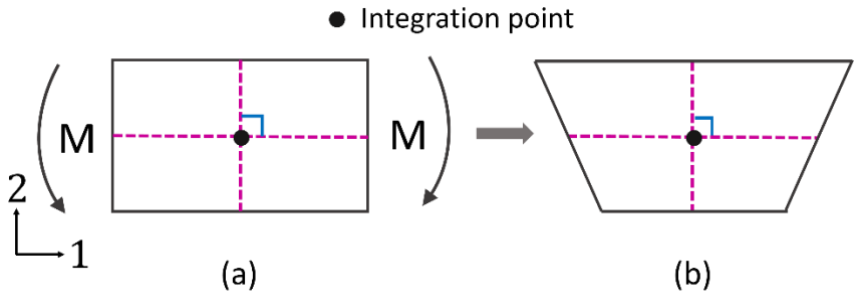

Figure 3.6 Illustration of hourglassing in a reduced-integration linear-element under a bending moment M, (a) before deformation, (b) after deformation.

As extra new elements are created when refining the mesh, the same cubic-spline function [149] is applied to interpolate between the in-plane fibre orientation angles stored in Map-B. After that, a local 3D fibre orientation in each ply element is calculated based on this in-plane fibre angle (φ) within the element and the node coordinates giving the out-of-plane angle (θ), based on an assumption that the gradient of the fibre-located x_y plane is mid-way between the gradients of the upper and lower surfaces of the element. The local 3D stiffness-axes in each element of the model are orientated based on this fibre orientation because the element is transversely isotropic with a high stiffness along the fibre direction and a lower but uniform stiffness radially to the fibres. The 3D stiffness orientations of all ply elements (not COH elements) are recorded in the Orientation.inp file (Table 3.1). As explained in Figure 3.7, each element is defined by 8 nodes to form a brick element (6 surfaces), nodes that will have been defined by the NDT data or simulator data. Points O, M_1 and M_2 are located at the mid-

point of their corresponding edges and define the mid-plane of the ply represented by this element and its adjacent elements. Each element has a square horizontal (X, Y) cross-section and four vertical through-thickness (Z) edges defined by the NDT data pitch, here due to the applicability to in-plane waviness model simultaneously, the definition of horizontal (X, Y) plane is allowed to a more general case of parallelogram shape (Figure 3.7). Hence two coordinate systems can be defined at point O: global system of (X, Y, Z) with the grey horizontal plane and local system of (A, B, C) with the blue plane defining the mid-plane of the ply along which the fibres are assumed to be aligned, determined by vectors $\overrightarrow{OM_1}$ and $\overrightarrow{OM_2}$. As depicted in Figure 3.7, vector $\overrightarrow{OA}$ represents the fibre direction, which is projected to the global horizontal plane (grey) to form a vector $\overrightarrow{OA'}$. Point A is chosen to make $\overrightarrow{OA'}$ a unit vector. Then the out-of-plane and in-plane angles can be obtained, labelled as θ and φ, respectively.

For the local system (A, B, C), its $\overrightarrow{OA}$ axis and $\overrightarrow{OB}$ axis are aligned within the blue plane. Hence, the local $\overrightarrow{OC}$ axis can be calculated as the cross product of $\overrightarrow{OM_1}$ and $\overrightarrow{OM_2}$ by

$$\overrightarrow{OC} = \overrightarrow{OM_1} \times \overrightarrow{OM_2} \tag{3.1}$$

After the projection, the vector $\overrightarrow{OA'}$, based on the global system equals $(cos\varphi, sin\varphi, 0)$. Further to this, the vector $\overrightarrow{OA}$ can be explained by $(cos\varphi, sin\varphi, A_z)$ based on the global coordinate system and A_z is decided through

$$A_Z = \left|\overrightarrow{AA'}\right| = tan\theta = \frac{-\overrightarrow{OA'} \cdot \overrightarrow{OC}}{\overrightarrow{OZ} \cdot \overrightarrow{OC}} \tag{3.2}$$

For the last step to finalise the definition of the local system, the local $\overrightarrow{OB}$ axis is determined to be orthogonal to the $\overrightarrow{OA}$ and $\overrightarrow{OC}$ axes by:

$$\overrightarrow{OB} = \overrightarrow{OC} \times \overrightarrow{OA} \tag{3.3}$$

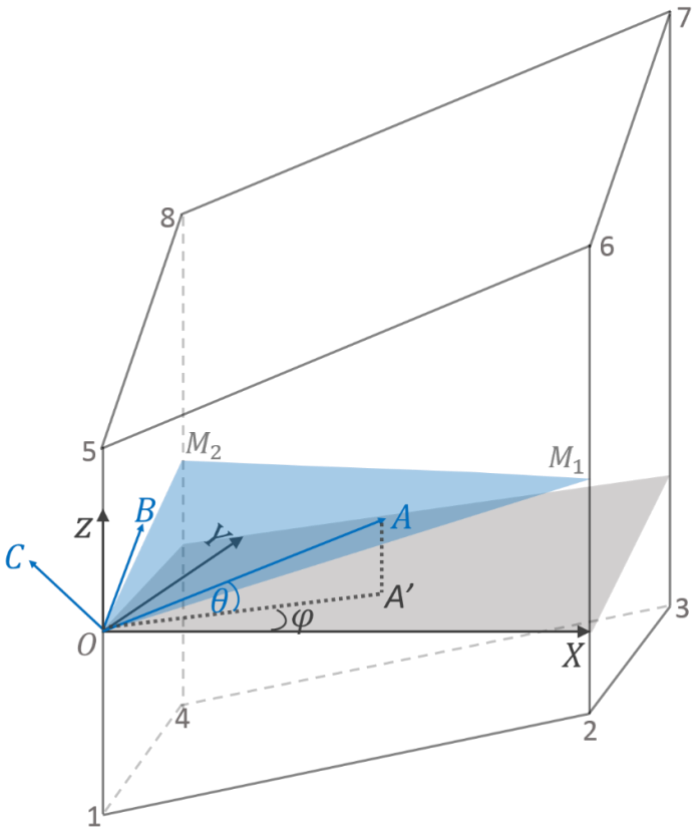

Figure 3.7 Schematic explaining the definition of the local material orientation on a brick element. (X, Y, Z) represents the global coordinate system with the grey horizontal (X, Y) plane, and (A, B, C) means a local system with the blue (A, B) plane, containing points O, M_1 and M_2, which are the mid-points on related edges of the brick element in question, $\overrightarrow{OA}$ is the fibre direction and $\overrightarrow{OA'}$ is the projection of $\overrightarrow{OA}$ on the global horizontal plane, angles θ and φ stand for out-of-plane and in-plane fibre orientations, respectively. Based on the global system, the location of point A' is $(cos\varphi, sin\varphi, 0)$ and the coordinate for point A is $(cos\varphi, sin\varphi, A_z)$.

3.5 Validation of transfer-process assumptions

Before making use of the developed models, it is appropriate to discuss whether the assumptions made during the transfer process will have a significant influence on the predicted results.

3.5.1 Ply and resin-layer thicknesses

For the first assumption about thickness, it is reasonable to assume the ply thickness remains the same if there are no wrinkles, as this is correct if minor errors from the manufacturing process is ignored. In terms of the interface thickness, considering the fact that an interface layer is quite thin, less than

0.015 mm [147], two models with the interface thickness fixing at 0.01 mm or 0 mm, were computed to show the negligible effect of thickness. Their predicted failure stress were 404.37 MPa and 404.73 MPa, respectively, which indicates that COH thickness being fixed at 0.01mm is quite reasonable.

3.5.2 Wrinkle geometrical shape

In order to validate the assumption of the smooth shape, it is necessary to study whether the transfer process can correctly capture the geometrical features from the NDT inversion inputs and transform them into FE meshes after a spline interpolation. The reconstructed FE meshes in Abaqus were compared qualitatively with the direct imaging capability within the simulator, as well as quantitatively with the actual equation that the simulator uses to create the wrinkle shape by

$$d = Ae^{-x^2/w_1^2}\cos(\frac{2\pi x}{L}) \tag{3.4}$$

Where, d means the wrinkle's displacement, A and L represent the amplitude and wavelength of a wrinkle, as described in Figure 3.11. w_1 is called Wrinkle Gaussian Half-Width, which will be explained in detail in chapter 4.

Based on the realistic wrinkle shape and severity, measured geometrical-related parameters (details in Chapter 4) from the edge images of experimental samples [1] were used to determine a Gaussian-envelope cosine-shape function (Eq. (3.4)) with a best-fit of the maximum wrinkle curve, which is located at the middle interface.

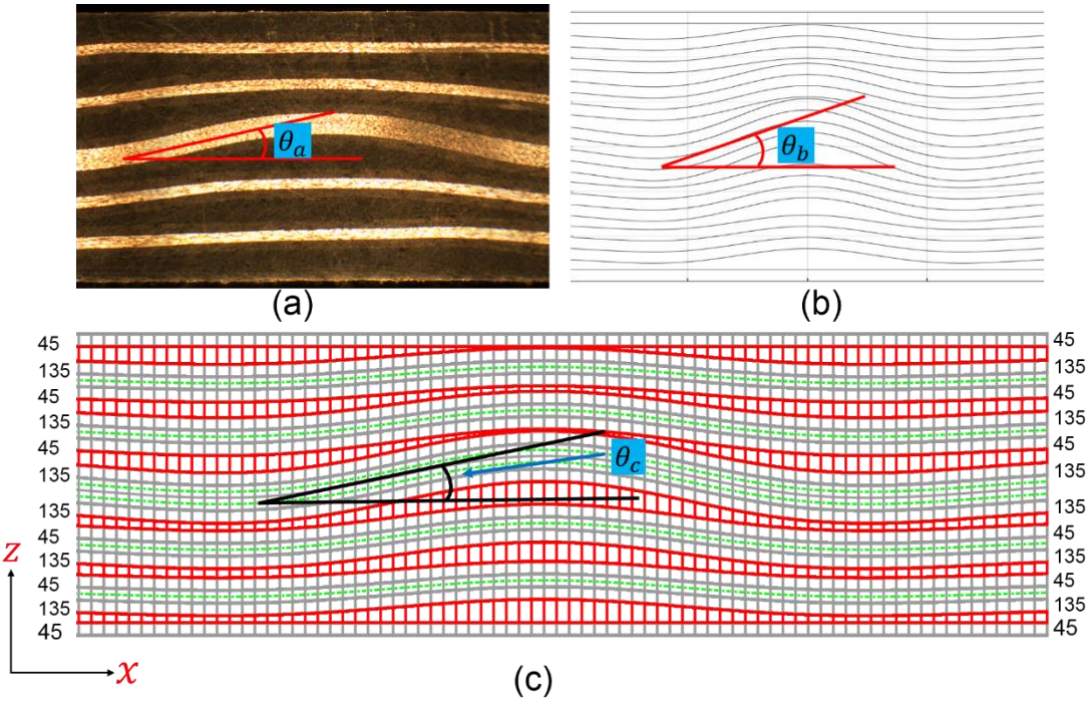

Figure 3.8 (a) photographic edge image of experimental sample, (b) wrinkle region in the simulator, (c) reconstructed FE mesh by transfer process in Abaqus/Explicit. Red plies are the 90-degree plies with designated numbers (1 to 5) of 0.125 mm layers.

These fitted parameters were input into the simulator to create Map-A and Map-B. Figure 3.8 (a) to (c) show the wrinkled region of the sample edge, the characterisation map created by the simulator and the reconstructed FE mesh in Abaqus. Qualitatively, it is obvious that all the three images contain similar wrinkled regions. The maximum angle at the middle plane was measured using the Image J software for the FE-mesh image (Figure 3.8 (c)), giving θ_c in Table 3.2, and the angle in Figure 3.8 (b) is calculated by taking the arc-tangent of the maximum of the first-order derivative of Eq. (3.4), labelled as θ_b. Angle comparisons based on all three wrinkle-severity levels tested in [1] are listed in Table 3.2. Another five comparisons based on the simulated Gaussian-envelope cosine shapes are also displayed in Table 3.2. All the differences between θ_b and θ_c, in both experimental cases and simulated shapes, are within 0.5°, hence this proves that, through the transfer process, the geometrical features of samples can be transferred into finite-element software automatically without adding any significant error (less than 0.5 degrees).

Table 3.2 Lists of the measured angles by image J of the reconstructed FE mesh in Abaqus, and calculated angles by Eq. (3.4) for the characterisation map created by the simulator, based on three wrinkle-severity levels [1], angles listed below the sample cases were from the simulated cosine-shape wrinkles, using the same procedures.

Wrinkle-Severity	Sample edge (θ_a)	Characterisation map (θ_b)	FE mesh (θ_c)
Level_1	~12°	11.9°	11.4 °
Level_2	~10°	9.7°	9.6°
Level_3	~6°	6.7°	6.5°
Simulate_1		4.3°	4.6°
Simulate_2		8.1°	8.3°
Simulate_3		11.5°	11.3°
Simulate_4		17.9°	17.8°
Simulate_5		20.0°	19.9°

3.5.3 3D stiffness axes

According to the third assumption, out-of-plane fibre angle is derived from the mean slope of the top and bottom interfaces of ply elements. Images from the model in ABAQUS in Figure 3.9 qualitatively show that this assumption is appropriate to align the fibre tows to the wrinkle-shape trend in the numerical model. Even around the maximum-angle locations (Figure 3.9 (a)) and in a compressed region where the maximum curvature exists (Figure 3.9 (b)), fibre distributions all retain the trend of ply angles. Material-property maps (Map-B) record the in-plane fibre angles, Figure 3.10 showed the success in transferring these angles into FE meshes by the transfer process.

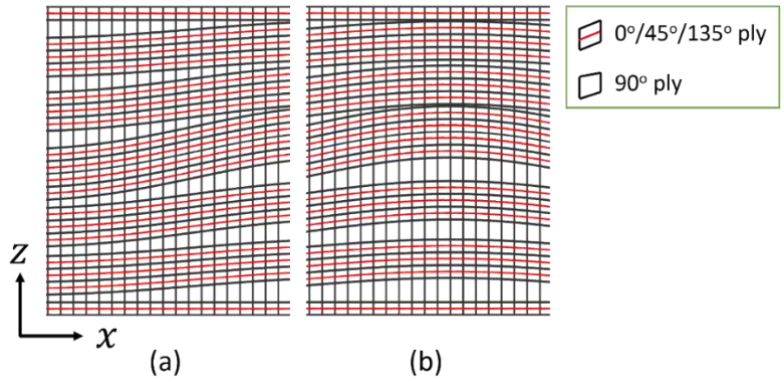

Figure 3.9 Images captured from part of FE meshes in Abaqus/Explicit, indicating the distribution of fibre orientations in a wrinkled model after the transfer process, black lines are the interfaces of each ply, red lines shows the fibre orientation in 0/45/135 plies. (a) A region containing the maximum wrinkle angle; (b) a region including the highest amplitude and maximum curvature of the plies.

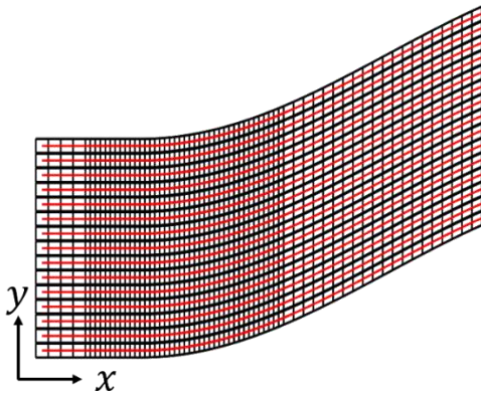

Figure 3.10 Similar images captured from part of FE meshes in Abaqus/Explicit, indicating the distributions of fibre orientations following the in-plane waviness, after the transfer process, squares formed by black lines represent ply elements, red lines shows the fibre orientation within the ply.

3.5.4 Fibre volume fraction (FVF)

The investigation of the last assumption regarding FVF required the use of validated FE models containing the out-of-plane wrinkles (Figure 3.11), so the details of the process for creating those models to present the discussion about FVF assumption will be explained in section 4.3 (Chapter 4). From those discussions, it was concluded that the uniform-FVF assumption made in the transfer process is reasonable and appropriate for the specimens concerned, which retained uniform FVF as a way of forcing a wrinkle. Hence, the models reported in this chapter assumed a uniform FVF over the whole structure.

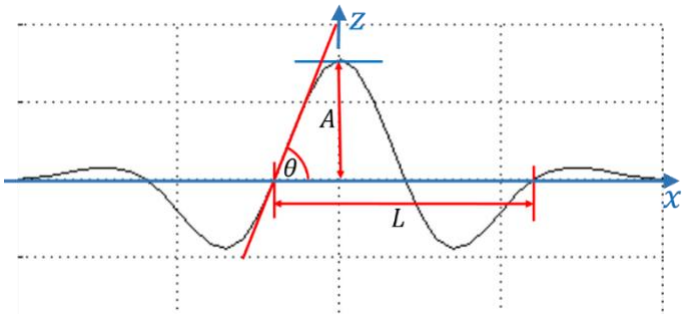

Figure 3.11 The schematic of a wrinkle, A stands for the amplitude, L means the wavelength and θ represents the maximum wrinkle angle.

3.6 Summary

A transfer process has been developed to create FE models based on material-property maps from inverted NDT data or simulations. Investigations have shown that fixing the thickness of resin layers in the model at 0.01mm is acceptable, and the assumption of uniform fibre volume fraction (FVF) over the whole structure is appropriate for the specimens used in this chapter, whilst a more realistic variation in FVF is reported in detail in section 4.3.

Based on the study above, with appropriate assumptions, all the models mentioned in this thesis follow this 5-step NDT-to-Model transfer process:

1) obtain appropriate parameters to represent key geometrical features of structures if using the simulated NDT data;
2) create two material-property maps by the simulator: Ply-Interface Depth map (Map-A) and In-plane Orientation map (Map-B);
3) transfer Map-A and Map-B into files for creation of finite-element models;
4) reconstruct models in Abaqus/Explicit and complete the computation;
5) validate transfer process and models by comparisons between tested results and model predictions.

Chapter 4
Parametric study of out-of-plane wrinkle severity, shape and extent

As reviewed in chapter 2, out-of-plane wrinkling in continuous-fibre reinforced composites has a significant influence on compressive failure stress, which needs to be considered and evaluated during the design, manufacture and inspection stage, to achieve high-performance composite components. As discussed in chapter 2, there is a lack of consensus in the literature over the key wrinkle metrics for non-destructive measurement. This illustrates the need for a rigorous and controlled multi-dimensional parametric study to identify and understand the interdependencies of parameters and determine a hierarchy of wrinkle-parameter importance, in order to provide guidance for the industrial quality-assurance processes for components with manufacturing-induced wrinkles, especially for their non-destructive measurement. Therefore, this chapter reports an investigation of the significance of various wrinkle metrics in predicting compressive strength of wrinkled composites to realise this aim. The methodology involves a novel combination of: (1) a custom MATLAB wrinkle simulator, (2) a novel transfer process, (3) a powerful numerical analysis using validated failure mechanisms [1].

To fulfill the investigation, the transfer process from chapter 3 was used with a simulator described in section 4.1 to create numerous numerical models of composites containing a wide range of values of several out-of-plane wrinkle metrics, the wrinkle-topology definition for the following study is also explained in section 4.1. Section 4.2 addresses the validation of the accuracy of models for predicting failure under compressive load by comparison with experimental test results. In section 4.3, the validated out-of-plane wrinkle model is used to investigate whether the assumption of uniform fibre volume fraction (FVF) would lead to a significant influence on the predicted compressive failure stress. In section 4.4 the parametric study of wrinkle-metric significance is reported with the aim of investigating which parameters govern the knock-down of failure stress of composites with embedded wrinkles. The investigated parameters were categorised into three aspects relating to a wrinkle:

severity, shape and extent. Finally, a summary is given in section 4.5. All the models mentioned in this chapter, were based on simulated material-property maps (details in chapter 3).

Most of the work in this chapter, except for section 4.3, has already been published in the journal of Materials and Design [9]. Here, the contents of that paper are reproduced with a few changes and additions, such as the treatment of FVF, to present the thesis as a coherent narrative.

4.1 Description of the custom Matlab simulator and wrinkle-topology definition

4.1.1 Description of the custom Matlab simulator

An initial custom matlab-based simulator (Appendix B) was created before the start of the work in this thesis by another member of the team. As the work in the thesis proceeded, the simulator was validated and modified by that team member to accurately simulate the wrinkles according to the user defined parameters. This validation process was based on the requirement of the transfer process to create as-manufactured models and led to some changes and additions to the simulator until it provided output files consistent with its input parameters.

The simulator was designed to create material-property maps, Map-A and Map-B in this thesis, as shown in the lower track of Figure 3.1. The material-property maps embodied either the out-of-plane wrinkle geometry, based on a few input parameters defining wrinkle severity, shape and extent, as used in this chapter, or the in-plane waviness distribution and severity, which is presented in chapter 6. The input parameters could be either from the measurement of coupon edge images (section 4.2) or from user-defined inputs (sections 4.3, 4.4 & chapter 6). For the version of the simulator used in this thesis (Appendix B), it simulated the out-of-plane wrinkle shape along the x direction by a sine or cosine curve within a Gaussian envelope, along with these choices:

1) User-controlled inputs of amplitude, wavelength, etc, to define wrinkles or waviness;
2) Sine or cosine phase along the x direction to simulate wrinkles (Figure 4.1);
3) A uniformly distributed wrinkle along the width (y) direction or with a Gaussian-controlled variation;

4) Choice of amplitude reduction-ratio depth profile from central interface to top/bottom surfaces along z direction as either stepwise reduction (section 4.2) or continuous reduction (section 4.3 & 4.4);
5) definition of the loading direction for the wrinkle-case, along the x or y direction;
6) definition of the in-plane waviness shape by a sine or half-sine phase;
7) choice of specific plies containing in-plane waviness.

4.1.2 Wrinkle topology definition

There is a variety of causes of out-of-plane wrinkles during the manufacturing process. Potter et al. [91][92] categorised them into four groups, with the wrapping of prepreg during storage and transportation, friction between the tool and composite during autoclave cure and residual thermal stress being the major sources causing local fibre misalignment in flat laminates. The wrinkle topology defined here aims to reflect the range of misaligned fibres and fibre undulations that can occur in the out-of-plane direction, with some idealisations in terms of shape and distribution for ease of analysis and quantification.

Wrinkled fibres in both the 0-degree (x) and 90-degree (y) directions are considered in the chapter. The wrinkle topology defined along the x direction (0-degree fibre direction) is expressed as a Gaussian-modulated cosine-wave profile. Figure 4.1 (a) illustrates the cosine profile, the wrinkle displacement (fibre misaligned undulation), d, is governed by a generic equation for a 3D wrinkle as:

$$d = Ae^{-(x-x_0)^2/{w_1}^2} cos\left(\frac{2\pi(x - x_0 - x_1)}{L}\right) \tag{4.1}$$

A wrinkle in the x direction is described by six parameters (noted in Figure 4.1): Amplitude, A; Wavelength, L; Wrinkle Gaussian Half-Width, w_1; maximum wrinkle angle, θ; wrinkle-centre location, x_0 and an x-offset phase parameter, x_1, which can convert this to a sine wave if $x_1 = {L}/{4}$. The maximum angle, θ, is a non-independent parameter that is determined by the other parameters. w_1 describes the wrinkle extent in the x direction. For the y (width) and z (thickness) directions, the profile of wrinkle amplitude, A, from its value A_0 at the wrinkle's centre, (x_0, y_0, i_0), can also be

controlled by a Gaussian function requiring two more extent parameters (Figure 4.1 (b)), the Transverse Wrinkle Half-Width, w_2 and Wrinkle Half-Height, n, as shown in the definition of A by

$$A = A_0 e^{-[(y-y_0)^2/{w_2}^2+(i-i_0)^2/n^2]} \tag{4.2}$$

where, i and n are in units of plies.

An additional non-Gaussian step-reduction profile for wrinkle amplitude distribution in the z direction was required to better represent wrinkles that were embedded in the experimental validation samples, and this specific distribution is covered in Section 4.2, Section 4.4.1 and Section 4.4.2.

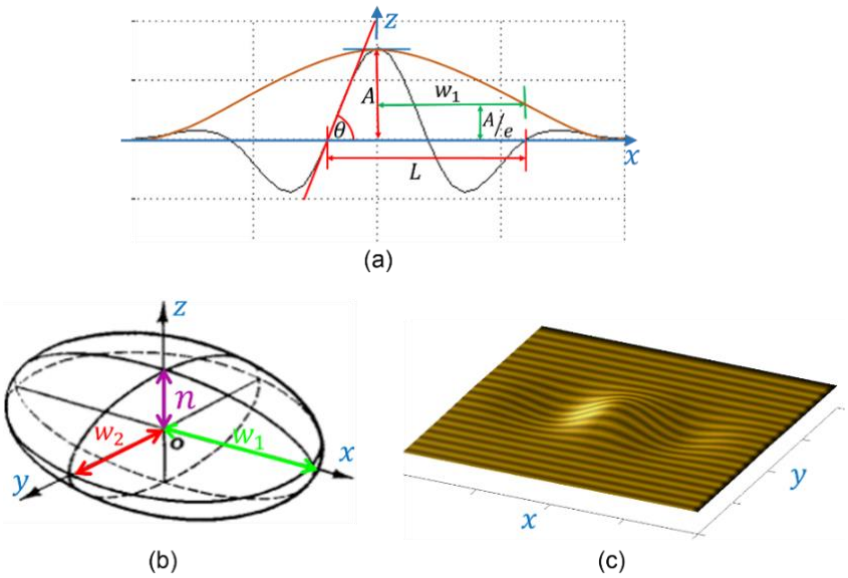

Figure 4.1 (a) Depiction of wrinkle shape in the x (0-degree fibre) direction. The black line represents the cosine wrinkle shape modulated by the brown line, which shows the Gaussian-modulation function (envelope) to limit the wrinkle volume. (b) $1/e$ iso-surface of the Gaussian-governed wrinkle profile in all three directions. (c) An example of Gaussian-governed cosine wrinkle in the (x, y) plane.

4.2 Validation of the out-of-plane wrinkle-modelling methodology

As explained in chapter 3, the geometrical information for the numerical models in Abaqus/Explicit was automatically created by the transfer process, based on simulated material property maps (Map-A & Map-B). The process by which different failure-mode algorithms were assigned to the plies, was also accomplished in the transfer process. Those failure modes were embedded as user subroutines

(VUMAT) into the Abaqus software, based on Mukhopadhyay's work [1]. The details of the related modelling techniques and theories were reviewed in section 2.5, and used as follows:

- cohesive elements [152] were inserted between plies to model delamination
- matrix cracking [45] could only occur in the 90-degree and +/-45-degree plies
- fibre failure [50,61] was modelled only in the 0-degree plies

The FE models developed by the transfer process were then solved in Abaqus/Explicit under compression loading parallel to the 0-degree fibre direction. The whole process is described schematically as the lower track in Figure 3.1.

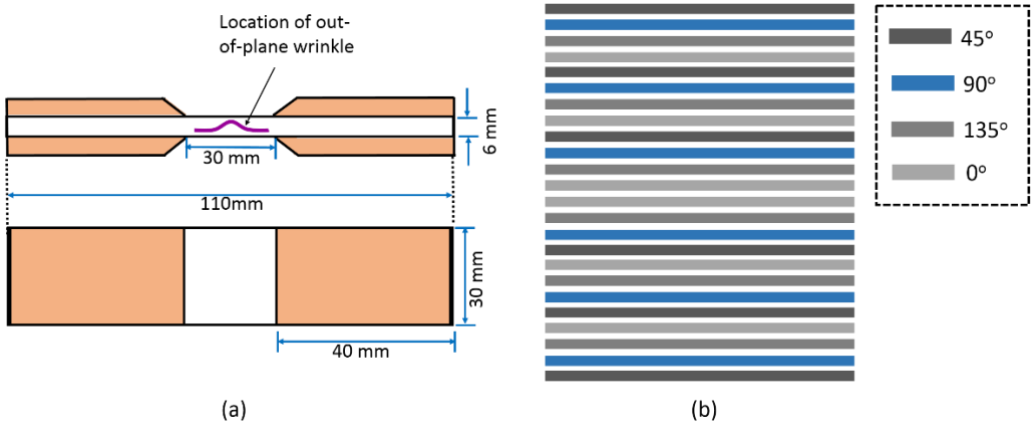

Figure 4.2 (a) geometry of wrinkle specimens, (b) layup of wrinkle specimens.

Based on Mukhopadhyay's [1] experimental work, the Matlab-based simulator described above was applied to search for the best Gaussian-envelope cosine-shape fit to wrinkles in images of the edge of the experimental coupons (Figure 3.7 (a)) and the two material-property maps were simulated for the amplitude, wavelength and envelope-width corresponding to this best fit. The coupons (Figure 4.2), with the geometry of 30 mm × 30 mm × 6 mm, had 24 plies with lay-up $[45/90/-45/0]_{3s}$ to form a quasi-isotropic ply sequence, using the IM7/8552 [148] fibre/resin system, as explained in [1], with extra 90-degree strips of different widths being inserted in, or removed from, the 90-degree plies to form the artificial wrinkled region with a designed wrinkle severity. The wrinkles appeared in the other plies by forming groups of 3 plies: [-45/0/45] (but 4 plies at the mid-plane: [-45/0/0/-45]), separated by 90-degree plies with the thickness variations. The wrinkled region in Figure 3.8 (a)

showed a step-reducing amplitude from the central plane to the top/bottom surfaces with ratios of 1.0 : 0.63 : 0.39 : 0.0 for the ply groups separated by 90-degree plies [1]. The simulator thus used these ratios to create the wrinkles in the material-property files. Figure 4.3 (b) displays a full coupon-size model that was developed in Abaqus/Explicit from a simulated data set using the Matlab transfer process. The model only covers the middle 'gauge' region of the test samples (Figure 4.3 (a)). The static compressive load was applied in the displacement-controlled form at a rate of -0.02 mm/s on the two (y, z) faces, to simulate the damage events that were captured in the experimental studies [1].

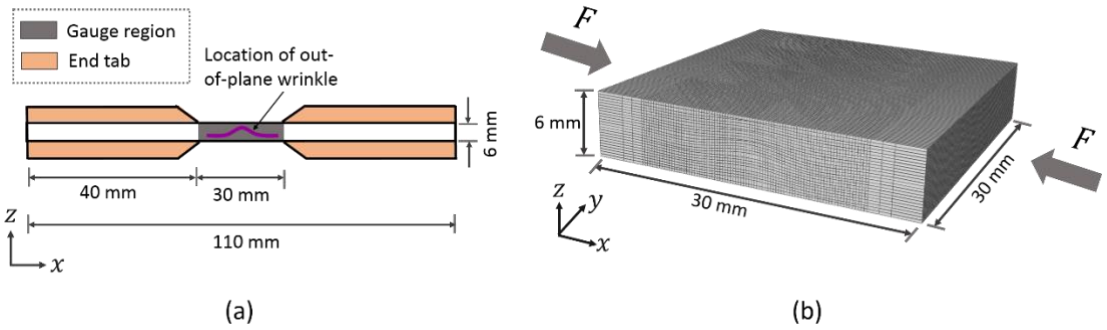

Figure 4.3 (a) (x, z) view of a wrinkle sample, (b) geometry of full-size wrinkle models covering the middle 'gauge' region of the sample in (a).

The comparison of the overall geometrical shape of the wrinkled region in Figure 3.8 (a) with the finite-element mesh in Figure 3.8 (c) shows qualitatively that the characteristics of the wrinkled regions in the coupons have been captured by the transfer process. The maximum wrinkle angles in the two figures (θ_a vs. θ_c) were measured using 'Image J' image-analysis software, and their comparisons for all three wrinkle-severity levels are listed in Table 4.1. The angle differences for each severity level are within 0.5°, which is significantly less than the uncertainty in determining wrinkle angles using non-destructive methods with an accuracy of $\pm(2^\circ + 17\%)$ [17], or the analysis of the sample-edge photographs. Hence, this proves quantitatively that the geometrical features of samples can be transferred into finite-element models automatically without adding any error that is significant in comparison to other errors in the process.

Table 4.1 Lists of the angles measured using image J of wrinkled region of the sample edge [1] and the reconstructed FE mesh in Abaqus.

Wrinkle-Severity	Sample edge (θ_a)	FE mesh (θ_c)
Level_1	11.7°	11.4 °
Level_2	9.4°	9.6°
Level_3	6.2°	6.5°

The wrinkle displacement in the x (0° fibre ply) direction, d, at the interface between two plies, was governed by

$$d = A_i e^{-x^2/{w_1}^2} cos\left(\frac{2\pi x}{L}\right) \tag{4.3}$$

The wrinkle amplitude in the y (90 ° fibre ply) direction was uniform. The parameters of Eq. (4.3) are the same as in Eq. (4.1), except that A_i is defined to represent the depth-dependent maximum displacement and subscript i denotes the interface index.

In the thickness (z) direction, the amplitude A_i reduced stepwise from a maximum at the central interface to zero at the surfaces, following the ratios: 1.0 : 0.63 : 0.39 : 0.0, which reflected the real distribution of the wrinkle amplitudes in the mechanical-test coupons [1].

Mukhopadhyay et al. [1] manufactured specimens with three different severity levels (maximum wrinkle angles of 6°, 10° and 12°) to study the wrinkles' influence on the compressive failure process. For each wrinkle severity level, three coupons were chosen to validate the capability of the prediction by models developed by the transfer process, two of each severity (sample numbers 1 and 8) were from edges of the 8-coupon panel and one (number 5) was chosen from the middle of the panel. Material-property maps for these samples were simulated iteratively to home in on wrinkle amplitude, wavelength and extent values that gave good agreement with the characteristics of the wrinkle in the edge photographs. These best-fit simulations were passed to the transfer process to create finite-element models for strength predictions, using the actual specimen width of 30 mm (Figure 4.2 (a)). The predicted failure stress was identified at the peak point (labelled as *P* in Figure 4.4) of the stress vs. displacement curve for each model, once enough global failure has been accumulated that it could

not sustain any further load through the damaged elements in the model; failures which were triggered and controlled by the mechanisms discussed in section 2.5. The initial horizontal stress-line area (labelled as *A* in Figure 4.4) was the thermal stress stage, which is added to simulate the cool-down process when composites are removed from autoclave with high temperature to the room-temperature environment [11].

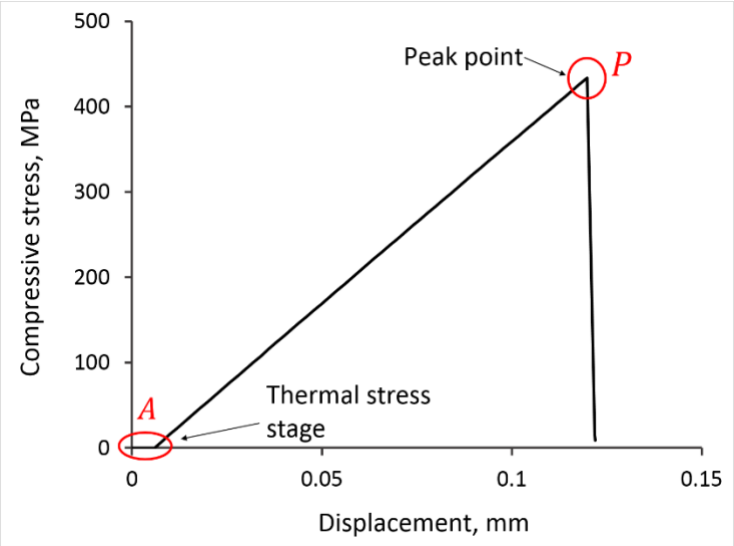

Figure 4.4 Predicted compressive stress vs. displacement curve from a wrinkle model that was used to plot Figure 4.5, the peak point *P* represents the model failure and the related stress at this point is the predicted failure stress, the horizontal stress line stage, labelled as *A*, is the thermal-stress stage.

Comparisons of predictions by transfer-process models with the mechanical-test results are shown in Figure 4.5 for each coupon. Also shown in Figure 4.5 are results from specimens with a reduced width of 20 mm following the same procedures as the full-size models. In the 20 mm-width models only the most severely wrinkled central two 0° plies had the fibre-kink failure model activated. Both the reduction in model size and the confinement of the fibre-kink failure to the central plies were aimed at reducing computation time, which is of benefit in the subsequent parametric study involving a large number of models.

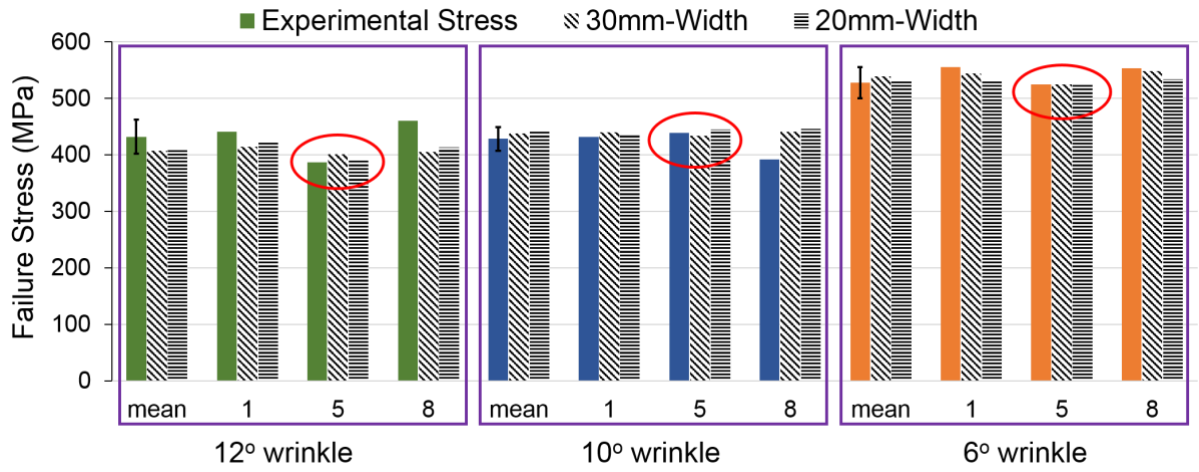

Figure 4.5 Comparison between results from 20 mm and 30 mm width models, created by the transfer-process and experimental test results for 30 mm-wide coupons [1]. Green, blue and orange bars are experimental values for coupons of severity levels (maximum angles) 12°, 10° and 6° respectively, showing mean values for all eight coupons and individual results for specimen numbers 1, 5 and 8. Error bars on the mean experimental values are the standard deviation from tests.

For both model sizes, similar failure stress levels were obtained and both predictions are in good agreement with the experiment for both types of model, as their means of predictions for specimens no. 1, 5 and 8 fell within one tested standard deviation in each severity level. Therefore 20 mm-width models with the fibre-kink failure mode only in the central two 0° plies give acceptable predictions for compressive failure stress influenced by wrinkles, and this method was applied in the following parametric studies in section 4.4.

On closer examination of the results it can be noted that, for both model widths, the predictions of the edge-coupon strengths (no. 1 and 8) are not as good as for middle coupons (no. 5) for each wrinkle-severity case. This may originate from the local variation in the wrinkle shape within the edge regions. Further investigations will be conducted in the future, to study this issue by creating models directly from inverted NDT data on specific coupons, rather than simulated data based on photographic edge-image measurements. However, considering the standard deviation in the experimental mean strength of each wrinkle severity, indicated by black error bars in Figure 4.5, the coupon-based predictions, through this methodology, are still acceptable compared with the overall test results.

4.3 Discussion of the influence from Fibre Volume Fraction (FVF)

The models in section 4.2 used a uniform-FVF assumption as stated in Chapter 3. Whilst it is unlikely that this is the case in a real wrinkle, it is a reasonable approximation for the specimens manufactured for validation of the model [1] (section 4.2). The number of 0.125 mm layers in the 90-degree plies was varied locally between 1 and 5 (Figure 3.3) to deliberately cause a wrinkle due to the tendency for FVF to even out during cure, making a uniform-FVF assumption entirely appropriate. However, in a realistic production component, the formation of a wrinkle or waviness would squeeze fibres together to form resin-poor regions in some local areas, and other regions will accordingly become resin-rich. The resin-poor and resin-rich regions definitely would have different FVF and a uniform-FVF would be inappropriate in this more realistic scenario. Hence it is valuable to investigate how a more realistic assumption about FVF mapping would affect the performance predictions, which then informs the validity of the uniform-FVF assumption in the rest of this thesis.

This investigation uses the wrinkled models, validated in section 4.2, to investigate the influence caused by the variance of FVF. The definition of the embedded wrinkles was similar to that used in section 4.2, the reduction trend of amplitude, A_i, was governed by a Gaussian function:

$$A_i = A_{i_{mid}} e^{-(i-i_{mid})^2/n^2} \tag{4.4}$$

where, A_i means the amplitude in the ith interface and $A_{i_{mid}}$ is the mid-ply amplitude.

In order to allow the element properties in the model to vary in accordance with FVF, a formula was added into the transfer process to achieve it. In general, properties with a constant FVF are assigned to the FE model, because in [1] the wrinkles were produced by using the natural tendency of FVF to even out across the sample during cure. However, this is not always the case and Melro [153] has shown that the local FVF variance does affect the material properties - when FVF of AS4/3501-6 changed from 45% to 65%, its longitudinal Young's modulus increased by 40%. This proves further the necessity to have an investigation about the FVF influence on the failure stress.

Different mechanisms [14,154–156] have been suggested for generation of effective-medium homogeneous elastic properties based on the ratio of constituents of a composite material. Here, the

effective-medium model is based on Melro's work [153], and used Melro's values for AS4/3501-6 fibre/resin material, as listed in Table 4.2. The technique to calculate the homogeneous elastic properties was the Mori-Tanaka method [153,154] (Table 4.3**Error! Reference source not found.**), to represent the variance of FVF from 10% to 90%. 60% was chosen as a baseline, as this is the nominal FVF value indicated by Hexcel [157].

Table 4.2 Elastic properties of AS4 and 3501-6 [153].

Unit: MPa	E11	E22	G12	G23	ν_{12}
AS4	225,000	15,000	15,000	7000	0.2
3501-6	4200	4200	1567	1567	0.34

Table 4.3 Calculated homogeneous elastic properties of 9 cases representing different FVF rates from 10% to 90%, by Mori-Tanaka method [153,154].

FVF	**10%**	**20%**	**30%**	**40%**	**50%**	**60% (Base)**	**70%**	**80%**	**90%**
E11 (MPa)	26289	48376	70461	92544	114624	136703	158780	180855	202928
E22 (MPa)	5114	5689	6308	7008	7814	8756	9875	11226	12892
E33 (MPa)	5114	5689	6308	7008	7814	8756	9875	11226	12892
v12	0.32	0.31	0.29	0.28	0.27	0.25	0.24	0.23	0.21
v13	0.32	0.31	0.29	0.28	0.27	0.25	0.24	0.23	0.21
v23	0.46	0.45	0.42	0.39	0.36	0.32	0.27	0.22	0.15
G12 (MPa)	1844	2174	2575	3072	3704	4537	5681	7354	10030
G13 (MPa)	1844	2174	2575	3072	3704	4537	5681	7354	10030
G23 (MPa)	1752	1966	2217	2515	2875	3318	3878	4605	5590

Properties required for simulating matrix cracking and fibre failure, and most properties used for modelling delamination, were the same as IM7/8552, and they were listed in Table 2.3 and Table 2.4 [1]. Two interface strengths for governing the initiation of delamination in this FVF-investigation model, $\sigma_{\mathrm{I}max}$ and $\sigma_{\mathrm{II}max}$, were taken from the Hexcel website [157], which equalled 45 MPa and 48 MPa, respectively.

4.3.1 Dependence of compressive failure stress on uniform FVF value

During the first stage, nine models, for which the elastic properties relating to the specific FVF value were listed in Table 4.3, were computed where FVF was assumed to be uniformly distributed within each model, covering the distributions from 10% to 90% in 10% steps. All other parameters and properties of those models were unchanged. The predicted failure stresses are shown in Table 4.4. The manufacturer's recommended FVF of AS4/3501-6 is 60% as indicated by the manufacturer, Hexcel [157], and the predicted failure stress with this FVF was chosen as a baseline. The comparison with the baseline is shown in Table 4.4 as a percentage to check the influence of FVF. It is clear that the changes of FVF do cause a systematic variation in the predicted failure stress. Moreover, considering the situation that FVF does change locally within most wrinkled or wavy components, it is necessary to investigate this FVF-affected influence in a more realistic case.

Table 4.4 Predicted results and homogeneous properties of 9 models representing different FVF rates from 10% to 90%.

FVF	10%	20%	30%	40%	50%	60% (Base)	70%	80%	90%
Predicted Failure stress (MPa)	247	249	260	268	282	292	309	317	316
Percentage failure-stress change w.r.t[1] 60% FVF (%)	-15.50	-15.00	-10.96	-8.31	-3.45	0.00	5.63	8.52	7.94

4.3.2 Comparison of FVF assumptions for compressive failure stress

The next step is to create models reflecting the more realistic situation where FVF changes in a local region, rather than uniformly in the whole structure, using the assumption that fibres do not move laterally. In order to realise this investigation, the transfer process was modified to allow the user to select between a uniform (specified) FVF and a FVF that varies according to a different assumption:

[1] w.r.t: abbreviation for 'with respect to'.

that no fibres move laterally. In the latter case, the *FVF / nominal-FVF* ratio in a ply is assumed to be inversely proportional to the *ply-thickness / nominal-ply-thickness* ratio, as:

$$FVF_{local} = FVF_{nom}\left({thickness_{nom}}/{thickness_{local}}\right) \tag{4.5}$$

where the nominal ply thickness is that required to produce the designed nominal FVF.

As showed in Figure 3.11, a wrinkle [135] can be defined by amplitude (A), wavelength (L) and their corresponding maximum angle (θ). Because the total number of fibres in a lateral distance is assumed to stay the same, obviously, among these three parameters, wrinkle amplitude is the most important parameter for influencing FVF as it decides the local ply thickness directly. Therefore, five amplitudes from 0.2 mm to 0.6 mm in 0.1 mm steps were chosen, to investigate the influence of locally-varying FVF, whilst keeping all other parameters the same in the model. Based on the above assumption, the local FVF is calculated by Eq. (4.5). During this investigation, the nominal FVF, FVF_{nom}, was 60%, and nominal ply thickness was 0.24 mm.

Once the value of local FVF is obtained, elastic properties can be calculated for that specific region, which are then assigned to the relevant area in the model for computation. In this study, it simplifies matters that the wrinkle is uniform in the width direction (y). Based on the symmetrical lay-up line in the middle, each half-ply was divided into 9 blocks along the 0° fibre direction as shown in Figure 4.6 and the block-arrangement in the opposite half remained symmetrical. The middle 8 blocks were chosen to have a small width of 1 mm (covering 4 elements), to reflect local variance of FVF without causing too many separate material definitions in Abaqus (each FVF requires a new set of material definitions), and the 9th block (cyan block in Figure 4.6) at the end covers the remaining region, as the far-end region is set to be flat and without any FVF fluctuation. Then FVF within each block can be approximated with the same local ply thickness value. Here, the symmetry is possible because, the wrinkles were simulated with a cosine-phase wrinkle (maximum deviation in the middle). Finally, for each block, its local FVF is calculated by Eq. (4.5) and there were in total 216 blocks across the total of 24 plies in this example.

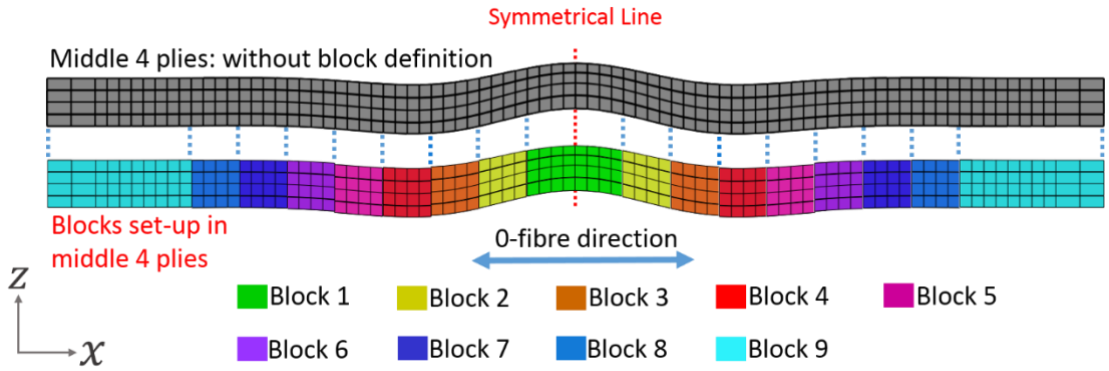

Figure 4.6 Schematic of block arrangements to represent local FVF distributions along 0-fibre direction, each block assumes to have the same local FVF value. Only middle 4 plies are plotted here as an example and block-divisions in the rest of the plies keep the same as the middle 4 plies plotted.

In each amplitude case (in total five amplitudes, from 0.2 mm to 0.6 mm), two models were computed, one contained uniform FVF and the other a non-uniform FVF following the ply-thickness variations but both had a nominal FVF value of 60%. The predicted results are shown in Table 4.5. It shows that the differences of stress predictions between uniform FVF and non-uniform FVF are within 4% for every amplitude case, and less than 1% for the cases of amplitude at 0.4 mm and 0.5 mm. The biggest difference (3.60%), for the case of 0.6 mm amplitude, may be caused by the unrealistic FVF distribution calculated in some local regions, where the highest FVF reaches an impossible 97%. In another two cases, when the amplitude equals 0.2 mm and 0.3 mm, the differences are also a little larger compared to the 0.4 mm and 0.5 mm amplitude cases. In the models, properties (those listed in Table 4.3) assigned to the plies differed between uniform and non-uniform FVF cases; these differences would have further influences in the initiation and propagation of ply failures, such as fibre failure. Mukhopadhyay et al. [1] have discovered that the failure would be fibre-failure dominated for the lower wrinkle angle but it changed to delamination dominated for the higher wrinkle angle, the failure transition point was between 8° and 9°. For the 0.2 mm and 0.3 mm amplitude simulations, their maximum angles are close to this transition range, 7.9° and 11.7° respectively. Hence, besides the delamination, there is also a possibility to trigger the fibre failure (ply failure) or the fibre failure dominates the failure process, especially for the 0.2 mm-amplitude case,

which might be the reason accounting for the difference between uniform and non-uniform FVF predictions for the 0.2 mm and 0.3 mm amplitude cases.

However, considering that a $\geq 4\%$ experimental CV ($CV = \frac{standard\ deviation}{average\ value}$) is common for the same type of samples, 6.3% for the wrinkle-free samples test and 6.9% for the 12°-wrinkle samples test as the example (Figure 4.5) [1], it could be regarded that the 4% difference influenced by the local FVF variance is acceptable for the studies in this thesis, as it is below the mechanical-test uncertainty for this simple assumption for the local FVF definition. However, for future modelling of real wrinkles containing FVF changes, where it will be crucial to demonstrate the modelling accuracy and instil confidence in simulation replacing experimental testing, the modelling of variable FVF could become significant.

Table 4.5 Predicted failure stress distributions with uniform and non-uniform FVF, when wrinkle amplitude varies in the range of 0.2 mm to 0.6 mm, for a wrinkle wavelength of 8 mm.

Wrinkle Amplitude (mm)	Predicted Failure Stress (MPa)		Percentage difference in failure stress for non-uniform vs 60% uniform-FVF	Min. Local FVF (%)	Max. Local FVF (%)	Max. Wrinkle Angle
	Uniform FVF (60%)	Non-uniform FVF				
0.2	338	347	2.5 %	53	69	7.9°
0.3	338	342	1.2 %	50	74	11.7°
0.4	292	292	0.0 %	48	80	15.5°
0.5	252	253	0.2 %	46	88	19.1°
0.6	230	239	3.6 %	43	97	22.6°

Finally, two more models for amplitudes of 0.3 mm and 0.4 mm were created for the purpose of validating whether just 9 different FVFs in each ply are enough to represent the local FVF variance. The local FVF values in these two new models, were calculated based on every single element of each ply through Eq. (4.5), rather than a block of 4 elements to use one thickness (Figure 4.6). When

changing from 9 different FVFs to specific FVF in each element, the predictions for 0.3 mm-amplitude case were 342.27 MPa (9 FVFs with 50% min. FVF and 74% max. FVF) and 342.42 MPa (specific FVF with 50% min. FVF and 76% max. FVF), respectively, while the modelled results for the 0.4 mm-amplitude case were 292.41 MPa (9 FVFs with 48% min. FVF and 80% max. FVF) and 292.56 MPa (specific FVF with 47% min. FVF and 83% max. FVF), respectively. In either case, 0.3 mm-amplitude or 0.4 mm-amplitude, the model with 9 different FVFs gave nearly the same prediction as the one using specific FVF in each element. Hence, this clearly demonstrates that just 9 different FVFs can satisfactorily reflect the local FVF variance.

4.3.3 Discussion of limitations about FVF-assumption investigations

The study of the influence of FVF presented here has three essential limitations:

1) The theoretical maximum possible FVF value that could be observed in the component is 91% if the fibres are in a unidirectional hexagonal close-packed configuration or 78% for square packing. The theoretical maximum has thus been exceeded in the 0.6 mm amplitude wrinkle case and the 0.5 mm wrinkle also exhibits highly unlikely maximum FVF.
2) It lacks any experimental validation with wrinkles exhibiting realistically variable FVF.
3) Most of the properties to simulate failures have been taken from IM7/8552 material, while the effective homogeneous properties were calculated based on AS4/3501-6, which means the investigation of FVF was actually performed on a model of a 'pseudo' material.

The first limitation - the unrealistic peak FVF - was caused by the choice of wrinkle wavelength. It is possible to reach the same maximum wrinkle angles with smaller amplitudes and, therefore, smaller peak FVF, if a shorter wrinkle wavelength is chosen. Another pair of models, uniform and non-uniform FVF, were computed to support this explanation, which possessed the same maximum angle of 22.6^{o} as 0.6 mm-amplitude case had in Table 4.5, the reason to fix the angle was due to the dominant effect of this parameter to the compressive failure of wrinkled composites, as will be demonstrated in section 4.4.1. The amplitude and wavelength of this pair of models were chosen to be 0.4 mm and 5.443 mm respectively, to make the lower/upper limit of FVF distributions at 49% and

78%. The predicted failure stresses for this pair of models were 229 MPa (Uniform) and 231 MPa (Non-uniform), with only 0.9% difference; this suggests that the large difference (3.6%) for the 0.6-mm amplitude case could be explained by FVF being above the high-FVF limit, or that it is influenced not just by maximum wrinkle angle, but by amplitude or wavelength as well.

Regarding the second limitation concerning validation, all the failure mechanisms have been validated by the experimental work of Mukhopadhyay et al. [1] with the constant FVF samples as stated in section 4.2, it is assumed that the failure modes would be the same when fibre distributions become non-uniform. Hence, to this extent, the model is reliable for showing the trends, even without experimental validations for the non-uniform FVF case.

In terms of the third limitation, although a 'pseudo' material was used, this study was still acceptable for the purpose of investigating FVF effects, since the study was focused only on the trends in the predictions, not relying on absolute failure-stress values. The 4% maximum difference between uniform and non-uniform FVF model predictions (Table 4.5), which is smaller than the typical mechanical test uncertainties for the coupon-set of 8 pieces, also provides supporting evidence that the model, which was only validated for constant FVF wrinkles, will also be valid for 'realistic' wrinkles within $\pm$4%, where FVF is in inverse proportion to the ply thickness.

However, those limitations should be investigated further, and validated by the experiments with varying FVF, in the future. At the current stage, the uniform-FVF assumption is reasonable to be used over the whole structure, as the investigations above indicate the influence on failure stress due to local FVF variance is small enough to be less than the experimental uncertainties.

4.4 Parametric study

As noted, the 'severity' of a wrinkle has a significant influence on compressive strength but, from the various studies in the literature, it is not clear precisely which parameters for severity are most influential on the strength. Smith et al. [6] highlighted a range of parameters, such as wrinkle shape, number of wrinkle cycles in a given wrinkled region, percentage of wrinkled fibres, maximum deviation of fibres, etc. that may have influential effects. It is important to understand how wrinkle

severity, shape and extent influence the mechanical performance. The new modelling technique described and validated above provides the capability to investigate this in a systematic and rigorous manner, as is described in this section.

Wrinkle shape can vary depending on the cause of the wrinkle in the production process. For the purposes of this study, only cosine-wave and sine-wave shapes are considered. For these two shapes, as discussed below in subsection 4.4.1, it shows that the out-of-plane wrinkle severity can be defined in the load (x) direction by an envelope parameter (w_1), an amplitude (A_i) and a wavelength (L). The maximum misalignment angle (θ) is linked to these parameters geometrically (Figure 4.1) but it is not an independent variable. Hence, the first study, reported in Section 4.4.1, is an investigation of wrinkle severity, influenced by amplitude, wavelength and maximum angle in the load (x) direction on compressive failure stress. A comparison of the cosine and sine shapes is then provided in Section 4.4.2. A study of wrinkle-extent parameters in the x, y and z directions is reported in Section 4.4.3. In Section 0, this parametric study is completed by changing the wrinkle orientation, and finally a discussion is presented in Section 4.4.5. All the models created for the parametric studies had 24 0.25-mm thick plies with a stacking sequence of $[45^o/90^o/\text{-}45^o/0^o]_{3S}$ and the modelled part of the coupon was 20 mm by 20 mm.

4.4.1 Investigation of wrinkle severity - Angle, amplitude and wavelength (fixed wrinkle volume)

In this section, the displacement, d, of ply interfaces in the wrinkled region is defined along the x direction by the product of a cosine wave, with wavelength L, a Gaussian envelope with a $1/e$ half-width, w_1 and an amplitude A_i (see Eq. (4.3)). The volume of the wrinkle envelope is fixed in these studies since the Wrinkle Gaussian Half-Width (w_1) remains unchanged at $w_1 = 4$ mm whilst the wrinkle extends uniformly across the width of the coupon (y direction) – see Figure 4.7. The z-direction variation in amplitude took one of two different profiles – one that matched the experimental coupons (see Figure 3.3) and the other followed a Gaussian profile, which is more realistic for naturally occurring wrinkles at manufacture. These profiles are described in full below.

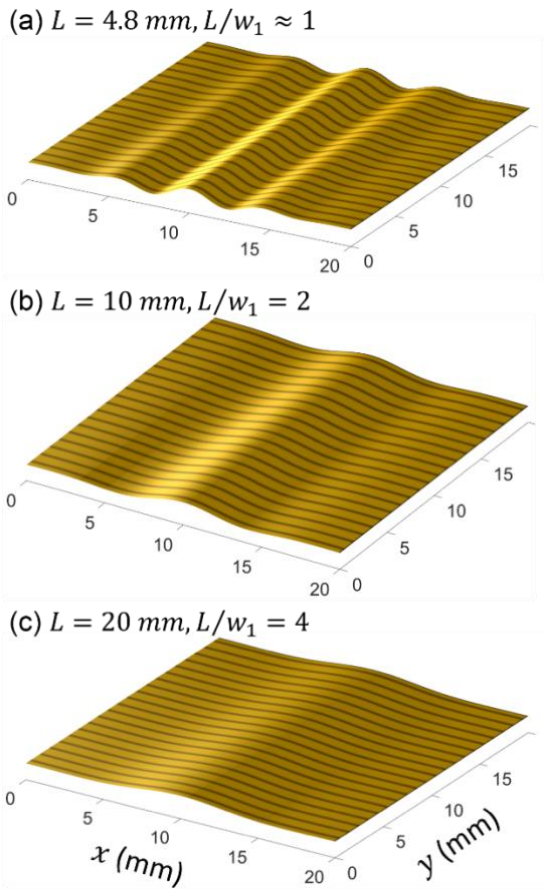

Figure 4.7 Wrinkle shape as influenced by the relationship of wavelength (L) and Wrinkle Gaussian Half-Width (w_1), w_1=5 mm, A=0.4 mm, with (a) L=4.8 mm ($L/w_1 \approx 1$), (b) L=10 mm ($L/w_1 = 2$) and (c) L=20 mm ($L/w_1 = 4$).

The maximum wrinkle angle (θ), based on a cosine shape, can be calculated by taking the arc-tangent of the maximum value of the derivative of Eq. (4.3). This derivative is given by

$$\frac{\partial d}{\partial x} = -A_i e^{-x^2/w_1^2}\left[\frac{2x}{w_1^2} cos\left(\frac{2\pi x}{L}\right) + \frac{2\pi}{L} sin\left(\frac{2\pi x}{L}\right)\right] \tag{4.6}$$

It is clear that maximum angle is dependent on w_1, A_i and L, and is not an independent variable. Therefore, for a single interface, i, only the three parameters w_1, A_i and L were changed independently, but maximum wrinkle angle (θ) could be calculated. For a fixed amplitude (A_i) and Wrinkle Gaussian Half-Width (w_1), wrinkle shapes will change with different wavelengths (L). When the ratio L/w_1 is less than approximately 1.5, the wrinkle shape tends to contain multiple cosine

cycles (Figure 4.7 (a)) but it gradually changes into a single Gaussian-governed general shape when the ratio, L/w_1, becomes larger than 4 (Figure 4.7 (c)).

In terms of the thickness direction (z-direction), two studies were undertaken, with the aforementioned two profiles of amplitude-reduction ratios, A_i, from the central interface to the top and bottom surfaces of the specimens, as shown in Figure 4.8. One was a Gaussian profile and the other used an amplitude reduction in stepped blocks of four interfaces, which more closely follows the experimental geometry. In the Gaussian thickness profile, local amplitude A_i of ply-interface i reduces continuously from central ply, i_{mid} having the maximum amplitude $A_{i_{mid}}$, towards the upper and lower surfaces corresponding to the Gaussian law as defined in Eq. (4.4) . n is the Wrinkle Half-Height, in units of the number of plies, which controls the thickness profile of wrinkle amplitude. In the stepped models the amplitude reduction follows the ratios: 1.0 : 0.63 : 0.39 : 0.0 as determined from the experiments [1]. Figure 4.9 shows examples of these two amplitude profiles.

For all models, the wrinkle Gaussian Half-width (w_1) was fixed at 4 mm, while the wavelength (L) was changed from 6 mm to 16 mm and mid-ply amplitude ($A_{i_{mid}}$) was changed from 0.2 mm to 0.6 mm, with the maximum misalignment angle (θ) being calculated in each case.

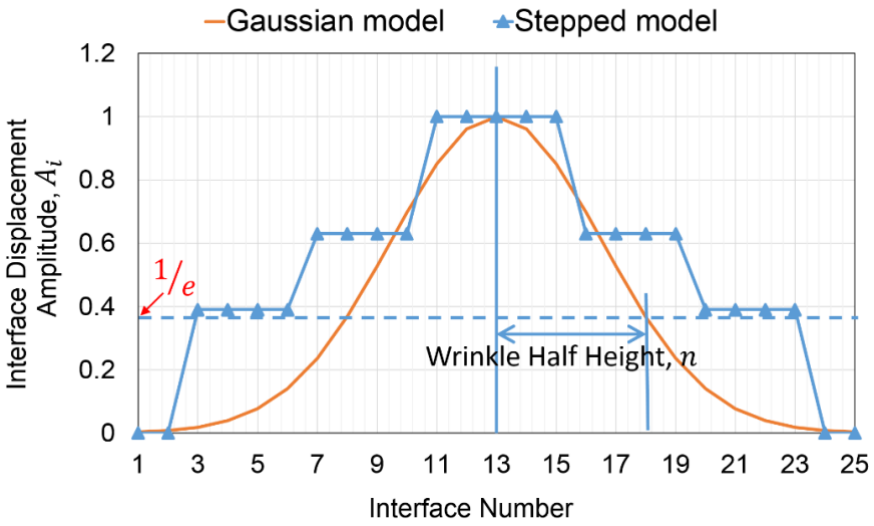

Figure 4.8 Amplitude reduction-ratio depth profile from central interface to top/bottom surfaces, the blue lines stand for the Stepped model and the orange curve is for a Gaussian model with $n = 5$.

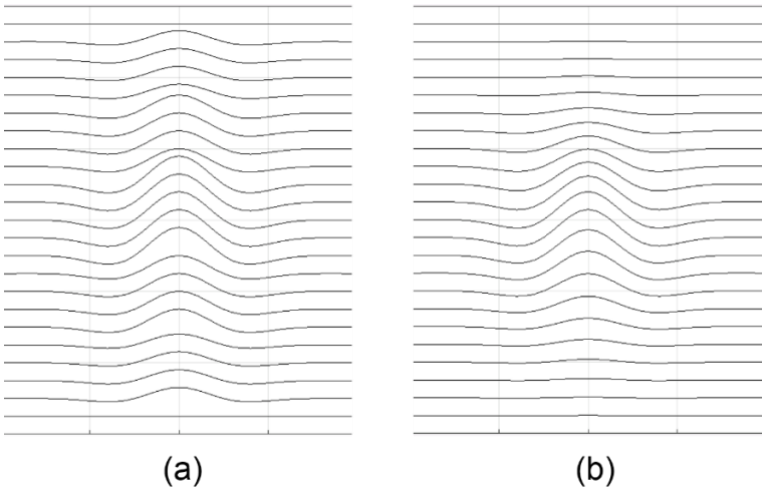

Figure 4.9 Images of the two kinds of amplitude thickness profiles, the light grey lines are gridlines, (a) Stepped models with reduction ratio of 1.0 : 0.63 : 0.39 : 0.0, and (b) Gaussian models with $n = 5$.

Figure 4.10 illustrates the dependence of modelled failure-stress knock-down (colour scale) and maximum angle (vertical axis) on the amplitude and wavelength for both types of model. The percentage knock-down in failure stress is defined as the modelled pristine value (647 MPa) minus the wrinkle predicted failure stress, and then divided by the pristine value. For both types of model, the knock-down in failure stress follows the same trend, being related to the maximum angle, rather than wavelength or mid-ply amplitude alone. This indicates that maximum angle is the major influence on failure stress, while wavelength and amplitude have an indirect influence due to their joint involvement in governing maximum angle. The failure stress knock-down, in both model types, varied by more than 40% when the maximum angle varied from 4° to 28°, showing the importance of careful non-destructive angle measurement when assessing wrinkled-component performance. Moreover, when comparing the distributions of failure-stress knock-down between the two types of amplitude through-thickness profile (Figure 4.10 (a) and Figure 4.10(b)), it is clear that the distributions are quite similar, which suggests that the through-thickness profile has only a slight influence on failure stress, not as significant as the maximum angle. The same data is shown as contour plots in Figure 4.11 (a) and (b), from which three different regions can be identified (for w_1 = 4 mm), as follows.

i. Wavelengths greater than 7 mm ($L/w_1 \geq 2$) with maximum angles greater than 8°

The failure-stress knock-down (magenta solid lines) follows the trend of the maximum angle (black dashed lines) very closely when the wavelength is greater than 7 mm and maximum angle is greater than 8°.

ii. Wavelengths less than 7 mm ($L/w_1 < 2$)

However, for shorter wavelengths, the wavelength parameter appears to become more important. A possible explanation is that, below a wavelength of approximately 8 mm ($L/w_1 < 2$), there are multiple cycles in the wrinkle, as shown in Figure 4.7 (a), and this could be influential in introducing a wavelength dependence for smaller wavelengths. By contrast, when the wavelength increases to more than 12 mm ($L/w_1 > 3$) the wrinkle tends to be a single Gaussian-governed shape as shown in Figure 4.7 (c).

iii. Maximum angles less than 8°

At small maximum angles, there is evidence of a periodic effect, possibly linked to the ratio of wavelength to Gaussian half-width. A further study of low-angle wrinkles would be required to investigate this further.

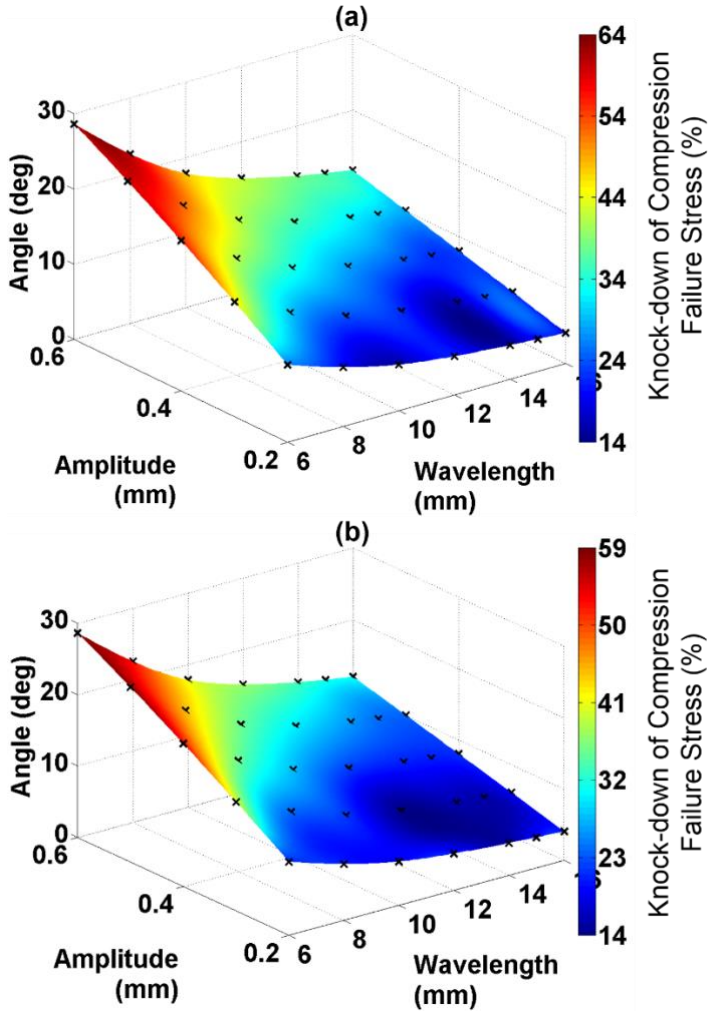

Figure 4.10 Relationship between failure-stress knock-down (colour scale in %) and maximum angle (vertical axis), as a function of mid-ply amplitude $A_{i_{mid}}$ and wavelength L. Black 'x' locations represent the predicted values before interpolation. (a) Stepped models, (b) Gaussian models with $n = 5$. In both cases, 35 models were computed covering all combinations of seven wavelengths and five amplitudes.

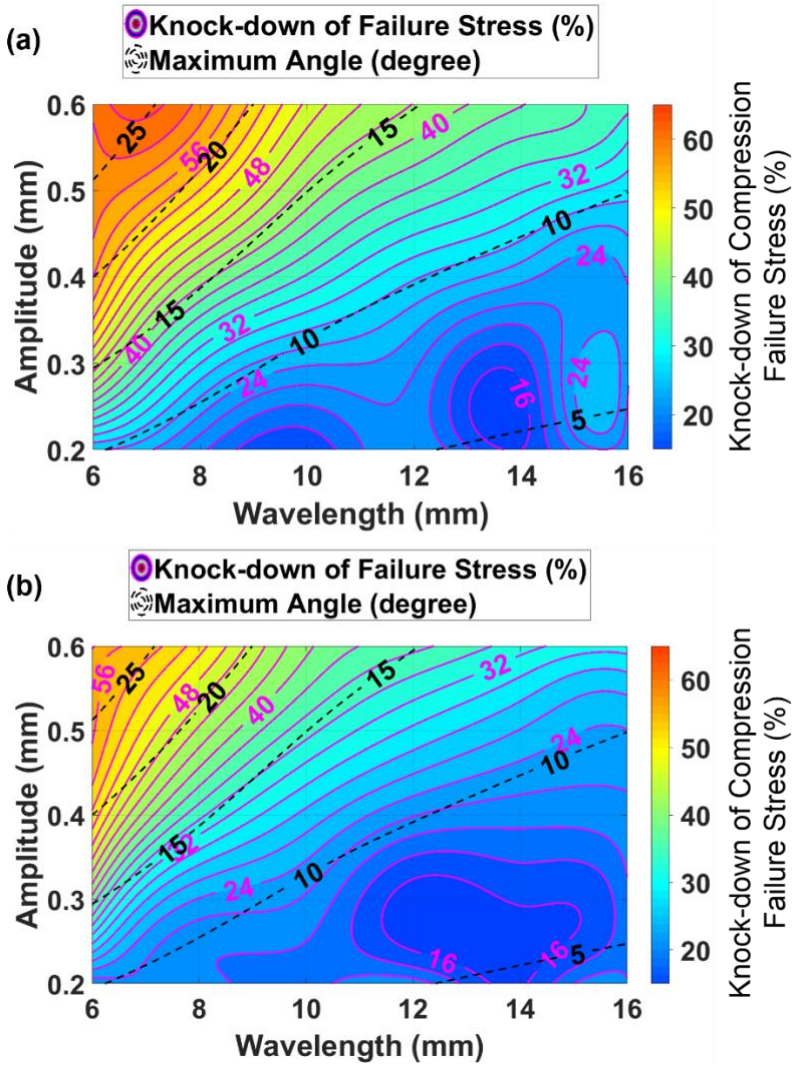

Figure 4.11 Contour plot showing failure stress knock-down (%) (magenta solid lines and colour scale) and maximum angle in degrees (black dash lines) as a function of mid-ply amplitude $A_{i_{mid}}$ and wavelength L, from (a) Stepped models, (b) Gaussian models with $n = 5$.

4.4.2 Investigation of wrinkle shape (cosine-phase to sine-phase)

There are many options for shape investigations, but the change from a cosine shape to a sine shape was chosen for this study in order to move the maximum angle to the centre of the wrinkle, where the Gaussian envelope always has a value of unity (Figure 4.12). This was in preparation for the wrinkle-extent study reported in Section 4.4.3. The experimental validation of the model used a cosine shape with maximum *displacement* in the wrinkle centre. The validated model can then be used to investigate whether a change in shape is likely to make a significant difference to the compression strength.

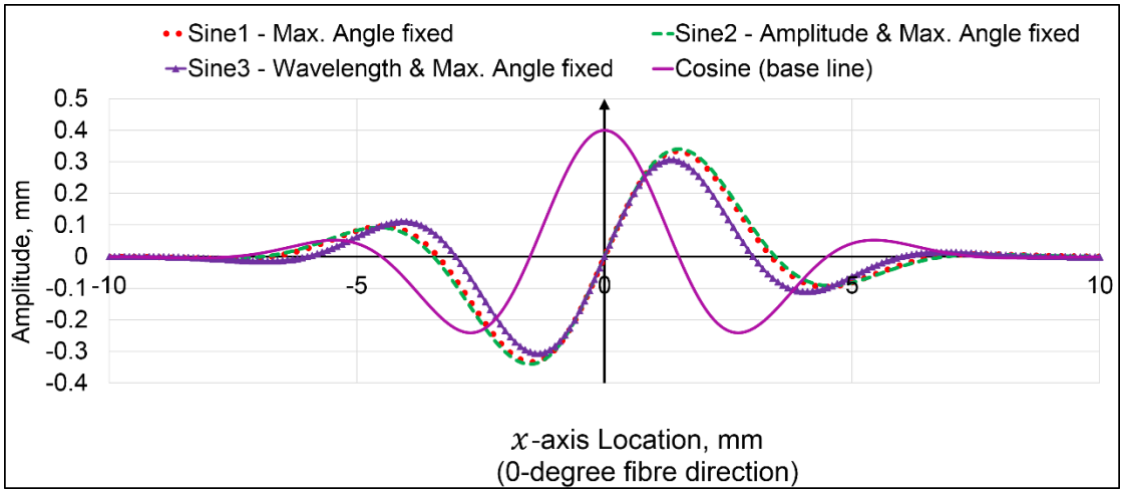

Figure 4.12 Description of cosine curve (magenta solid) and three potential sine curves (other colours) for wrinkle shapes.

A series of models were created using the simulator and the transfer process to investigate if a sine shape gives similar failure-stress levels to the cosine, provided maximum angle remains the same. Seven maximum angles were chosen for comparison, using the cosine shape as the comparison baseline. Whilst the main criterion was to keep maximum angle the same as for the baseline (cosine) shape, due to interactions between amplitude, wavelength and angle, there are three different methods of achieving this:

1) Keep angle exactly the same and change amplitude and wavelength
2) Keep angle and amplitude exactly the same and change wavelength
3) Keep angle and wavelength exactly the same and change amplitude

Figure 4.12 shows the shapes of the three sine curves and one baseline cosine curve (amplitude is 0.4 mm and wavelength is 6 mm), with a maximum angle of 20 degrees, as an example. Both Stepped models and Gaussian models were studied and Figure 4.13 shows the results for (a) stepped models and (b) Gaussian models. It can be seen that the difference in failure stress level when moving from cosine-shape to sine-shape is not significant if the maximum angle remains the same, for both Stepped and Gaussian models. According to the study in Section 4.4.1, angle and wavelength are the most important factors. Fixing these parameters (Case 3) gives similar predictions to the cosine baseline and so was used for the study in Section 4.4.3. Overall, this provides sufficient evidence that the shape

difference between sine and cosine is insignificant and that the sine shape is suitable for the following wrinkle-extent parameter studies.

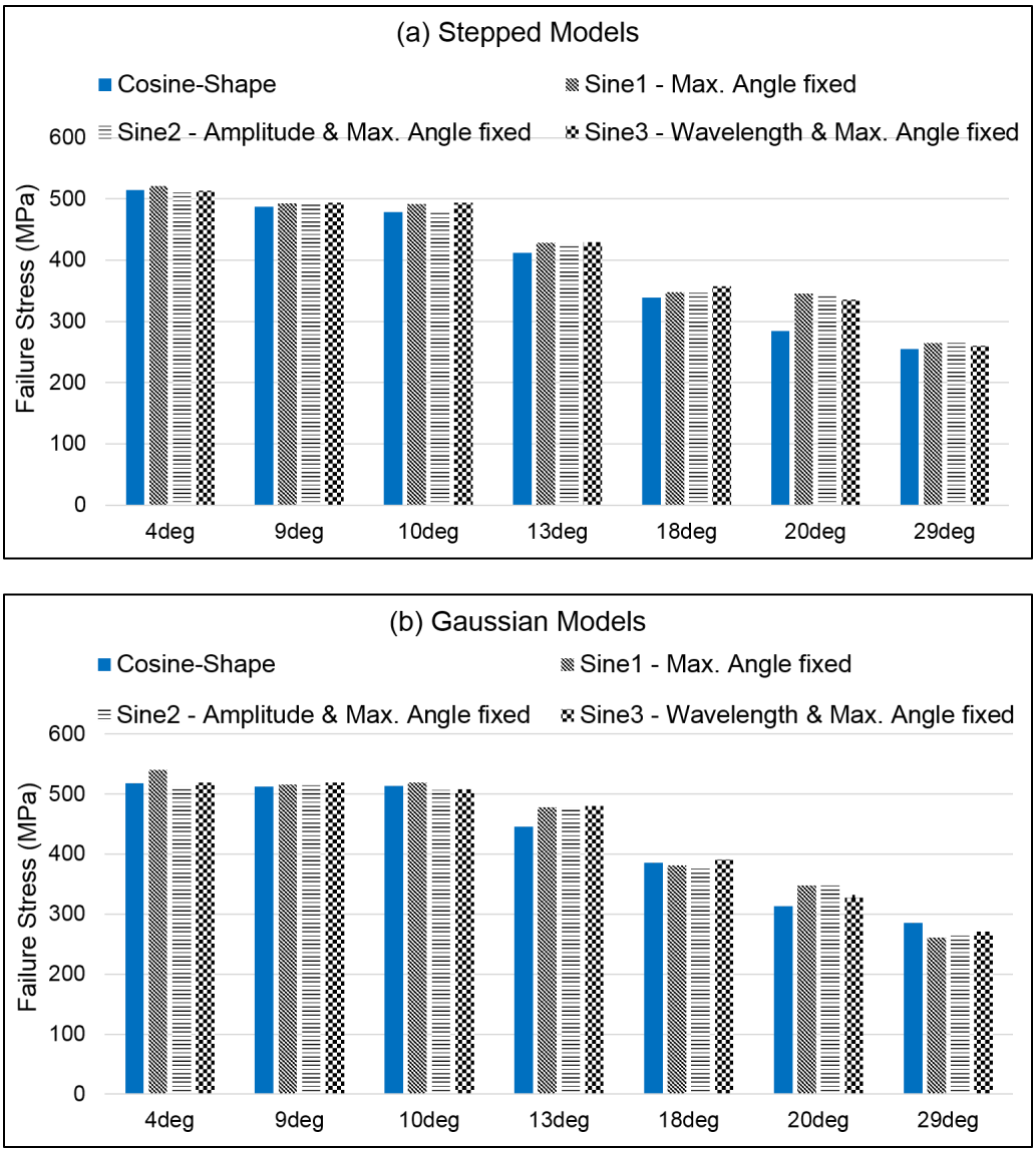

Figure 4.13 Comparison of compressive failure stress between sine-phase with base line of cosine-phase. Seven different angle levels were included (4°, 9°, 10°, 13°, 18°, 20°, 29°). In each angel case, blue bars present cosine-phase and three black bars stands for three sine-phases deviating with different kinds of pattern-fills. (a) Stepped models, (b) Gaussian Models.

4.4.3 Investigation of wrinkle extent

In the case of the cosine curve, wrinkle extent is controlled by the Gaussian Half-Width (w_1), which also affects the maximum angle as a side-effect. In this section, a sine curve is used to remove this side-effect as the maximum angle of the sine curve, being always located at the wrinkle centre,

depends only on amplitude and wavelength, and is independent of the Gaussian Half-Width. The model-creation process and details are the same here as in Section 4.2, but the broader geometrical definition derived from Eq. (4.1) and Eq. (4.2) by setting $x_1 = {}^{L}/_{4}$, was used to determine the wrinkle displacement, *d*, as:

$$d = A_0 e^{-[(x-x_0)^2/{w_1}^2+(y-y_0)^2/{w_2}^2+(i-i_0)^2/n^2]} sin\left(\frac{2\pi(x-x_0)}{L}\right) \tag{4.7}$$

where (x_0, y_0, i_0) is the centre of the wrinkle, at which the displacement is A_0, and i is in units of the number of plies. This also allows a variation of the wrinkle parameters across the width of the specimen.

The simulated wrinkle cross-sectional area (perpendicular to the load) is elliptical and an iso-amplitude curve forms an ellipse with semi-axes *b* and *c* in the *y* and *z* directions respectively – see Figure 4.14. However, depending on the ratio of each semi-axis of this ellipse to the specimen half-width or half-thickness, there are three possible cases for the wrinkle cross-sectional area. For clarity, here the discussion is only focused on the width direction (y), while the semi-axis (c) along z (thickness) direction is fixed, so the three cases as the semi-axis (b) in y (width) direction changes are:

1) for $b \leq y_{width}/2$ the iso-amplitude forms a complete ellipse;
2) for $b > y_{width}/2$, the iso-amplitude ellipse will exceed the width of the sample and, as a result, covers only a truncated ellipse;
3) for $b \gg y_{width}/2$, the part of the iso-amplitude occupied by the sample is a rectangle.

The equations to calculate the wrinkle cross-sectional area for all three possible cases, are defined in:

$$Area\_wrinkle = \begin{cases} \pi bc, & b \leq y_{width}/2 \\ 4\left(\int_0^{Y_{width}/2}\left(c\sqrt{1-\frac{y^2}{b^2}}\right)dy\right), & b > y_{width}/2 \\ 2cy_{width}, & b \gg y_{width}/2 \end{cases} \tag{4.8}$$

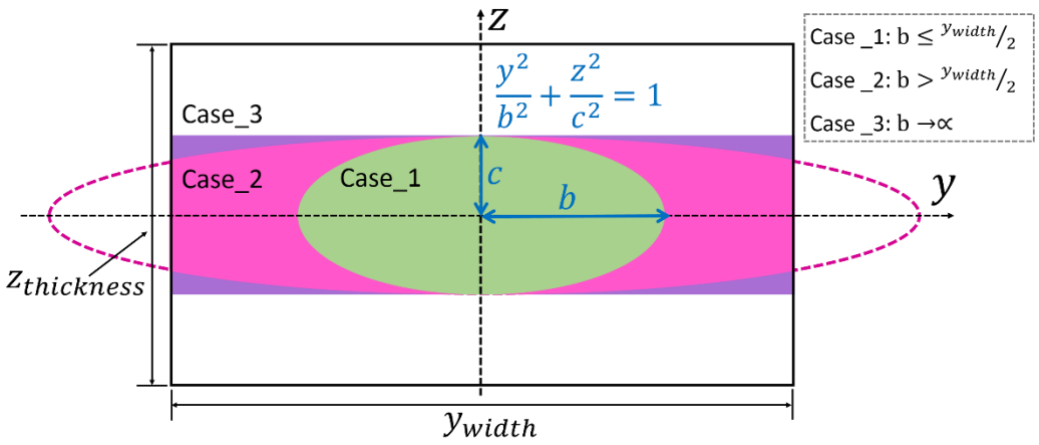

Figure 4.14 Schematic description of three possible cases of cross-sectional area along the width direction (y), depending on the relationship of the semi- axis (b) of an ellipse and the half-width of the sample ($y_{width}/2$).

Figure 4.15 shows a 3D example of case 1. As aforementioned, the amplitude envelope in the load (x), width (y) and thickness (z) directions are defined as Gaussian functions, so the shape of the wrinkled region described by any iso-amplitude surface is thus an ellipsoid. As indicated in Figure 4.15 (c), the particular case of a $1/e$ iso-amplitude surface is an ellipsoid where the semi-axes along the x, y and z directions in this specific wrinkle-extent study are defined respectively as: the Wrinkle Gaussian Half-Width (w_1), the Transverse direction Wrinkle Half-Width (w_2) and the Wrinkle Half-Height (n), where *n* is in units of the number of plies.

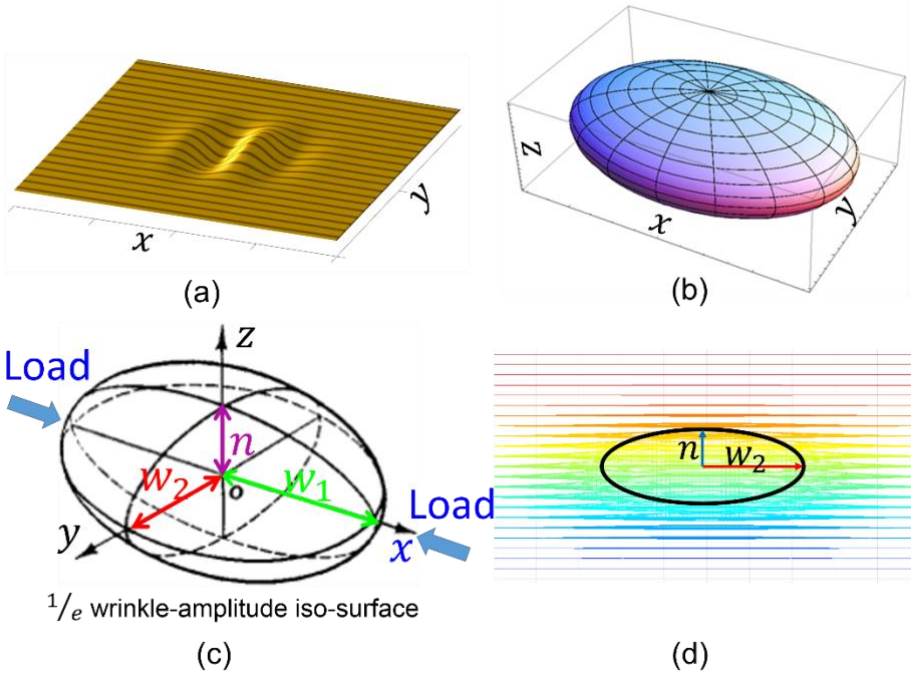

Figure 4.15 Overall shape of wrinkled region defined by Gaussian functions in all load (x), width (y) and thickness (z) directions. (a) Wrinkle shape at a single interface, (b) Overall shape of wrinkled region as an iso-amplitude ellipsoid, (c) $1/e$ iso-amplitude surface, (d) $1/e$ iso-amplitude ellipse in the cross-section perpendicular to the load direction.

An amplitude, A_0, of 0.35 mm and a wavelength, L, of 6.0 mm were fixed in the Gaussian models for the study of wrinkle extent in this section, resulting in a maximum angle of 20° at the wrinkle centre for all cases. The rationale behind this choice was that the amplitude should be small enough to avoid unrealistically large changes in ply thickness, whilst the maximum angle needs to be large enough that the modelled knock-down effects are significant and could vary both up and down to determine the effect of the wrinkle extent. The use of Gaussian envelopes provides a continuous reduction of amplitude through the thickness, which is more realistic for naturally occurring manufacturing defects than the stepped method. It is straightforward to control the wrinkle extent in all three directions by changing w_1, w_2 or n (see Figure 4.15 (c)).

The area of the coupon cross section within the $1/e$ iso-amplitude surface, $Area\_wrinkle$, encompasses all wrinkle-envelope locations greater than A_0/e (i.e. 37% of A_0). The wrinkle extent on the cross sectional area is defined by

$$Cross\ Sectional\ Area(\%) = {Area\_wrinkle}/{(y_{width} z_{thickness})} \quad (4.9)$$

Having explored different iso-amplitude values to define the extent of the wrinkle (Eq. (4.9)**Error! Reference source not found.**, $1/e$ was chosen for convenience on the basis that different iso-amplitude levels have no unexpected influence on the relationship between failure stress and cross-sectional wrinkled area, as shown in Figure 4.16 (a). The distributions of six different polynomial-fitted curves have similar trends and positions to expectations given that the area within the iso-amplitude (see Eq. (4.9)) changes predictably.

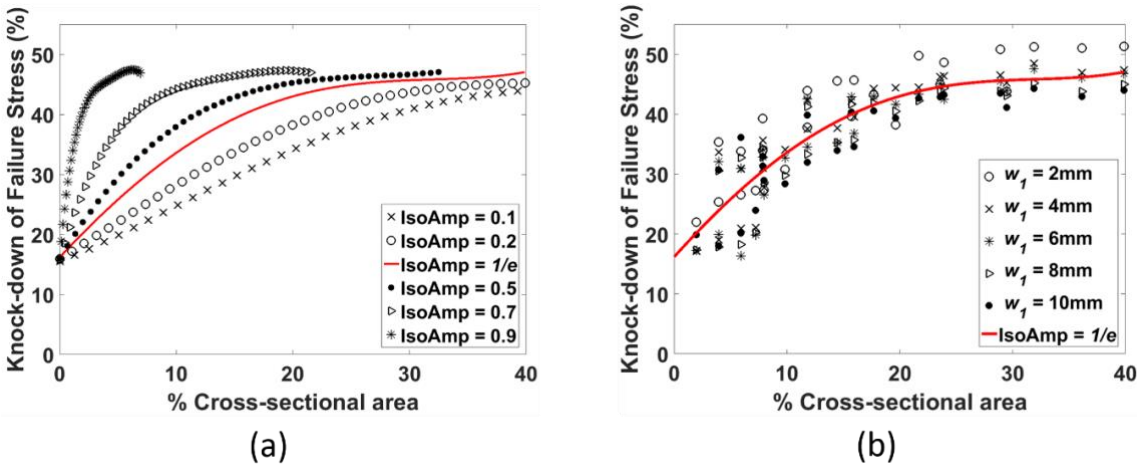

Figure 4.16 (a) Polynomial curve fits of predicted knock-down in failure stress as a percentage, based on the pristine value of 647.0 MPa. These curves show the same data set plotted for six different iso-amplitude choices, which change the measurement wrinkled cross-sectional area. (b) The example to show the original data for plotting the $1/e$ iso-amplitude fitted curve.

The aim of this section is to investigate whether n, w_2, the $Area(\%)$ or w_1 is most significant in governing the knock-down of failure stress, since the first three parameters decide the wrinkle extent at the cross-section view, while the last one defines the wrinkle extent in the loading direction. Numerous models were created spanning a wide range of extents in all three dimensions. All models were simulated with a Gaussian-modulated sine-wave shape along the load direction. The wrinkle Gaussian Half-Width (w_1) was varied between 2 mm and 10 mm. The Transverse Wrinkle Half-

Width (w_2) was varied in the range 3 mm to 20 mm, and the wrinkle half-height (n) was varied between 1 and 5 ply thicknesses.

The first comparison shows the effects of cross-sectional dimensions on failure stress. Figure 4.17 (a) presents the effect on percentage knock-down of failure stress by changing w_2 and n when w_1 is fixed at 4 mm. It is clear that both w_2 and n have an influence on the trend of knock-down of failure stress since the colour map is not uniform in either the w_2 or n axes. However, it does not follow the $1/e$ cross-sectional area (Eq. (4.9)) contours in Figure 4.17 (b)), indicating a more complex relationship between w_2, n and failure-stress knock-down. Hence, at this stage it can be concluded that both w_2 and n have an effect on the failure stress. The combination as a percentage of cross-sectional area also has some influence, the variation of which from 2% to 40%, caused more than 30% change in the failure stress knock-down.

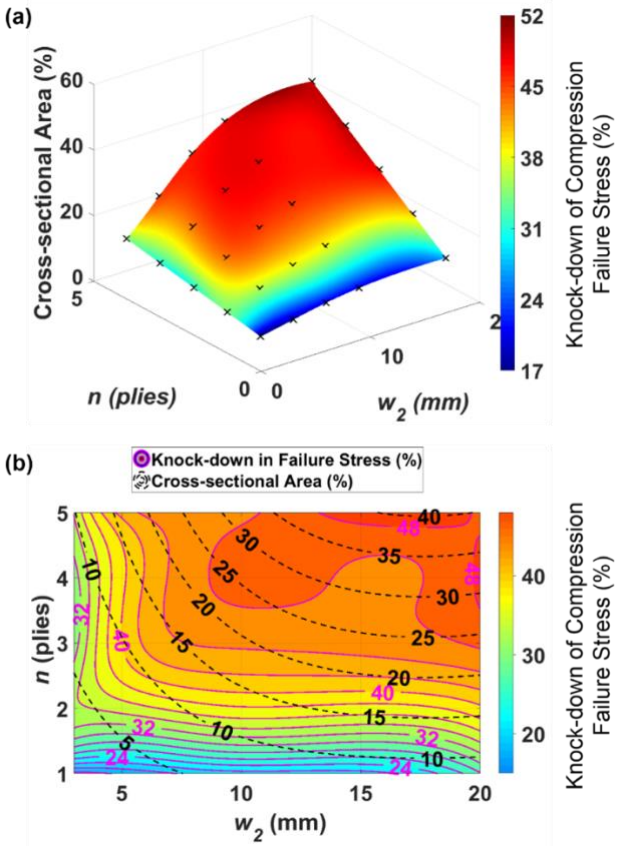

Figure 4.17 (a) Relationship between failure-stress knock-down (colour scale in %) and $^1/_e$ cross-sectional area as a percentage of the coupon area (vertical axis), as a function of n and w_2, when w_1 is fixed at 4 mm. Black 'x' locations represent the predicted values before interpolation. (b) Contour plot with same data used in (a), magenta contours show failure-stress knock-down, black dashed curves are the $^1/_e$ cross-sectional area as a percentage of the coupon area.

Considering the poor fit of $^1/_e$ cross-sectional area and failure-stress contours in Figure 4.17 (b), a parameter, a, combining w_2 and n is suggested to better fit the dependence of failure stress on w_2 and n as:

$$a = min\left(^{C(n-D)}/_{N}, {}^{w_2}/_{y_{width}}\right) \tag{4.10}$$

where N stands for the total number of plies, y_{width} is the width of the coupon in the y direction, and parameters C and D adjust where the 'corners' occur in the contours of parameter a. C is most likely to depend on the aspect ratio of the coupon: $y_{width}/z_{thickness}$, although this has yet to be investigated.

Similar plots to Figure 4.17 (b) but replacing cross-sectional area (%) with parameter a, are presented for $C = 4$ and $D = 1$ in Figure 4.18. The magnitudes of C and D are chosen from several trials to obtain the best-fit. From Figure 4.18 (a), it is clear that, when plotting against parameter a, the contours of a follow those of failure stress better than $1/e$ cross-sectional area (%). Hence, this means both the area and the smallest linear dimension in the cross section have effects on failure stress.

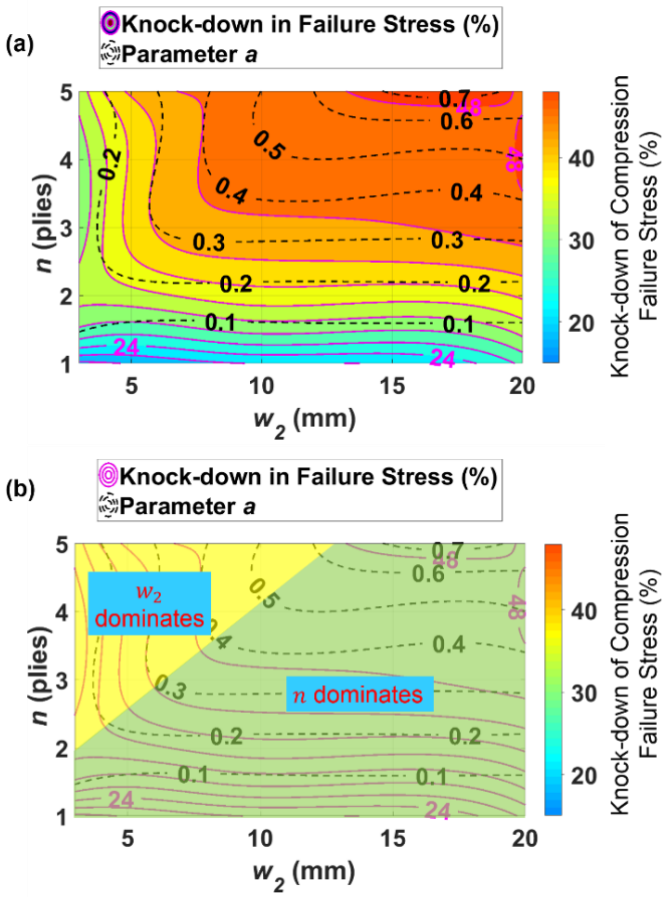

Figure 4.18 (a) Relationship between failure stress knock-down (magenta contours) and the suggested parameter a (black dashed curves) with $C = 4$, as a function of n and w_2, when w_1 is fixed at 4 mm. (b) As (a) but with shaded regions showing where n or w_2 dominate.

The $n - w_2$ space in Figure 4.18 (a) divides into two zones, shown in Figure 4.18 (b). The interface between the two zones is determined from the transition points of each contour curve – i.e. where each contour transitions from horizontal to vertical. Two zones are thus formed – one where the knock-down is independent of w_2 because the contours are approximately horizontal, and the other where knock-down is independent of n as the contours are approximately vertical. Thus, in the top left

corner, covered by yellow shading, the more vertical contours indicate that the knock-down is dominated by w_2, while in the green-shaded zone at the bottom right, the knock-down is controlled by n, as the contours are more horizontal. The angle of the diagonal line between these two zones is dependent on C and its location depends on D. At present a physical mechanism for this dependence has not been determined, but one theory is that the dominant parameter is the one that governs the proportion of straight fibres. When one extent parameter is large, the wrinkle affects the whole coupon in that corresponding dimension, so the other parameter dictates the proportion of fibres that are not wrinkled.

The final investigation focused on wrinkle extent in the load direction (x), which is controlled by w_1. Figure 4.19 shows plots of polynomial fitting curves based on five different w_1 values. At each w_1 value, the variances of w_2 and n are in the same range and maximum wrinkle angle is constant at 20°. When the value of w_1 is small, the curve is at a higher position, with a larger knock-down, while as w_1 becomes larger, the knock-down value reduces. This implies that small w_1 causes higher stress concentrations in the wrinkled region, which influences the failure stress negatively.

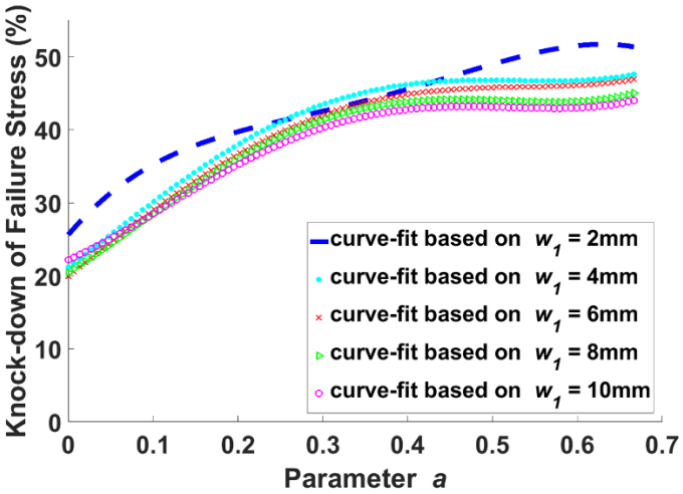

Figure 4.19 Polynomial curve-fit of knock-down of failure stress (%) based on pristine value at 647.0 MPa, against suggested parameter (a), based on five w_1 values, with the same variance range of w_2 and n.

Further investigations have been carried out to investigate the reason why the trend deviates from the main path when w_1 is 2 mm. There is a possibility that the mesh is not fine enough to capture the

stress changes when the wrinkle is so localised. Research from Fletcher et al. [158] has stated the necessity to model each ply with more than one element to accurately capture the through-thickness stress-distribution changes. They used 6 linear elastic elements per ply and 2 elements for each interface layer to predict stress, without the introduction of progressive damage. Here, it is not possible to use more than one cohesive element to simulate a single interface layer. Considering the extraordinarily huge storage space and time needed for the model computation as the result of user-subroutines inserted in the model to capture the failure events, a trial investigation was undertaken limited to 1 cohesive element per interface layer and 3 elements per ply, to search for any influence from mesh refinement on the predictions when w_1 is to 2 mm. In addition to the mesh refinement through the thickness, the in-plane (x, y) mesh size covering the central wrinkled region (Figure 4.20) was also reduced separately, to investigate this issue. The results are reported below.

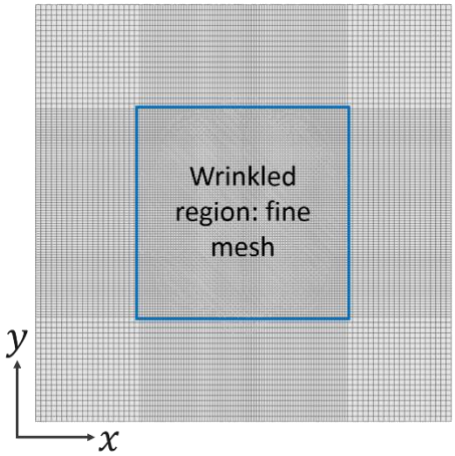

Figure 4.20 In-plane view (x, y) image showing the mesh refinement in (x, y) plane covering the central wrinkled region.

Figure 4.19 clearly shows that the biggest difference in the trend when $w_1 = 2$ mm is located in the ranges of a equalling 0 to 0.2 or 0.5 to 0.7. Since the suggested parameter a is dependent on a complex combination of w_2 and n, three points were chosen for this further study where $a = 0$, $a = 0.1$ and $a = 0.6$:

- $a = 0$, w_2 was chosen to be 3 mm and n was 1 ply to make the waviness highly localised. The first numerator of $(n - D)$ in Eq. (4.10) makes it possible for a going to zero.

- $a = 0.1$, w_2 and n were specifically set to be 2 mm and 4 plies, respectively. Since the values of w_2 and n used in Figure 4.19 could not make a equal to 0.1, here, a new choice of w_2 and n was made to give $a = 0.1$.
- $a = 0.6$, w_2 and n were 12 mm and 5 plies, respectively.

In all three cases, w_1 was fixed at 2 mm, A and L also remained the same as used in Figure 4.19 at 0.35 mm and 6 mm, respectively. For each case of a, two more models (three models were created for $a = 0.1$ case) were developed to compare with the baseline results:

1) base line mesh distribution (as in Figure 4.19): mesh size in (x, y) plane is 0.25 mm, 1 element per ply, 1 element per interface layer. For $a = 0.1$ case, the baseline model was newly computed, while the data for the other two cases were taken from Figure 4.19.
2) in-plane mesh refinement: mesh size in (x, y) plane covering the wrinkled region (Figure 4.20) is 0.125 mm, 1 element per ply, 1 element per interface layer;
3) through-thickness mesh refinement: mesh size in (x, y) plane is 0.25 mm, 3 elements per ply, 1 element per interface layer.

The predicted results of three mesh distributions and their comparisons to the baseline mesh are reported in Table 4.6. Relative to the baseline results, when $a = 0$, where wrinkles are highly localised, there is a negligible change in the predicted strength values in either in-plane or through-thickness mesh refinement – less than 5%. This change goes higher to 8.8% for $a = 0.1$ with in-plane mesh refinement, and less than 3% with through-thickness mesh refinement. For the third case, when $a = 0.6$, the difference is less than 0.03% (almost the same) for the in-plane mesh refinement and only 0.5% for the through-thickness mesh refinement scenario. However, for the latter case (through-thickness mesh refinement when $a = 0.6$), the model was computed with a smaller time increment, otherwise it terminated before reaching the peak failure point. The matrix cracking failure mode was confined to the central two [45/90/-45] groups (the layup is: $[45/90/-45/0]_{3s}$) to reduce the otherwise incredibly long computation time. This choice was based on a detailed check of other models to show that the failure was only limited to the central plies and the adjacent interface layers. Hence, from the

comparison above, it indicates that results with a finer mesh distribution in both in-plane and through-thickness directions has a minimal difference, with all cases being less than 10% difference to the baseline and all but one being less than 5% difference. In general, it can be said that the in-plane mesh refinement has more effect than the through-thickness refinement.

Table 4.6 Predicted failure stress values of three mesh-distribution cases for $a = 0$, $a = 0.1$ and $a = 0.6$, and knock-down of failure stress (%) predicted by three mesh distributions based on pristine value at 647.0 MPa .The data of baseline mesh distribution of $a = 0.1$ case is newly computed, while the baseline results for the other two cases are taken from Figure 4.19.

a		Baseline mesh distribution	In-plane mesh refinement	Through-thickness mesh refinement
0	Predicted failure stress (MPa)	505.0	483.7	493.4
	Difference caused by mesh refinement based on the baseline		4.2%	2.3%
	Knockdown of failure stress based on pristine value	**22.0%**	**25.2%**	**23.7%**
0.1	Predicted failure stress (MPa)	482.6	440.2	471.1
	Difference caused by mesh refinement based on the baseline		8.8%	2.4%
	Knockdown of failure stress based on pristine value	**25.4%**	**32.0%**	**27.2%**
0.6	Predicted failure stress (MPa)	316.8	316.7	315.1[2]
	Difference caused by mesh refinement based on the baseline		0.0%	0.5%
	Knockdown of failure stress based on pristine value	**51.0%**	**51.1%**	**51.3%**

[2] Modelling with smaller time increment and matrix crack was confined in the central two groups of [45/90/-45] plies.

In Figure 4.19, the trend of failure stress knockdown when $w_1 = 2$ mm case would move downwards and become closer to the main trend with other four w_1 cases, if mesh size is a contributory factor to the deviation of this trend line from the others. Hence, the knockdown of failure stress based on pristine value (647.0 MPa) is calculated for each mesh distribution case and they are also reported in Table 4.6. From the comparison, it shows that for each case of a studied here, the predicted stress knockdown becomes larger than the baseline mesh scenario, which would make the $w_1 = 2$ mm trend line even higher, especially for the two cases of $a = 0$ and $a = 0.1$, which contain the most localised wrinkles, as shown in Figure 4.21. From this graph, where the raw data from all the models contributing to the trend line are plotted, it can be seen that not too much weight should be put on the exact shape of the (4th order polynomial fitting curve) trend line. Therefore, this provides evidence that the conclusion made from Figure 4.19 is reasonable and efficient, and the mesh refinement may not be the only reason to account for the different trend of the $w_1 = 2$ mm curve. As the original data to plot the curve in Figure 4.21 is quite scattered, this suggests the necessity of a further study to obtain more original data points to investigate this issue in the future.

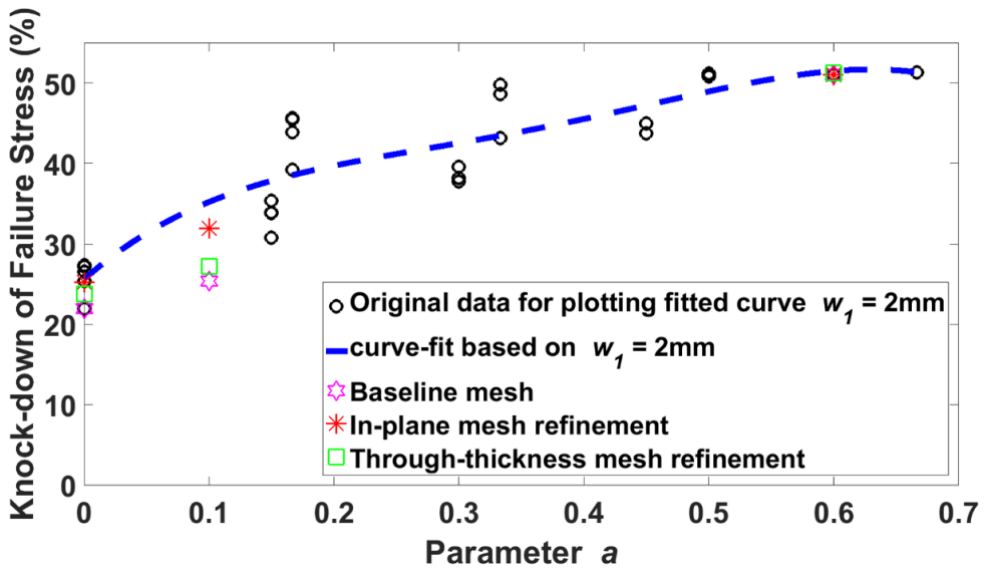

Figure 4.21 4th order polynomial curve-fit of knock-down of failure stress (%) based on pristine value at 647.0 MPa, against suggested parameter (a), when $w_1 = 2$ mm, with the same variance range of w_2 and n. Black circles represent the original raw modelled data to fit the curve, symbols of star, asterisk and square stand for the original 'baseline' mesh, in-plane mesh refinement and through-thickness mesh refinement, respectively, when a is chosen to be 0, 0.1 or 0.6.

Before closing this investigation, a detailed check of stress distributions was made. From Mukhopadhyay's work [1], when the wrinkle angle is larger than 9°, the failure can be expected to be delamination dominated, initiated by the through-thickness shear stress (s_{13}). Hence, s_{13} was checked in detail for every mesh-refinement scenario, and all three cases of a gave similar conclusions. Here, the stress distributions for $a = 0.6$ are reported as an example. From Figure 4.22, when the stress distributions were recorded at the same applied displacement during the loading process for each mesh refinement scenario, all the scenarios gave a similar stress distributions in the central ply (middle element layer of the central ply for Figure 4.22 (c) & (d) as three elements through the thickness were used to simulate one ply). In Figure 4.22 (d), although there was a different time increment setting in the model and confinement of matrix cracking within the central two [45/90/-45] groups, the stress was still similar to the other three images. A further check was carried out on the model of Figure 4.22 (d) that had through-thickness mesh refinement. A comparison of the s_{13} distributions in the three layers of elements that were used to simulate one ply are shown in Figure 4.23. The comparison indicates that the through-thickness stress do have some variations from top elements to the bottom elements within one ply, this should be because the top and bottom elements of the ply play a role to transfer the stress from/to the adjacent plies, as in the research from Fletcher et al. [158]. However, as the baseline mesh used in Figure 4.19 could give a similar stress prediction to the middle element layer (Figure 4.22 (d)) and the predicted differences of failure stress (Table 4.6) from different mesh-refinement scenarios are not very significant, it was reasonable, again, to conclude that the baseline mesh distribution is fine enough to capture the stress distributions and the conclusion in Figure 4.19 is efficient. But, from the through-thickness stress difference shown in Figure 4.23, more research should be carried out to address this issue further in the future.

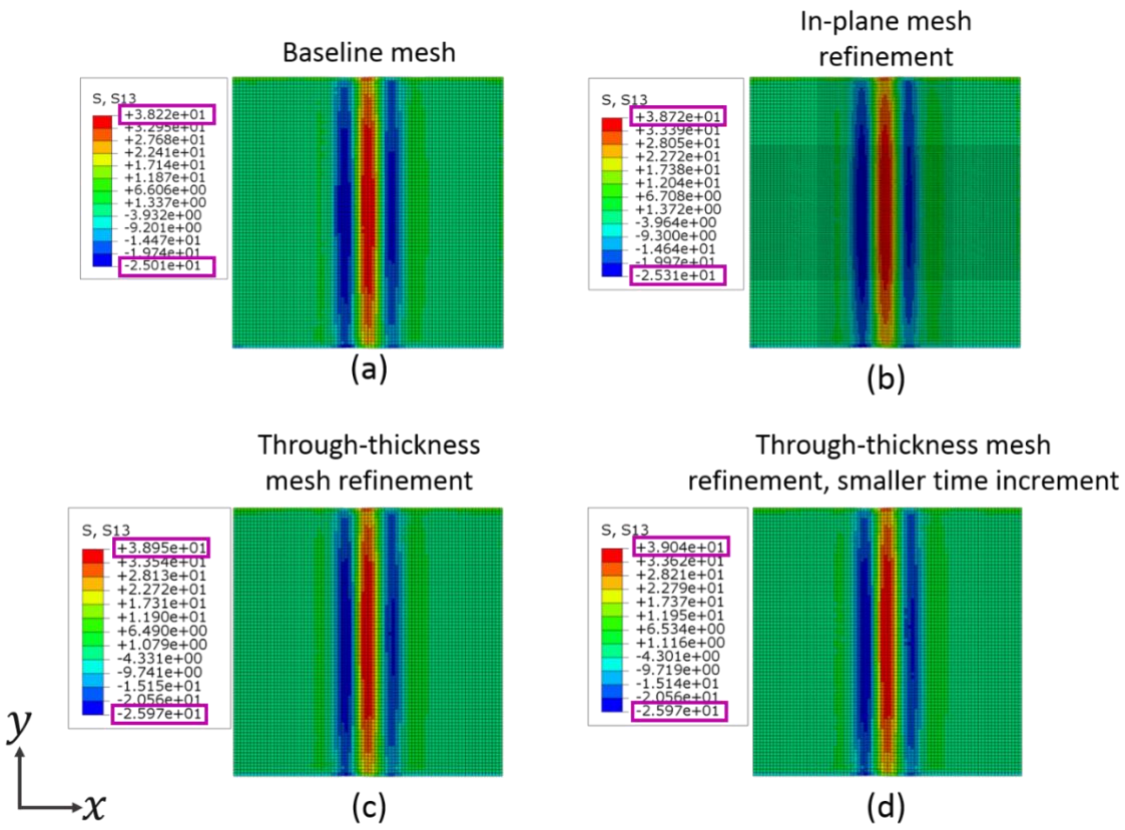

Figure 4.22 In-plane view (x, y) images showing the through-thickness shear stress (s_{13}) distributions at the same applied displacement during the loading process when $a = 0.6$. (a) baseline mesh, (b) in-plane mesh refinement, (c) and (d) through-thickness mesh refinement. (c) used the same time increment of (a) and (b), (d) used the smaller time increment with matrix cracking confined within the central two groups of [45/90/-45] plie, (a) and (b) were taken from a central ply, and (c) &(d) were the middle element layer of the central ply as three elements were used to simulate one ply.

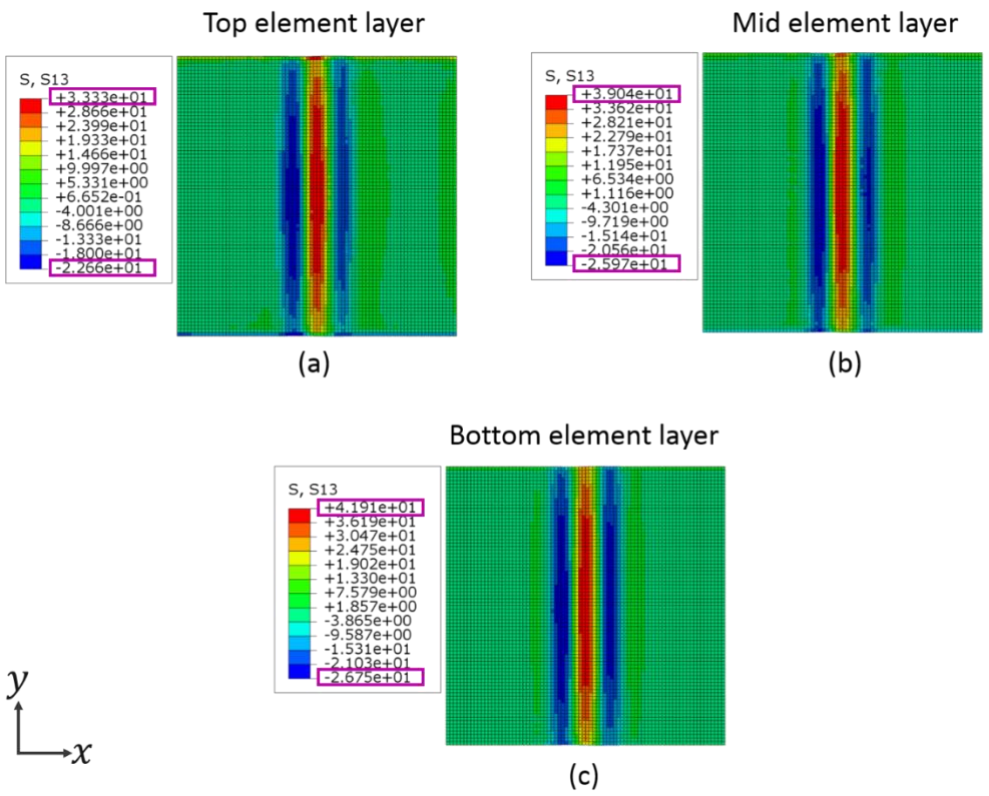

Figure 4.23 In-plane view (x, y) images showing the through-thickness shear stress (s_{13}) distributions before failure at the element layer during the loading process when $a = 0.6$ with through-thickness mesh refinement scenario, when using three elements to simulate one ply with the smaller time increment and matrix cracking confined within the central two groups of [45/90/-45] plie. (a) top element layer, (b) middle element layer, same as Figure 4.22 (d), (c) bottom element layer.

As a conclusion, the study above about the mesh refinement indicates that, mesh distribution in both in-plane and through-thickness directions, should be considered to capture the stress changes accurately, especially for the very localised wrinkles. But, considering that the experimental uncertainty in the testing of coupons used for the validation of the modelling technique, as explained in section 4.2, is about 6% [1] but the most predicted differences in Table 4.6 are smaller than 5%, and the baseline mesh scenario could give the similar stress distribution predictions as the two mesh-refinement scenarios (Figure 4.22), it would be reasonable to regard the conclusions drawn from Figure 4.19 useful and efficient. However, more detailed and further study about the modelling techniques focusing on this point should be carried out in the future.

4.4.4 Parametric study for change of wrinkle orientation

The parametric study presented above is for the case of the loading being in the same direction as the main sine-curve wrinkle direction, but there are many manufacturing scenarios where wrinkles can run at 90° to this – see Figure 4.24. If the wrinkle's cross-sectional profile (in the $y-z$ plane in Figure 18) is constant along the whole component in the load direction (the x direction in Figure 4.24), all the load-bearing fibres are still straight and so there will be no knock-down in failure stress. However, this is rarely the case - a wrinkle generally has a finite extent in the load (x) direction. It has not been possible to consider all shapes governing the load-direction extent but a simple Gaussian shape has been modelled here, to determine whether there is a need for further investigation. The same process and wrinkle-definition scenarios are used as previously, but the wrinkle is rotated by 90 degrees in the x_y plane as shown in Figure 4.24. The ply out-of-plane deviation can be governed by a similar equation as Eq. (4.7), but swapping the directions of w_1 and w_2 to get the final form as:

$$d = A_0 e^{-[(x-x_0)^2/{w_2}^2+(y-y_0)^2/{w_1}^2+(i-i_0)^2/n^2]} cos\left(\frac{2\pi(y-y_0)}{L}\right) \qquad (4.11)$$

Then maximum angle to the load direction is determined by the combined effect of A and w_2. Here L was fixed as well as the cross-section parameters w_1 and n; A was changed from 0.2 mm to 0.6 mm and w_2 in the range 1 mm to 5 mm.

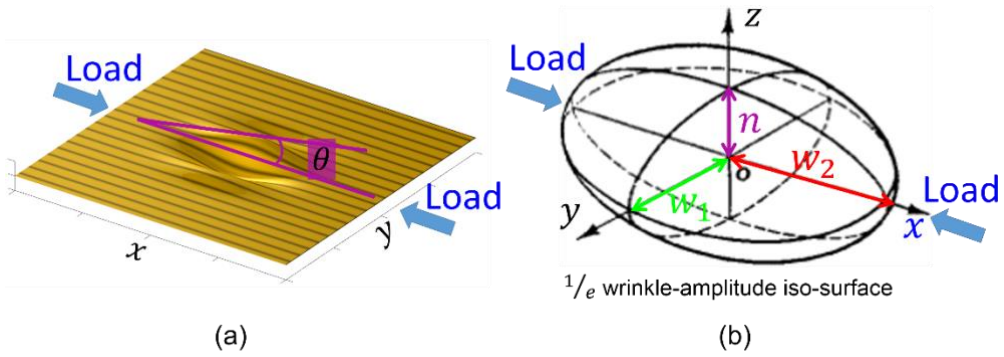

Figure 4.24 Description of load scenario when the wrinkle orientation is rotated by 90° in the (x, y) plane, θ means maximum wrinkle angle along load direction.

A similar modelling process was carried out and the distributions of failure-stress knock-down (%) with maximum angle as colour map and contour map are presented in Figure 4.25 (a) and (b). Both maps indicate that the distribution of failure-stress knock-down follows the trend of maximum angle to the load direction, which proves that this is again the main factor influencing the failure stress, even when the load is aligned transverse to the direction used for the study in Section 4.4.1.

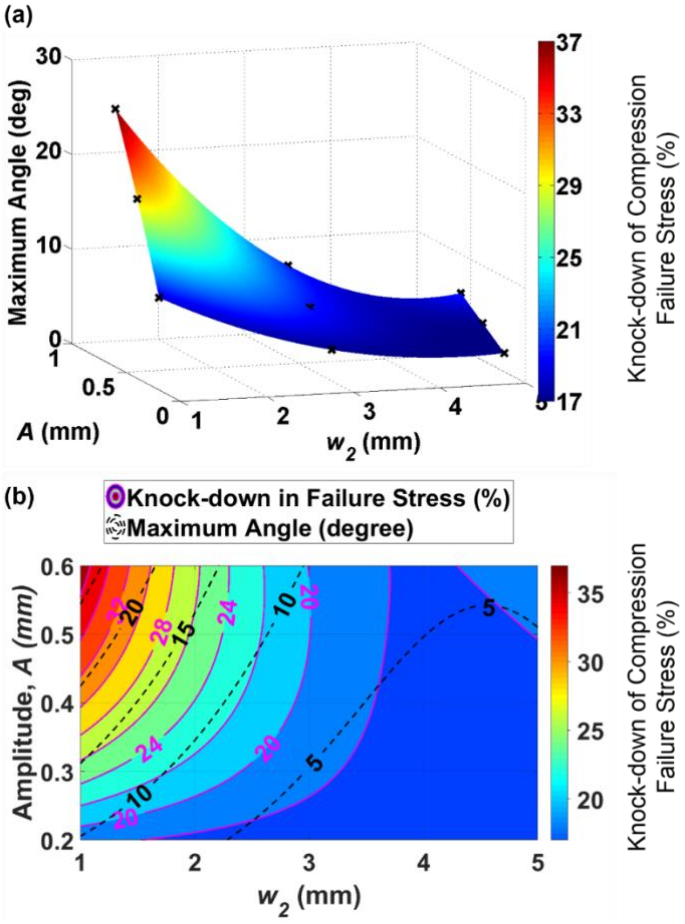

Figure 4.25 (a) Relationship between failure-stress knock-down (colour scale in %) and maximum angle to the load direction (vertical axis), as a function of A and w_2, when w_1 is fixed at 4 mm. Black 'x' locations represent the predicted values before interpolation. (b) Contour plot with same data used in (a); magenta contours are for failure-stress knock-down in percentage, black dashed lines are the maximum angle in degrees.

4.4.5 Discussion

In the future, when NDT information from real samples is available and used to create FE models of as-manufactured wrinkle defects, there will be no need for assumptions in terms of shape or

distribution of wrinkles. For the purposes of this study, to determine which wrinkle parameters are structurally significant, it has been necessary to bound the scope and assume flat external-surface laminates, cosine or sine-wave wrinkle shapes and Gaussian profiles. Those limitations are listed below, followed by a comparison of the results with other related researches.

1) The modelling techniques used in this study builds on the Mukhopadhyay's work [1]. Hence, the current study was limited to flat pre-preg laminates. The modelling technique validated in [1] may not be suitable for other manufacturing techniques, and has not yet been validated for wrinkles that appear at the surface. Thus caution should be exercised when applying the results in this study to components that are beyond its current scope.
2) The wrinkle topologies defined and studied in this thesis are idealised for the purposes of providing trend information, to aid understanding of the dependencies of mechanical compressive strength on various wrinkle parameters. There are many more morphologies of wrinkes in industrial components that have not been studied here, such as non-symmetrical or with random shapes that are difficult to depict by a simple mathematical equation. The interdependencies of wrinkle parameters summarised from the sine and cosine shapes can, however, still provide useful insight on the overall sensitivities.
3) Although the experimental coupons were manufactured with artifically induced wrinkles and were represented by stepped models, the small differences in strength between these and Gaussian-profiled models shown in Figure 4.10 and Figure 4.11 suggests that there is little dependence of mechanical performance on this profile.

Due to the lack of either a consensus on wrinkle metrics or an approved standard to evaluate wrinkles, it is difficult to thoroughly compare the influence of wrinkle-parameters from data presented in the literature. Seon et al. [8] have similarly investigated the effect of imperfections (e.g. wrinkles and waviness) on mechanical performance using a method of automatically transferring the NDT data into structual FE models. Most of their research focused on other loading scenarios, like fatigue or bending. For the static in-plane compression case, the wrinkled samples in Lemanski et al. [94], had similarities to those used for this study [1], but the wrinkles were introduced differently: two central

plies were dropped to form a half-cycle wrinkled region (the exact equation to simulate the wrinkle geometry was not explained). Based on the discontinuous-plies direction (0° or 90°) and the ply quantities, there were four cases: L2, L10, T2 and T10 (L refered to 0° and T for 90°). The wrinkle distribution was kept constant in their work. The maximum angle for L2 and T2 was 8°, while this angle for the other two cases was 30°. In both their experimental and numerical modelling results, the failure load reduction was around 55% for either L or T cases, when the angle was changed from 8° to 30°, but it is likely that the dropped plies will have an influence on the failure, allongside that of the wrinkled plies. Also for uniformly distributed wrinkles along the width, research conducted by Elhajjar and Shams [159] identified that compressive-strength reduction would be ~30% when the wrinkle angle changed from 20° to 30°, in samples with wrinkles introduced using metallic rods. In Section 4.1.1 of this chapter, where wrinkles were also uniform across the coupon width, the failure strength reduction was about 40%, when the maximum angle increased from 4° to 28°, and this reduction would be around 10% if the angle changed from 20° to 28°. The differences observed in compression-strength knock-down can be accounted for by the different wrinke-introduction methods.

As stated above, the material-property maps used to create FE models were from a simulation process and governed by Eq. (4.1) and (4.2). In future work, direct NDT-inversion material maps will be applied to assist the model creation and control the wrinkle topology. This will allow the suggested methodology in this study to be applied to more general wrinkle geometries. Within the stated limitations, the study presented here is sufficient for initial guidance on wrinkle metrics for flat laminates under in-plane compressive loads.

4.5 Summary

To assist the performance evaluation of composite components containing wrinkles, a systematic and rigorous parametric study was undertaken, to compare the dependence of compressive failure stress on various wrinkle parameters. The combination of simulation and numerical analysis by an transfer process, was implemented to achieve this aim, by creating a large number of numerical models with controlled wrinkle geometries. The investigations showed a primary dependence on the maximum

wrinkle angle relative to the load direction, as well as secondary dependencies on the wrinkle wavelength and wrinkle extent in all three dimensions. Quantitative results applying to the modelled case of the IM7/8552 [148] fibre/resin system with 24 plies in the sequence $[45/90/-45/0]_{3s}$, are summarised as follows.

1) In terms of the influence of potential wrinkle-severity parameters of amplitude, wavelength and angle in the load (x) direction, for a fixed wrinkle volume and shape, the maximum wrinkle angle is more important than amplitude and wavelength, and caused a predicted 40% knock-down of failure stress when the wrinkle angle increased from 4° to 28° when wrinkles were uniform across the coupon width, with an additional dependence on wavelength when the wavelength is small (less than 8 mm in this case).
2) Changing wrinkle shape from a cosine to a sine wave, within a Gaussian envelope, has little influence on compressive failure stress.
3) For wrinkle-extent parameters:

- A very localised wrinkle in the load direction, where there is less than one cycle of wrinkle, concentratres the stress and enhances the knock-down in compressive failure stress.
- In the plane perpendicular to the load direction, knock-down in compressive failure stress increased by 30% as the $1/e$ iso-amplitude surface cross-sectional area of the wrinkled region increased from 2% to 40% and when the maximum angle remained at 20°. Between the two dimensions of the wrinkle in cross-section, the smaller as a proportion of the coupon size seems to have a dominant role, possibly because it governs the number of non-wrinkled fibres remaining in the coupon.

4) When the wrinkle orientation is rotated by 90 degrees in the x_y plane, the maximum angle to the load direction is still the main factor determining the compressive failure stress for a Gaussian profile in all directions.

Based on the study above, when wrinkles exist in composites, the recommended NDT wrinkle metrics could be summaried: 1) Maximum wrinkle angle, 2) Wrinkle wavelength, 3) Extent of wrinkled

region – i.e. equivalent $1/e$ Gaussian half-width in all three dimensions if possible. Of these, the maximum angle is the most critical measurement.

In addition, the investigation of FVF based on this validated model proves that the assumption of uniform FVF in the models used for the parametric study, will not cause significant influence on the failure-stress trends.

In this work, the only wrinkle shapes considered were cosine and sine wrinkles in one direction, weighted with Gaussian profiles in both in-plane directions. The range of real manufacturing wrinkle shapes is much wider than this and it is recommended that a further study of load-direction and wrinkle shape should be performed, for obtaining a more accurate evaluation of component performance with wrinkles. The study of mesh distributions shows that the mesh refinement in both in-plane and through-thickness directions, should be considered in the future to capture the stress changes accurately.

Chapter 5
Experimental study of laminates with in-plane waviness under compression loading

5.1 Introduction

Similarly to out-of-plane wrinkles, the in-plane fibre path can also deviate from its specified trajectory within the laminate plane to form in-plane waviness. The reviewed literature in chapter 2 has shown the negative influence of this type of fibre misalignment in the compressive performance of composites but the related failure events and their sequences are still not fully clear. Hence, an experimental study (chapter 5) and a numerical study (chapter 6) were designed, to better understand the initiation and propagation of failures affected by in-plane waviness when it occurs in a laminate.

The layout of the experimental study, presented in this chapter, starts with the definition of the waviness that will be introduced into laminates in section 5.2, followed by a description of the procedures required to manually embed waviness into samples with controlled severity in section 5.3. Before the summary in section 5.5, results of the compressive experimental tests of the waviness samples are reported and discussed in section 5.4, including the failure stress knockdown and failure modes captured by high-speed photography and X-ray CT imaging techniques.

5.2 In-plane waviness geometrical definition

In-plane waviness can be defined by different geometrical shapes and parameters following previous research [91][121]. Chapter 6 uses the sine-phase equation to simulate the fibre misalignment path and the experimental work in this chapter attempts to produce a similar waviness shape in real coupons for validation purposes. The wavy region introduced into the samples is approximated by a half-sine shape (named kink-shape) (Figure 5.1). Using the parameters of Wavelength (L) and Amplitude (A), its displacement is controlled by

$$y = Asin\left(\frac{2\pi x}{L}\right) \tag{5.1}$$

The maximum wavy angle, θ_{max}, is thus located at the central point with a known value given by the arc-tangent of the first derivative (dy/dx) at $x = 0$ of Eq. (5.1), providing the wavelength (L) and the amplitude (A) are known, and the form of this equation is:

$$\theta_{max} = arctan\left(\frac{2\pi A}{L}\right) \tag{5.2}$$

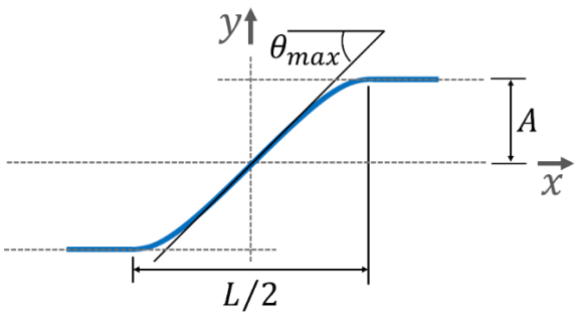

Figure 5.1 Schematic of the definition for the in-plane waviness, with amplitude A, wavelength L and maximum angle θ.

5.3 Procedures to introduce in-plane waviness into laminate

5.3.1 Waviness-introduction shear-rig

In-plane waviness of the desired sine-phase kink shape was introduced by a specially designed rig (Figure 5.2) [122]. This shear rig was constructed with two identical but opposite parts (Part A and Part B as labelled in Figure 5.2) separated in the x direction (Figure 5.2). Each part contained two flat plates stacked together, one L-shape plate on the top and two handles connected to lead-screws at left/right and front/back ends. The ply was inserted between the two flat plates and the wavy region was formed by the opposing shear movement of the flat plates in the y direction, controlled by the y-direction handles and lead-screws. The L-shape piece was mounted to clamp the ply in place through friction. The positions of the two parts in the x direction was controlled by the left/right handles and lead-screws, and their gap defines the width of the wavy region ($^{L}/_{2}$). Along the y direction, the

movement of the two parts was controlled by the front/back handles and lead-screws, to control the waviness amplitude (A). Thus these movements governed the waviness severity (maximum wavy angle, θ_{max}), and the width of the wavy region.

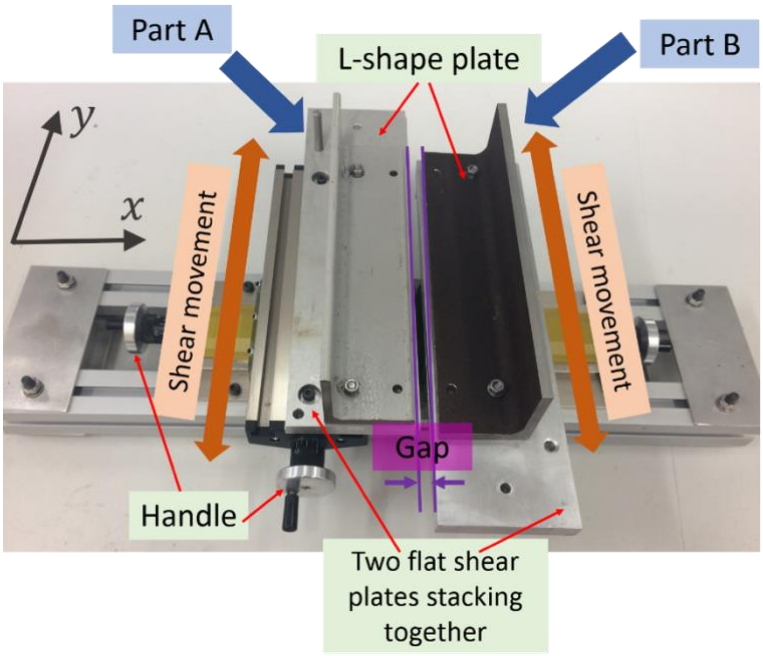

Figure 5.2 Schematic of the shear rig to introduce in-plane waviness [122].

5.3.2 Discussion of factors influencing waviness introduction

The experimental study was designed to investigate the dependence of compressive failures on the waviness severity. Those experimental recordings would then be regarded as the validation baseline for the numerical models described in chapter 6. Therefore, it was important to introduce waviness in a controlled way without introducing unwanted local buckling of fibre tows. Before the introduction of waviness into samples (section 5.3.3), a study to seek the best quality of waviness from the rig-shearing process (Figure 5.2) was undertaken and is presented here, aiming to control the waviness in the designed shape, with minimal local buckling at the gap region of the rig.

Several factors were considered and tested to obtain a controllable wavy region with the fixed width (defined by the gap of the rig in Figure 5.2). First, since the viscosity of Hexcel 8552 resin starts to reduce when the temperature is above 60 degrees [148], the ply was heated to between 80 and 90 degrees (measured using a thermal camera) using a heat gun, in order to achieve easy shear movement

when rotating the handles to make the waviness. Other factors that may also have had influence are discussed below:

1) Release film (Figure 5.3):

   It was considered whether to insert a release film at the contact surfaces between the ply and the flat shear plates to prevent damage to the CFRP ply. However, this would reduce friction between the plates and the ply and the results proved that not having release film would produce better quality waviness without a significant negative influence on the ply. The reason for this phenomenon was that the smoothness of the release film reduced the friction so much that it reduced the formation of waviness.

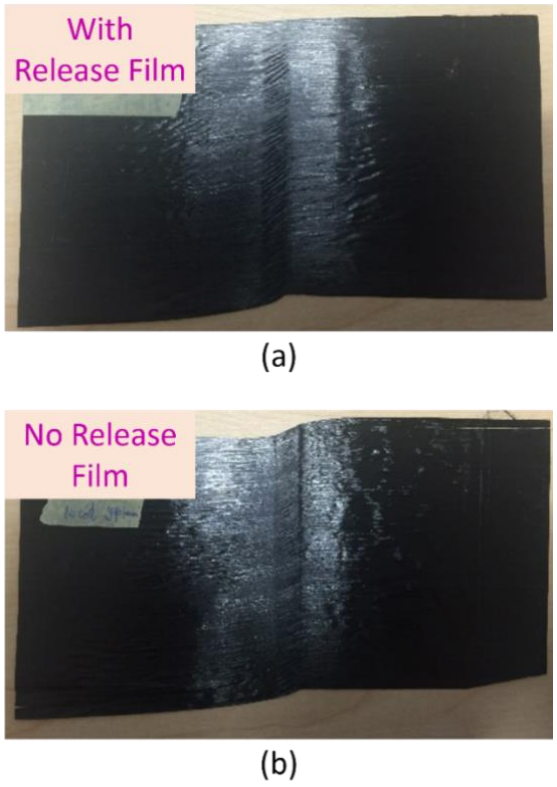

Figure 5.3 Images of a wavy ply, (a) with and (b) without a release film during the shearing process.

2) Metal block (Figure 5.4):

   With a similar objective to the L-shape plates mounted onto the rig, extra metal blocks were added on top of L-shape plates to ascertain whether increasing the friction could improve waviness quality further. As shown in Figure 5.4, this factor indicated a positive result with

metal blocks. However, the influencing extent of this factor is not as significant as the release film (Figure 5.3).

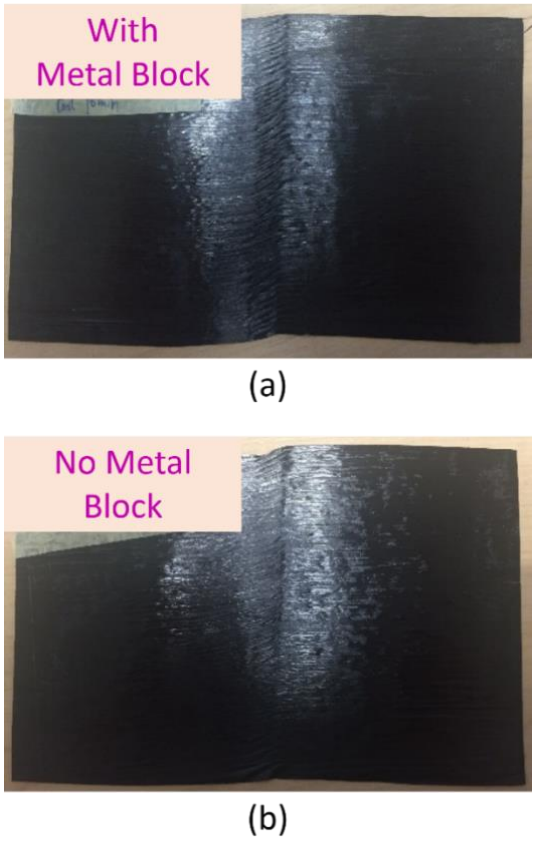

Figure 5.4 Images of wavy lamina, (a) with and (b) without metal blocks, added on the top during the shearing process.

3) Strip width:

Another noticeable problem was the buckling effect during the shear movement process to form the waviness, as the fibre in the ply could not be freely elongated. This buckled the fibres in the wavy region (gap area in Figure 5.2), accompanied by some fibre-tow rotations. To reduce this negative effect, part of the ply was deliberately cut into narrow strips (Figure 5.5) before the shear movement. The shear force was effectively applied to each strip independently, which reduced the accumulated buckling effect that happened if no strips were prepared. Several strip widths were tested before the final decision to use 2 mm (Figure 5.6).

Another advantage of making strips, compared to the non-strip process, was the easier removal of a ply from the rig, once the waviness had been introduced.

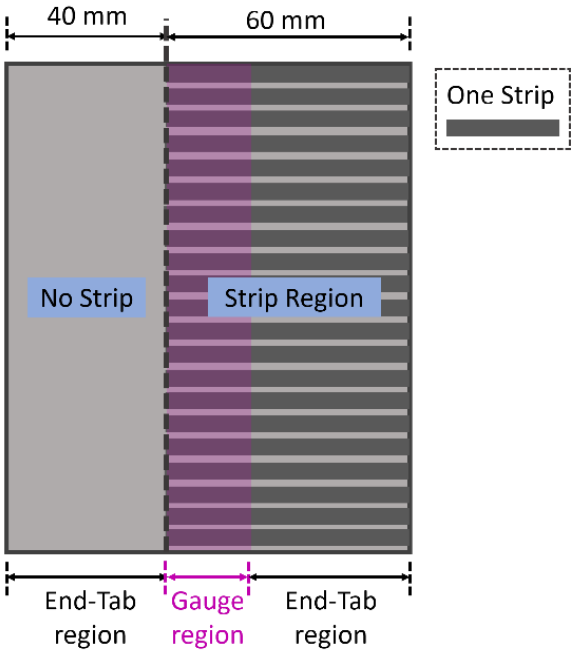

Figure 5.5 Schematic of the layout of deliberately introduced strips into the ply to form waviness.

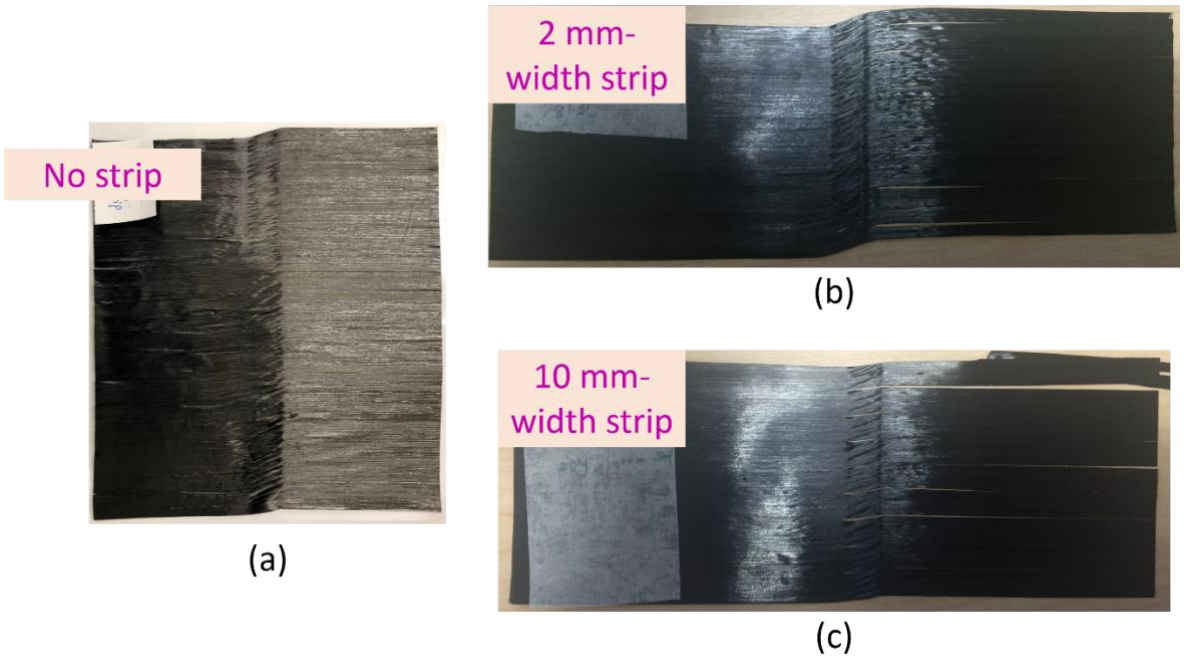

Figure 5.6 Images of a ply cut into (a) no strip, (b) 2 mm-width strips, and (c) 10 mm-width strips to form waviness.

4) Other factors:

   Besides those listed above, other factors relating to the easy removal of a ply from the rig were also studied, including: (1) two plies with the same fibre orientation stacked together before the shear movement; and (2) wavy ply left in the air to be cooled to room temperature before removal. For the whole shearing process, it was also discovered that only rotating one handle (the back one on Part B or front one on Part A) at a very slow speed to change the waviness amplitude (A) could improve the waviness.

In summary, with the combined considerations of the multiple influential factors, the final choices and manufacturing procedures to manually introduce the waviness into the ply were as follows:

I. Two plies with the same fibre orientation were stacked together.
II. Part of the 2-ply stack was cut into 2 mm-width strips.
III. The 2-ply stack with strips was put onto the lower flat plate of the rig.
IV. The ply was heated to between 80 and 90 degrees centigrade.
V. Upper flat plates and L-shape plates were bolted down onto the heated ply, with extra metal blocks on the top. The flat plates were pre-heated, as well.
VI. Rotate back handle on Part B slowly by a predetermined number of turns.
VII. Take the metal blocks, L-shape, and upper flat pieces from the rig.
VIII. Allow to cool down naturally in the open air to room temperature.
IX. Remove the ply from the rig.

5.3.3 Waviness severity introduced into samples

The material for the experimental study of in-plane waviness was IM7/8552 from Hexcel [160], the same as used for out-of-plane wrinkles. The stacking sequence of the samples for the compression test is quasi-isotropic ($[45_2/90_2/135_2/0_2]_{2s}$) (Figure 5.7) with 32 0.125 mm-thickness plies. For clarity, the layup expression can be simplified to $[45/90/135/0]_{2s}$ with effectively 16 0.25 mm-thickness plies for the purposes of this thesis. The selection of this material was to facilitate comparison with the

numerical study (which will be reported in chapter 6) as the properties of IM7/8852 have been identified and validated from previous studies [1].

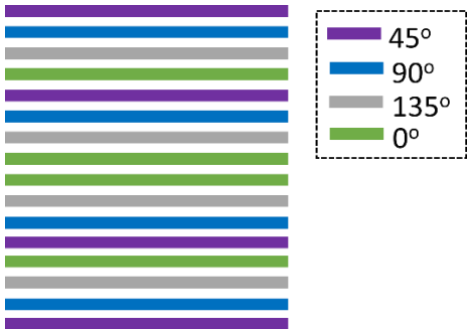

Figure 5.7 Schematic of stacking sequence of in-plane waviness samples ($[45_2/90_2/135_2/0_2]_{2s}$).

Following the waviness-introduction procedures explained in section 5.3.2, the waviness in the compressive-test coupons was introduced with a fixed wavy-region width (gap between Part A and Part B in Figure 5.2) of 10 mm, which defined the waviness wavelength (L) at approximately 20 mm. The amplitude (A) was varied using different numbers of handle-rotation cycles. Figure 5.8 shows an example of the waviness with the wavelength (L) of 20 mm and an amplitude (A) of 1.1 mm and it was found by experiment that this amplitude was achieved with 10 handle-rotation cycles.

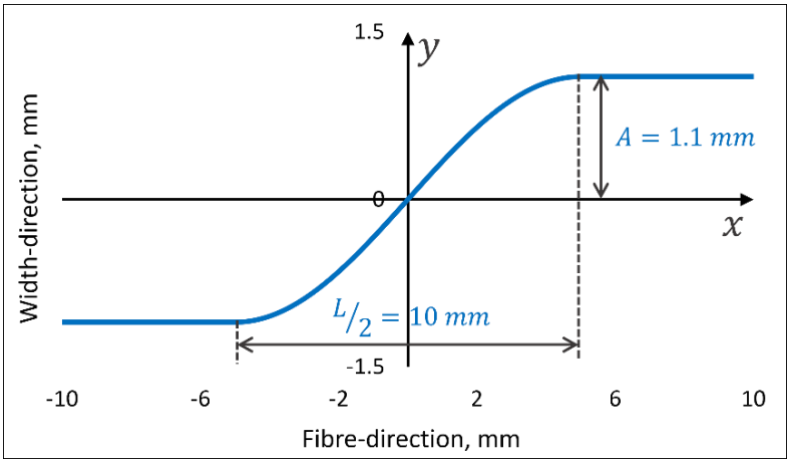

Figure 5.8 An example of waviness with $L = 20\ mm$, $A = 1.1\ mm$.

For the compressive-test coupons described in this chapter, waviness was introduced either to some or to all 0° plies, with the remaining plies unchanged. The waviness severity in a coupon was controlled in two ways. The first was by the number of wavy plies contained in the coupon: waviness was pre-

introduced into either all four or only the middle two 0° plies (Figure 5.9). The former approach was named ‘Allwavy’, whilst the latter was called ‘Midwavy’. The second way to control the severity was more straightforward; specifically, by changing the amplitude, A. This chapter uses two amplitude levels, distinguished by rotating the handle by five cycles (low-amplitude) or ten cycles (high-amplitude). Figure 5.10 displays photographs of wavy plies at these two amplitude levels. The software of ‘Image J’ was used to measure the angle for each case. The measured mean angle for the low-amplitude case was 14.1° and for the high-amplitude case it was 21.7° (Table 5.1).

Table 5.1 Lists of measured angles of wavy region in the uncured ply and autoclaved samples after polish.

Waviness level	low-amplitude (uncured ply) θ_{5c}	Level-1-Mid θ_1	Level-1-All θ_2	high-amplitude (uncured ply) θ_{10c}	Level-2-Mid θ_3	Level-2-All θ_4
Mean measured angle	14.1°	13.5°	13.9°	21.7°	17.6°	19.4°

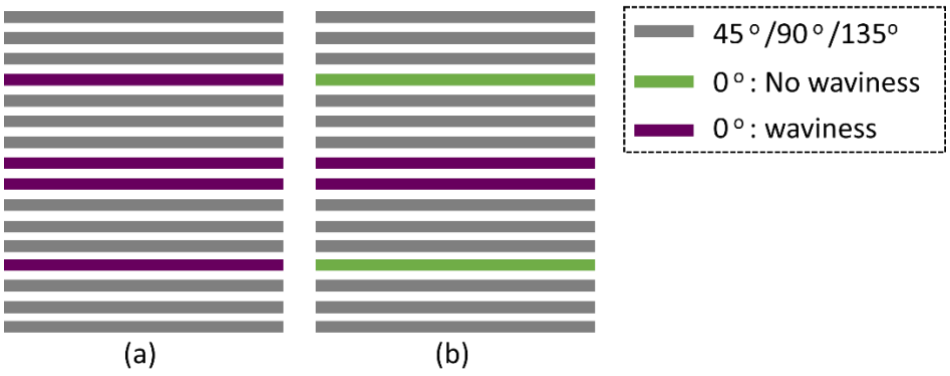

Figure 5.9 Diagram of number of plies containing waviness: (a) all 0° plies have waviness (‘Allwavy’) and (b) only middle two 0° plies contain waviness (‘Midwavy’).

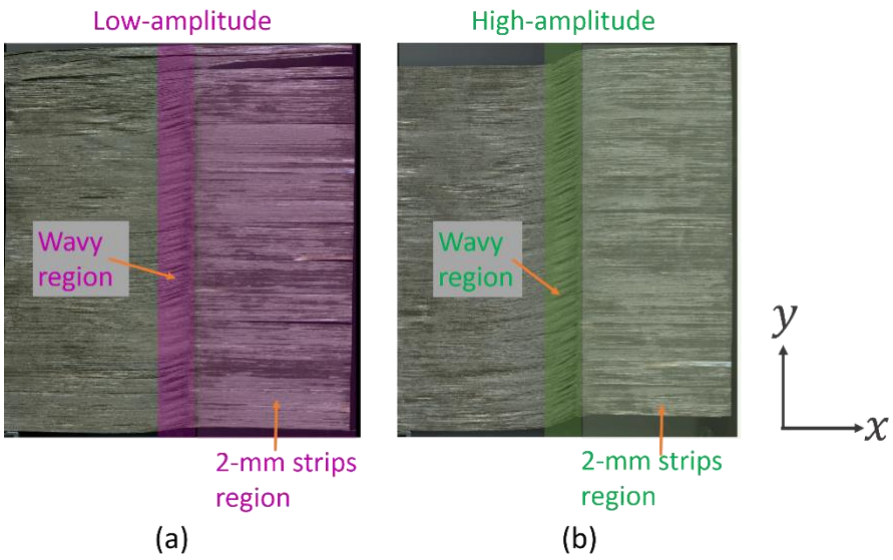

Figure 5.10 Photographs of two waviness-severity levels of uncured plies: (a) low-amplitude level with 5-Cycle handle-rotation and (b) high-amplitude level with 10-Cycle handle-rotation.

When the two ways to control the waviness severity were combined, four different waviness sample types were designed and manufactured for the compressive test. The waviness severity increased from Level-1-Mid to Level-2-All and the detailed definition for the waviness severity of each level is as follows:

- Level-1-Mid: middle two 0° plies with low-amplitude waviness, sheared by 5 cycles of handle-rotation.
- Level-1-All: all four 0° plies with low-amplitude waviness, sheared by 5 cycles of handle-rotation.
- Level-2-Mid: middle two 0° plies with high-amplitude waviness, sheared by 10 cycles of handle-rotation.
- Level-2-All: all four 0° plies with high-amplitude waviness, sheared by 10 cycles of handle-rotation.

Before moving to the presentation of the mechanical test results, a validation was made to confirm that the manual wavy region in the coupons remained at the designed level after the autoclave process, with the required pressure and temperature. To realise this aim, samples taken from the edge of the

panel were polished ply-by-ply until the internal wavy region was visible. Photograph was created for the wavy region and 'Image J' was used again to measure the angle of this region. The measured mean results are reported in Table 5.1. Compared with the measured angle (14.1°) of the low-amplitude case of the uncured ply (Figure 5.11 (a)), the maximum wavy angle showed a small decrease when the wavy plies were laid up and autoclaved to form the coupons (Figure 5.11 (b) and (c)). This reduction was more obvious in respect of the high-amplitude case, when the uncured wavy ply (Figure 5.12 (a)) contained a maximum angle of 21.7°, while the wavy angles in the coupons (Figure 5.12 (b) and (c)) were 17.6° (Midwavy) and 19.4° (Allwavy). The reason for this may be that the measured locations on the uncured ply (Figure 5.11 (a) and Figure 5.12 (a)) were chosen across the whole width (y direction), covering four coupons' width and the remaining sections at the edges. The coupon's wavy angles reported in Table 5.1 were obtained from measurement of the remaining edges of the autoclaved panel (areas labelled * in Figure 5.13 (a)). Manufacturing inconsistencies from batch to batch could also account for this. However, the percentage of the tested CV ($CV\ (\%) = \frac{Standard\ deviation}{Mean\ value} \times 100$) among samples from different batches (Table 5.2) is not significant, suggesting that the differences between batches do not have obvious negative influence, thus the compressive experimental results are reliable.

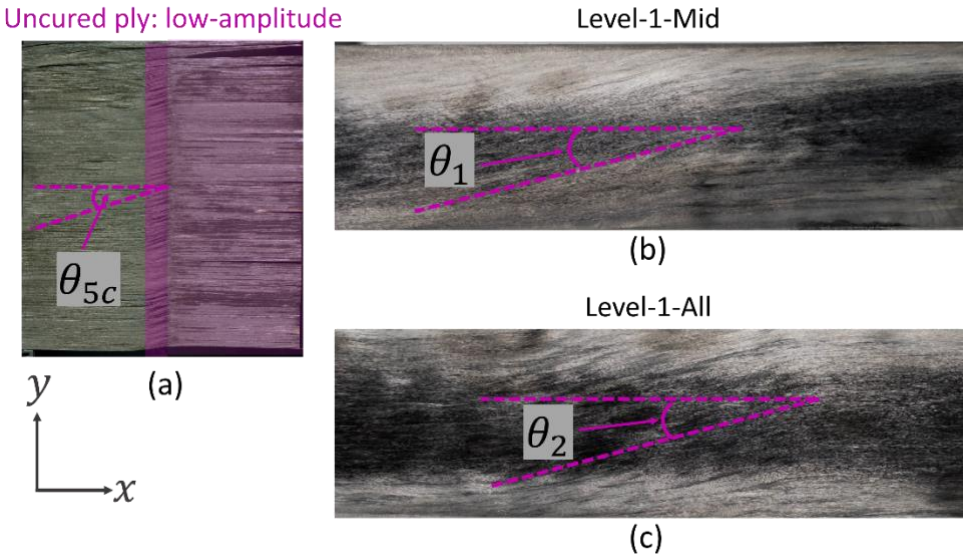

Figure 5.11 Measured angle of low-amplitude waviness, (a) at uncured ply, (b) and (c) at one wavy ply of autoclaved laminate after polish, (b) for Level-1-Mid and (c) for Level-1-All.

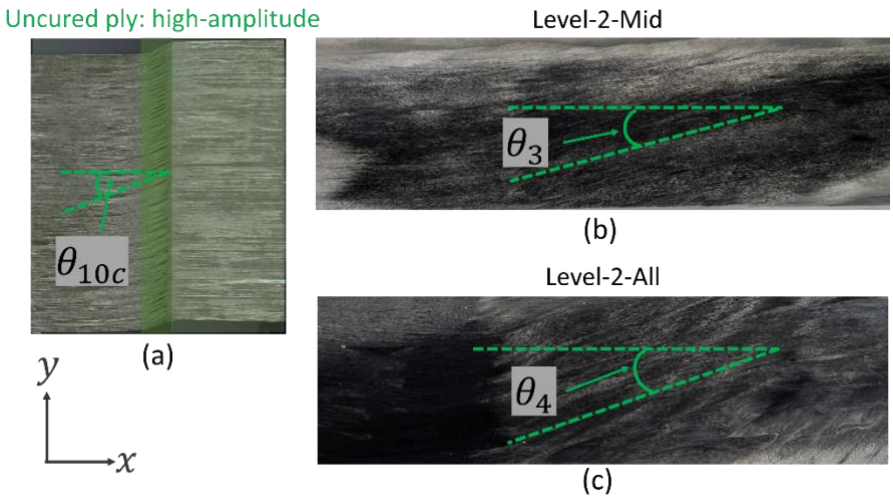

Figure 5.12 Measured angle of high-amplitude waviness, (a) at uncured ply, (b) and (c) at one wavy ply of autoclaved laminate after polish, (b) for Level-2-Mid and (c) for Level-2-All.

5.4 Compression test

5.4.1 Coupon layout and test set-up

The samples for the compression test (Figure 5.13) were cut from a panel to the dimensions of 100 mm × 25 mm × 4 mm. Each sample contained a gauge length of 20 mm in the middle, between the two 40 mm-length end tabs. The edges of each sample were ground to slide fit into the 25mm width testing fixture (Figure 5.14). Thus, the wavy fibres were terminated at the top/bottom edges and formed the terminated-fibre regions (Figure 5.13 (c)). The ICSTM compression test fixture designed by Imperial College [124] was chosen to generate a uniform one-dimensional stress state and keep transverse stress to a minimum. The gauge length (20 mm) was determined to ensure that compressive failure occurred before Euler instability [10]. The larger width (25 mm) than the gauge length (20 mm), was intended to contain more continuous fibres in the samples.

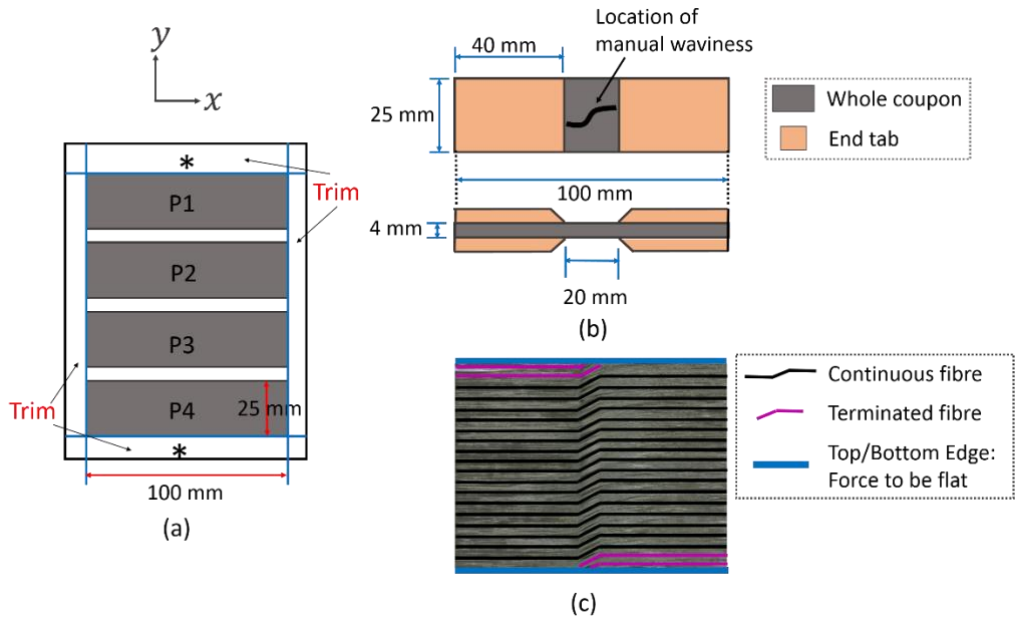

Figure 5.13 (a) Schematic of sample-cut layout: areas labelled * are the remaining samples for measuring the angle of a wavy ply in the autoclaved laminate after polish, (b) geometry of samples, (c) the gauge region showing the terminated fibre areas at top/bottom edges.

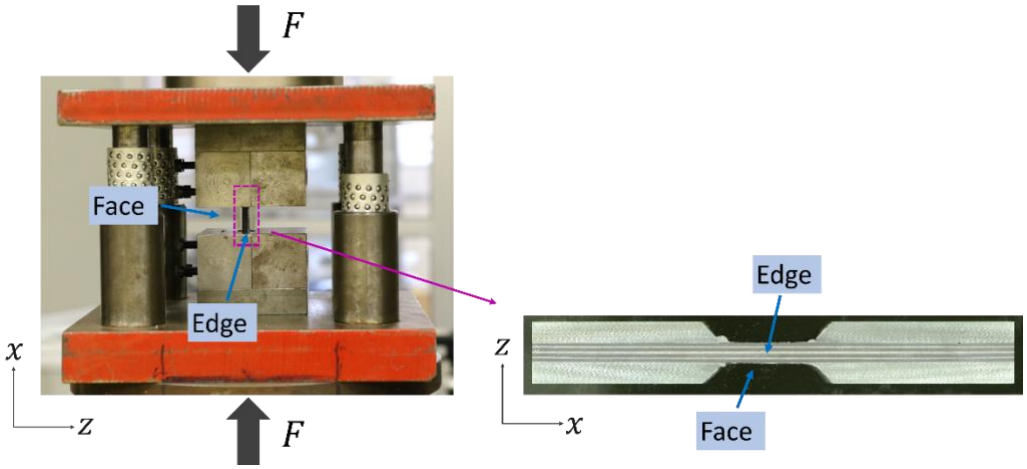

Figure 5.14 Image of coupons set-up inside of Imperial fixture for compression test.

All samples were tested in a ZWICK_1478 testing machine with a 100KN capacity at a loading rate of 0.1 mm/min. Due to the sudden and catastrophic nature of compressive failure, two Photron SA-1 high-speed video cameras were set up separately and focused on the edge and front face of the gauge section (Figure 5.14), in order to capture the failure sequences. The frame rate of the camera was chosen at 100,000 frames/second. The load-displacement response was also recorded for each sample.

As a slight pre-crack noise could be heard in advance of the catastrophic failure, a few coupons were prevented from reaching full failure, to carry out X-ray CT scans with dye-penetration, in order to identify the pre-failure internal damage state.

5.4.2 Failure stress level

At least six coupons were tested for each level of waviness severity and the pristine case to reduce the statistical error. The percentage knockdown of compressive stress for each severity level was calculated relative to the tested pristine value and these are shown in Table 5.2 below. It clearly demonstrates that with the increase of waviness severity, created by increasing either the number of wavy plies or the waviness maximum angle, the failure stress had an obvious reduction. For severity Level-1-Mid, in which only the middle two 0° plies contained the low-severity waviness, the knockdown percentage was the smallest of the four cases, at about 11%. This knockdown percentage nearly doubled to 20% when waviness with a similar maximum angle was applied to all four 0° plies (Level-1-All). For the larger maximum-angle waviness in Level-2-Mid, with only the middle two 0° plies including the wavy region, the knockdown increased to 23%, a small increase compared to Level-1-All but more than a doubling of the Level-1-Mid value as a result of just a 30% increase in maximum waviness angle in the same two middle plies. Then, when this large-severity waviness was introduced in all the four 0° plies (Level-2-All), the knockdown reached its maximum of 32%. This knockdown trend indicates that the misalignment of fibres within the plane does have a significant negative influence on the compressive failure stress: the failure stress values reduce as the waviness severity (maximum waviness angle, θ_{max}) increases and as the number of wavy plies increases. Table 5.3 presents a summary of failure stress knockdown as a function of both the maximum waviness angle and the number of wavy plies.

Table 5.2 Tested failure stress of each case and their knockdown as percentage based on the pristine value.

		Pristine	**Level-1-Mid**	**Level-1-All**	**Level-2-Mid**	**Level-2-All**
Mean	MPa	**662.2**	**589.6**	**529.8**	**506.8**	**450.6**
Standard deviation	MPa	21.2	24.9	41.8	31.9	32.8
CV	%	3.2	4.2	7.9	6.3	7.3
Knockdown based on Pristine	%		**11**	**20**	**23**	**32**

Table 5.3 A summary of the failure stress knockdown as a function of both the maximum waviness angle and the number of wavy plies.

		# Number of wavy plies	
		# 2	**# 4**
Low-amplitude	Maximum angle	13.5°	13.9°
	Knockdown (%)	**11**	**20**
High-amplitude	Maximum angle	17.6°	19.4°
	Knockdown (%)	**23**	**32**

5.4.3 Failure modes

Under compressive load, composites tend to fail under the combined effects of delamination, matrix cracking, and fibre failure [1]. Section 5.4.2 focused on the failure-stress knockdown influenced by the in-plane waviness introduced into the samples. This section aims to identify the failure mechanisms that trigger or dominate the catastrophic damage.

For each waviness-severity level, the loading process of specimens was recorded with the high-speed photography due to the sudden nature of compressive failure. However, Figure 5.15 shows that before

the ultimate failure, some pre-cracks (Magenta spots) had already occurred. Since the high-speed photography could only record the exterior failure mode of the sample and cover only a fleeting period encompassing the ultimate damage, penetrant-enhanced X-ray CT scans were used to check the damage activity in the interior of the specimen before the complete failure. For each severity-level case, at least five samples had their loading interupted prior to the occurrence of complete failure. Radio-opaque dye penetrant was then applied to the specimen, which would be drawn into any cracks or delaminations through capillary action. The dye penetrant was: ZnI_2 in Isopropyl alcohol/water and the coupons were soaked in this for about 24 hours to enhance the contrast of damage and non-damange areas, and to make the internal failure areas more clearly visible. According to the average loading value which caused the ultimate failure of each severity level, loading of these specimens was interupted in the range of 55% to 95% of failure-load levels, to reflect the internal damage conditions at that moment by the CT technique. More detailed explanations are presented below.

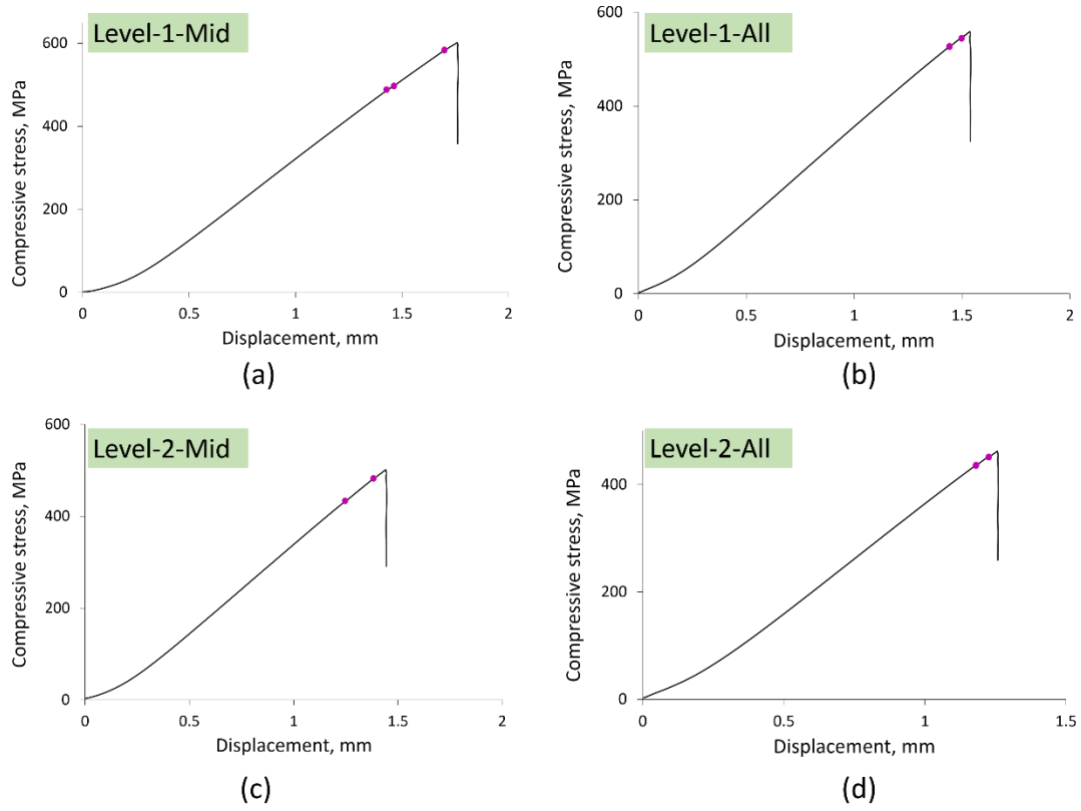

Figure 5.15 Compressive stress (MPa) against the displacement (mm) curve for a typical specimen of (a) Level-1-Mid, (b) Level-1-All, (c) Level-2-Mid and (d) Level-2-All. Magenta spots indicate the small curve-fluctuations, representing the pre-crack occurrences.

5.4.3.1 Failure modes near the moment of full damage

I. Level-1-Mid

When the waviness severity remained small, high-speed photography in Figure 5.16 shows a clear failure mode of delamination, located between the middle wavy and adjacent 135° plies, accompanied by a very slight fibre failure, which was hard to recognise in the earlier captured images (Figure 5.16 (b)) but became clear later in Figure 5.16 (c). Three out of six samples of Level-1-Mid showed similar failure locations and sequences.

However, in the CT scan image of this severity level (Figure 5.17), a delamination (bright region) at the same interface between a middle wavy ply and its adjacent 135° ply was clearly observed (as in Figure 5.16), splitting and fibre failure (bright lines) were also obvious in the CT image. Both failures were located within the wavy plies (middle 0° ply). Fibre failure grew across the fibre tows at a corner (see Figure 5.17 (b)) and was oriented at about 60 degrees to the edge, while splitting started from the edge and propagated into the sample, following the waviness orientation.

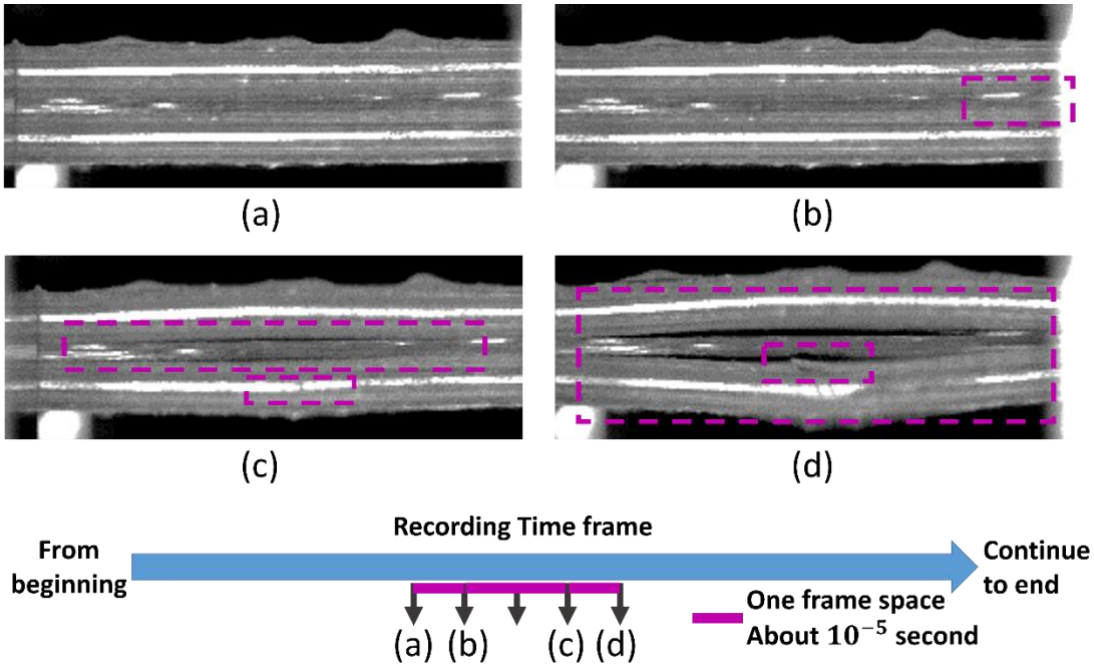

Figure 5.16 High-speed photographic images in a Level-1-Mid specimen: (a) immediately prior to damage, (b) fibre failure in a wavy ply, (c) delamination and further fibre failure, (d) further delamination and fibre failure, accompanied by matrix cracking. Dashed-line boxes highlight the failure modes in each image.

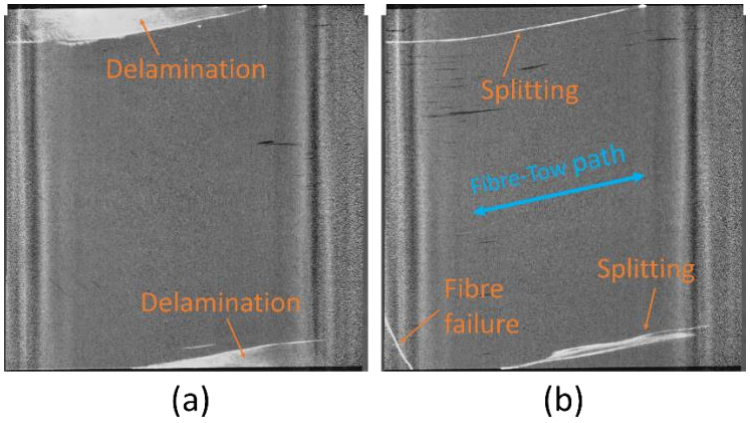

Figure 5.17 CT image in a Level-1-Mid specimen interrupted at 85% of the mean failure load: (a) delamination at ($0_w - 135^\circ$) interface, (b) fibre failure and splitting within the wavy ply. Bright areas and lines represent the damage.

II. Level-1-All

Level-1-All samples contained waviness with a similar amplitude and maximum angle as Level-1-Mid, but with the number of wavy plies doubled to four. Typical failure mechanisms recorded by the high-speed camera are shown in Figure 5.18. Delamination was the main mode causing the full damage, with fibre failure and matrix cracking only observable when the failure became severe, here in the case of Figure 5.18, fibre and matrix damages turned to be visible until to the moment of image (d). In the CT images of this instance (Figure 5.19), fibre failure did not appear in the image and only delamination and splitting were captured. With the combined findings from Figure 5.18 and Figure 5.19, it suggests that at the loading stage before ultimate failure, fibre failure is not the main mode causing the damage at this level.

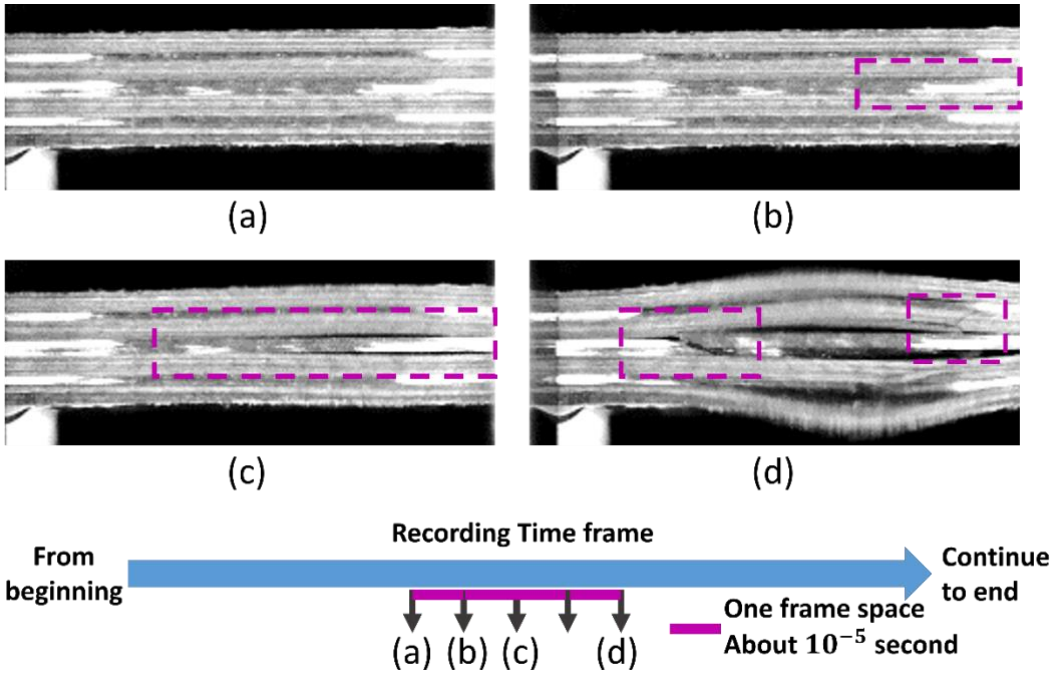

Figure 5.18 High-speed photographic images in a Level-1-All specimen: (a) immediately prior to damage, (b) delamination between wavy and adjacent plies, (c) further delamination, (d) further delamination accompanied by fibre failure and matrix cracking. Dashed-line boxes highlight the failure modes in each image.

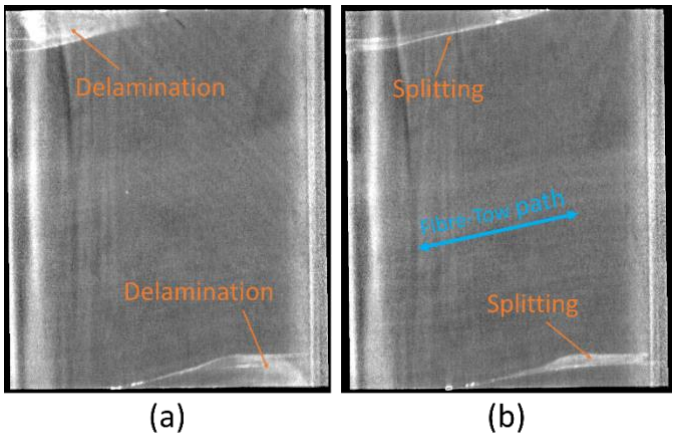

Figure 5.19 CT image in a Level-1-All specimen at 86% of the full damage: (a) delamination at $(0_w - 135^\circ)$ interface, (b) splitting within the wavy ply. Bright areas and lines represent the damage.

III. Level-2-Mid

For the high-amplitude waviness on the middle two plies, similar failure-mode sequences occurred as in Level-1-All. Delamination between the middle 0° wavy ply and the adjacent 135° ply was still the

major mode governing the final failure (Figure 5.20). When the delamination-dominated damage became severe, fibre failure on both wavy and non-wavy plies appeared. When the CT images shown in Figure 5.21 were checked for the mode information at the moment before the damage became severe, only delamination at the interface and splitting within the ply was observable, as in Level-1-All. Once again, the splitting followed the trend of fibre tows which were sheared to form the waviness. Therefore, in Level-2-Mid, delamination and splitting were the two failure modes governing the ultimate damage.

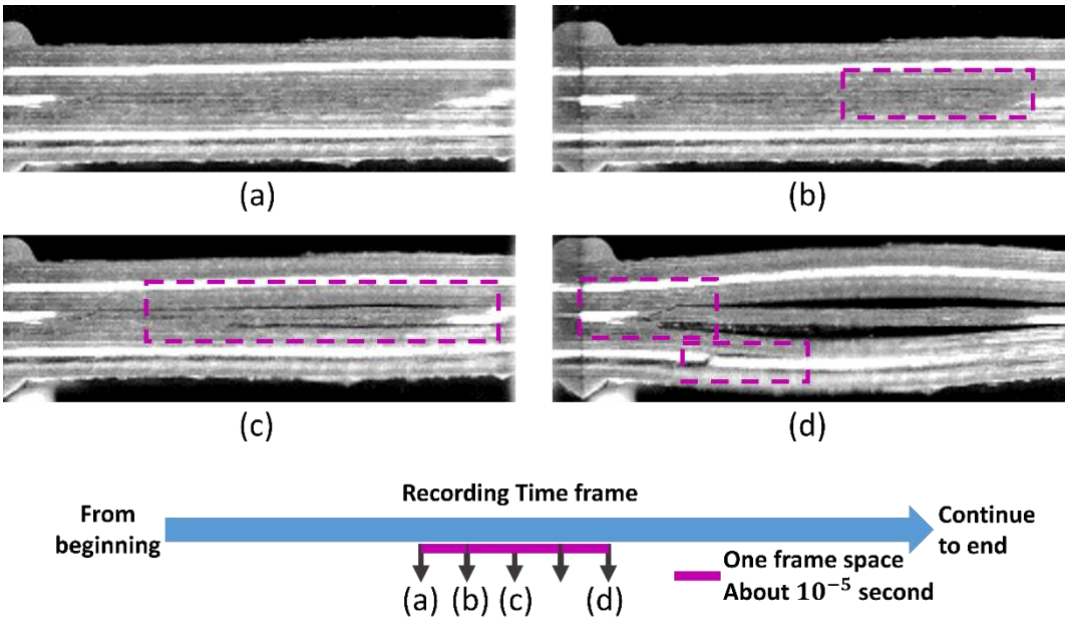

Figure 5.20 High-speed photographic images in a Level-2-Mid specimen: (a) immediately prior to damage, (b) delamination between wavy and adjacent plies, (c) further delamination, (d) further delamination accompanied by fibre failure. Dashed-line boxes highlight the failure modes in each image.

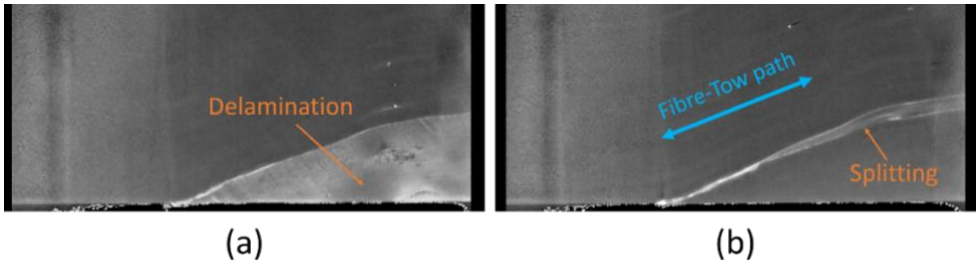

Figure 5.21 CT image in a Level-2-Mid specimen interrupted at 91% of full damage: (a) delamination at ($0_w - 135^\circ$) interface, (b) splitting within the wavy ply. Bright areas and lines represent the damage.

IV. Level-2-All

Finally, in respect of Level-2-All, with the most severe waviness in four plies, the high-speed photography (Figure 5.22) showed that fibre failure appeared in the middle wavy plies at an early stage (Figure 5.22 (b)), whilst delamination at the interface between 0° wavy ply and the adjacent 135° ply had not yet become severe. CT scan images of this instance (Figure 5.23) also validated this trend. The delamination at the similar position as recorded in high-speed images (Figure 5.22) is clear in Figure 5.23 (a). Obvious fibre failure is also observable within the middle 0° wavy ply, orientated at about 47° to the coupon edge. Additional splitting within the same ply was connected to the fibre failure, forming a 'branch' shape. Hence, delamination, fibre failure, together with the splitting, created a combined cause of the ultimate failure.

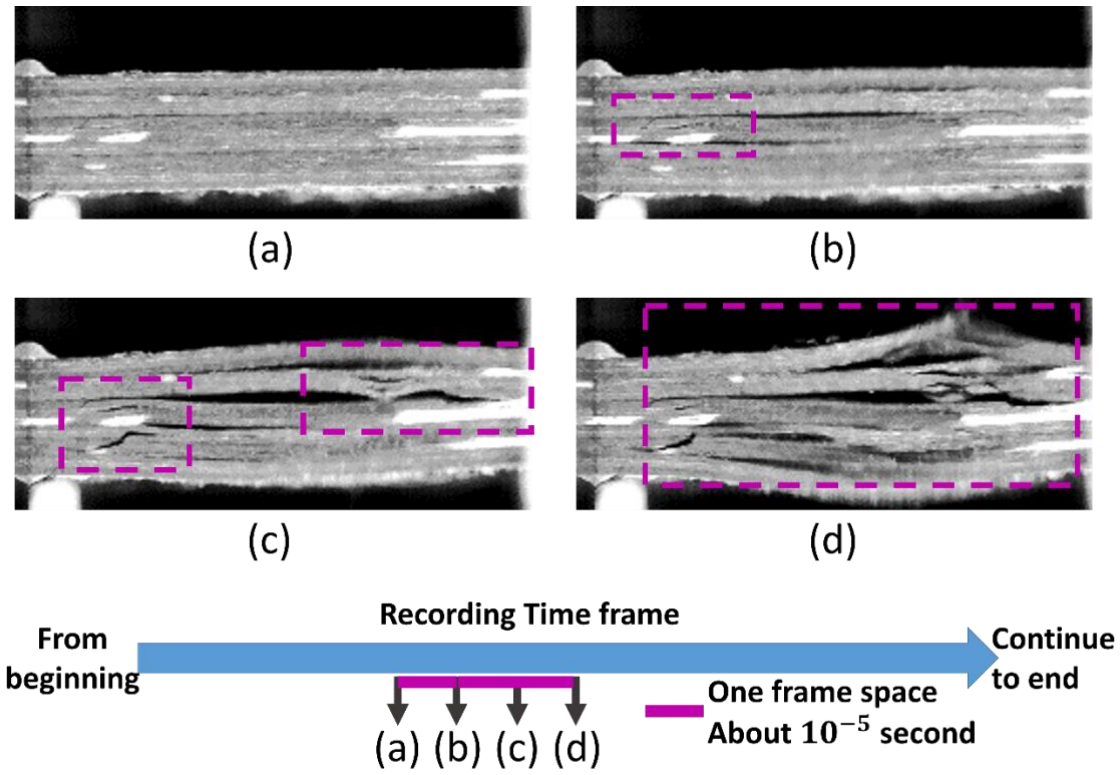

Figure 5.22 High-speed photographic images in a Level-2-All specimen: (a) immediately prior to damage, (b) fibre failure in the wavy ply and delamination between wavy and adjacent plies, (c) further delamination and fibre failure accompanied by matrix cracking, (d) further damage. Dashed-line boxes highlight the failure modes in each image.

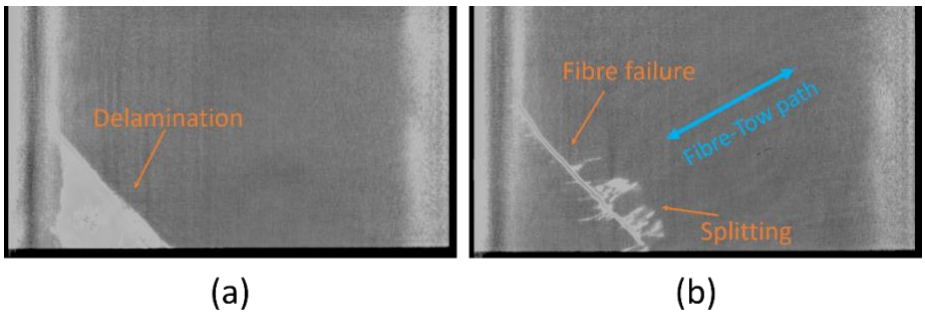

Figure 5.23 CT image in a Level-2-All specimen interrupted at 95% of the full damage: (a) delamination at ($0_w - 135^\circ$) interface, (b) fibre failure and splitting within the wavy ply, forming a 'branch' shape. Bright areas and lines represent the damage.

5.4.3.2 Internal Failure modes before full damage

Studies above indicated the failure modes at the stage near the ultimate failure. However, it was unclear which failure mechanism arose first or what the internal condition was in the pre-crack

moments labelled in Figure 5.15. The CT scan technique was used again to investigate these aspects. For each severity level, specimens were chosen to be unloaded at specific percentages of the full-damage loading levels. The CT results of percentage-loading specimens of each level are displayed in Figure 5.24 - Figure 5.27.

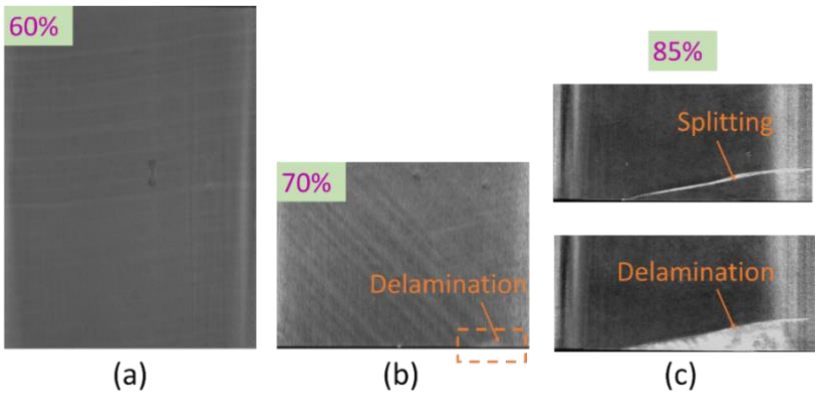

Figure 5.24 CT images of Level-1-Mid specimens unloaded at specific load levels, based on the full-damage loading value (a) 60% (b) 70% (c) 85%.

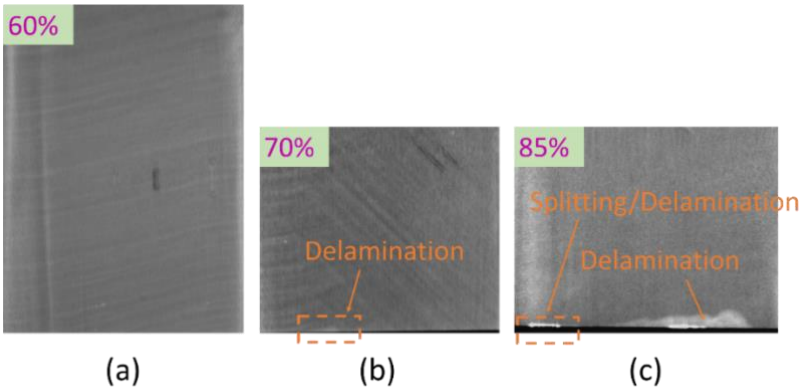

Figure 5.25 CT images of Level-1-All specimens unloaded at specific load levels, based on the full-damage loading value (a) 60% (b) 70% (c) 85%.

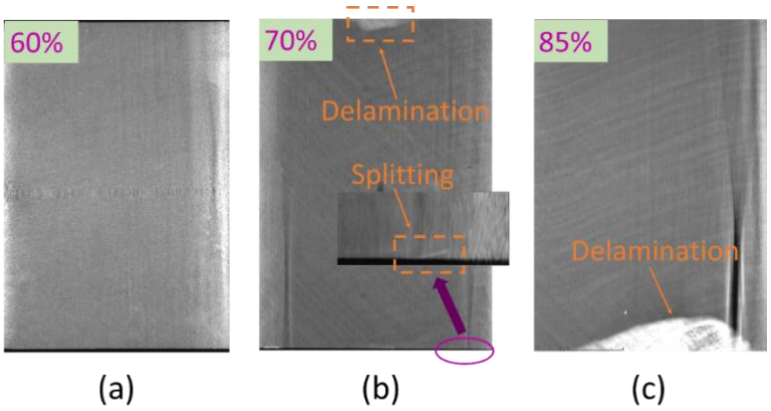

Figure 5.26 CT images of Level-2-Mid specimens unloaded at specific load levels, based on the full-damage loading value (a) 60% (b) 70% (c) 85%.

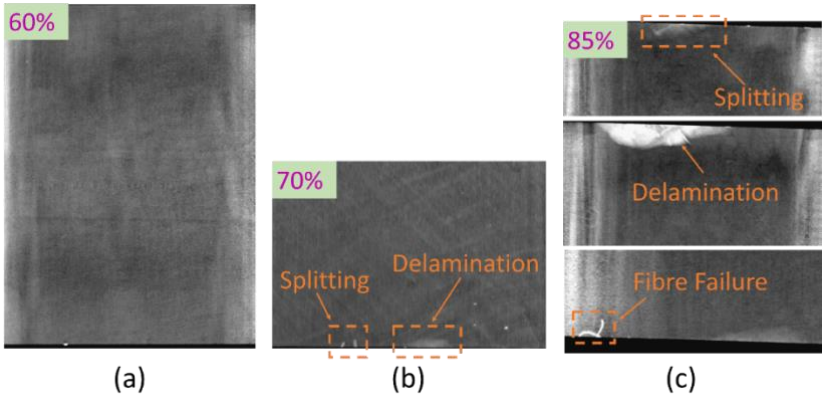

Figure 5.27 CT images of Level-2-All specimens unloaded at specific load levels, based on the full-damage loading value (a) 60% (b) 70% (c) 85%.

After checking the percentage-load CT images, it was concluded that no damage was initiated in any severity-level specimens when the loads were less than 60% of failure stress. This observation agreed with the pre-crack locations shown in Figure 5.15, in which all pre-cracks occurred above 60% of the strength. In terms of the failure mechanisms, delamination at the interface between wavy and adjacent plies was the first mode to be triggered from the edge of all severity-level samples. Splitting was also initiated from the edge of the wavy ply at an early loading stage, accompanied either with occurrence of a delamination (Level-2-Mid and Level-2-All) or a short time after this (Level-1-Mid and Level-1-All). Fibre failure only played an obvious role for the Level-2-All case, and matrix cracking was not the main failure type for all waviness severity levels.

5.5 Summary

Manual in-plane waviness was introduced into individual plies by a specifically-designed waviness-introduction shear rig. Several influencing factors that may potentially affect the introduction of waviness were investigated. The results indicate that the method used to increase the friction effect between tooling and the ply was the key factor in obtaining the desired waviness.

Depending on the change of either the number of wavy plies or the maximum angle of the wavy region, four levels of waviness severity were designed and manufactured into quasi-isotropic ($([45/90/135/0]_{2s}$) specimens. The compression test validated that the failure-stress levels reduced as either the maximum waviness angle or the number of wavy plies increased. When the fibre tows in the 0^o waviness plies were misaligned by 20^o, the knockdown could be as high as 30%.

Delamination at the interface between wavy and adjacent plies and splitting within wavy plies were the two major failure modes causing ultimate failure, regardless of the waviness severity. They were both initiated from the edge of the wavy plies and splitting propagated following the orientation of wavy fibres. Other failure types were gradually triggered as these two failure types became severe and, in combination, they led to the catastrophic damage. In detail:

- Level-1-Mid: when the waviness severity was not severe, in addition to delamination and splitting, fibre failure might also have some contribution in causing the compressive failure.
- Level-1-All & Level-2-Mid: For the low-severity waviness in all 0^o plies or greater severity in just the middle plies, only delamination and splitting led to the ultimate failure, and fibre failure or matrix cracking occurred only after the overall failure became severe.
- Level-2-All: when waviness maximum angle became large and wavy regions were introduced into all 0^o plies, as well as the delamination, fibre failure orientated at about 47^o to the wavy ply edge was triggered to form a ‘branch’ shape, connected with the splitting, before the final sudden failure.

Chapter 6
Numerical study of laminates with in-plane waviness under compression loading

6.1 Introduction

Following the experimental study of compressive failures of laminates containing in-plane waviness reported in Chapter 5, this chapter describes a numerical study that was carried out to further investigate this failure process and better understand the origins of mechanisms accounting for the catastrophic failures. The details of the modelling techniques used in this chapter were explained in Chapter 2. The mechanical behaviour of the ply elements (C3D8R) and interface elements (COH3D8) is governed by a previously defined material model (VUMAT) coded by Mukhopadhyay et al. [1][135], also presented in Chapter 2. The same material type as experimentally tested in Chapter 5 (IM7/8552 from Hexcel [160]) was modelled here and the relevant properties assigned to the models were listed in Table 2.2 – Table 2.4.

The chapter begins with a description of the model set-up in section 6.2, followed by an explanation of mesh generation in section 6.3. Lists of modelling results and their comparison to the experimental recordings are presented in section 6.4, before the close of this chapter with the summary in section 6.5.

6.2 Model set-up

The section simulated in the numerical model is only the middle 'gauge' region of the experimental samples and thus forms a model size of 20 mm x 25 mm x 4 mm (Load direction x Width direction x Thickness direction), see Figure 6.1. This has the quasi-isotropic stacking sequence of $[45/90/135/0]_{2s}$ (Figure 5.7) with 0.25 mm ply thickness. The static compressive load was applied in the form of displacement controlled at a rate of -0.01 mm/s in Abaqus/Explicit, on the two y_z surfaces (Figure 6.1). In-plane waviness was introduced to the middle region (Figure 6.1) at the specific plies (note the

terms ‘Allwavy’ and ‘Midwavy’, as described in Figure 5.9), depending on the waviness severity levels (Level-1-Mid to Level-2-All). The definition of the wavy region assigned to the model was the same as the experimental study, using a half-cycle sine wave centred on zero (Eq. (5.1)) to simulate the kink shape (Figure 5.1). Therefore, three parameters, namely: amplitude (A), wavelength (L), and maximum angle (θ_{max}), were sufficient to fully define the severity of the wavy region.

In the manufacturing procedures for introducing the waviness into a lamina, the wavelength (L) was fixed for all models at 20 mm. Different amplitudes (A), together with the number of wavy plies defined, were used to govern the different severity-level cases (Level-1-Mid to Level-2-All). Table 5.1 lists the measured mean maximum waviness angle of specimens tested in Chapter 5, for each severity level. The amplitude at each level can thus be calculated in terms of the maximum angle from Eq. (5.2), when the wavelength remains unchanged (20 mm). The calculated amplitude values were input into the models for the simulation of the failure process of that specific case. The magnitudes for the waviness-related parameters assigned to the models are listed in Table 6.1 for each level.

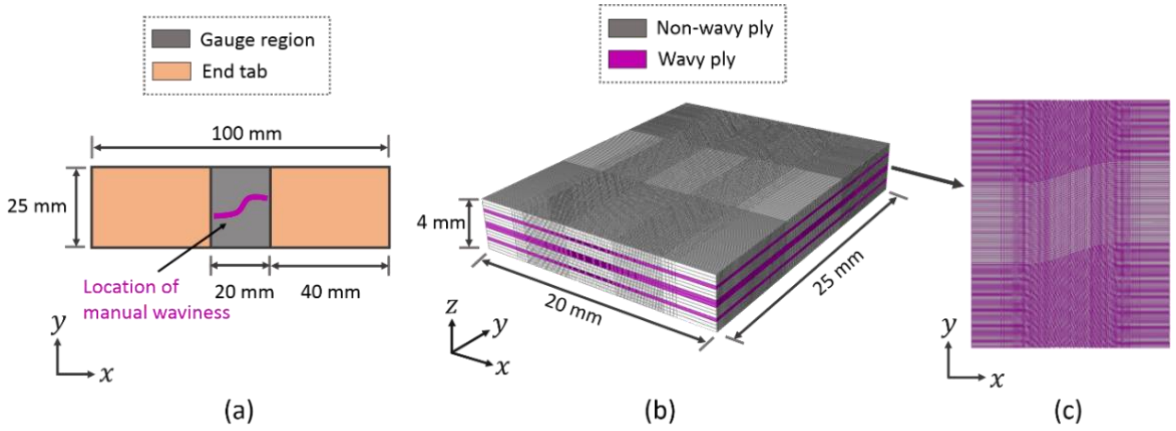

Figure 6.1 Schematic description of, (a) (x, y) view of a sample, (b) geometry of the model covering the gauge region, (c) overall shape of a wavy ply.

Table 6.1 Amplitude values put into the model for each waviness severity-level case.

Waviness severity level	Level-1-Mid	Level-1-All	Level-2-Mid	Level-2-All
Wavelength, L	$L = 20\ mm$			
Mean measured max. angle	13.5°	13.9°	17.6°	19.4°
Amplitude, A (mm)	0.77	0.79	1.01	1.12

6.3 Mesh generation

As explained in Chapter 3, the FE-mesh generation for the in-plane waviness model was controlled through the simulator described in Chapter 4 and the transfer process from Chapter 3 via the two material-property maps (Map-A and Map-B) and deployed in Abaqus/Explicit for the computation. The plies were modelled using 8-node solid elements (C3D8R) with one element through the thickness of each ply. Cohesive elements (COH3D8) with 0.01 mm thickness were inserted into interfaces between plies to simulate the resin layers that occur naturally and to allow delamination to occur. Fibre volume fraction (FVF) was assumed to be uniform over the whole model, even though there was a possibility that FVF might become non-uniform around wavy regions, since the study in Chapter 3 indicated that the change of this factor could be ignored for small changes of FVF. The method used to manufacture in-plane waviness in Chapter 5 was chosen to minimise the variation in FVF in the wavy region; in cases of experimental evidence for naturally occurring in-plane waviness where FVF changes significantly, this parameter should be included in the model and determined from the NDT data as a 3D map. However, due to the lack of characterised 3D FVF map in the current stage, a simple investigation of the influence of FVF variance originating from the in-plane waviness was carried out and explained at the end of this chapter (Section 6.4.4.3), in order to identify this FVF influence was not that significant to affect the simulation results, if the waviness was introduced following the way in Chapter 5.

For the non-wavy plies, the mesh was generated as normal rectangular-shaped brick elements (Figure 6.2), named 'Rectangular-mesh'. The interface layers, simulated by cohesive elements between these non-wavy plies, followed the same trend and distribution of the non-wavy solid elements.

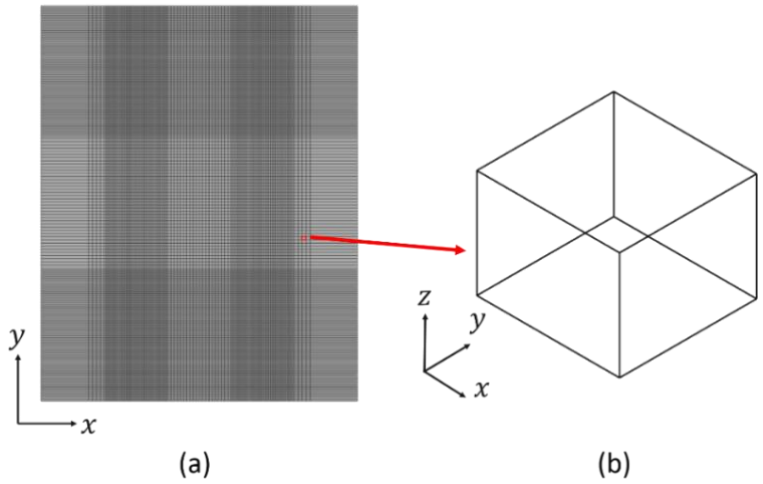

Figure 6.2 (a) Mesh-generation for a non-wavy ply, (b) rectangular shape of an element in a non-wavy ply.

In terms of the wavy plies in the samples, the nominal 0° fibre tows have been sheared to the desired angle to form a wavy region. Thus, in the numerical model, a 'skew-mesh' was generated for the wavy plies. Each row of ply elements was also simulated by C3D8R but following the trend of the waviness to form a kink-shape as illustrated in Figure 5.1. Figure 6.3 gives a schematic as to how to transform the rectangular-mesh to the skew-mesh. The calculation of the y-coordinate movement of the nodes in question used the local in-plane fibre orientation, φ_i in each element i and was controlled by

$$\Delta y_i = x_i \tan(\varphi_i) \tag{6.1}$$

where, i is element ID, Δy_i means y-coordinate movement of the ith element, x_i stands for length in x direction of the ith element, obtained from Map-A and φ_i is in-plane fibre orientation of the ith element, obtained from Map-B.

Figure 6.4 shows the comparison of a wavy ply before and after the transformation to the skew-mesh in the model. It is clear that through this method each row in the skew-mesh closely follows the trend of the fibre tows, which were sheared to form a kink-shape in the lamina.

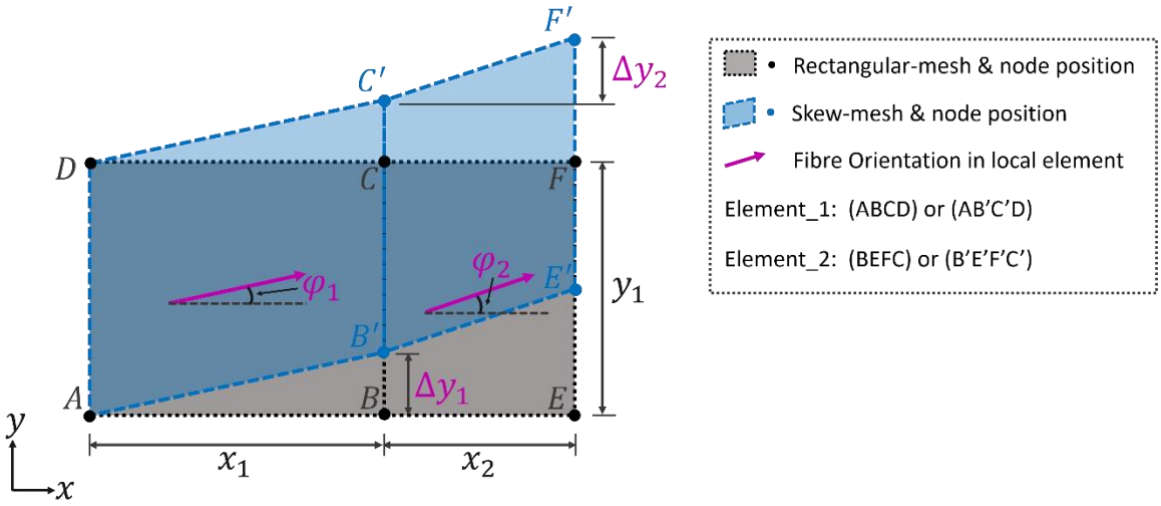

Figure 6.3 The schematic of the transformation from the rectangular-mesh to the skew-mesh, based on the fibre orientation of each element.

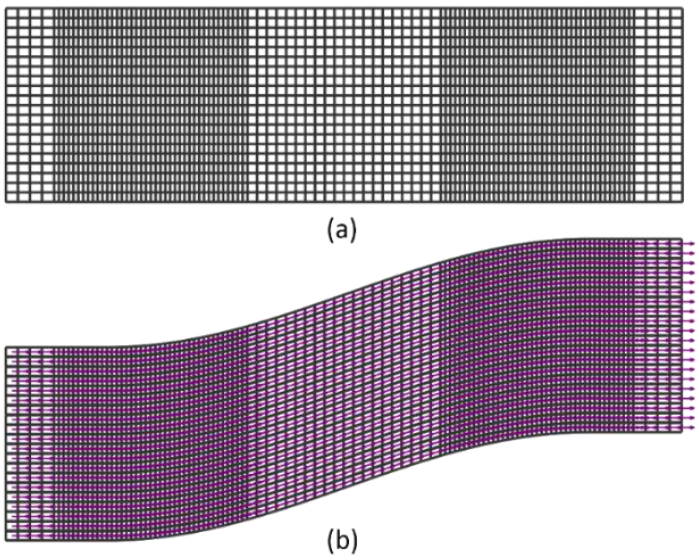

Figure 6.4 (a) Rectangular-mesh of a wavy ply, (b) Skew-mesh after the transformation of the same ply in (a), magenta arrows represent the fibre orientation.

In the experiment, the top/bottom edges in a wavy ply were made straight when the panel was cut and ground into coupons; thus, the continuous fibres were terminated suddenly (Figure 6.5 (a)). In the

numerical models, when the mesh of this ply was transformed into the skew-mesh, wedge elements (C3D6) were assigned to the fibre-terminated locations, in order to reflect these specific features (Figure 6.5). However, this type of element only provides accurate predictions with a very fine mesh [160], hence subsequently they were removed. In fact that this did not influence the model results, since the generation of intralaminar splitting sufficiently reduced the local stress concentration at the edges, and the predicted failure distributions and trends gave good agreement with the experimental results qualitatively.

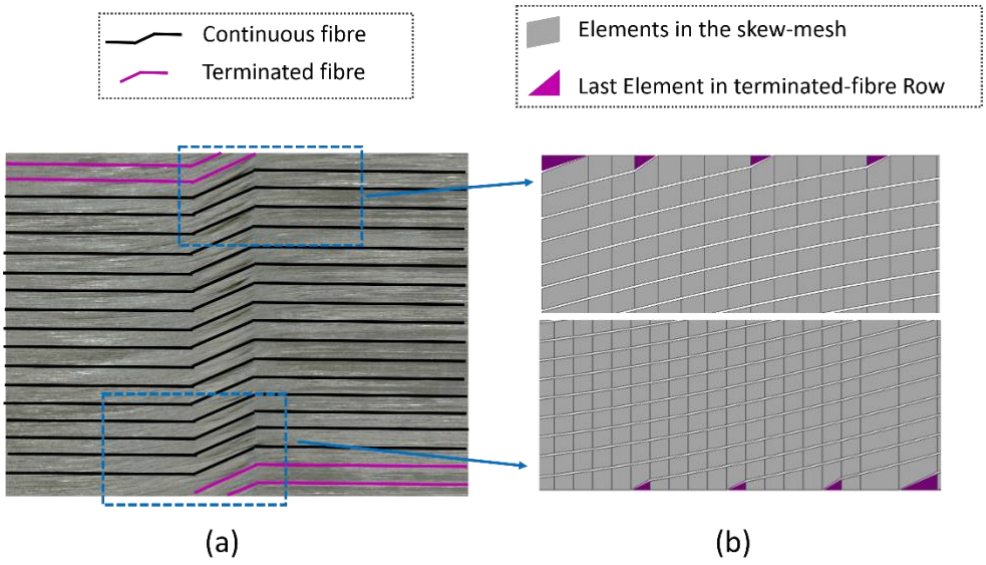

Figure 6.5 (a) Terminated-fibre regions in the wavy specimen, (b) part of modelled upper/lower edges within the wavy ply.

As summarised in Chapter 5, in addition to delamination, intralaminar splitting at the wavy ply was another major mechanism causing the ultimate catastrophic failure. In order to simulate this phenomenon, the cohesive zone modelling technique [11][143] was applied again, with the same material properties (Table 2.3) and same type of cohesive elements (COH3D8) as delamination, since previous experimental studies have identified comparable interlaminar and intralaminar behaviour for IM7/8552 [161]. These intralaminar cohesive elements were inserted between the lines of solid elements within each wavy ply to allow for the separation of fibre tows within a ply. Figure 6.6 illustrates this solid/cohesive arrangement within the wavy ply. Cohesive elements were located between solid elements in the y direction and followed the kink path in the x direction. The thickness

direction of these cohesive elements was assigned to be global y direction and the thickness value was 0.01 mm.

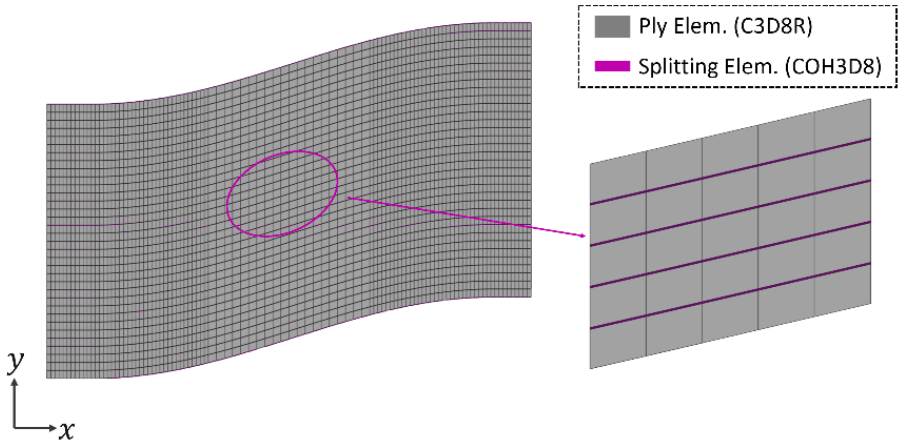

Figure 6.6 Schematic of cohesive elements inserted within the wavy ply (skew-mesh) to simulate splitting.

There was an obvious problem when the skew-mesh was introduced to the wavy ply. Mesh differences would occur between the plies when moving from the rectangular-mesh to the skew-mesh regions, which meant that a contiguous mesh could not be used for all of the model. A surface-based tied constraint [162] was defined to overcome this issue, constraining the nodes on the slave surface to behave in the same way as the closest nodes on the master surface (Figure 6.7). For the specific case in the numerical model created here, wavy plies (part or all 0° plies) were connected to either 45° or 135° plies, which retain the rectangular mesh, with the cohesive interface layers located between them. Those cohesive interface layers, located above and below the wavy plies, were also transformed to follow the skew mesh, thus containing the same mesh densities and distributions as the wavy plies. The tied constraint was then defined between the skew-mesh interface layers and the adjacent 45°/135° plies. The master surface was assigned to 45°/135°. Figure 6.8 gives an example to indicate how the tied constraint was defined in the numerical model in Abaqus/Explicit for this thesis.

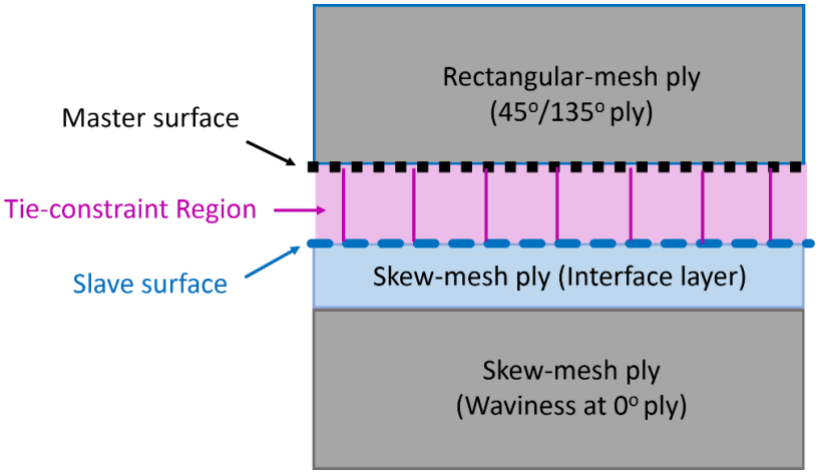

Figure 6.7 The illustration of tie-constraint set-up between the rectangular-mesh ply and skew-mesh interface layer. The tied region in pink area is magnified for the clear explanation.

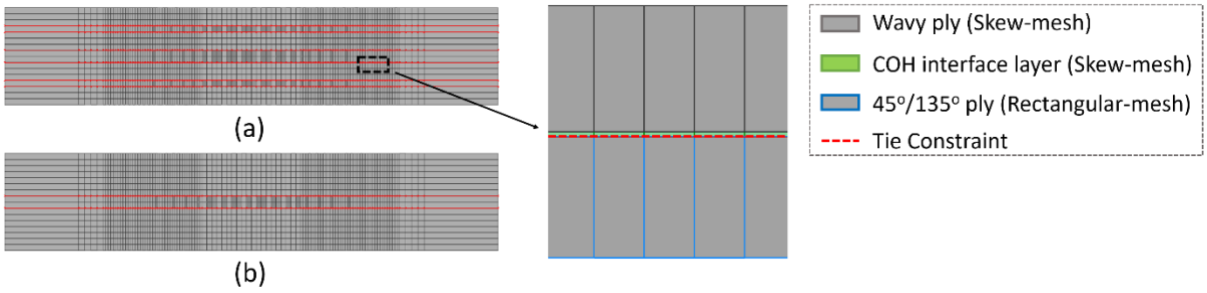

Figure 6.8 The illustration of an example to show the tie-constraint set-up in the FE mesh, (a) 'Allwavy' case, (b) 'Midwavy' case.

6.4 Model results

According to the experimental observations reported in Chapter 5, delamination and splitting were the two major failure mechanisms which led to the complete compressive damage for all four waviness-severity level cases. Therefore, at the first stage of model investigations only the cohesive zone technique [11][143] was applied to simulate the experimental failure modes due to the manually introduced waviness. Investigations about whether matrix cracking in the non-zero plies (based on Puck's law [45][46]) and kink failure [50][61] of the 0° plies had a critical influence on the ultimate failure are presented in sections 6.4.2 and 6.4.3.

6.4.1 Results predicted by cohesive zone model (CZM)

6.4.1.1 Maximum stress levels

Figure 6.9 illustrated the stress vs. displacement curves predicted by the cohesive-zone technique models for all the four level cases. At point 'A', the stress showed a small jump at the transition point from the thermal step to the loading step. This was due to the adjustment of the tied constraint [162][163] to make the motion of slave nodes in accordance with the master nodes. As shown in Figure 6.9, when the failure process was modelled with the cohesive-zone technique, without considering fibre breakage, Level-1-All and Level-2-All gave a prediction of failure stress (peak point) at 545.4 MPa and 513.9 MPa respectively. For Level-1-Mid and Level-2-Mid, the computations were terminated automatically before the stress reached the peak point, due to the excessive distortions of some elements. The terminated stress values of these two levels were 613.2 MPa and 570.6 MPa, respectively. The reason that computation for the two 'Midwavy' models (Level-1-Mid and Level-2-Mid) was terminated before the accumulation of damage was sufficient to affect the global behaviour may be because, whilst having similar waviness maximum angles (Level-1-Mid vs. Level-1-All, Level-2-Mid vs. Level-2-All), the loading process for the 'Allwavy' models containing more wavy plies would accumulate greater damage energy.

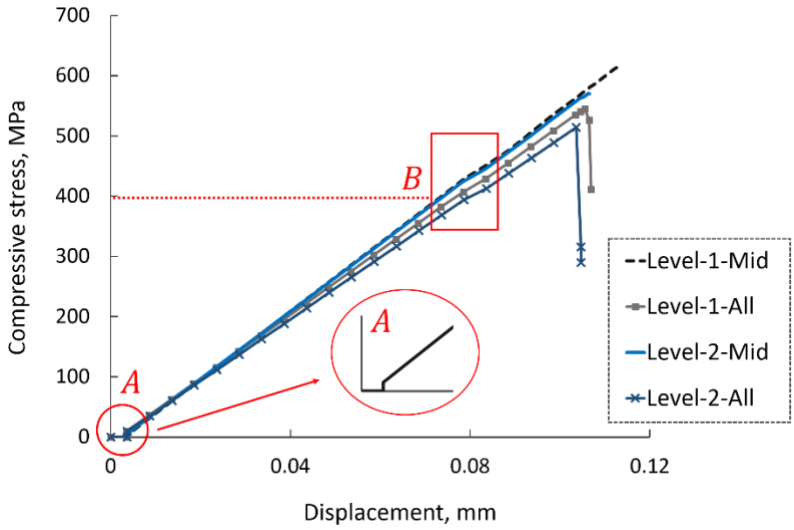

Figure 6.9 Predicted compressive stress vs. displacement curves from cohesive-zone models of the four level cases, point '*A*' indicates the adjustment due to tied constraint during the loading process, area '*B*' includes the initiation points for the delamination and splitting.

Comparing the predicted maximum stress values with the experimental test results (Table 6.2) it was discovered that, when allowing only for the delamination and splitting in the model and omitting fibre failure and matrix cracking, Level-1-Mid and Level-1-All gave quite close (within 4%) predictions to the experimental mean value. This indicated that the delamination and splitting were the key mechanisms governing the compressive failures for the Level-1-All, reinforced by the fact that no fibre failure or matrix cracking was observed in the experiments for Level-1-All. Although the prediction of Level-1-Mid was close to the tested values, the computation of the model was terminated before reaching the peak point and the experimentally observed fibre failure (Figure 5.17) was not included in the model. This suggested some other mechanisms might also have contributed to trigger the catastrophic damage. In terms of the Level-2-Mid and Level-2-All, both predictions were higher than the tested failure stress, by more than 10%. This suggested that allowing only for the delamination and splitting was not enough to give accurate performance estimations for these greater amounts of waviness and other failure modes should also be modelled to either re-distribute the stresses or directly affect the failure process.

Table 6.2 Comparison of maximum compressive stresses predicted by cohesive zone models with experimentally tested values.

Maximum compressive stress		**Pristine**	**Level-1-Mid**	**Level-1-All**	**Level-2-Mid**	**Level-2-All**
Experimental test mean value	MPa	**662.2**	**589.6**	**529.8**	**506.8**	**450.6**
Predicted max. value	MPa	624.7	613.2[3]	545.4	570.6[4]	513.9
Difference between tested and predicted values	%	**6**	**4**	**3**	**13**	**14**

[3] Early-terminated stress, not peak (failure) stress.
[4] Early-terminated stress, not peak (failure) stress.

6.4.1.2 Predicted failure modes

Unlike the over-predicted failure-stress values, both the initiation locations and propagation paths of the modelled failure modes for each level case were in good agreement with the phenomena observed in the experiments. As shown in Figure 6.9, the modelled stress vs. displacement curves remain almost linear, except for a slight fluctuation, highlighted as 'B', around a stress of 400 MPa. A detailed check of model results has confirmed that before this fluctuation point ('B'), there was no damage initiated for either case and the fluctuation was caused by the initiation of delamination or splitting, or both. Following the sequence from Level-1-Mid to Level-2-All, the detailed predictions for the failure distributions are reported below.

I. Level-1-Mid

Figure 6.10 shows the comparison between the failure distributions captured in the experiments and predicted by the cohesive zone models for the Level-1-Mid case. From the side view (Figure 6.10 (a) and (b)), both the test and model present a similar location of delamination at the interface between the central wavy plies and their adjacent non-wavy plies. The in-plane view of wavy plies (Figure 6.10 (c) and (d)) shows an even better agreement with the experiment and indicates almost the same edge locations and shapes following the wavy path for both delamination and splitting, except that a fibre failure was only captured in the CT images, as no fibre failure was included in this model.

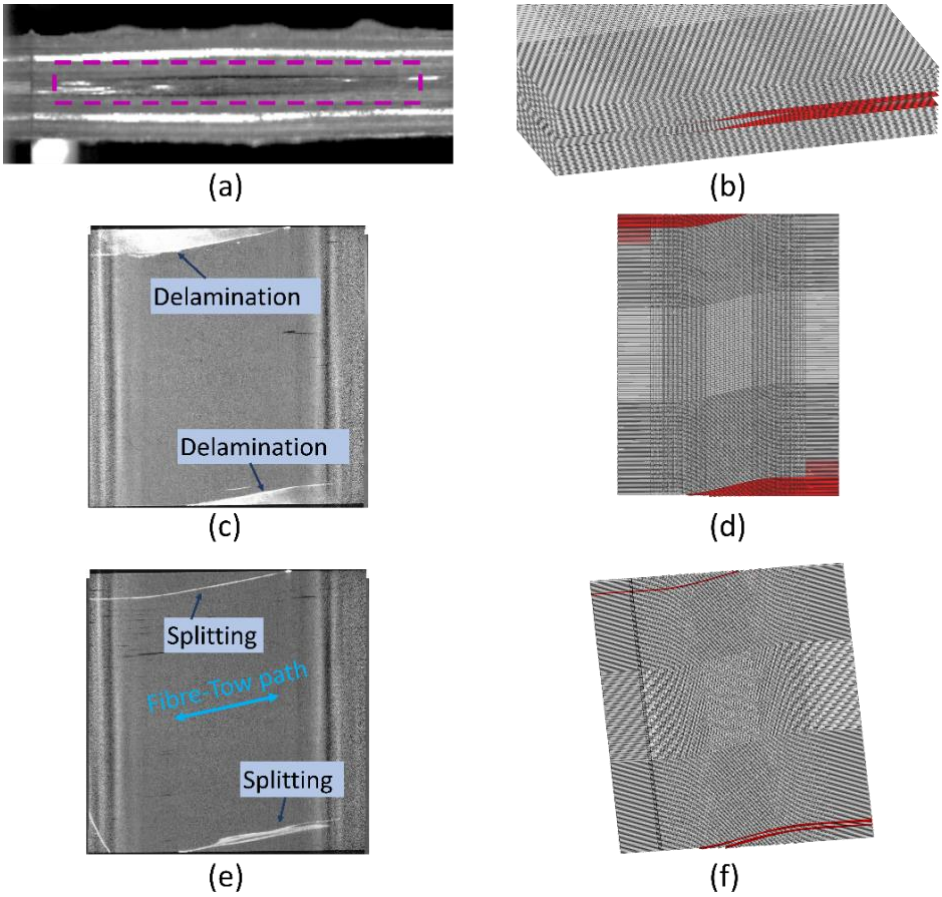

Figure 6.10 Comparison of tested and predicted failure modes from cohesive zone model for Level-1-Mid, (a) and (b) shows the delamination location from the edge view, (c) and (d) show the delamination at the interface between a wavy ply and its adjacent ply, whilst (e) and (f) show the tested and simulated splitting in the wavy ply. The red areas and curves in (b), (d) and (f) indicate the predicted damages.

II. Level-1-All & Level-2-Mid

Similar conclusions as for Level-1-Mid can be drawn for Level-1-All and Level-2-Mid, as shown in Figure 6.11 & Figure 6.12 respectively. In both cases, the delamination was initiated at the central interfaces (wavy plies vs. adjacent 45^{o} /135^{o} plies) and splitting existed within the central wavy plies, even though Level-1-All contained waviness in all 0^{o} plies. The models have exactly re-created these phenomena.

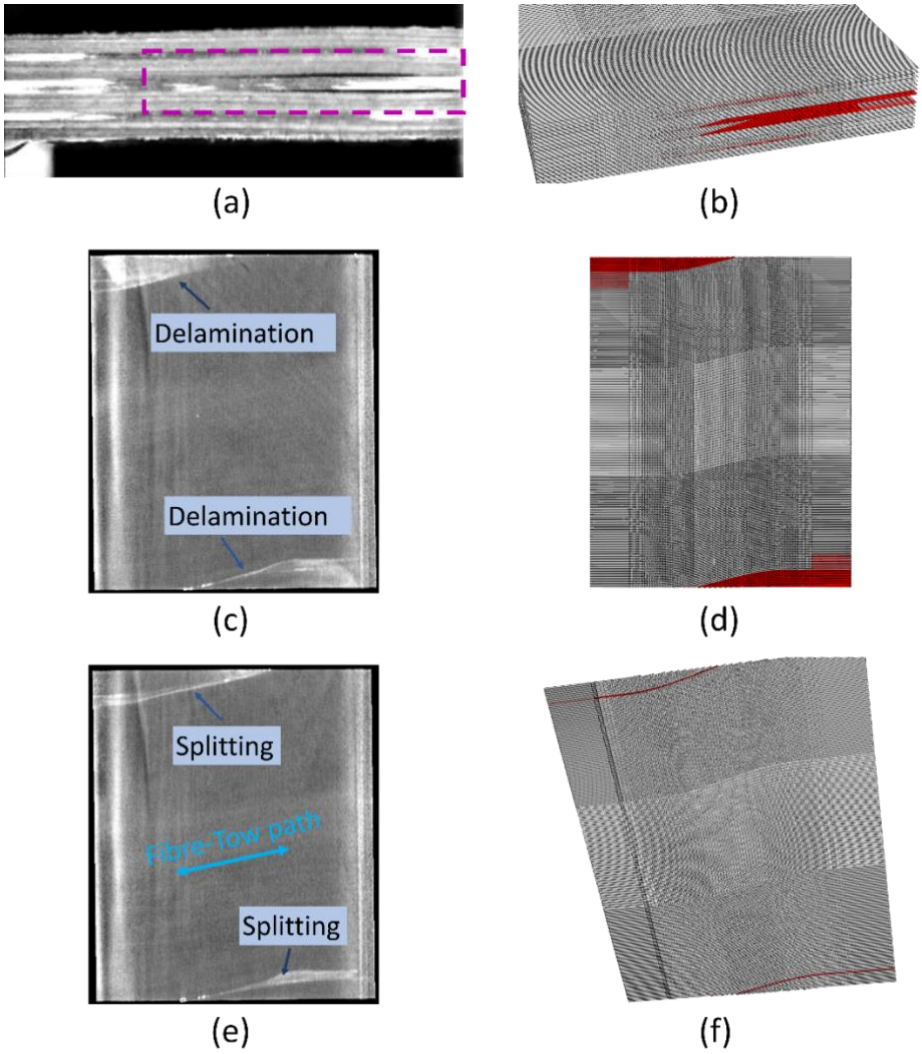

Figure 6.11 Comparison of tested and predicted failure modes from cohesive zone model for Level-1-All, (a) and (b) show the delamination location from the edge view, (c) and (d) show the delamination at the interface between a wavy ply and its adjacent ply, whilst (e) and (f) show the tested and simulated splitting in the wavy ply. The red areas and curves in (b), (d) and (f) indicate the predicted damages.

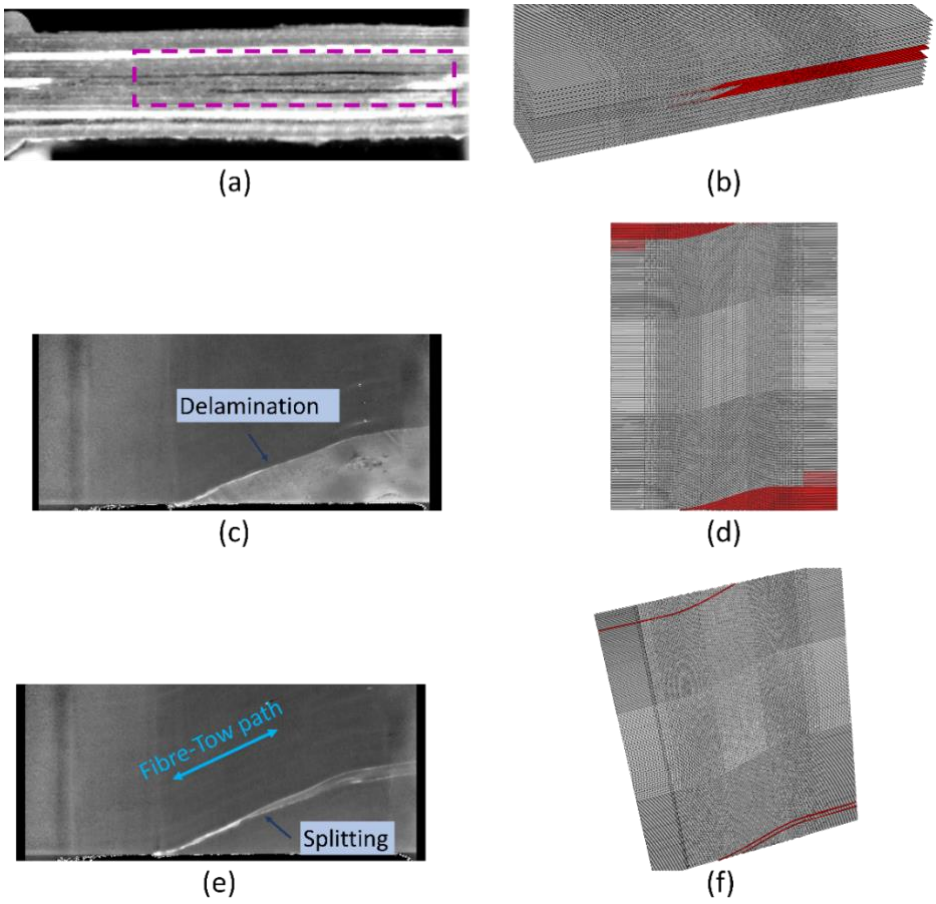

Figure 6.12 Comparison of tested and predicted failure modes from cohesive zone model for Level-2-Mid, (a) and (b) show the delamination location from the edge view, (c) and (d) show the delamination at the interface between a wavy ply and its adjacent ply, whilst (e) and (f) show the tested and simulated splitting in the wavy ply. The red areas and curves in (b), (d) and (f) indicate the predicted damages.

III. Level-2-All

The position is different for the Level-2-All case, in which the most severe waviness was introduced to all 0^o plies and fibre failure was observed to be another mechanism for triggering the damage. Figure 6.13 shows the comparison between test and model results. First, the delamination distributions from the side view also present good agreement, as labelled by the numbers on Figure 6.13 (a) and (b). However, due to the interaction with fibre failure, the predicted in-plane view for the delamination and splitting were not in good agreement when only cohesive elements provided failure modes. Figure 6.13 (c) and (e) are CT images recorded at the same moment before the ultimate failure in the experimental test. Due to the influence of fibre breakage, splitting formed a ‘branch’ shape and

the propagation of delamination followed the orientation of fibre failure, rather than the wavy path as in the other three cases. Figure 6.13 (d) and (f) are model images also from the same moment but immediately after the predicted peak point (predicted strength), showing the in-plane view of delamination and splitting that is clearly different from the experimental test results. However, Figure 6.13 (f) shows the trend of this 'branch' phenomenon; in general, due to the lack of a fibre-failure mechanism in the model, the 'branch' shape was not exactly predicted as the experimental recordings, and the modelled splitting (Figure 6.13 (f)) was also more serious than that captured by the CT image of the experimental test.

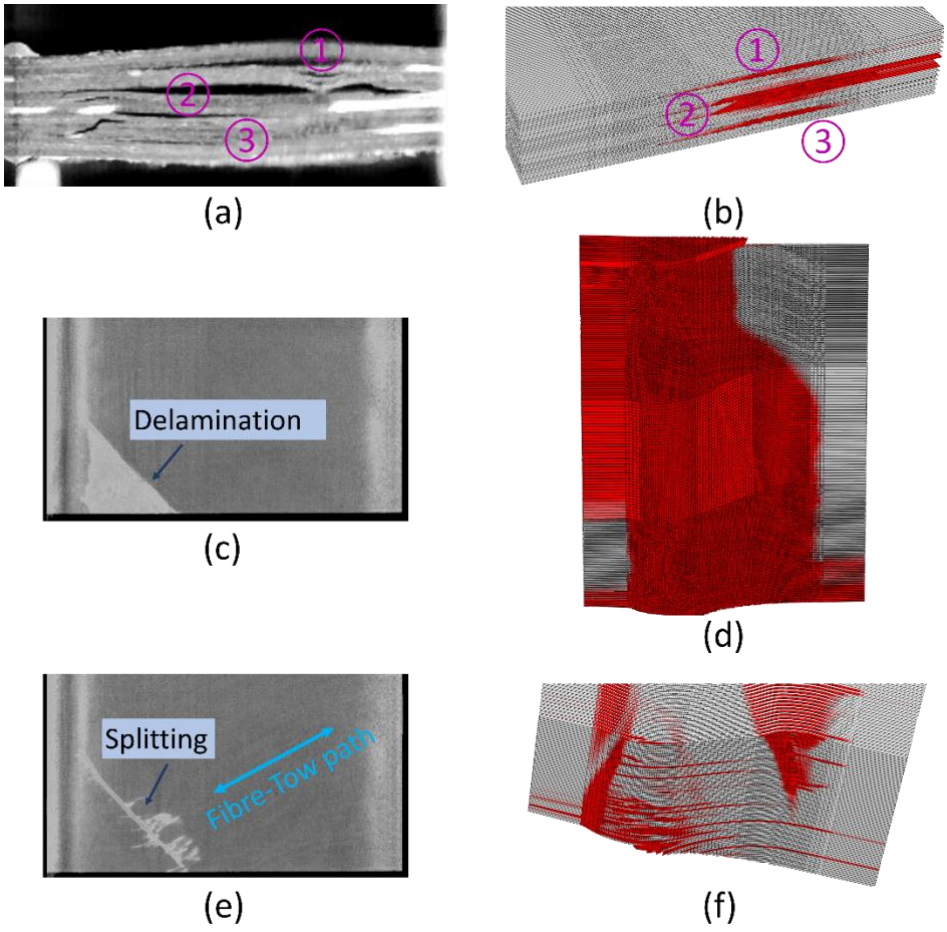

Figure 6.13 Comparison of tested and predicted failure modes from cohesive zone model for Level-2-All, (a) and (b) show the delamination location from the edge view, (c) and (d) show the delamination at the interface between a wavy ply and its adjacent ply, whilst (e) and (f) show the tested and simulated splitting in the wavy ply. The red areas and curves in (b), (d) and (f) indicate the predicted damages.

6.4.1.3 Discussion of failure mechanisms predicted by cohesive zone models

The inevitable terminated-fibre edge regions (Figure 6.14 (a)) caused by this waviness-introduction method might lead to an effect on the stress distributions during the loading process, and this stress would further influence the damage initiation and propagation. The detailed check of the growth process for delamination and splitting modes in the model (Figure 6.14 (b) and (c)) using Level-2-All as an example identified that the initiation of both modes was from the edge possessing the terminated fibres, with propagation following the wavy path as the load increased. For the other three models of Level-1-Mid to Level-2-Mid, this growth trend was also maintained until the computation was terminated. For the Level-2-All model, prior to reaching the peak load, delamination and splitting demonstrated this tendency but suddenly changed to a 'branch' shape of splitting and thorough delamination in that interface, once the global damage had been accumulated.

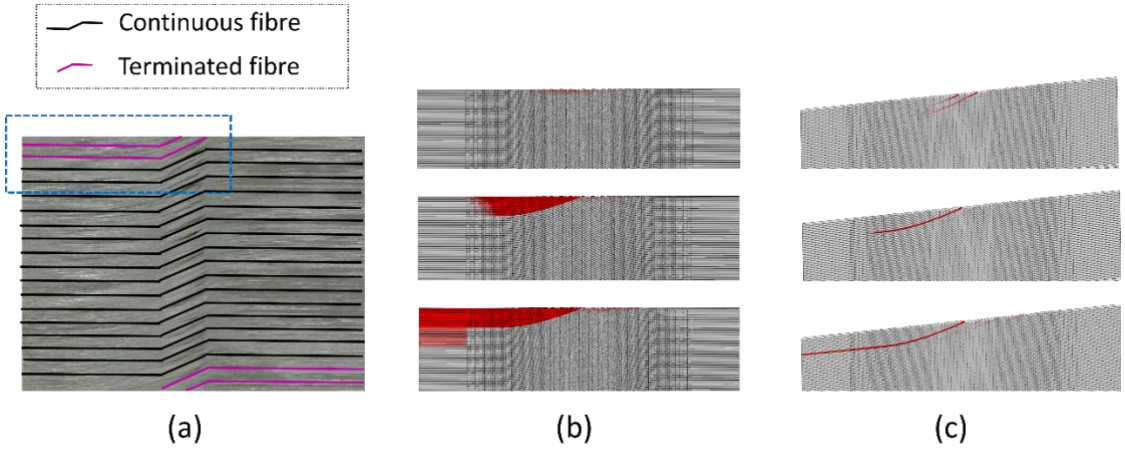

Figure 6.14 (a) Illustration of the area with non-continuous fibres (highlighted by a blue rectangle), whilst (b) and (c) show the predicted growth of delamination and splitting (Level-2-All as an example) within the blue-rectangle area in (a).

For a better understanding of the reason that failures initiated at the edge terminated-fibre regions, detailed checks of stress distributions have confirmed that the splitting within the wavy ply was caused by the in-plane longitudinal shear stress (S_{12}) generated due to the existence of fibre waviness. Figure 6.15 presents this shear-stress distributions, S_{13} which is labelled in Figure 6.15 (suffices 1 and 3 stand for the local directions on intralaminar cohesive elements and refer to the x and y directions

respectively, for the model [164]) on intralaminar cohesive elements (COH3D8) of the Level-2-All model. It indicates the highest shear stress was focused on the edge cut-fibre areas. Once the splitting was triggered, the concentrated stress would be released as the edge part separated from the ply. Checks of stress distribution on the other three level cases gave a similar conclusion. This might imply that the compressive failure of wavy specimens is dominated by the existence of cut-fibre areas, over the severity of in-plane waviness. The increase of knock-down in compressive strength (Table 5.2), as the waviness-severity increased, could be linked to the fibre angle at the edge-terminated fibre regions.

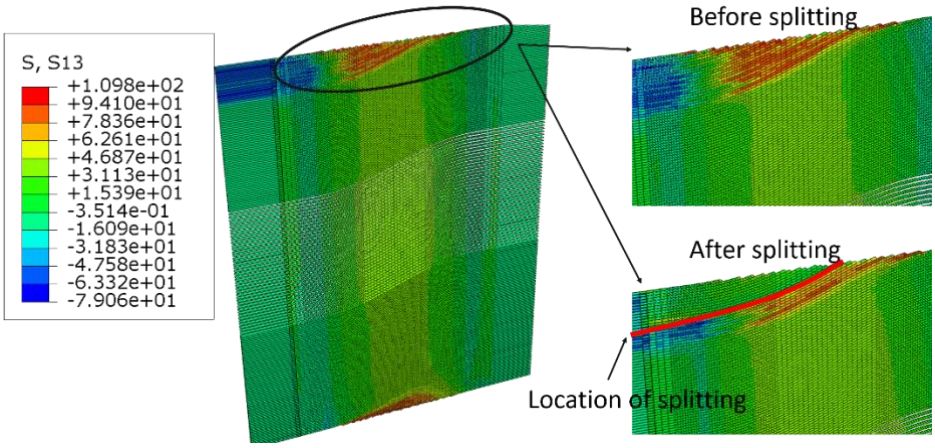

Figure 6.15 In-plane longitudinal shear stress distributions (labelled S_{13} means S_{12} for the model [164]) of Level-2-All on cohesive elements within wavy plies to simulate splitting.

6.4.1.4 Study of the sensitivity of results to cohesive zone model (CZM) mesh density

Finally, a mesh-sensitivity study was performed to confirm that a fine enough mesh density had been used for the CZM. For the models created in section 6.4.1, non-uniform mesh densities (Figure 6.2) were assigned, with the finest mesh density at the four corners being 0.1 mm × 0.1 mm where damages were initiated and the coarsest being 0.2 mm × 0.2 mm for other regions where waviness was introduced, to reduce the computation time. Since the skew-mesh depends on the waviness severity (in terms of both number of wavy plies and maximum waviness angle), this causes a slight difference in the total quantities of elements created for different severity levels (Level-1-Mid to Level-2-All). Here, the mesh-refinement study was carried out on the Level-2-All CZM, which

contained 918,060 elements as the baseline (non-uniform mesh distribution). Two uniform mesh-density distributions were created for the same Level-2-All model, their constant element size in the wavy region was 0.1 mm × 0.1 mm or 0.2 mm × 0.2 mm, to give comparative cases, resulting their element quantities being 1,298,260 and 349,080, respectively. Figure 6.16 plots the predicted curves of compressive stresses against displacements. The two curves of the baseline (918,060 elements) and a finer mesh (1,298,260 elements) almost overlap each other with nearly the same failure strength, while the predicted failure stress was a little higher when the mesh became coarse (349,080 elements). Therefore, this proved the mesh distribution used in this chapter (termed 'baseline') was at an acceptable size of elements to give an accurate prediction, within +/- 3.5%.

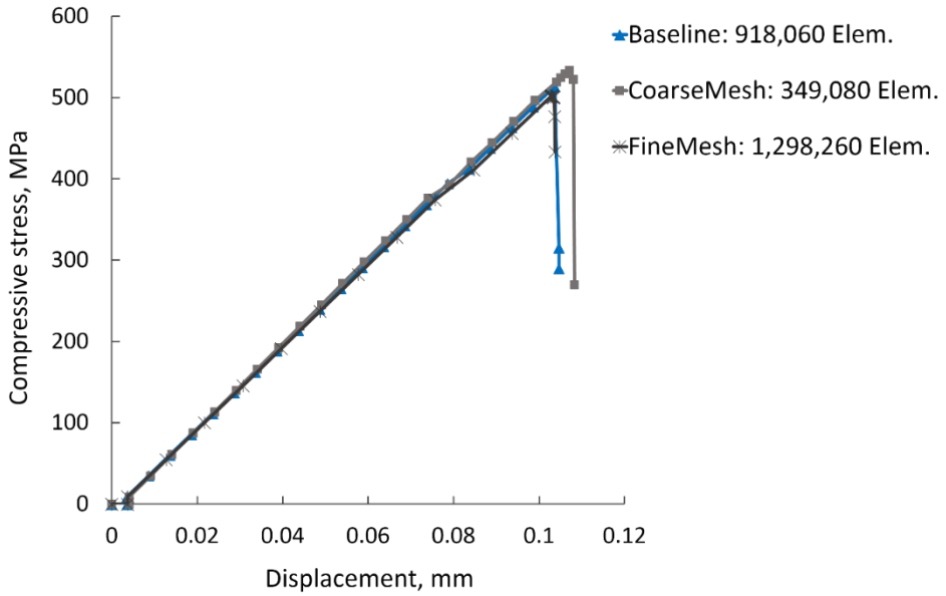

Figure 6.16 Mesh refinement studies based on the Level-2-All cohesive zone model. The graph shows the model-predicted stress as a function of applied compressive displacement and the sudden drop in stress indicates total failure. The three cases are identical except for the element sizes in the mesh.

6.4.2 Matrix cracking study

Although matrix cracking was not observed to be a major mechanism of failure in the experiments, it was still necessary to use modelling techniques to confirm that it is not important enough to have to include it in the models. Figure 6.17 plots the predicted stress vs. displacement curves for all four

waviness severity levels from either 1) the CZM method alone, or 2) CZM coupled with the matrix cracking mode. Matrix cracking was governed in the model by Puck's law [45][46] and fulfilled by VUMAT code from Mukhopadhyay et al. [1]. The details relating to this mechanism were presented in chapter 2. The overlapping pair of curves (Figure 6.17) predicted by the same waviness-severity models, with (symbols) or without (lines) matrix cracking coupled, clearly supported the negligible influence of matrix cracking on the compressive failures for Level-1-Mid to Level-2-Mid, in accordance with the experimental observations. As reported in Chapter 5 (Figure 5.16, Figure 5.18 and Figure 5.20), matrix cracking was not captured by high-speed camera, or only appeared in the high-speed photography when full failure had occurred. However, for the highest waviness severity (Level-2-All), experiment high-speed recordings (Figure 5.22) identified the existence of matrix cracking before the complete failure. This phenomenon was also predicted by the numerical models (Magenta curves in Figure 6.17 (b)). When matrix cracking was allowed in the model, the redistributed stress caused an over-distortion to some local elements, and thus terminated the model before the global damage has been accumulated.

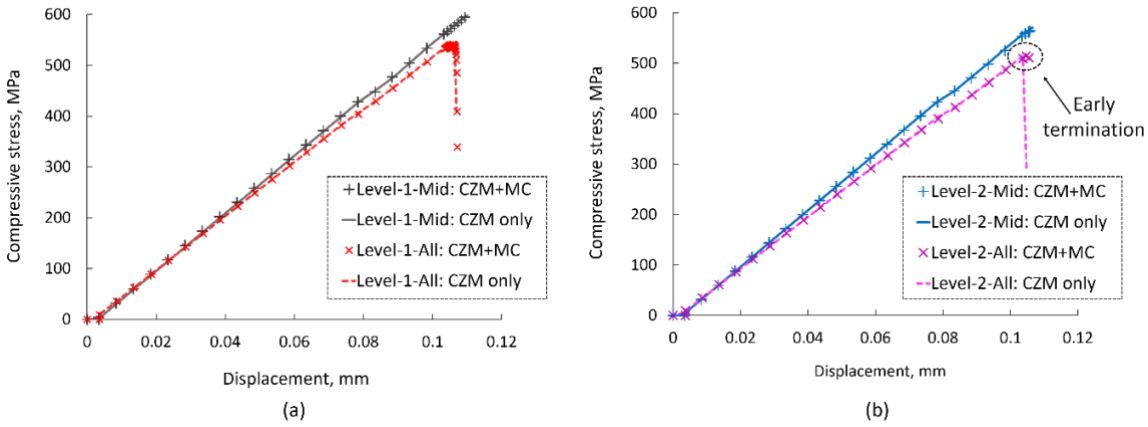

Figure 6.17 Predicted compressive stress vs. Displacement curves, from matrix cracking coupled with cohesive zone models (symbols) and from CZM-only models (lines), (a) Level-1-Mid and Level-1-All, (b) Level-2-Mid and Level-2-All.

Considering that the predicted stress magnitude at early termination due to matrix cracking is comparable to the prediction from the CZM-only model for Level-2-All, and taking account of the insignificant influence from matrix cracking to the other three models (Level-1-Mid to Level-2-Mid),

it could be concluded that the models with embedded cohesive zones, but no matrix cracking, were capable of capturing and estimating the failure process of laminates with manually introduced in-plane waviness, at least up to the Level-2-Mid severity.

6.4.3 Fibre-kink failure study

6.4.3.1 S_{11} stress in CZM only models

In respect of the CZM only model in 6.4.1, Figure 6.18 shows the predicted S_{11} (along-fibre stress) of one wavy ply of the Level-1-Mid and Level-2-All cases, before and after the initiation of delamination and splitting. In the experimental work on these two levels (Level-1-Mid and Level-2-All), fibre failure was reported to be initiated from the edge and accompanied by the delamination and splitting in the coupons. The predicted maximum stress in the wavy ply, S_{11}, was both above the fibre direction compressive strength of 1690 MPa [10] at the moment when delamination and splitting were triggered. This raises the significant possibility that fibre failure could occur along with delamination and splitting simultaneously; hence, the kink mechanism [50][61] was also included, along with the CZM model in the analysis, aiming to capture this fibre failure.

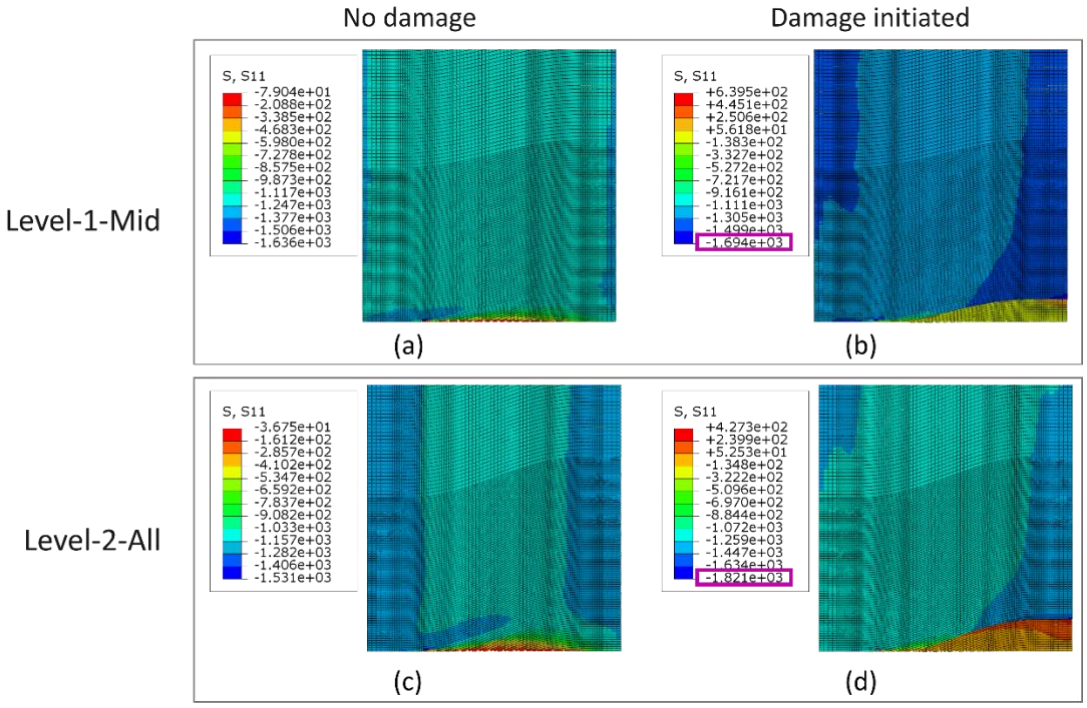

Figure 6.18 Predicted stress distributions (S_{11}) of a wavy ply of Level-1-Mid ((a) &(b)) and Level-2-All ((c) &(d)) by the CZM-only model, (a) and (c) were captured before the initiation of delamination or splitting, while (b) and (d) were the moments after the initiation of damage.

6.4.3.2 Addition of progressive fibre-damage model

As stated above, fibre failure could also be an important mechanism accounting for compressive failure. Hence, models with CZM coupled with a fibre-failure mechanism were created here to investigate the ability to predict this mode and the potential benefit. This failure prediction was realised by the fibre-kink mechanism [50][61] coded as a VUMAT[1], as used for the estimation of wrinkles in Chapter 4, and embedded into wavy plies (part or all 0^o plies).

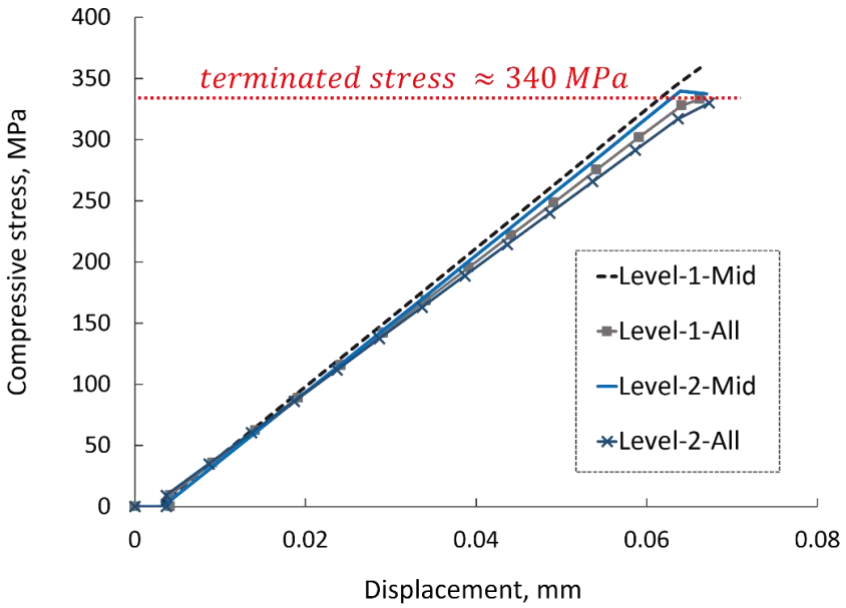

Figure 6.19 Predicted compressive stress vs. displacement curves from fibre failure coupled with CZM models of four level cases.

Figure 6.19 plots the predicted curves of compressive stress against displacement for each level case, when the CZM model is coupled with the fibre-kink mechanism. All the models were terminated automatically at around 340 MPa, which is far lower than the experimental failure values for each case. This might show the inability of kink mechanism to accurately predict the fibre failures in this in-plane waviness model. The early over-distortion of elements terminated the computation, which could be caused by the inherent sensitivity of first-order hexahedral elements (C3D8R) to the initial skewed element shape [165], in addition, the full integration has also been exercised and gave the similar situation as reduced elements behaved. In the wavy plies, the elements had been initially sheared to be skewed so that they followed the fibre tows through the waviness. This skewness was even more severe for the elements in the edge termination regions (Figure 6.5 (b)). The high stress in those regions (Figure 6.15) leads to local damage in cohesive elements between fibres. The stresses on damaged elements are then redistributed to the surroundings (solid or cohesive elements), which increases the stresses of the nearby solid elements with fibre-kink failure mechanism included. The local damage on the solid elements through fibre failure would further increase the surrounding stress field, and, consequently, could lead to excessive distortion. Figure 6.20 illustrates the shear stress

(labelled S_{13} means S_{12} for the model) comparisons from CZM only models (a) and (b) and CZM / kink-mechanism 'coupled' models (c) and (d), to support this explanation. Before any damage was triggered, models (a) and (c) gave similar distributions for S_{12} (ranging from approximately -60 MPa to approximately +107 MPa). As fibre failure was initiated, (note that damage in cohesive elements was also initiated), Figure 6.20 (c) and Figure 6.20 (d) show differences. The negative shear stress around the fibre-failure region in the coupled model (Figure 6.20 (d)) has been released, as captured in the experiment (Figure 6.13 (e)), thus showing a similar negative stress value (approximately -66 MPa) to the condition before the damage was triggered - Figure 6.20 (c). By comparison, the splitting in the CZM-only model (Figure 6.20 (b)) was triggered at a much higher displacement than that in the coupled model and could withstand a higher negative stress (approximately -84 MPa). This provided evidence that the existence of fibre failure could pre-trigger the damage in cohesive elements. A further check of the locations of the excessively distorted elements causing termination of the computations, which were in the interface layers (COH3D8) with the skew mesh and connected to the wavy plies (with fibre failure allowed), also supported this explanation. In general, the specific terminated edges caused the model to be unstable, and this instability further led to the loss of efficiency in the kink-mechanism coupled CZM model to accurately predict the fibre failure.

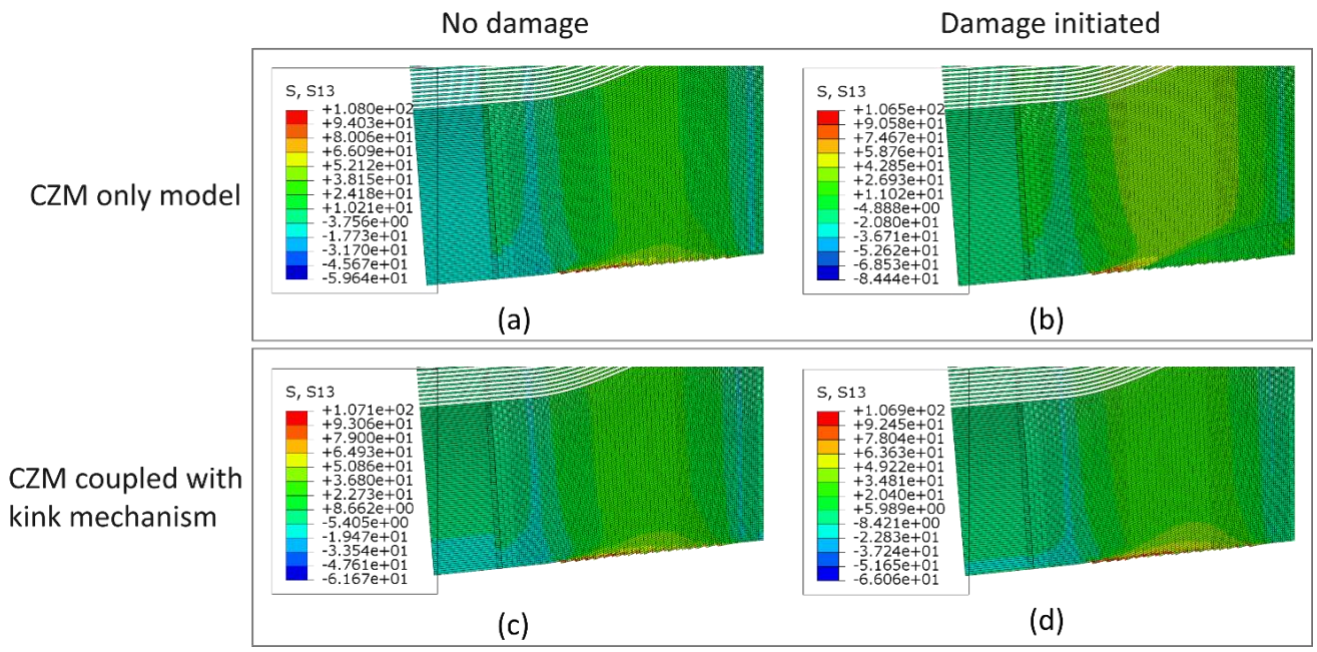

Figure 6.20 Shear stress distributions (labelled S_{13} means S_{12} for the model) of Level-2-All on intralaminar cohesive elements, predicted by (a) and (b) for the CZM-only model at the moments when no damage and splitting was triggered, and by (c) and (d) for the CZM coupled with fibre-kink mechanism. (c) was at the same moment as (a), (d) was at the moment when fibre failure was initiated.

6.4.4 Discussion

In this section the model is used to study the effect of the tied constraint on the model stability and the influence of waviness on failure modes and mechanisms in a way that cannot easily be done experimentally using real samples. It is a deviation from the experimental coupons of Chapter 5, which had edges and terminated fibres.

6.4.4.1 Influence of Tied constraint set-up

Since the critical elements causing the early termination of computation in the models above were on the skew-mesh interface layers, the tied constraint setup was investigated as the potential cause. The tie was modified such that the mesh on the interface adjacent to the wavy plies was retained to be a rectangular-mesh rather than a skew mesh and the surface-based tied constraint was assigned between this interface and wavy plies, with a master surface set up on the wavy plies (Figure 6.21). The results showed that the critical elements were still on those interface layers with tie-constraint and the model

also had an early termination (between 300 MPa and 400 MPa), once the fibre-failure mechanism was included, even when the tie setup was changed. This suggested the instability of models might not be attributed to the tied-constraint set-up.

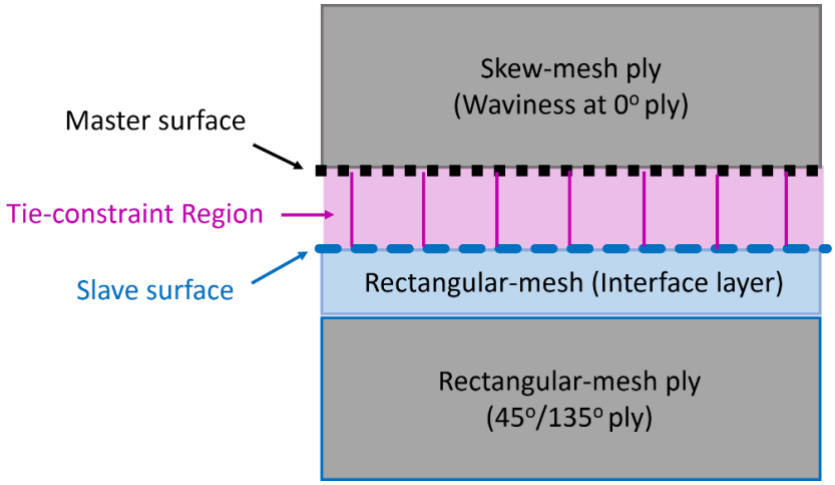

Figure 6.21 The illustration of the new tie-constraint set-up between the rectangular-mesh COH layer and skew-mesh wavy ply.

When the master surface was assigned to the wavy ply, it made this independent of other plies and potentially able to behave like the unidirectional material [10]. Thus, although the accuracy of the prediction for the failure strength could not be improved, the shape for fibre failure predictions in Level-2-All model became a bit closer to that of the tests shown in Figure 6.22, in which the inclined fibre failure path and its 'branch' shape connected to the splitting are in trend.

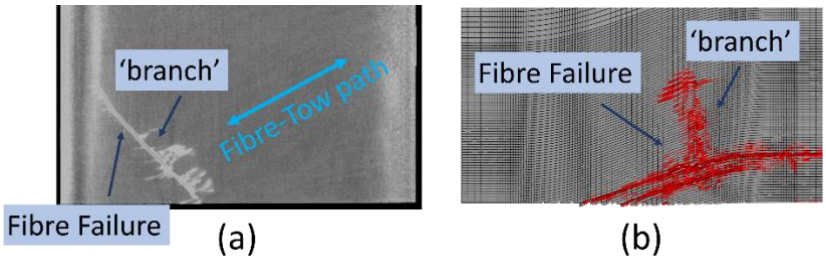

Figure 6.22 The comparison of tested (a) and predicted (b) fibre failure on Level-2-All case, with the new tie-constraint set up in the model.

6.4.4.2 Influence of specimen edges including periodic boundary conditions (PBCs)

It has been shown that the high stress that triggered the damage was located at the edge fibre-terminated region (Figure 6.15), rather than at the maximum wavy-angle region in the middle or within the left/right maximum-curvature areas (Figure 6.23). This implies the possibility that the edge effect from this specific fibre-terminated region is the key factor to cause the subsequent damage. In order to explore the influence of the terminated fibres it is necessary to try to remove them from the model. Therefore, to simulate a continuous plate without edge effects and remove the stress concentrations that exist around the fibre terminated region, periodic boundary conditions (PBCs) were added to the model using linear constraints between the top/bottom nodes for the translational degrees of freedom in Abaqus/Explicit [166].

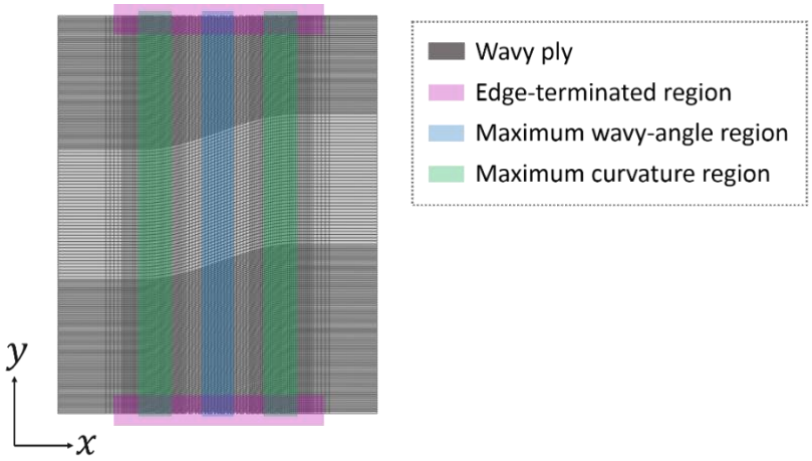

Figure 6.23 The illustration of three representative regions within the wavy ply.

Figure 6.24 illustrates the constraint equations defined for each top-bottom pair of nodes for the whole model and the equations assigned to the models to realise this aim are through

$$u_1^A - u_1^B = 0 \tag{6.2}$$

$$u_2^A - u_2^B = 0 \tag{6.3}$$

$$u_3^A - u_3^B = 0 \tag{6.4}$$

where A and B stands for the corresponding nodes of each pair on the top and bottom edges; subscript 1, 2 or 3 means the translational degree of freedom in x, y or z direction respectively; for example, u_2 is the displacement in the y direction.

A pre-process was applied to the skew-mesh plies to remove terminated fibres at the top and bottom, in order to match the top and bottom edges with no fibres cut or terminated.

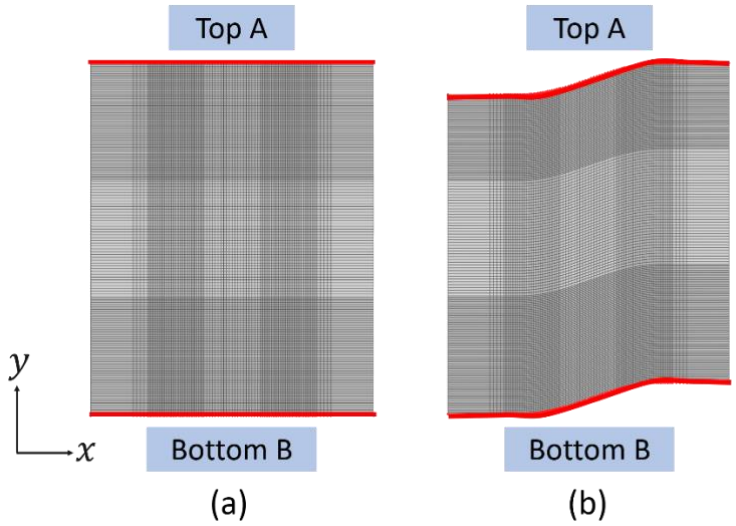

Figure 6.24 The illustration of defining the periodic boundary conditions (PBCs) at the upper/lower edge, (a) rectangular-mesh model, (b) skew-mesh model.

Once the linear constraint equations were defined on the CZM/matrix cracking/kink-mechanism 'coupled' models, the failure for the *pristine* model was transformed from a delamination accompanied by a slight fibre failure, to severe fibre failure in the 0^o plies and delamination at the adjacent interface layers (Figure 6.25). The originated damage locations were also changed from top-left corner (bottom image in Figure 6.25 (a)) when PBCs were not used, to the middle region along the left edge (bottom image in Figure 6.25 (b)) when PBCs were defined. This is because, when PBCs were assigned to the model, the edge effects on the top/bottom edges (Figure 6.24) have been removed; then the straight fibres can carry more of the applied load to reach the point that triggers the fibre failure. However, since the left/right edges still have some edge effects as being the load applied area, the damage in both situations, either PBCs included or not, is initiated in a region close to the load-applied edges.

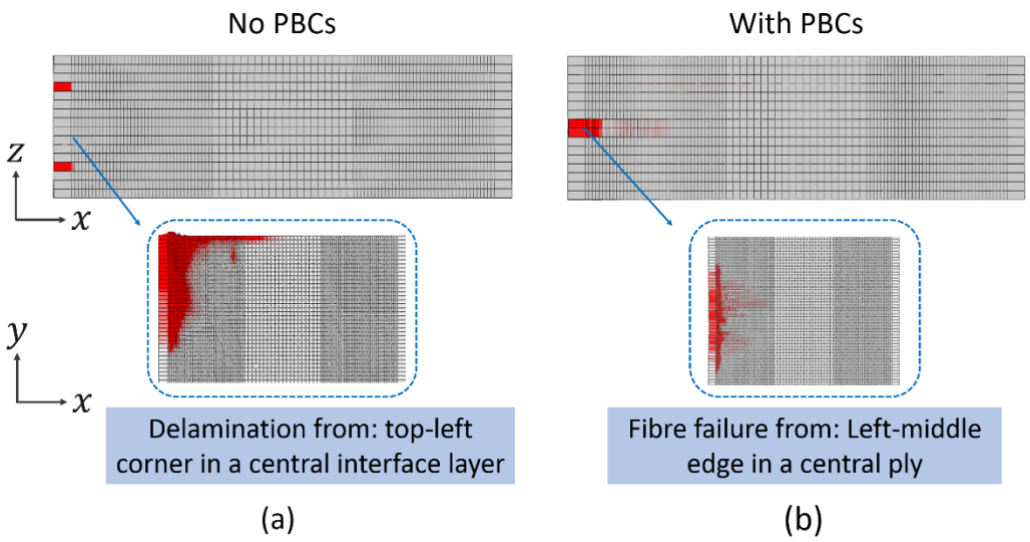

Figure 6.25 The top side-view (x, z) images showing the comparison of predicted fibre failure of Pristine model and the bottom in-plane view (x, y) indicating the damage initiation locations, (a) without PBCs, (b) with PBCs. The red areas of the bottom image in (a) represent the delamination, and red areas in other three images are fibre failure damages.

When the PBCs were assigned to models containing waviness, also due to the removal of the edge effects, the predicted failure locations have been moved from the terminated-fibre regions as discussed in the previous subsection 6.4.1, to the central region of a wavy ply for fibre failure and splitting, or to the interface layer adjacent to the central wavy ply for delamination, as shown in Figure 6.26. It is clear that when PBCs are defined, the damage-initiation region is the area which contains the maximum waviness angle (blue area in Figure 6.23). This is reasonable as this area should have higher shear stress due to the wavy fibres, which could then trigger the fibre failure and splitting, as well as the delamination. Figure 6.26 uses the Level-2-Mid case as an example but the other three cases showed similar damage modes and locations. It should be noted that, although two cases contain waviness in all four 0° plies, their predictions of damage events and locations are still dominated by the inner wavy pies, not by the two outer wavy plies. Therefore, from this study, it proves that the edge effects in the experimental test coupons and original models without PBCs have a critical role to trigger the damage, as presented in chapter 5 and in the models as discussed in previous sections of this chapter.

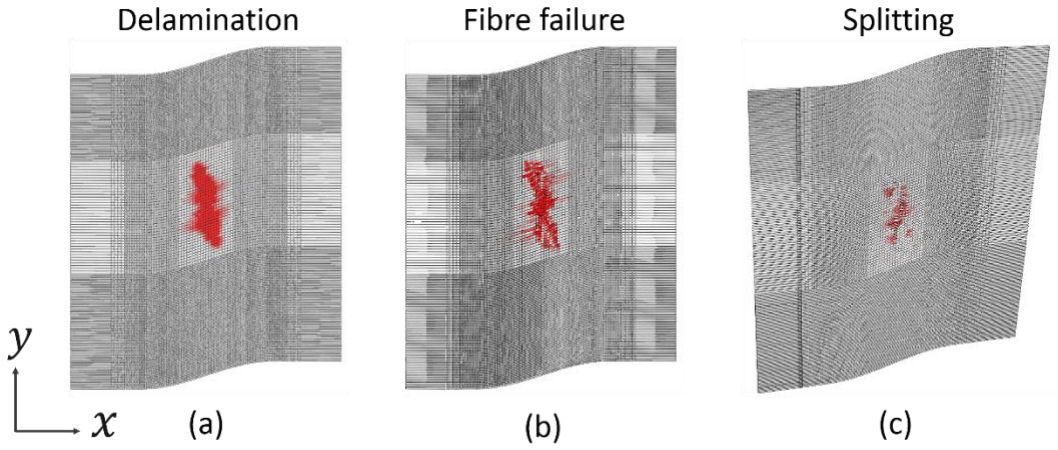

Figure 6.26 The in-plane view (x, y) images showing the predicted failures at the central wavy ply or at the interface layer adjacent to the central ply, of Level-2-Mid model when PBCs are defined, (a) delamination, (b) fibre failure, (c) splitting with a little manual image rotation for a clear image (i.e. this is not rotation occurring in the modelling). The red areas in each image indicate the damage locations of the related failure type.

The stress at termination for the waviness models with PBCs, and the peak failure stress for the pristine model with PBCs, are listed in Table 6.3. Previously reported results from CZM/kink-mechanism 'coupled' models without PBCs (Figure 6.19) and mean values of experimental failure stress of each case are also listed in Table 6.3. The pristine result predicted by the non-PBCs model in Table 6.3 is taken from Table 6.2. It clearly indicates that all the predictions show higher failure stresses as a result of assigning PBCs to the models to remove the artificial edge effects. In addition, compared to the predicted value of the pristine model with PBCs, predicted knockdown in each waviness model case with PBCs has been recorded due to the different waviness severities that could cause the shear stress. Hence, it could be concluded that the waviness itself has a significant negative influence on the compressive failure performance, once the artificial edge effects have been removed by PBCs.

Table 6.3 Maximum compressive stresses predicted by CZM/matrix cracking/kink-mechanism 'coupled' models when PBCs defined, predicted maximum stresses by CZM/kink-mechanism 'coupled' models without PBCs (from Figure 6.19) and experimentally tested values for each case. The pristine result predicted by the non-PBCs model is taken from Table 6.2.

Maximum compressive stress		**Pristine**	**Level-1-Mid**	**Level-1-All**	**Level-2-Mid**	**Level-2-All**
Mean Experimental failure stress	MPa	662.2	589.6	529.8	506.8	450.6
Knockdown based on Pristine Sample	%		**11**	**20**	**23**	**32**
Non-PBCs Model Predicted max. stress	MPa	624.7[5]	358.6	333.1	339.7	330.0
Knockdown based on Pristine Model without PBCs	%		**43**	**47**	**46**	**47**
PBCs Model Predicted max. stress	MPa	1031.1[6]	730.2	650.0	695.3	608.8
Knockdown based on Pristine Model with PBCs	%		**29**	**37**	**33**	**41**

Before moving to the conclusion of this PBCs subsection, it is necessary to check the stress distribution along the width (y) direction. In theory, once PBCs are assigned, the stress should be uniform in the y direction and a narrower model should also have the similar trend. Here, as shown in Figure 6.27, the in-plane shear stress (s_{12}) almost remains uniform along the width direction. However, there are some variations between different regions as labelled in Figure 6.27, which is probably caused by the different mesh refinement distributions as shown in Figure 6.1(c). In fact, the stress distributions in Region 1 and Region 3 are almost the same, as the mesh refinement in these two

[5] Predicted peak (failure) stress by the pristine model without PBCs defined.
[6] Predicted peak (failure) stress by the pristine model with PBCs defined.

regions are similar. In addition, if just focusing on a single region in Figure 6.27 (for example just Region 2), it might be regarded as a reduced-width model with PBCs but retains a uniform stress distribution in the width direction, as expected. However, a fuller study to create models with completely uniform mesh distributions and variation in width was considered beyond the scope of the current thesis as the models presented here are sufficient to highlight the limitations of a finite width specimen. More extensive studies and specimen redesign should be carried out in the future.

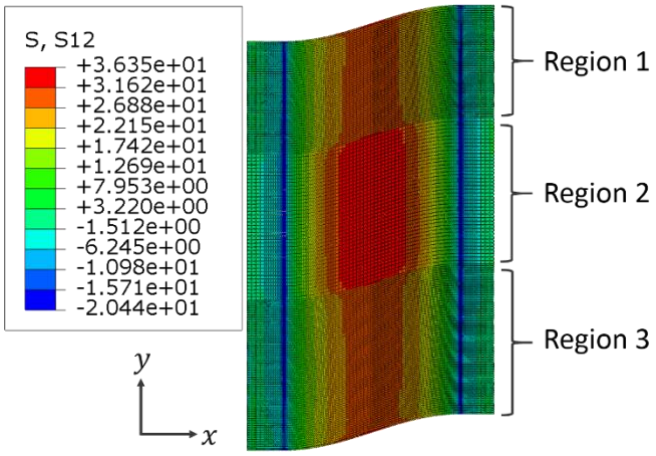

Figure 6.27 The in-plane view (x, y) image showing the in-plane shear stress distribution in one moment during the loading process, in the central wavy ply of Level-2-Mid model when PBCs are defined. Three regions are labelled along width (y) direction to identify the different uniform stress distribution areas.

From the PBCs investigation above, it could be concluded that the manually introduced edge effect is an artificial factor in causing the ultimate failure, as it introduces a stress concentration at the terminated fibre regions. As a consequence, this study reduces the realism of what has been obtained through experimental study presented in chapter 5, in terms of guidance about the effect on compressive failure performance of in-plane waviness, since the waviness in reality would almost be located inside components, rather than at the edges. For the waviness itself, its severity also affects the failure stress knockdown due to the in-plane shear stress caused by the wavy fibres, when artificial edge effects are supressed by PBCs. As a whole, it suggests a necessity of the further study with the more realistic waviness in the future.

6.4.4.3 Assumption of uniform FVF

As mentioned above, the FVF was assumed to be consistent within the wavy ply in the model, its local variation during the waviness formation process was neglected. However, as illustrated in Figure 6.28, due to the shearing movement that was required to deliberately introduce the waviness, the same fibre quantity would be distributed in a narrower area, from the grey-background region to the green area, neglecting the curved-fibre regions. Hence, the new local maximum FVF could be estimated by

$$FVF_{local} = FVF_{nom} \times (\frac{aw}{awcos\theta}) \quad (6.5)$$

The local FVF is related to the nominal FVF by the maximum waviness angle, assuming that thickness remains constant. This local FVF variance could have an effect on the ultimate failure stress but, considering the validation that the FVF influence on failure stress levels was less than 4% in the out-of-plane waviness case, as discussed in Chapter 4, and the experimentally introduced in-plane waviness angles for the four cases were between 13^o and 20^o (Table 5.1) that would cause an increase in local FVF above the nominal FVF (57.7%) [148] of 2.6% for 13^o and 6.4% for 20^o. It seems that this uniform-FVF assumption is reasonable. Following the same procedures as explained in Chapter 3 and using the same material properties in Table 3.3 for the 'pseudo' material which has the nominal FVF at 60%, two pairs of CZM / kink-mechanism 'coupled' models (A5 &A10) were created for each waviness angle case, 13^o or 20^o. In each pair models, one was defined with the material properties at the nominal FVF (60%), while the other model was assigned the high-FVF properties to the wavy plies that was calculated when FVF increasing by 2.6% to 62% (13^o case) or by 6.4% to 64% (20^o case), with rest plies keeping unchanged at 60% FVF. The predicted results are displayed in Table 6.4, it suggests again the influence of FVF when in-plane waviness is introduced in the way of Figure 6.28 is not that significant on the compressive stress, within +/- 4.0%.

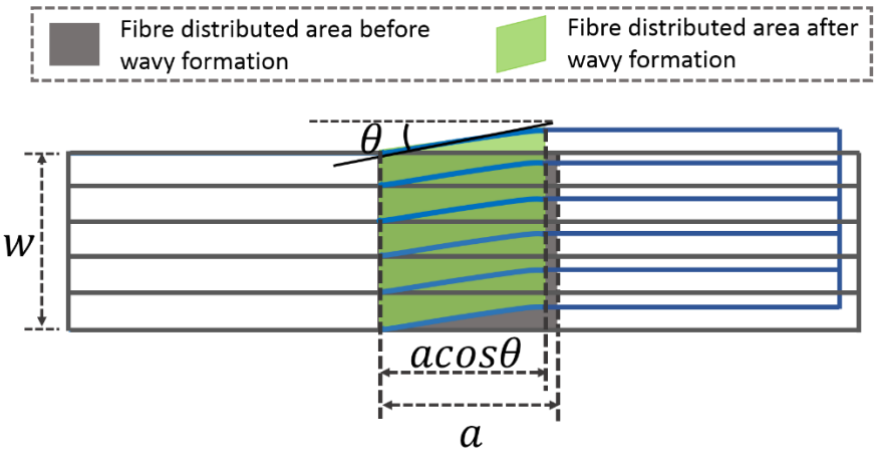

Figure 6.28 Illustration of fibre distributions within the wavy region before and after waviness was formed.

Table 6.4 Comparisons of failure-stress predictions from CZM / kink-mechanism 'coupled' models when assuming FVF was or was not changed for the A5 and A10 cases, respectively.

Unit: MPa	**A5 Case, $\theta = 13°$**		**A10 Case, $\theta = 20°$**	
FVF	60%	62%	60%	64%
Predicted Failure stress (MPa)	343	348	263	253
Percentage failure-stress change w.r.t[7] 60% FVF (%)		**1.4%**		**-4.0%**

Therefore, the uniform FVF assumption during the in-plane waviness model creation was considered to be appropriate for the performance predictions with the current experimental limitations.

6.5 Summary

Further to the experimental study for compressive failures caused by in-plane waviness described in Chapter 5, a numerical study has been described in this chapter. The manually introduced kink-shape in the experiment was replicated as a skew-mesh in the model. A surface-base tied constraint was created to accommodate the mesh density transition between rectangular-mesh and skew-mesh. Intralaminar cohesive elements were inserted into the wavy ply to allow the splitting, as well as the

[7] w.r.t: abbreviation for 'with respect to'.

cohesive elements at interfaces for simulating delamination. The model predictions confirmed the experimental conclusions, namely that delamination and splitting were the major modes causing the ultimate failure when the in-plane waviness was contained.

The CZM only model has the capability to accurately predict the location, shape, and propagation path for the experimental failure modes: delamination and splitting. The addition of the matrix cracking failure mode to the CZM model confirmed the insignificant effect of matrix cracking in the non-wavy plies in accordance with the test results. When the fibre-kink failure mechanism was added, the model became unstable and the computation was terminated early due to the influence of edge fibre-terminated regions. In addition, due to the effect of this fibre-terminated region, none of the model types could accurately predict the failure strength for every waviness-severity case against the testing levels. However, the CZM-only model could give a prediction for the failure strength with a difference from the experimental results of less than 15% for all waviness severity samples simulated.

Detailed checks of stress distributions in the model suggested the in-plane shear stress (s_{12}) was critical to the damage (splitting and delamination) and that this high stress was concentrated at the wavy-ply edges where the continuous fibres were terminated. Taking the simulation beyond what had been investigated experimentally, further investigations were performed to explore the influence of the waviness on the failures. This was achieved using periodic boundary conditions to remove the stress concentration around terminated fibre regions at the edge. The models indicated that the artificial edge effect around the terminated fibres was the key factor controlling the ultimate failure. When this edge effect has been removed through PBCs, the study suggested that the waviness severity itself also had effects on the failure stress knockdown due to the shear stress caused by the wavy fibres.

Chapter 7
Conclusions and future work directions

7.1 Conclusions

The main objective of this PhD research project was to bridge the gap between non-destructive detection of out-of-plane and in-plane wrinkles in composites and understanding their effect on performance of a component. The basis of the solution is to transfer 3D NDT-characterisation data on wrinkles into finite-element models, thus integrating the advantages of NDT methods that provide internal as-manufactured structural details with numerical modelling techniques that possess the capability to determine strength and predict the damage and failure-mode details. This will reduce future experimental workload at the design stage and provide otherwise-inaccessible information in the situation where the damage process is difficult to observe or capture experimentally. Model creation based on structural NDT information incorporates specific geometrical details closer to those actually existing in the composite components and can thus give more accurate performance predictions and simplified assumptions. Another advantage is that the deep and thorough understanding of the failure process developed through modelling the effects of wrinkles mean that the key wrinkle parameters governing composite failure can be explored and this can guide NDT measurement strategies to capture the key metrics of wrinkles.

The manufacturing imperfections of interest - fibre misalignments in the form of both out-of-plane wrinkles and in-plane waviness - were investigated numerically by creating finite-element models using simulated NDT data to govern the geometry, conveniently separating the transfer-process and modelling work of this project from the NDT data acquisition and analysis, which is beyond the scope of the project. This well-controlled and rapid method for NDT-data simulation and model generation allowed a comprehensive parametric study to be conducted, exploring a wide range of wrinkle geometries and metrics for out-of-plane wrinkles. In the case of in-plane waviness, new modelling methods were explored and refined by comparison with results of an extensive experimental

programme. The common industry-used quasi-isotropic layup was chosen: $[45^o_2/90^o_2/-45^o_2/0^o_2]_{3s}$ for the out-of-plane wrinkle investigations and $[45^o_2/90^o_2/-45^o_2/0^o_2]_{2s}$ for the in-plane waviness study. All the research was carried out using the IM7/8852 prepreg from Hexcel [148]. A summary and the main conclusions are given below in the sequence in which they appear in the main chapters of this thesis.

1) A Matlab-based transfer process was developed to automatically transfer the inverted NDT information into finite-element models. This involved interpretation of the information in terms of local ply geometry and in-plane fibre orientation, creation of an appropriate mesh and assignment of failure-mode capability to elements in plies and ply interfaces. The modelling of failure modes was based on previous numerical studies for out-of-plane wrinkles coded and validated experimentally by Mukhopadhyay et al. [1]. The inverted NDT data was generated by a Matlab-based simulator of wrinkled composite laminates, which created two 3D material-property maps defining 1) the locations of ply interfaces (Map-A) and 2) local fibre alignments (Map-B). Out-of-plane wrinkles thus could be recorded by Map-A and in-plane waviness was reflected by Map-B. During the automatic model-creation process, a 0.01 mm-thick resin-rich layer of cohesive elements was inserted at each interface and the ply-thickness was adjusted to keep the total model thickness in accordance with the component. The investigations showed that a uniform fibre volume fraction assumption during the transfer process was reasonable, within the current limits of experimental validation, although a more refined assumption is recommended for future models as modelling and experimental methods converge. Finally, a 5-step automatic NDT-to-Model transfer process was described, with the appropriate assumptions, and this process was provided with a Graphical User Interface (Appendix A) and used in the model-creation for the wrinkle and waviness studies.
2) The modelling techniques were exercised repeatedly using the simulator and the 5-step transfer process to perform a study of the interdependencies of wrinkle parameters that have a governing influence on the composite's compressive strength. Certain models in the study were validated by comparison with the experimental work conducted by Mukhopadhyay et al.

[1]. The multi-dimensional parametric study was focused on three aspects of wrinkle defects: (1) wrinkle severity; (2) wrinkle shape; and (3) wrinkle extent. The wrinkled profile was simulated using a Gaussian-governed cosine or sine shape to provide a systematic method of isolating the effects of different parameters. Thus, six main parameters (amplitude, wavelength, maximum wrinkle angle and three Gaussian half-width parameters in the three dimensions) were studied and analysed to identify a hierarchy of wrinkle-parameter importance. The study concluded that maximum wrinkle angle is the most critical measurement but that, at high angles, wrinkle wavelength becomes important. The greater the extent of the wrinkle, as a proportion of the component cross-section perpendicular to the load, the larger the knock-down in compressive strength but a small extent in the load direction causes a higher stress concentration and larger knock-down in strength. Further to these conclusions, guidance for the basic NDT measurement requirements has been suggested.

3) In addition to the out-of-plane wrinkles, in-plane waviness was investigated using experiment and numerical modelling. A specially-designed rig was used to manually introduce waviness into 0^o plies in an experimental laminate. An initial investigation indicated that the key influences on introducing high-quality in-plane waviness were: the temperature above which the resin viscosity reduces, the friction between the lamina and the rig, and the shear-movement region of lamina being cut into appropriate-width strips to reduce buckling effects. For the full-laminate static-compression test, two high-speed video cameras were set up focusing on the edge and face of the gauge region (20mm × 25mm × 4mm) to capture the damage sequences near the moment of sudden catastrophic failure. After initial trials, some tests were halted at certain stages prior to the expected failure and a penetrant-enhanced X-ray CT technique was applied to identify the internal damage mechanisms before the ultimate damage. The experimental recordings suggested that delamination at the interfaces adjacent to the waviness ply and intralaminar splits within the wavy ply are the two major mechanisms accounting for the compressive failure with in-plane waviness.

4) Further to the in-plane waviness experimental work, a numerical study was conducted in Abaqus/Explicit. The cohesive-zone technique was used both at the interface and within the wavy ply to allow the delamination and splitting as observed in the experimental recordings. The predictions showed good agreement with experimental results. Then matrix cracking, coupled with the cohesive-zone technique, was allowed for the non-zero solid plies. The predictions were again in accordance with tests, as both models and coupon testing showed no obvious matrix cracking. Finally, fibre failure was simulated by the kinking mechanism and coupled with the cohesive-zone method; the model predicted the fibre-failure triggered locations in agreement with the experimental tests. Further investigation using periodic boundary conditions suggested that the artificial edge effect, where wavy fibres are terminated, is the key factor governing the ultimate failure when in-plane waviness was introduced, and waviness severity itself also has some effects on failure stress knockdown due to the shear stress caused by the wavy fibres, when this edge effect has been removed.

7.2 Future research scope

Considering inevitable limitations reported here and the discovery of additional potential research directions during the current research itself, the possible scope of future research is summarised below as follows.

1) When developing the transfer process from NDT data into FE models, uniform fibre volume fraction (FVF) was assumed but, if local FVF variation are calculated during the model creation using assumptions based on the ply thicknesses and in-plane fibre orientations, the models will become more realistic.
2) Also in terms of the model creation by the transfer process, simulated NDT material-property maps rather than inverted data from a real component was applied in the research for this thesis; the next stage is to apply the transfer process to inverted experimental data from real test coupons.

3) The wrinkle-governed parametric study was limited to flat laminates and simple Gaussian-governed cosine or sine functions to represent the wrinkle shape in this thesis; this could be extended in the future to other shapes, component geometries and materials, as follows:
    a) non-flat laminates either with external wrinkles, in which the wrinkles were not forced to be flat at the upper or lower surfaces, or where the components themselves are curved.
    b) beyond prepreg laminates to other manufacturing techniques such as resin infusion methods, to investigate wrinkle parameters when the damage-triggering origins are broader in scope.
    c) beyond the Gaussian-governed sine or cosine profiles used here, it is necessary to consider more realistic wrinkle shapes as seen in the industry to check the NDT-measurement guidance is still valid for these more practical situations.
4) Significant limitations of the in-plane waviness study reported in this thesis are the artificial waviness shape (approximately a half-cycle sine curve) and that the waviness continued to the coupon edge, forcing fibres to be terminated at the edge. This design was due to the current limitation from both the experimental and numerical sides. However, a more realistic in-plane waviness from industrial experience could be investigated, where local defects appear completely within the components, rather than extending to the edges. This interior waviness could be replicated by the dry fibre technique or induced by the z-pinning after lamination. Also, some alternative modelling techniques and mechanisms could be investigated to seek further improvements in the prediction accuracy, especially in terms of the fibre failures.
5) Once the in-plane waviness model is fully validated to give the robust predictions against experimental recordings, a similar exercise to the out-of-plane wrinkle parametric study could be performed to identify the governing factors influencing the compressive strength when in-plane waviness is incorporated in components. Guidance for basic NDT measurement requirements for this defect could thus be further suggested.
6) The representative defects - wrinkles, and waviness - studied in this thesis could be supplemented with other defect types, like gaps or porosity.

7) The fibre misalignment defect (wrinkles and waviness) investigated in this thesis was in couple-size scale, it is not clear whether the discovered damage events and knock-down percentages in this thesis would still keep in trend when the coupon-size wrinkles or waviness are appeared in a large structure, e.g. the wing. Hence, it deserves to have the further research on different size scales to identify this issue in the future.

Bibliography

[1] S. Mukhopadhyay, M.I. Jones, S.R. Hallett, Compressive failure of laminates containing an embedded wrinkle; experimental and numerical study, Compos. Part A Appl. Sci. Manuf. 73 (2015) 132–142. doi:10.1016/j.compositesa.2015.03.012.

[2] Boeing 787, (n.d.). http://www.boeing.com/commercial/787/by-design/#/advanced-composite-use (accessed August 14, 2017).

[3] A350 XWB, (n.d.). http://www.aircraft.airbus.com/aircraftfamilies/passengeraircraft/a350xwbfamily/ (accessed August 14, 2017).

[4] R.A. Smith, L.J. Nelson, M.J. Mienczakowski, P.D. Wilcox, Ultrasonic tracking of ply drops in composite laminates, in: AIP Conf. Proc., 2016: pp. 1–11. doi:10.1063/1.4940505.

[5] L.J. Nelson, R.A. Smith, Three-dimensional fibre-orientation characterisation in monolithic carbon-fibre composites, in: 11th Eur. Conf. Non-Destructive Test., Prague, Czech Republic, 2014: pp. 1–12. http://www.ndt.net/events/ECNDT2014/app/content/Paper/105_Smith_Rev1.pdf.

[6] R.A. Smith, S. Mukhopadhyay, A. Lawrie, S.R. Hallett, Applications of ultrasonic NDT to aerospace composites, in: 5th Int. Symp. NDT Aerosp., Singapore, 2013: pp. 1–12. http://www.ndt.net/article/aero2013/content/papers/59_Smith.pdf.

[7] M.P.F. Sutcliffe, S.L. Lemanski, A.E. Scott, Measurement of fibre waviness in industrial composite components, Compos. Sci. Technol. 72 (2012) 2016–2023. doi:10.1016/j.compscitech.2012.09.001.

[8] G. Seon, Y. Nikishkov, A. Makeev, B. Shonkwiler, Mesh morphing methodology for strength predictions in composites, Compos. Struct. 140 (2016) 612–620. doi:10.1016/j.compstruct.2015.12.021.

[9] N. Xie, R.A. Smith, S. Mukhopadhyay, S.R. Hallett, A numerical study on the influence of composite wrinkle defect geometry on compressive strength, Mater. Des. 140 (2018) 7–20. doi:10.1016/j.matdes.2017.11.034.

[10] J. Lee, C. Soutis, A study on the compressive strength of thick carbon fibre – epoxy laminates, Compos. Sci. Technol. 67 (2007) 2015–2026. doi:10.1016/j.compscitech.2006.12.001.

[11] W.-G. Jiang, S.R. Hallett, B.G. Green, M.R. Wisnom, A concise interface constitutive law for analysis of delamination and splitting in composite materials and its application to scaled notched tensile specimens, Int. J. Numer. Methods Eng. 69 (2007) 1982–1995. doi:10.1002/nme.1842.

[12] A. Makeev, G. Seon, E. Lee, Failure Predictions for Carbon/Epoxy Tape Laminates with Wavy Plies, J. Compos. Mater. 44 (2010) 95–112. doi:10.1177/0021998309345352.

[13] X.C. Sun, S.R. Hallett, Barely visible impact damage in scaled composite laminates: Experiments and numerical simulations, Int. J. Impact Eng. 109 (2017) 178–195. doi:10.1016/j.ijimpeng.2017.06.008.

[14] R.M. Jones, Mechanics of composite materials, 1999.

[15] H. Heuer, M. Schulze, M. Pooch, S. Gäbler, A. Nocke, G. Bardl, C.H. Cherif, M. Klein, R. Kupke, R. Vetter, F. Lenz, M. Kliem, C. Bülow, J. Goyvaerts, T. Mayer, S. Petrenz, Review on quality assurance along the CFRP value chain – Non-destructive testing of fabrics, preforms and CFRP by HF radio wave techniques, Compos. Part B Eng. 77 (2015) 494–501. doi:10.1016/j.compositesb.2015.03.022.

[16] K. Mizukami, Y. Mizutani, A. Todoroki, Y. Suzuki, Detection of in-plane and out-of-plane fiber waviness in unidirectional carbon fiber reinforced composites using eddy current testing, Compos. Part B Eng. 86 (2016) 84–94. doi:10.1016/j.compositesb.2015.09.041.

[17] R.A. Smith, L.J. Nelson, N. Xie, C. Fraij, S.R. Hallett, Progress in 3D characterisation and modelling of monolithic carbon-fibre composites, Insight - Non-Destructive Test. Cond. Monit. 57 (2015) 131–139. doi:10.1784/insi.2014.57.3.131.

[18] J.P. Zardan, C. Gueudré, G. Corneloup, Study of induced ultrasonic deviation for the detection and identification of ply waviness in carbon fibre reinforced polymer, NDT E Int. 56 (2013) 1–9. doi:10.1016/j.ndteint.2013.02.001.

[19] R. Lange, G. Mook, Structural analysis of CFRP using eddy current methods, NDT E Int. 27 (1994) 241–248. doi:10.1016/0963-8695(94)90128-7.

[20] W. Yin, P.J. Withers, U. Sharma, A.J. Peyton, Noncontact characterization of carbon-fiber-reinforced plastics using multifrequency eddy current sensors, IEEE Trans. Instrum. Meas. 58 (2009) 738–743. doi:10.1109/TIM.2008.2005072.

[21] G. Mook, R. Lange, O. Koeser, Non-destructive characterisation of carbon-fibre-reinforced plastics by means of eddy-currents, Compos. Sci. Technol. 61 (2001) 865–873. doi:10.1016/S0266-3538(00)00164-0.

[22] H. Heuer, M.H. Schulze, N. Meyendorf, High Resolution Inspection of Carbon Fiber Materials by Eddy Current Techniques, 2nd Int. Symp. NDT Aerosp. 2010. (2010) 1–13. http://www.ndt.net/events/NDTCanada2011/proceedings/papers/94_Heuer_Rev1.pdf.

[23] H. Heuer, M.H. Schulze, Eddy Current Testing of Carbon Fiber Materials by High Resolution Directional Sensors, Proc NDT Canada. (2011) 1–13. http://www.ndt.net/events/NDTCanada2011/proceedings/papers/94_Heuer_Rev1.pdf.

[24] G. Requena, G. Fiedler, B. Seiser, P. Degischer, M. Di Michiel, T. Buslaps, 3D-Quantification of the distribution of continuous fibres in unidirectionally reinforced composites, Compos. Part A Appl. Sci. Manuf. 40 (2009) 152–163. doi:10.1016/j.compositesa.2008.10.014.

[25] W. Whitacre, M. Czabaj, Automated 3D Digital Reconstruction of Fiber Reinforced Polymer Composites, AIAA Guid. Navig. Control Conf. (2015) 1–18. doi:10.2514/6.2015-0342.

[26] P. Latil, L. Orgéas, C. Geindreau, P.J.J. Dumont, S. Rolland du Roscoat, Towards the 3D in situ characterisation of deformation micro-mechanisms within a compressed bundle of fibres, Compos. Sci. Technol. 71 (2011) 480–488. doi:10.1016/j.compscitech.2010.12.023.

[27] G. Nikishkov, Y. Nikishkov, A. Makeev, Finite element mesh generation for composites with ply waviness based on X-ray computed tomography, Adv. Eng. Softw. 58 (2013) 35–44. doi:10.1016/j.advengsoft.2013.01.002.

[28] M.W. Czabaj, M.L. Riccio, W.W. Whitacre, Numerical reconstruction of graphite/epoxy

composite microstructure based on sub-micron resolution X-ray computed tomography, Compos. Sci. Technol. 105 (2014) 174–182. doi:10.1016/j.compscitech.2014.10.017.

[29] R.M. Sencu, Z. Yang, Y.C. Wang, P.J. Withers, C. Rau, A. Parson, C. Soutis, Generation of micro-scale finite element models from synchrotron X-ray CT images for multidirectional carbon fibre reinforced composites, Compos. Part A Appl. Sci. Manuf. 91 (2016) 85–95. doi:10.1016/j.compositesa.2016.09.010.

[30] S.T. Pinho, C.G. Dávila, P.P. Camanho, L. Iannucci, P. Robinson, Failure models and criteria for FRP under in-plane or three-dimensional stress states including shear non-linearity, Nasa/Tm-2005-213530. (2005) 1–64. doi:NASA/TM-2005-213530.

[31] S.C. Wooh, I.M. Daniel, Wave propagation in composite materials with fibre waviness, Ultrasonics. 33 (1995) 3–10. doi:10.1016/0041-624X(95)00003-L.

[32] J.P. Zardan, C. Gueudré, G. Corneloup, Study of induced ultrasonic deviation for the detection and identification of ply waviness in carbon fibre reinforced polymer, NDT E Int. 56 (2013) 1–9. doi:10.1016/j.ndteint.2013.02.001.

[33] D. Pain, B.W. Drinkwater, Detection of fibre waviness using ultrasonic array scattering data, J. Nondestruct. Eval. 32 (2013) 215–227. doi:10.1007/s10921-013-0174-z.

[34] A. Sandhu, T.J. Dodwell, R. Butler, An Automated Image Processing Algorithm To Determine Wrinkle Characteristics From B-Scans, in: 17th Eur. Conf. Compos. Mater., Munich, Germany, 2016: pp. 1–8.

[35] L.J. Nelson, R.A. Smith, M. Mienczakowski, Ply-orientation measurements in composites using structure-tensor analysis of volumetric ultrasonic data, Compos. Part A Appl. Sci. Manuf. 104 (2018) 108–119. doi:10.1016/j.compositesa.2017.10.027.

[36] R.A. Smith, L.J. Nelson, M.J. Mienczakowski, P.D. Wilcox, Ultrasonic Analytic-Signal Responses From Polymer-Matrix Composite Laminates, IEEE Trans. Ultrason. Ferroelectr. Freq. Control. 65 (2018) 231–243. doi:10.1109/TUFFC.2017.2774776.

[37] R.A. Smith, Use of 3D ultrasound data sets to map the localised properties of fibre-reinforced composites, PhD thesis, University of Nottingham, 2010. http://eprints.nottingham.ac.uk/31253/1/Full Thesis Chapters (2).pdf.

[38] R.A. Smith, L.J. Nelson, M.J. Mienczakowski, R.E. Challis, Automated analysis and advanced defect characterisation from ultrasonic scans of composites, Insight - Non-Destructive Test. Cond. Monit. 51 (2009) 82–87. doi:10.1784/insi.2009.51.2.82.

[39] P.D. Soden, M.J. Hinton, A.S. Kaddour, A Comparison of the Predictive Capabilities of Current Failure Theories for Composite Laminates, Compos. Sci. Technol. 58 (1998) 1225–1254.

[40] A.S. Kaddour, M.J. Hinton, P.D. Soden, A comparison of the predictive capabilities of current failure theories for composite laminates: Additional contributions, Compos. Sci. Technol. 64 (2004) 449–476. doi:10.1016/S0266-3538(03)00226-4.

[41] M.J. Hinton, A.S. Kaddour, P.D. Soden, A further assessment of the predictive capabilities of current failure theories for composite laminates: comparison with experimental evidence, Compos. Sci. Technol. 64 (2004) 549–588. doi:10.1016/S0266-3538(03)00226-4.

[42] Z. Hashin, A. Rotem, A Fatigue Failure Criterion for Fiber Reinforced Materials, J. Compos.

Mater. 7 (1973) 448–464. doi:10.1177/002199837300700404.

[43] Z. Hashin, Failure Criteria for Unidirectional Fiber Composites, J. Appl. Mech. 47 (1980) 329–334. doi:10.1115/1.3153664.

[44] C.T. Sun, B.J. Quinn, J. Tao, Comparative Evaluation of Failure Analysis Methods for Composite Laminates., U.S. Dep. Transp. (1996) 133. http://trid.trb.org/view.aspx?id=523207.

[45] A. Puck, H. Schürmann, Failure analysis of FRP laminates by means of physically based phenomenological models, Compos. Sci. Technol. 58 (1998) 1045–1067. doi:10.1016/S0266-3538(96)00140-6.

[46] A. Puck, H. Schürmann, Failure analysis of FRP laminates by means of physically based phenomenological models, Compos. Sci. Technol. 62 (2002) 1633–1662. doi:10.1016/S0266-3538(01)00208-1.

[47] C.G. Dávila, N. Jaunky, S. Goswami, FAILURE CRITERIA FOR FRP LAMINATES IN PLANE STRESS, in: 44th AIAA/ASME/ASCE/AHS Struct. Struct. Dyn. Mater. Confere, Norfolk, Virginia, 2003: pp. 1–11.

[48] C.G. Dávila, P.P. Camanho, C.A. Rose, Failure Criteria for FRP Laminates, J. Compos. Mater. 39 (2005) 323–345.

[49] F. París, E. Correa, J. Canas, Micromechanical view of failure of the matrix in fibrous composite materials, Compos. Sci. Technol. 63 (2003) 1041–1052. doi:10.1016/S0266-3538(03)00017-4.

[50] S.T. Pinho, L. Iannucci, P. Robinson, Physically-based failure models and criteria for laminated fibre-reinforced composites with emphasis on fibre kinking: Part I: Development, Compos. Part A Appl. Sci. Manuf. 37 (2006) 63–73. doi:10.1016/j.compositesa.2005.04.016.

[51] C.R. Schultheisz, A.M. Waas, Compressive failure of composites, Part I: Testing and micromechanical theories, Prog. Aerosp. Sci. 32 (1996) 1–42. doi:10.1016/0376-0421(94)00002-3.

[52] A. Jumahat, C. Soutis, F.R. Jones, A. Hodzic, Fracture mechanisms and failure analysis of carbon fibre/toughened epoxy composites subjected to compressive loading, Compos. Struct. 92 (2010) 295–305. doi:10.1016/j.compstruct.2009.08.010.

[53] R. Gutkin, S.T. Pinho, P. Robinson, P.T. Curtis, A finite fracture mechanics formulation to predict fibre kinking and splitting in CFRP under combined longitudinal compression and in-plane shear, Mech. Mater. 43 (2011) 730–739. doi:10.1016/j.mechmat.2011.08.002.

[54] S. Pimenta, R. Gutkin, S.T. Pinho, P. Robinson, A micromechanical model for kink-band formation: Part I — Experimental study and numerical modelling, Compos. Sci. Technol. 69 (2009) 948–955. doi:10.1016/j.compscitech.2009.02.010.

[55] T.J. Vogler, S. Kyriakides, Initiation and axial propagation of kink bands in fiber composites, Acta Mater. 45 (1997) 2443–2454. doi:10.1016/S1359-6454(96)00350-3.

[56] S. Vogler, T.J., Kyriakides, On the axial propagation of kink bands in fiber composites: Part I experiments, Int. J. Solids Struct. 36 (1999) 557–574.

[57] T.J. Vogler, S. Kyriakides, On the initiation and growth of kink bands in fiber composites. Part I. experiments, Int. J. Solids Struct. 38 (2001) 2639–2651.

[58] A.S. ARGON, Fracture of Composites, in: Treatise Mater. Sci. Technol. Vol.1|Treatise Mater. Sci. Technol. Vol.1, 1972: pp. 79–114. doi:10.1016/B978-0-12-341801-2.50007-2.

[59] B. Budiansky, Micromechanics, Comput. Struct. 16 (1983) 3–12. doi:10.1016/0045-7949(83)90141-4.

[60] B. Budiansky, N.A. Fleck, Compressive failure of fibre composites, J. Mech. Phys. Solids. 41 (1993) 183–211. doi:10.1016/0022-5096(93)90068-Q.

[61] S.T. Pinho, L. Iannucci, P. Robinson, Physically based failure models and criteria for laminated fibre-reinforced composites with emphasis on fibre kinking. Part II: FE implementation, Compos. Part A Appl. Sci. Manuf. 37 (2006) 766–777. doi:10.1016/j.compositesa.2005.06.008.

[62] S.H. Lee, C.S. Yerramalli, A.M. Waas, Compressive splitting response of glass-fiber reinforced unidirectional composites, Compos. Sci. Technol. 60 (2000) 2957–2966. doi:10.1016/S0266-3538(00)00159-7.

[63] M.S. Kumar, K. Raghavendra, M. Ambresh, H. Ramachandra, M. Venkataswamy, V. Ranganath, Fractographic analysis of compression failures in unidirectional carbon fiber reinforced plastic composites, Proc. Inst. Mech. Eng. Part L J. Mater. Des. Appl. 229 (2015) 439–446. doi:10.1177/1464420714525542.

[64] P. Prabhakar, A.M. Waas, Interaction between kinking and splitting in the compressive failure of unidirectional fiber reinforced laminated composites, Compos. Struct. 98 (2013) 85–92. doi:10.1016/j.compstruct.2012.11.005.

[65] R. Gutkin, S.T. Pinho, P. Robinson, P.T. Curtis, Micro-mechanical modelling of shear-driven fibre compressive failure and of fibre kinking for failure envelope generation in CFRP laminates, Compos. Sci. Technol. 70 (2010) 1214–1222. doi:10.1016/j.compscitech.2010.03.009.

[66] S.H. Lee, A.M. Waas, Compressive response and failure of fiber reinforced unidirectional composites, Int. J. Fract. 100 (1999) 275–306. doi:10.1023/A:1018779307931.

[67] G.R. Irwin, Analysis of Stresses and Strains Near the End of a Crack Traversing a Plate, J. Appl. Mech. 24 (1957) 361–364. doi:no DOI.

[68] A.A. Griffith, The Phenomena of Rupture and Flow in Solids, Philos. Trans. R. Soc. London. Ser. A, Contain. Pap. a Math. or Phys. Character. 221 (1921) 163–198.

[69] E.F. Rybicki, M.F. Kanninen, A finite element calculation of stress intensity factors by a modified crack closure integral, Eng. Fract. Mech. 9 (1977) 931–938. doi:10.1016/0013-7944(77)90013-3.

[70] R. Krueger, Virtual crack closure technique: History, approach, and applications, Appl. Mech. Rev. 57 (2004) 109–143. doi:10.1115/1.1595677.

[71] Z. Zou, S.R. Reid, P.D. Soden, S. Li, Mode separation of energy release rate for delamination in composite laminates using sublaminates, Int. J. Solids Struct. 38 (2001) 2597–2613. doi:10.1016/S0020-7683(00)00172-4.

[72] G.E. Mabson, L.R. Deobald, B. Dopker, D.M. Hoyt, J.S. Baylor, D.L. Graesser, Fracture interface elements for static and fatigue analysis, in: 16th Int. Conf. Compos. Mater. (ICCM 16), Kyoto, Japan, 2007: pp. 1–10. http://www.iccm-

central.org/Proceedings/ICCM16proceedings/contents/pdf/WedG/WeGA1-01sp_mabsong223561p.pdf.

[73] X. Li, Modelling Stress and Damage Interaction in Fibre Reinforced Composite Laminates, PhD thesis, University of Bristol, 2009.

[74] P.P. Camanho, C.G. Dávila, D.R. Ambur, Numerical Simulation of Delamination Growth in Composite Materials, NASA/TP-2001-211041. (2001) 1–24. doi:10.1.1.20.9217.

[75] D.S. Dugdale, Yielding of steel sheets containing slits, J. Mech. Phys. Solids. 8 (1960) 100–104. doi:10.1016/0022-5096(60)90013-2.

[76] G.I. Barenblatt, The Mathematical Theory of Equilibrium Cracks in Brittle Fracture, Adv. Appl. Mech. 7 (1962) 55–129. doi:10.1016/S0065-2156(08)70121-2.

[77] A. Hillerborg, M. Modéer, P.E. Petersson, Analysis of crack formation and crack growth in concrete by means of fracture mechanics and finite elements, Cem. Concr. Res. 6 (1976) 773–781. doi:10.1016/0008-8846(76)90007-7.

[78] A. Needleman, A Continuum Model for Void Nucleation by Inclusion Debonding, J. Appl. Mech. 54 (1987) 525. doi:10.1115/1.3173064.

[79] X.P. Xu, A. Needleman, Numerical simulations of fast crack growth in brittle solids, J. Mech. Phys. Solids. 42 (1994) 1397–1434. doi:10.1016/0022-5096(94)90003-5.

[80] V. Tvergaard, J.W. Hutchinson, The relation between crack growth resistance and fracture process parameters in elastic-plastic solids, J. Mech. Phys. Solids. 40 (1992) 1377–1397. doi:10.1016/0022-5096(92)90020-3.

[81] W. Cui, M.R. Wisnom, A combined stress-based and fracture-mechanics-based model for predicting delamination in composites, Composites. 24 (1993) 467–474. doi:10.1016/0010-4361(93)90016-2.

[82] J.C.J. Schellekens, R. De Borst, A non-linear finite element approach for the analysis of mode-I free edge delamination in composites, Int. J. Solids Struct. 30 (1993) 1239–1253. doi:10.1016/0020-7683(93)90014-X.

[83] Y. Mi, M.A. Crisfield, G.A.O. Davies, H.B. Hellweg, Progressive Delamination Using Interface Elements, J. Compos. Mater. 32 (1998) 1246–1272. doi:10.1177/002199839803201401.

[84] E.D. Reedy, F.J. Mello, T.R. Guess, Modeling the Initiation and Growth of Delaminations in Composite Structures, J. Compos. Mater. 31 (1997) 812–831. doi:10.1177/002199839703100804.

[85] W.C. Cui, M.R. Wisnom, M. Jones, A comparison of failure criteria to predict delamination of unidirectional glass/epoxy specimens waisted through the thickness, Composites. 23 (1992) 158–166. doi:10.1016/0010-4361(92)90436-X.

[86] J.C. Brewer, P.A. Lagace, Quadratic Stress Criterion for Initiation of Delamination, J. Compos. Mater. 22 (1988) 1141–1155. doi:10.1177/002199838802201205.

[87] C. Davila, P. Camanho, M. de Moura, Mixed-mode decohesion elements for analyses of progressive delamination, in: 42nd AIAA/ASME/ASCE/AHS/ASC Struct. Struct. Dyn. Mater. Conf. Exhib., Seattle, 2001: pp. 1–12. doi:10.2514/6.2001-1486.

[88] E.M. Wu, R.C. Reuter Jr., Crack Extension in Fiberglass Reinforced Plastics, Spons. by US Bur. Nav. Weapons, Rep. No. 275, Illinois Univ. Urbana Dept. Theor. Appl. Mech. (1965) 32.

[89] J.D. Whitcomb, Analysis of instability-related growth of a through-width delamination, NASA Tech. Memo. NASA TM 86 (1984) 1–54.

[90] M.L. Benzeggagh, M. Kenane, Measurement of Mixed-Mode Delamination Fracture Toughness of Unidirectional Glass/Epoxy Composites With Mixed-Mode bending Apparatus, Compos. Sci. Technol. 56 (1996) 439–449. papers3://publication/uuid/4A93C773-5F12-485B-AD94-FDB7722EACE5.

[91] K. Potter, B. Khan, M. Wisnom, T. Bell, J. Stevens, Variability, fibre waviness and misalignment in the determination of the properties of composite materials and structures, Compos. Part A Appl. Sci. Manuf. 39 (2008) 1343–1354. doi:10.1016/j.compositesa.2008.04.016.

[92] K.D. Potter, Understanding the origins of defects and variability in composites manufacture, in: 17th Int. Conf. Compos. Mater., Edinburgh, UK, 2009: pp. 1–19. http://www.iccm-central.org/Proceedings/ICCM17proceedings/Themes/Plenaries/P1.5 Potter.pdf.

[93] I. Sinclair, K. Potter, D. Bull, J. Barton, O.T. Thomsen, Privately obtained, 2017.

[94] S.L. Lemanski, J. Wang, M.P.F. Sutcliffe, K.D. Potter, M.R. Wisnom, Modelling failure of composite specimens with defects under compression loading, Compos. Part A Appl. Sci. Manuf. 48 (2013) 26–36. doi:10.1016/j.compositesa.2012.12.007.

[95] K. Croft, L. Lessard, D. Pasini, M. Hojjati, J. Chen, A. Yousefpour, Experimental study of the effect of automated fiber placement induced defects on performance of composite laminates, Compos. Part A Appl. Sci. Manuf. 42 (2011) 484–491. doi:10.1016/j.compositesa.2011.01.007.

[96] D. Kugler, T.J. Moon, Identification of the Most Significant Processing Parameters on the Developments of Fiber Wavinses in Thin Laminates, J. Compos. Mater. 36 (2002) 1451–1479. doi:10.1106/002199802023575.

[97] K. Potter, C. Langer, B. Hodgkiss, S. Lamb, Sources of variability in uncured aerospace grade unidirectional carbon fibre epoxy preimpregnate, Compos. Part A Appl. Sci. Manuf. 38 (2007) 905–916. doi:10.1016/j.compositesa.2006.07.010.

[98] B. Khan, K.D. Potter, M.R. Wisnom, Simulation of process induced defects in resin transfer moulded woven carbon fibre laminates and their effect on mechanical behaviour, in: 8th Int. Conf. Flow Process. Compos. Mater., Douai, France, 2006: pp. 261–270.

[99] K.D. Potter, M. Campbell, C. Langer, M.R. Wisnom, The generation of geometrical deformations due to tool/part interaction in the manufacture of composite components, Compos. Part A Appl. Sci. Manuf. 36 (2005) 301–308. doi:10.1016/j.compositesa.2004.06.002.

[100] P.P. Parlevliet, H.E.N. Bersee, A. Beukers, Residual stresses in thermoplastic composites - a study of the literature. Part III: Effects of thermal residual stresses, Compos. Part A Appl. Sci. Manuf. 38 (2007) 1581–1596. doi:10.1016/j.compositesa.2006.12.005.

[101] T.J. Dodwell, R. Butler, G.W. Hunt, Out-of-plane ply wrinkling defects during consolidation over an external radius, Compos. Sci. Technol. 105 (2014) 151–159. doi:10.1016/j.compscitech.2014.10.007.

[102] J.S. Lightfoot, M.R. Wisnom, K. Potter, A new mechanism for the formation of ply wrinkles due to shear between plies, Compos. Part A Appl. Sci. Manuf. 49 (2013) 139–147. doi:10.1016/j.compositesa.2013.03.002.

[103] P. Hallander, J. Sjölander, M. Åkermo, Forming induced wrinkling of composite laminates with mixed ply material properties; an experimental study, Compos. Part A Appl. Sci. Manuf. 78 (2015) 234–245. doi:10.1016/j.compositesa.2015.08.025.

[104] J. Sjölander, P. Hallander, M. Åkermo, Forming induced wrinkling of composite laminates: A numerical study on wrinkling mechanisms, Compos. Part A Appl. Sci. Manuf. 81 (2016) 41–51. doi:10.1016/j.compositesa.2015.10.012.

[105] A. Beakou, M. Cano, J.B. Le Cam, V. Verney, Modelling slit tape buckling during automated prepreg manufacturing: A local approach, Compos. Struct. 93 (2011) 2628–2635. doi:10.1016/j.compstruct.2011.04.030.

[106] H.M. Hsiao, I.M. Daniel, Effect of fiber waviness on stiffness and strength reduction of unidirectional composites under compressive loading, Compos. Sci. Technol. 56 (1996) 581–593. doi:10.1016/0266-3538(96)00045-0.

[107] J. Wang, K. Potter, K. Hazra, M. Wisnom, Experimental fabrication and characterization of out-of-plane fiber waviness in continuous fiber-reinforced composites, J. Compos. Mater. 46 (2012) 2041–2053. doi:10.1177/0021998311429877.

[108] M.R. Garnich, G. Karami, Localized fiber waviness and implications for failure in unidirectional composites, J. Compos. Mater. 39 (2005) 1225–1245. doi:Doi 10.1177/0021998305048748.

[109] D.O.H. Adams, S.J. Bell, Compression strength reductions in composite laminates due to multiple-layer waviness, Compos. Sci. Technol. 53 (1995) 207–212. doi:10.1016/0266-3538(95)00020-8.

[110] S. Eskandari, F.M. Andrade Pires, P.P. Camanho, A.T. Marques, Damage analysis of out of plane undulated fiber composites, Compos. Struct. 152 (2016) 464–476. doi:10.1016/j.compstruct.2016.05.062.

[111] D. Bradley, D.O. Adams, H.E. Gascoigne, Interlaminar strains and compressive strength reductions due to nested layer waviness in composite laminates, J. Reinf. Plast. Compos. 17 (1998) 989–1011.

[112] S.K. Chakrapani, V. Dayal, D. Barnard, Detection and characterization of waviness in unidirectional GFRP using rayleigh wave air coupled ultrasonic testing (RAC-UT), Res. Nondestruct. Eval. 24 (2013) 191–201. doi:10.1080/09349847.2013.786158.

[113] D. O'Hare Adams, M.W. Hyer, Effects of Layer Waviness on the Compression Strength of Thermoplastic Composite Laminates, J. Reinf. Plast. Compos. 12 (1993) 414–429. doi:10.1177/073168449301200404.

[114] L.D. Bloom, J. Wang, K.D. Potter, Damage progression and defect sensitivity: An experimental study of representative wrinkles in tension, Compos. Part B Eng. 45 (2013) 449–458. doi:10.1016/j.compositesb.2012.05.021.

[115] J. Wang, K.D. Potter, J. Etches, Experimental investigation and characterisation techniques of compressive fatigue failure of composites with fibre waviness at ply drops, Compos. Struct. 100 (2013) 398–403. doi:10.1016/j.compstruct.2013.01.010.

[116] B. Fedulov, F. Antonov, A. Safonov, A. Ushakov, S. Lomov, Influence of fibre misalignment and voids on composite laminate strength, J. Compos. Mater. 49 (2015) 2887–2896. doi:10.1177/0021998314557533.

[117] A. Caiazzo, M. Orlet, H. McShane, L. Strait, C. Rachau, The effects of marcel defects on composite structural properties, Compos. Struct. Theory Pract. 1383 (2000) 158–187. doi:Doi 10.1520/Stp14509s.

[118] M.R. Wisnom, J.W. Atkinson, Compressive failure due to shear instability: experimental investigation of waviness and correlation with analysis, J. Reinf. Plast. Compos. 15 (1996) 420–439.

[119] R.F. El-Hajjar, D.R. Petersen, Gaussian function characterization of unnotched tension behavior in a carbon/epoxy composite containing localized fiber waviness, Compos. Struct. 93 (2011) 2400–2408. doi:10.1016/j.compstruct.2011.03.029.

[120] L.M. Ferreira, E. Graciani, F. París, Three dimensional finite element study of the behaviour and failure mechanism of non-crimp fabric composites under in-plane compression, Compos. Struct. 149 (2016) 106–113. doi:10.1016/j.compstruct.2016.04.022.

[121] C. Zhao, J. Xiao, Y. Li, Q. Chu, T. Xu, B. Wang, An Experimental Study of the Influence of in-Plane Fiber Waviness on Unidirectional Laminates Tensile Properties, Appl. Compos. Mater. (2017) 1–17. doi:10.1007/s10443-017-9590-z.

[122] S.L. Lemanski, M.P.F. Sutcliffe, J. Wang, K.D. Potter, M.R. Wisnom, Fibre waviness defects in composite structures, Report, University of Bristol, 2012.

[123] M.R. Wisnom, J.W. Atkinson, Fibre waviness generation and measurement and its effect on compressive strength, J. Reinf. Plast. Compos. 19 (2000) 96–110. doi:10.1177/073168440001900201.

[124] J.G. Häberle, F.L. Matthews, An improved technique for compression testing of unidirectional fibre-reinforced plastics; development and results, Composites. 25 (1994) 358–371. doi:10.1016/S0010-4361(94)80006-5.

[125] S.L. Lemanski, M.P.F. Sutcliffe, Compressive failure of finite size unidirectional composite laminates with a region of fibre waviness, Compos. Part A Appl. Sci. Manuf. 43 (2012) 435–444. doi:10.1016/j.compositesa.2011.11.007.

[126] M.P.F. Sutcliffe, Modelling the effect of size on compressive strength of fibre composites with random waviness, Compos. Sci. Technol. 88 (2013) 142–150. doi:10.1016/j.compscitech.2013.09.002.

[127] B. Fedulov, F. Antonov, A. Safonov, A. Ushakov, S. Lomov, Influence of fibre misalignment and voids on composite laminate strength, J. Compos. Mater. 49 (2015) 2887–2896. doi:10.1177/0021998314557533.

[128] P.A. Zinoviev, S. V. Grigoriev, O. V. Lebedeva, L.P. Tairova, The strength of multilayered composites under a plane-stress state, Compos. Sci. Technol. 58 (1998) 1209–1223. doi:10.1016/B978-008044475-8/50016-0.

[129] J. Lee, C. Soutis, Thickness effect on the compressive strength of T800/924C carbon fibre-epoxy laminates, Compos. Part A Appl. Sci. Manuf. 36 (2005) 213–227. doi:10.1016/j.compositesa.2004.06.010.

[130] A.R. Melro, P.P. Camanho, S.T. Pinho, Influence of geometrical parameters on the elastic response of unidirectional composite materials, Compos. Struct. 94 (2012) 3223–3231. doi:10.1016/j.compstruct.2012.05.004.

[131] W. Rosen, Mechanics of Composite Strengthening, in: Fiber Compos. Mater., 1964: pp. 37–75.

[132] K.H. Lo, E.S.-M. Chim, Compressive Strength of Unidirectional Composites, J. Reinf. Plast. Compos. 11 (1992) 838–896. doi:10.1177/073168449201100801.

[133] G.M. Martinez, M.R. Piggott, D.M.. Bainbridge, B. Harris, The compression strength of composites with kinked, misaligned and Poorly adhering fibres, J. Mater. Sci. 16 (1981) 2831–2836.

[134] P. Ladeveze, E. LeDantec, Damage modelling of the elementary ply for laminated composites, Compos. Sci. Technol. 43 (1992) 257–267. doi:10.1016/0266-3538(92)90097-M.

[135] S. Mukhopadhyay, Failure of laminates containing embedded wrinkle defects - numerical and experimental study, PhD thesis, University of Bristol, 2015.

[136] D. Kondo, H. Welemane, F. Cormery, Basic concepts and models in continuum damage mechanics, Rev. Eur. Génie Civ. 11 (2007) 927–943. doi:10.3166/regc.11.927-943.

[137] P. Maimí, P.P. Camanho, J.A. Mayugo, C.G. Dávila, A continuum damage model for composite laminates: Part I - Constitutive model, Mech. Mater. 39 (2007) 897–908. doi:10.1016/j.mechmat.2007.03.005.

[138] P. Maimí, P.P. Camanho, J.A. Mayugo, C.G. Dávila, A continuum damage model for composite laminates: Part II - Computational implementation and validation, Mech. Mater. 39 (2007) 909–919. doi:10.1016/j.mechmat.2007.03.006.

[139] P.P. Camanho, M.A. Bessa, G. Catalanotti, M. Vogler, R. Rolfes, Modeling the inelastic deformation and fracture of polymer composites-Part II: Smeared crack model, Mech. Mater. 59 (2013) 36–49. doi:10.1016/j.mechmat.2012.12.001.

[140] G. Catalanotti, P.P. Camanho, A.T. Marques, Three-dimensional failure criteria for fiber-reinforced laminates, Compos. Struct. 95 (2013) 63–79. doi:10.1016/j.compstruct.2012.07.016.

[141] VUMAT, (n.d.). http://130.149.89.49:2080/v6.14/books/sub/default.htm (accessed June 6, 2018).

[142] Signum function, (n.d.). http://mathworld.wolfram.com/Sign.html (accessed June 20, 2018).

[143] P.W. Harper, S.R. Hallett, Cohesive zone length in numerical simulations of composite delamination, Eng. Fract. Mech. 75 (2008) 4774–4792. doi:10.1016/j.engfracmech.2008.06.004.

[144] cohesive elements, (n.d.). http://localhost:2080/v6.14/books/usb/default.htm (accessed June 27, 2017).

[145] S.W. Yurgartis, Measurement of small angle fiber misalignments in continuous fiber composites, Compos. Sci. Technol. 30 (1987) 279–293. doi:10.1016/0266-3538(87)90016-9.

[146] J. Fish, T. Belytschko, A First Course in Finite Elements, 2007.

[147] R.A. Smith, L.J. Nelson, M.J. Mienczakowski, Phononic band gaps and phase singularities in the ultrasonic response from toughened composites, in: AIP Conf. Proc., 2018: p. to be published.

[148] Hexcel 8552, (n.d.). http://www.hexcel.com/user_area/content_media/raw/HexPly_8552_eu_DataSheet.pdf (accessed June 9, 2017).

[149] C. de Boor, A Practical Guide to Splines - Revised Edition, 2001. doi:10.1007/978-1-4419-7055-8.

[150] Hourglassing, (n.d.). http://abaqus.software.polimi.it/v6.14/books/stm/default.htm (accessed June 9, 2017).

[151] hourglassing formation, (n.d.). http://localhost:2080/v6.14/books/gsa/default.htm (accessed June 16, 2017).

[152] W.G. Jiang, S.R. Hallett, B.G. Green, M.R. Wisnom, A concise interface constitutive law for analysis of delamination and splitting in composite materials and its application to scaled notched tensile specimens, Int. J. Numer. Methods Eng. 69 (2007) 1982–1995. doi:10.1002/nme.1842.

[153] A.R. Melro, Analytical and Numerical Modelling of Damage and Fracture of Advanced Composites, PhD thesis, University of Porto, 2011.

[154] T. Mori, K. Tanaka, Average stress in matrix and average elastic energy of materials with misfitting inclusions, Acta Metall. 21 (1973) 571–574.

[155] R. Hill, Theory of mechanical properties of fibre-strengthened materials: II. Inelastic behaviour, J. Mech. Phys. Solids. 12 (1964) 199–212. http://linkinghub.elsevier.com/retrieve/pii/0022509664900201.

[156] Z. Hashin, On elastic behaviour of fibre reinforced materials of arbitrary transverse phase geometry, J. Mech. Phys. Solids. 13 (1965) 119–134. http://www.sciencedirect.com/science/article/pii/0022509665900153%5Cnhttp://linkinghub.elsevier.com/retrieve/pii/0022509665900153.

[157] Hexcel 3501-6, (n.d.). http://www.hexcel.com/user_area/content_media/raw/HexPly_35016_eu_DataSheet.pdf (accessed June 9, 2017).

[158] T.A. Fletcher, T. Kim, T.J. Dodwell, R. Butler, R. Scheichl, R. Newley, Resin treatment of free edges to aid certification of through thickness laminate strength, Compos. Struct. 146 (2016) 26–33. doi:10.1016/j.compstruct.2016.02.074.

[159] R.F. Elhajjar, S.S. Shams, Compression testing of continuous fiber reinforced polymer composites with out-of-plane fiber waviness and circular notches, Polym. Test. 35 (2014) 45–55. doi:10.1016/j.polymertesting.2014.02.004.

[160] Hexcel, (n.d.). http://www.hexcel.com/ (accessed July 21, 2017).

[161] M.W. Czabaj, J.G. Ratcliffe, Comparison of intralaminar and interlaminar mode I fracture toughnesses of a unidirectional IM7/8552 carbon/epoxy composite, Compos. Sci. Technol. 89 (2013) 15–23. doi:10.1016/j.compscitech.2013.09.008.

[162] Tie, (n.d.). http://abaqus.software.polimi.it/v6.14/books/usb/default.htm?startat=pt08ch35s03aus132.html#usb-cni-ptiedconstraint (accessed July 26, 2017).

[163] T. Belytschko, W.K. Liu, B. Moran, K.I. Elkhodary, Nonlinear finite elements for continua and structures, John Wiley & Sons, Ltd, 2014.

[164] Abaqus Local Direction, (n.d.). http://abaqus.software.polimi.it/v6.14/books/usb/default.htm?startat=pt01ch01s02aus02.html (accessed December 5, 2017).

[165] Sensitivity of skewness of C3D8R, (n.d.). http://abaqus.software.polimi.it/v6.14/books/usb/default.htm?startat=pt06.html#usbechapter (accessed July 31, 2017).

[166] Pbc's - Equation, (n.d.). http://abaqus.software.polimi.it/v6.14/books/usb/default.htm?startat=pt08ch35s02aus129.html#usb-cni-pequation (accessed October 28, 2017).

Appendix A
Graphical User Interface (GUI) for NDT-to-Model transfer process

The graphical user interface (GUI) was created through Matlab Guide, the version of the transfer process created in this thesis was only suitable for the wrinkle and waviness model creations. Related explanations were presented in Chapter 3, and the instructive texts will be presented to explain the functions when positioning the cursor to the headings of each section in GUI. The layout was shown in Figure A.1.

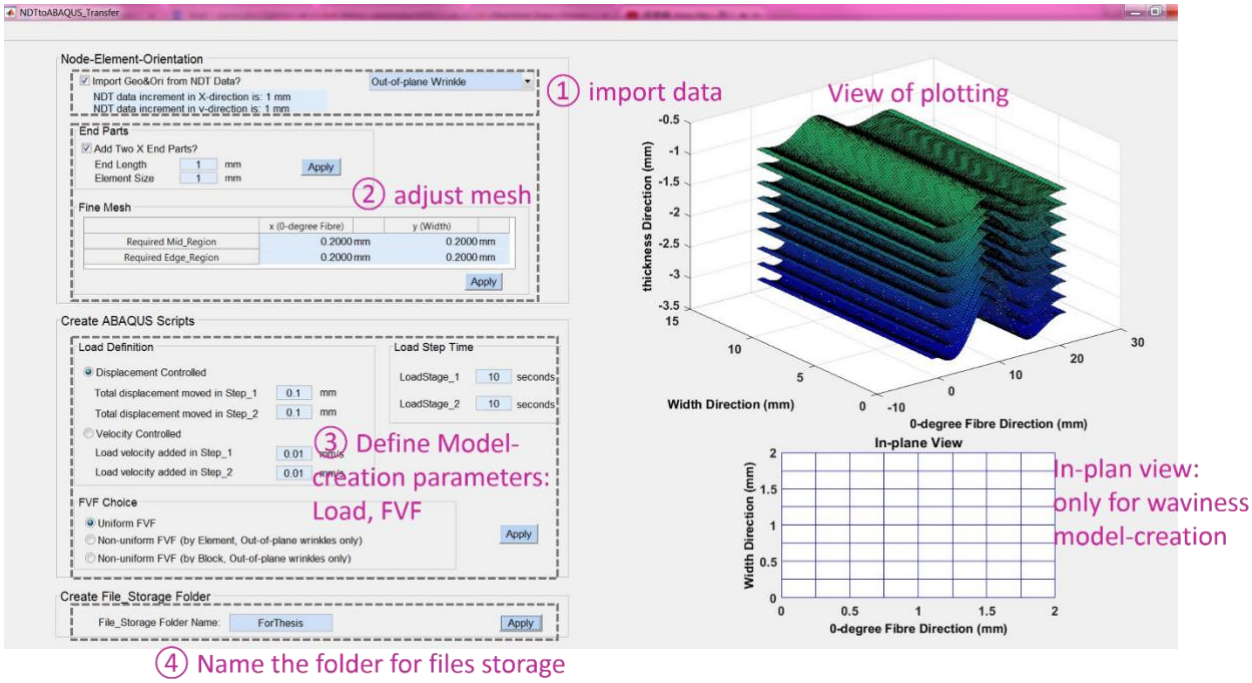

Figure A.1 Layout of transfer process GUI.

Appendix B

Graphical User Interface (GUI) for NDT-data simulator

NDT-based simulator developed by Guide could be used to simulate many aspects of NDT data, among its various functions, this thesis only used the ones relating to the definition for wrinkles and waviness, as well as the function for dimension definitions. Here, in Figure B.1, the used sections in this thesis (dimension definitions, wrinkles and waviness) are labelled.

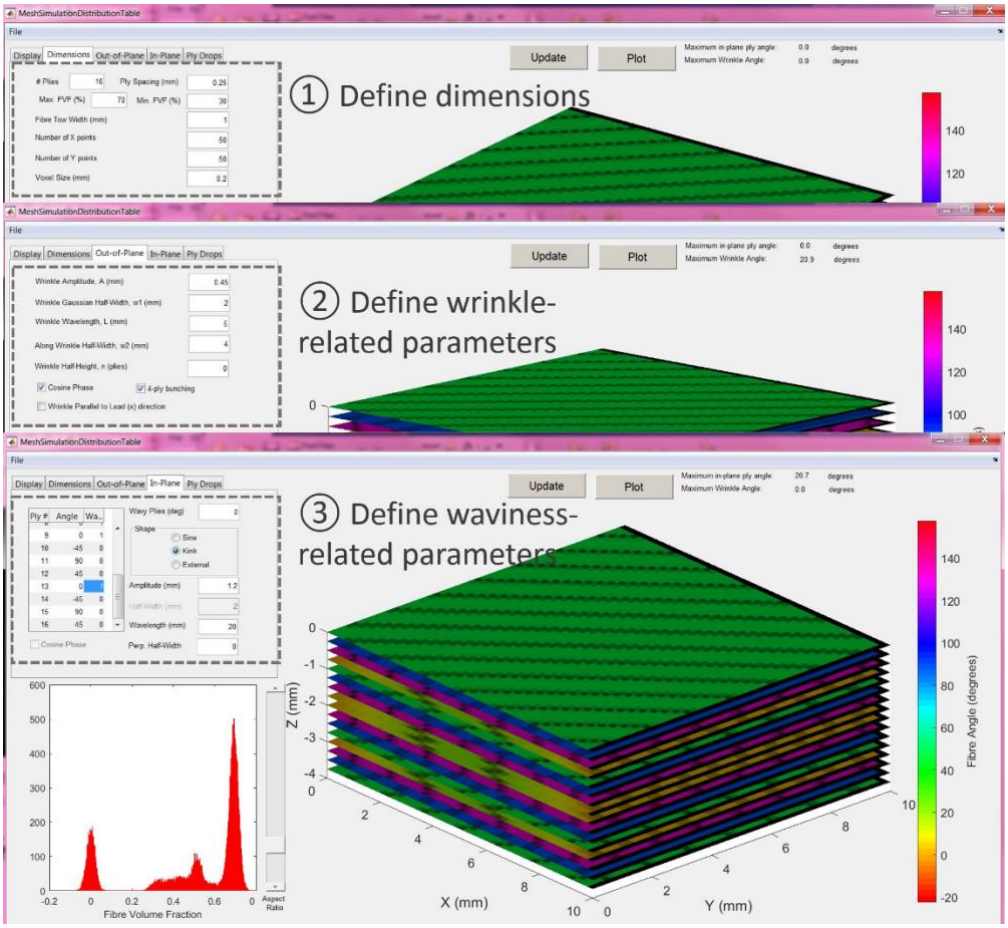

Figure B.1 Layout of simulator GUI.

Appendix C

Publications

The work presented in this thesis has been transferred to the following publications till now:

[1] N. Xie, R.A. Smith, S. Mukhopadhyay, S.R. Hallett, Modelling the mechanical properties of wrinkled composites from NDT data, in: 20th Int. Conf. Compos. Mater. (ICCM 20), Copenhagen, Denmark, 2015: pp. 1--9.

[2] N. Xie, R.A. Smith, S. Mukhopadhyay, S.R. Hallett, Mechanical Performance Modelling of Wrinkled Composites Based on NDT Data, in: 2nd China Int. Congr. Compos. Mater., Zhenjiang, China, 2015: pp. 1–12.

[3] N. Xie, R.A. Smith, S. Mukhopadhyay, S.R. Hallett, A numerical study on the influence of composite wrinkle defect geometry on compressive strength, Mater. Des. 140 (2018) 7–20. doi:10.1016/j.matdes.2017.11.034.

[4] R.A. Smith, L.J. Nelson, N. Xie, C. Fraij, S.R. Hallett, Progress in 3D characterisation and modelling of monolithic carbon-fibre composites, Insight - Non-Destructive Test. Cond. Monit. 57 (2015) 131–139. doi:10.1784/insi.2014.57.3.131.

[5] R.A. Smith, N. Xie, S.R. Hallett, Non-destructive characterisation of composite microstructures, JEC Compos. Mag. 53 (2016) 59–61.